UNIVERSIDADE FEDERAL DO RIO DE JANEIRO

INSTITUTO DE FÍSICA

Elastic and diffractive scattering of hadrons at high energies

Tese de Doutorado

Anderson Kendi Ramidan Kohara

Tese de Doutorado apresentada ao Programa de Pós-graduação em Física, Instituto de Física, da Universidade Federal do Rio de Janeiro, como parte dos requisitos necessários à obtenção do título de Doutor em Ciências (Física).

Orientador: Prof. Erasmo Ferreira

Co-Orientador: Prof. Takeshi Kodama

Co-Orientador: Prof. Cyrille Marquet

Rio de Janeiro

11/2015.

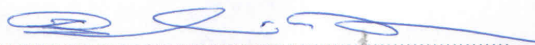# Elastic and diffractive scattering of hadrons at high energies

Anderson Kendi Ramidan Kohara

Erasmo Madureira Ferreira
Takeshi Kodama
Cyrille Michel Marquet

Tese de Doutorado submetida ao Programa de Pós-Graduação em Física, Instituto de Física, da Universidade Federal do Rio de Janeiro – UFRJ, como parte dos requisitos necessários à obtenção do título de Doutor em Ciências (Física). Aprovada por:

....
Prof. Erasmo Madureira Ferreira
(Presidente e Orientador)
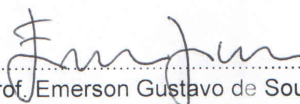
....
Prof. Takeshi Kodama
(Co-Orientador)
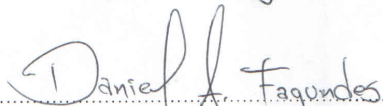
....
Prof. Cyrille Michel Marquet
(Co-Orientador)
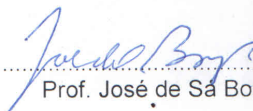
....
Prof. Marcio José Menon
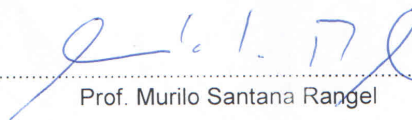
....
Prof. Emerson Gustavo de Souza Luna

....
Prof. Daniel Almeida Fagundes

....
Prof. José de Sá Borges Filho

....
Prof. Murilo Santana Rangel

Rio de Janeiro, RJ – Brasil
Dezembro de 2015

RESUMO

Espalhamento Elástico pp e pp̄

Anderson Kendi Ramidan Kohara

Orientadores: Erasmo Ferreira e Takeshi Kodama

Resumo da Tese de Doutorado submetida ao Programa de Pós-graduação em Física, da Universidade Federal do Rio de Janeiro - UFRJ, como parte dos requisitos necessários à obtenção do título de Doutor em Ciências (Física).
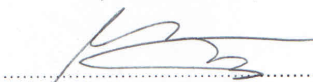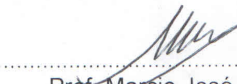
Neste trabalho de tese, investigamos processos de espalhamento elástico e difrativo em altas energias em colisões pp e pp̄.

Na primeira parte da tese estudamos o espalhamento elástico pp e pp̄ na região frontal, apresentando uma análise detalhada do processo, que é descrito por uma função complexa $F(s,t)$ de duas variáveis cinemáticas (variáveis de Mandelstam). Utilizamos as relações de dispersão derivadas para amplitudes e slopes (inclinações) em suas formas exatas e obtemos vínculos entre os parâmetros das partes real e imaginária. Criticando o tratamento das colisões elásticas feito pelo Particle Data Group (PDG) mostramos a necessidade de se analisar os dados experimentais levando em conta os efeitos de baixas energias nas relações de dispersão e as diferenças entre os valores dos slopes real e imaginário (B_R e B_I).

Para o tratamento dos dados em todos os valores t, utilizamos amplitudes baseadas no regime assintótico do modelo do vácuo estocástico, o qual é construído no espaço do parâmetro de impacto b, que é apropriado para a descrição geométrica dos processos de colisão. Como o espaço geométrico não é observável experimentalmente, é necessário passar ao espaço de momentos para descrever quantidades observáveis. Em nosso modelo a passagem das amplitudes $F(b,s)$ para $F(t,s)$ por transformada de Fourier é feita de forma analítica exata. Aplicando o modelo para cada uma das

energias existentes, estudamos sua dependência com a energia, mostrando que ela satisfaz os teoremas de Pomeranchuck generalizado, a forma assintótica do limite de Froissart-Martin, e obedecem os vínculos de unitaridade. Fazemos descrição de alta precisão para os experimentos do LHC a 7 TeV e apresentamos previsões para energias de futuros experimentos. Os parâmetros característicos das interações frontais são construídos obedecendo as relações de dispersão.

No estudo do comportamento das amplitudes no espaço geométrico mostramos que os dados de espalhamento pp para altas energias não seguem o comportamento assintótico de um disco negro. Os processos nas energias assintóticas podem ser descritos em termos de uma única variável combinando parâmetro de impacto e energia (propriedade de escala).

Aplicamos nossa análise ao espalhamento p-ar observado em raios cósmicos utilizando nossas amplitudes no formalismo de Glauber. Obtemos importantes previsões para os raios cósmicos, descrevendo os dados experimentais em um largo espectro de energia.

Comparamos nosso modelo com outros modelos teóricos, identificando diferenças e semelhanças. Entendemos que qualitativamente algumas propriedades das amplitudes são universais, devendo ser obedecidas por todos os modelos, tais como, a existência de pelo menos dois zeros da parte real e dois da imaginária. O deslocamento do primeiro zero real como função da energia obedece previsão de um teorema de André Martin. O segundo zero da parte imaginária somente aparece para muito alta energia e alto $|t|$.

Finalmente analisamos processos difrativos quasi-elásticos. Neste estudo investigamos a estrutura do Pomeron em termos de constituintes fundamentais da Cromodinâmica Quântica. Aplicamos as distribuições de partons difrativas medidas nos experimentos do acelerador HERA (DESY) em um simulador Monte Carlo para processos hadron-hadron do LHC e obtemos previsões para 13 TeV.

Ao longo de todo o trabalho de tese, insistimos no princípio de que os dados exper-

imentais devem ser estudados e descritos em termos de amplitudes de espalhamento com identificação explícita das partes real e imaginária. Essa descrição completa deve construir uma ponte entre teoria e experimento. Obtemos importantes previsões que podem auxiliar modelos teóricos e análises de futuros experimentos com raios cósmicos e aceleradores.

Palavras-chave: Espalhamento Elástico, Seção de Choque Diferencial, Seção de Choque Total, Relações de Dispersão.

Rio de Janeiro

11/2015

vii

Agradecimentos

Aproveito esta oportunidade para agradecer à pessoas envolvidas na minha formação pessoal e intelectual.

Comecei minha vida científica, trabalhando e aprendendo com o Professor Takeshi Kodama. Meses mais tarde fui apresentado ao Professor Erasmo Ferreira e então começamos a trabalhar juntos. Desde esse período aprendi muitas coisas com eles e levo para toda a minha vida conselhos importantes. Agradeço a Erasmo por muitas razões, em primeiro lugar, por ensinar-me os passos importantes para seguir na vida científica, tais como, compromisso, foco, persistência e paixão pelo trabalho e segundo, agradeço-lhe por ser um bom amigo durante todos esses anos. Do Professor Kodama adquiri conselhos relevantes desde o início e, cada vez que ia ao seu escritório para discutir sobre Física ali estava ele, trazendo 'luz' para nossas ideias. Considero-o um verdadeiro 'Samurai' em termos de ética, responsabilidade, precisão e disciplina. Agradeço-lhe por contribuir para minha formação profissional e, também, pela amizade. Agradeço a Murilo Rangel, Victor Gonçalves, Christophe Royon e Cyrille Marquet os esforços investidos em mim para fazer meu 'sanduíche' PHD, na École Polytechnique, em Paris. E em especial agradeço a Christophe e Cyrille pela recepção calorosa e conselhos durante minha estada na França.

Agradeço a muitos ótimos professores que tive durante a minha graduação em Física.

Agradeço a Daniella Szilard por me ajudar a construir o capítulo de comparação de modelos desta tese.

E como eu não quero perder um nome agradeço coletivamente a todos os meus amigos, na Universidade, todos esses anos juntos. Tivemos muitos bons momentos e discussões produtivas no corredor e na hora do almoço.

Agradeço aos meus pais, Tania e Yoshichi pelo apoio desde sempre. E, em especial, agradeço à minha mãe pela força incrível em manter a família unida e pelos valores que adquiri.

Agradeço a minha esposa Danielle por caminhar comigo em nossa jornada pela vida. O amor e a cumplicidade dedicada à nossa relação me faz forte e completo. Agradeço a seus pais Heloísa e Fernando por todos esses anos de solidariedade.

Agradeço aos meus irmãos Wagner, Richard e Mayer pela solidariedade absoluta e pela contribuição para o meu desenvolvimento pessoal.

Finalmente, agradeço ao Instituto de Física da Universidade Federal do Rio de Janeiro pela atmosfera de valores acadêmicos e científicos, e a CAPES e CNPQ pelo apoio financeiro e por todo o suporte para minha formação e aquisição de conhecimentos.

Acknowledgements

I take this opportunity to thank people involved in my personal and intellectual formation.

I started my scientific life working and learning with Professor Takeshi Kodama. A few months latter I was introduced to Professor Erasmo Ferreira and then we started to work together. Since this period I learned many things with them, and I received important advises. I thank Erasmo for many reasons, first, for teaching me important steps to follow in scientific life, such as, commitment, focus, persistence and passion for the work, and second, I thank him for being a good friend during all these years.

Kodama gave me important advices since the beginning. Each time I went to his office to discuss about physics he brought light to our ideas. He is really a 'Samurai' in terms of ethics, responsibility, precision and discipline. I thank him for contribute to my professional formation and also for friendship.

I thank Murilo Rangel, Victor Gonçalves, Christophe Royon and Cyrille Marquet for the efforts invested in me to do my sandwich PHD in France at École Polytechnique. Especial thanks to Christophe and Cyrille for the warm reception and advices during my stay in France.

I thank many excellent teachers I had during my graduation in physics.

I thank Daniella Szilard for helping me to construct the chapter of comparison of models of this thesis.

As I don't want to miss a name I thank collectively all my friends at the university for all these years together. We had many good moments and productive discussions in the corridor and at lunch time.

I thank my parents, Tania and Yoshichi for the support since ever. I specially thank my mother for the incredible strength in keeping family together.

I thank my wife Danielle for walking with me in our life journey. The love and complicity dedicated to our relationship makes me strong and complete. I thank her

parents Heloisa and Fernando solidarity in all for all these years together.

I thank my brothers Wagner, Richard and Mayer for the absolute solidarity and the contribution to my personal development.

Finally, I thank the Institute of Physics of UFRJ for the atmosphere of academic and scientific values, and CAPES and CNPQ for the financial support.

Contents

Chapter 1

Theory and phenomenology of strong interactions

The study of strong interactions has been a permanent challenge for almost one century suffering from the absence of a fundamental theory, and only recently Quantum Chromodynamics (QCD) is universally accepted as its fundamental basis. QCD was formulated in the early 70's in terms of a non-Abelian gauge field theory (Yang-Mills theory) with SU(3) color symmetry [1], [2]. Ref. [3] gives a short historical review of the emergence of QCD, written by one of its founders. The dynamical degrees of freedom are fields of quarks and gluons, with the Lagrangian density

$$\mathcal{L}_{QCD} = \sum_f \bar{\mathbf{q}}^{(f)} \left[i\gamma^\mu \hat{D}_\mu - m_f \right] \mathbf{q}^{(f)} - \frac{1}{4} \hat{F}_{\mu\nu}(x) \, \hat{F}^{\mu\nu}(x) , \qquad (1.1)$$

where $\bar{\mathbf{q}}^{(f)}$ is Dirac spinor field for the quark of flavor f (there are six flavors), with mass m_f, having the vector structure in color space,

$$\mathbf{q}^{(f)} = \begin{pmatrix} q_1^{(f)}(x) \\ q_2^{(f)}(x) \\ q_3^{(f)}(x) \end{pmatrix} , \qquad (1.2)$$

and $\hat{D}_\mu$ is the covariant derivative defined as

$$\hat{D}_\mu = \partial_\mu - ig\hat{A}_\mu \ . \tag{1.3}$$

Here, $\hat{A}_\mu$ denotes the gluon field in the (3×3) Hermitian matrix form, which can be represented as

$$\hat{A}_\mu = \sum_{a=1}^{8} \hat{\tau}^a A_\mu^a(x) , \tag{1.4}$$

where $\{\hat{\tau}^a\}$ are 8 generators of the SU(3) color group in the fundamental representation $(3 \times 3$ matrices$)$. The set of Lorentz 4-vectors $\{A_\mu^a(x)\}$ represents 8 gluon fields in the adjoint representation with corresponding color indices a.

The gluon field strength (which corresponds to the color electromagnetic field) $\hat{F}_{\mu\nu}$ is defined as the commutator of the covariant derivatives,

$$\hat{F}_{\mu\nu} = \hat{\tau}^a F_{\mu\nu}^a = \frac{i}{g}\left[\hat{D}_\mu, \hat{D}_\nu\right] , \tag{1.5}$$

with g being the strong coupling constant. Using the structure constants of the group $\{f^{abc}\}$, we can also write

$$F_{\mu\nu}^a = \partial_\mu A_\nu^a - \partial_\nu A_\mu^a + g\sum_{b,c=1}^{8} f^{abc} A_\mu^b A_\nu^c \ . \tag{1.6}$$

From the mathematical point of view, QCD is a beautiful and direct extension of Quantum Electrodynamics (QED), constructed by generalization of the gauge symmetry from the gauge group U(1) to SU(3). The color quantum numbers play the role of the electric charge of Electromagnetism.

However, there are several fundamental differences between QCD and QED. First of all, the basic degrees of freedom of QCD are fields of quarks and gluons, and differently from electron and electromagnetic fields in Electrodynamics, they are not observable particles in isolated form. Physically observable strongly interacting

particles (hadrons) are colorless composite objects formed by quarks and gluons, constructed by QCD dynamics.

Another important difference is that the gluons, which play the role of photons in Quantum Electrodynamics (QED), interact with themselves. This self interaction comes from the non-linear terms in Eq.(1.6). These two aspects lead to crucial differences from the well-established QED, and we are submitted to these differences throughout this thesis. For the sake of bookkeeping, we list below some basic properties of QCD without any demonstration (some of them are not even proven). For more details, we refer to text books [4], [5].

1. In a quantum field theory, the perturbative scheme is performed in terms of the degrees of freedom of the theory. Thus, in QCD, the perturbation scheme is applied to the dynamics of quarks and gluons.

2. The vacuum state of the QCD degrees of freedom (the state defined as null eigenstate for quark and gluon number operators, which is simply called QCD vacuum) is not the physical vacuum of the world described by QCD, which is defined as the ground state of the system described by the theory. The structure of the physical vacuum state is not reachable in terms of perturbation theory from the QCD vacuum.

3. All known hadrons are composed as color singlet states in terms of a minimum number of quarks, which are referred to as valence quarks. There are two classes of hadrons: the baryons, which correspond to the totally color antisymmetric states of three quarks (or anti-quarks), and the mesons, composed by a quark and an antiquark, also in color singlet states. Possible existence of hadrons without valence quarks is suggested as glueballs, but this existence is not yet confirmed.

4. Isolated quarks or gluons are not observable in Nature. This is an empirically established fact. QCD degrees of freedom are confined inside hadrons in such a way that any physically observable object should be in the state of null color charge. This (assumed) property of QCD is called "confinement".There are several indications, but

a general proof of the confinement mechanism of QCD is not known yet.

5. It has been shown [6], [7] that the running coupling constant of QCD decreases as $\sim 1/\ln(Q^2)$, where Q^2 is the momentum transfer squared. This property is called "asymptotic freedom", which permits the use of perturbative schemes for the dynamics of quarks and gluons at very high energies.

6. An ab-initio non-perturbative method, the lattice QCD framework (lQCD) [8], has been extensively developed for the study of the physical vacuum and its spectrum and of the hadronic structure. However, is spite of admirable efforts and progresses the reliable results on hadronic properties still remain limited.

7. Although the explicit dynamics of quarks and gluons is not apparent in the hadronic world due to the confinement, properties of the physical vacuum become more and more important at high energies, mapping non-perturbative and perturbative aspects of QCD, entangled in a complicated way in the dynamics of hadronic collision processes.

8. In spite of this entanglement, factorization theorems of QCD [9] in hard collisional processes allow a separation of interactions into scales of short and large distances. Due to factorization theorems, the high energy behavior of hadronic interactions can be discussed quantitatively by combining the short scale partonic cross sections, calculated perturbatively in QCD, with long range, non-perturbative ingredients of hadronic properties such as parton distribution functions (PDFs).

9. In some reactions, very energetic quarks or gluons are ejected out of the hadronic domain, but they excite the physical vacuum along their trajectory and eventually turn into a sequence of hadrons, which are observed as "jets". Jets are considered as direct signals of the hard scattering of quarks and gluons (partons).

10. When a sufficient amount of energy is deposited into a finite domain of space-time reaching the thermodynamic equilibrium, then the quarks (anti-quarks) and gluons are excited from the physical vacuum and melt into the so-called plasma of quarks and gluons (QGP), giving way to thermodynamical degrees of freedom that

can be used to describe the system. Such a plasma state is supposed to have been created in the beginning of the Universe, and during the last decade these appeared evidences that such a state is created in laboratory in ultra-relativistic collisions of heavy ions. These evidences are considered as indication that the physical vacuum is composed of quarks and gluons.

Having the above aspects of QCD in mind, in this thesis we study the high energy behavior of proton-(anti)proton (pp, p$\bar{\text{p}}$) scattering processes in terms of a QCD based model for the scattering amplitudes, in particular, their elastic scattering amplitudes. Elastic scattering processes hold a very unique position in the study of high energy hadronic collisions. First of all, for a given center of mass energy, $\sqrt{s}$, elastic scattering is completely specified just by a single complex function $F(\sqrt{s}\,;t)$ of one unique variable t, the four-momentum transfer squared. Once this complex function is known, we can express the integrated elastic cross section, σ_{elas}, and using the optical theorem, the total cross section σ, and hence the total inelastic cross section σ_{inel} . Furthermore, general properties required for the scattering amplitudes such as unitarity give some constraints on the functional behavior.

In classical physics, when two massive composite objects collide very energetically, the fraction of elastic processes, in which the incident objects survive, becomes very small, as we usually see in everyday life. When we hit two water glasses against each other violently, they certainly break into many pieces. A first intuitive classical estimate would lead that the ratio of the integrated elastic cross section to the total cross section, $\sigma_{\text{elas}}/\sigma$, would decrease as $\sim 1/n$, where n is the number of the open inelastic channels at that energy.

However, in quantum mechanics, particles behave as waves and the above argument does not hold. For example, as it is well-known, the high energy limit of the total cross section of a particle, scattered by a potential corresponding to a complete black disk is just twice the geometrical cross section of the disk. A black disk is somewhat equivalent to the system in which, for any impact parameter, there is

an infinite number of inelastic channels. The factor 2 comes from the two different ways of modifying the incident wave: in one, the absorption from the incident plane wave excites inelastic processes inside the disk, and in the other a diffracted wave is created to refill the shadowed region behind the disk. This last process gives rise to a sharp peak in the differential cross section in the very forward domain. Such a peak can be observed in the case of scattering of light by a black disk as a bright spot at the center of the shadow, known as Poisson's bright dot, and is a general feature of the mechanism of scattering of waves. Thus, it is also expected that such a view for elastic scattering of p-p (p-p̄) at very high energies might be valid, since at very high energies the internal structure becomes less important and only the geometrical extension of the matter is expected to be relevant. In fact, the differential elastic cross section has a sharp peak in the forward region, followed by a complex diffractive structure for larger values of the momentum transfer (larger scattering angles). However, the factor between total and integrated elastic cross section is not 2, showing that black disk does not provide a realistic description of hadronic scattering. Thus, naively speaking, one might attribute the sharp forward peak behavior of the differential cross section as the result of a diffraction from a (an almost) black-disk nature of the proton structure at very high energies, representing the opening of many inelastic channels within their interaction distance. That is, the elastic process could be expected as the diffraction of the incident waves scattered by an opaque object. In such an image, we would expect that from the analogy in the black disk potential, the total cross section at very high energy would tend to a constant value, corresponding to the geometrical size of a proton. However, with the advent of new accelerators in the early 60´s which were able to measure the total cross section of p-p (p-p̄) above 20 GeV, such a naive picture was forced to encounter a great surprise. There, although the total cross sections of p-p and p-p̄ are started to converge to become equal as conjectured in the theorem of Pomer-

anchuck $[10, 11]^1$, their values do not stay constant and increase with the incident energy.

From the pure theoretical point of view, the possibility that the asymptotic behavior of p-p (p-p̄) cross section does not necessarily converges to a finite constant value was not discarded within the framework of the S-matrix theory developed in mid 50´s. The S-matrix approach was intensively studied in order to circumvent the incapability of field theoretical approaches for strong interactions before QCD was discovered. The behavior of the total cross section indefinitely increasing as function of the incident energy is really difficult to understand in terms of a simple non-relativistic quantum mechanical model of p-p interactions. On the other hand, in a relativistic field theory where infinite degrees of freedom can participate in the scattering process, this possibility is already perceived, because the proper renormalization scheme and resulting effective coupling constant (form factor) may depend on the energy scale. However, there was no concrete quantitative theory in the pre-QCD era, since the strong interactions were not treatable within a framework of quantum field theories known at that time.

The experimental discovery of increasing total cross sections opened great interest in the high energy phenomenology of the scattering amplitude within the S-matrix formalism. As mentioned above, in the theoretical scheme of general S-matrix theory, the possibility that the total cross section does not stay constant at high energies had already been noticed. Among others, we cite the works of T. Regge, L. Pomeranchuck, Froissart, Martin and Luckaszuk, who studied the possibility of the increase of the cross section in terms of the structure of the S matrix.

The theoretical structure in the study of the bound on the total hadronic cross section has passed through several improvements since the first formulation. In particular, Froissart [12] derived the upper-bound of the total cross section as function

---

[1]The theorem states that in $A+B$ and $\bar{A}+B$ collisions, if both of cross section tends to constant at the limit of infinite incident energy, the two cross sections should approach the same value. H. Miyazawa also arrived at the same theorem in the same year as Pomeranchuck, as published in a Japanese journal.

of energy, known as Froissart (or unitarity) bound (1961), which states that as far as unitarity of the S-matrix is satisfied, the p-p (p-p̄) cross section is bounded as

$$\sigma\left(s\right) \sim \mathrm{C} \times \ln^2 \sqrt{\frac{s}{s_0}}, \quad s \gg s_0 \tag{1.7}$$

where C and s_0 are unknown constants. This theorem was first proved assuming the Mandelstam representation. This assumption might not be valid, for example, if there are rising Regge trajectories. Later (1966) Martin proved the bound rigorously in a much more general framework of axiomatic local field theory as applied to hadrons [13]. Then Lukaszuk and Martin (1967) wrote the bound [14] in the form

$$\sigma_{\mathrm{tot}} \leq \frac{4\pi}{(t_0 - \epsilon)} \log^2(s/s_0) \equiv \sigma_{\mathrm{max}} \tag{1.8}$$

where t_0 is the next singularity and ϵ is nonzero and arbitrarily small. The bounds are written in terms of a quantity σ_{max}, where s_0 and ϵ are unknown quantities.

Some difficulties remained in the proofs of bounds, due to assumptions not rigorously proved. In a recent paper [15] the authors claim that the shortcomings (such as the unknown constants) were removed. Martin and Roy study specifically the $\pi_0\pi_0$ system, and establish bounds for an energy average of the total cross section free of the quantity ϵ, and relate the scale s_0 with a property of the system in the t-channel (D-wave scattering length).

The paper shows that for c.m. energy $\sqrt{s} \to \infty$, the weighted average of the cross section defined by

$$\bar{\sigma}(s, \infty) = s \int_s^\infty \frac{ds'}{(s')^2} \sigma_{\mathrm{tot}}(s\prime) \tag{1.9}$$

is bounded by

$$\bar{\sigma}(s, \infty) \leq \frac{\pi}{m_\pi^2} \left[\log(s/s_{\mathrm{sc}}) + (1/2)\log\log(s/s_{\mathrm{sc}})\right]^2 . \tag{1.10}$$

The constant quantity

$$C = \frac{4\pi}{4m_\pi^2} = \frac{4\pi}{|t|_0} \tag{1.11}$$

is determined by the position of the nearest t channel singularity $|t|_0$ in $\pi\pi$ scattering.

The value of the scale s_{sc} depends on the hadron-hadron system studied. For the $\pi\pi$ system, the predicted value is

$$\frac{1}{s_{\text{sc}}} = 17\pi\sqrt{\frac{\pi}{2}}\frac{1}{m_\pi^2} \ . \tag{1.12}$$

However, compared to the phenomenology and data in $\pi\pi$ scattering, the bounds are too high, so the the s_{sc} is unrealistic, or the bound is not useful.

Nowadays it is known that the behavior of the collision processes at high energies is intimately related with the structure of the physical vacuum of QCD. Actually, studying the elastic scattering amplitudes in terms of a QCD based model, we are able to extract important information which may clarify the role of the physical vacuum. The pioneering work in this direction was done by H.G. Dosch, E. Ferreira and A. Kramer in 1992-1994 [16], incorporating the behavior of the correlation function of the Wilson loops of QCD obtained in the Stochastic Vacuum Model [17], and calculating total cross sections and forward slope, for baryon-baryon and meson-baryon for fixed energy. In subsequent works [18], [19], the profile functions of the scattering amplitude based on the SVM were studied in detail with analytical form in terms of the impact parameter. These studies gave the complete b and consequently t dependence of the pp amplitudes.

In the present work, we further pursuit in detail this approach and perform the detailed analysis of the experimental data up to the highest energies available from LHC and cosmic ray experiments, building a complete and natural energy dependence for our model. From this analysis, we arrive at complete analytic expressions for $F(s,t)$ [20,21]. The most important point of our approach is that, different from a simple phenomenological model that to be ajusted to the experimental data, we

work with the complex amplitudes extracted from the QCD based theory, and from this, we propose a disentanglement, from the experimental data of the contributions of the real and imaginary parts of the amplitude.

Other observations in p-p (p-p̄) scattering show that there exist inelastic channels in which the final state protons (the so-called *leading particles*) exhibit a very similar behavior to those of the elastic scattering case. We refer to those events as diffractive inelastic processes. Differential cross sections of these events are characterized by a very steep angular distribution of the final state protons as seen in the elastic channels, but the rapidity distribution of associated produced hadrons is characterized by the presence of a large gap, differently from non-diffractive inelastic events. Furthermore, the multiplicities of produced particles are rather small compared to the average multiplicity. The presence of such a large rapidity gap suggests that no color charge flow occurs in such events. This occurs because, due to the confinement, it is very difficult to produce hadrons with a large momentum gap in terms of perturbative, hard QCD process. This is exactly the case of elastic scattering, where there is no color exchange between the two protons (naturally, the rapidity gap between the two protons in the elastic channel is the largest possible). This characteristic property of the diffractive events suggest that they can be considered as the excitation of one of the protons (single diffractive) or both (double diffractive) associated with their diffractive scattering, with subsequent decay with emission of hadrons. Thus, the basic scattering mechanism may be almost the same as elastic scattering. In spite of the similarities with elastic scattering, our present formulation does not describe the inelastic channels.

It is more than 40 years since the unified approach to deal elastic and diffractive inelastic scatterings has been proposed in terms the exchange of a hypothetical particle in t-channel, called Pomeron [22], within the Regge Pole approach [23]. Pomeron is assumed to be a colorless object and have different excitation spectra compared to a normal hadron. Several phenomenological schemes under this hypothesis have

been studied extensively. In terms of QCD, it is suggested that Pomeron might be classified as member of the family of glueballs [22].

In recent studies, the QCD-based technique of evolution equations in the rapidity space to obtain the gluon distribution function plays the central role in the description of the structure of Pomerons [4]. On the other hand, this approach has several aspects in common with the Stochastic Vacuum Model, in which our scattering amplitudes are constructed, although our model does not starts with the presence of Pomeron explicitly. Aiming to understand in future how the Pomeron approach can be understood within our approach and extend the model to inelastic processes, we present several studies within the scheme of so-called "Resolved Pomeron Model" [24] developed during the author´s visit to Ecole Polytechnique within the Sandwich Graduate Program of the CAPES, Ministry of Education, Brazil in Collaboration with Dr. Cyrille Marquet.

1.0.1   Contents of the Thesis

The structure of this thesis is as follows. In Chapter 2, we describe concisely the formalism of our model for elastic scattering. For this purpose, we first introduce basic ingredients and variables, such as S-matrix and its analytic properties, dispersion relations, and eikonal representation. More details are given in Appendix A. We then sketch the basic concepts of the Stochastic Vacuum Model (SVM) to represent the correlation functions of Wilson loops. These correlation functions are associated to the imaginary part of the scattering amplitude of colored objects, and implemented to construct the S-matrix elements through the eikonal representation (impact parameter space). There, we write the scattering amplitudes as convolution of the distribution of colored objects inside the colliding hadrons with the eikonal amplitude given by SVM. From this, the asymptotic behavior of hadron-hadron amplitudes for all b is studied. The basic ingredients of the interaction, representing non-perturbative properties of the QCD vacuum is the gluon condensate. On the

other hand, phenomenologically it is known that the very forward scattering amplitudes are well characterized by its exponential dependence in t, corresponding to a Gaussian form of the profile function in b-space. To satisfy this phenomenological boundary condition, we introduce an interpolating formula as the sum of the Gaussian distribution form, and the distribution which has asymptotic behavior given by SVM, the so-called shape function, which represents properties of QCD vacuum field and has more extended range in b-space. This term describes the deviation from a pure Gaussian form typical of Pomeron physics framework, for finite values of b. To give full treatment in b-space, four real parameters are introduced in each real and imaginary part of the amplitude for a given energy. These parameters depend on the energy scale involved, since they somewhat represent the effective distribution of the scattering centers, which are to be determined from the experimental data. SVM describes how the vacuum behaves as the mediator of the interaction among these scattering centers. The $F(s, t)$ amplitudes are obtained analytically by Fourier Transform. In the present work we determine the energy dependence of the amplitudes as functions of the energy, to obtain a full, analytic expression of scattering amplitudes for any values of s and t.

Before the analysis for the construction of the scattering amplitude for all s and t values, in Chap.3 we pay special attention to a detailed analysis of the experimental data in the forward region, that imposes important constraints for the behavior of the amplitudes for all t, and gives connection between real and imaginary parts through Dispersion Relations (DR). Careful analysis of the forward scattering amplitudes using data at several energies is made. The use of the dispersion relations is shown to be very important and with the correct Coulomb interference terms, we show in fact that both real and imaginary parts should be treated as independent exponential functions in t, as treated in our approach for the full-t amplitudes.

In Chap.4 we proceed to study the energy dependence of the parameters introduced in the full amplitudes presented in Chap.2. For this purpose, the wide-range t

dependence of the observed data is carefully investigated, especially paying attention to the behavior of dips and bumps in the differential cross section, in addition to the forward scattering behavior. We show that the complex amplitude near the first zero of the imaginary part is connected to the position and the forms of dips and bumps, as was first discussed in Ref. [19]. Properties of the real part are studied, and it is shown that they play crucial role in the determination of the behavior of the dip, bump and tail (where the imaginary part is not totally dominant as in the forward direction). After analyzing all data for available energies up to 7 TeV, we find that the energy dependence of the parameters behave very regularly and smoothly. This permit us to construct analytic expressions of these parameters, imposing constraints from the unitarity conditions. Energy dependence of some of them are clearly given by a straight line or a quadratic curve in $\ln s$. After determining this energy dependence, a kind of iterative analysis for the rest of parameters is made, with the help of constraints imposed by the unitarity and DR. This process converges to express all parameters as simple analytic forms in $\ln s$, and the final form of the amplitude $F(s; t)$ is written for arbitrary values of s and t. Using this amplitude (referred to as KFK, from Kohara-Ferreira-Kodama) [20, 21], we compare the predicted values of total and differential cross sections to the data obtained recently for $\sqrt{s} = 7$ and 8 TeV.

In Chap.5 we discuss the properties of KFK amplitudes in b-space. We found that the profile functions at high energies show precise geometrical scaling. We further obtain that profile function is not that of a sharp black disk, but rather possesses an appreciable diffused surface structure. This leads to a prediction that the asymptotic value of the ratio, $\sigma_{\text{elas}}/\sigma$ does not converge to $1/2$, but to a smaller value (about $1/3$). We compare this result with other work [25].

In Chap.6, using the advantage of simple, explicit analytical expressions of the amplitudes, we apply them to the calculation of proton-nucleus within the Glauber formalism and compare results [26] with the cosmic ray data [27–34]. We also

discuss the geometric properties and asymptotic behavior of the p-A cross section in the Glauber model, obtaining a finite asymptotic limit for the $\sigma_{\mathrm{pp}}/\sigma_{\mathrm{p-air}}$ ratio.

In Chap. 7 we perform a comparative study of our model with other known models frequently used in the literature, showing similarities and differences, which can be checked in future experiments.

In Chap. 8, as an additional study to the analysis of the elastic scattering amplitudes, we present an analysis developed within the framework of the Resolved Pomeron Model. We investigate the double Pomeron exchange process leading to prompt photon production.

Chap. 9 is dedicated to the discussion and perspectives of our line of work.

Chapter 2

Elastic scattering: amplitudes in the Stochastic Vacuum Model

In this chapter we describe elastic scattering of hadrons in terms of the S-Matrix formalism. The scattering amplitudes are complex quantities functions of two kinematical variables s and t. Causality and analyticity constrain the real and imaginary forward parts through dispersion relations (DR). Many models describe the scattering amplitudes, but still, no solution covers all experimental data with high precision. At high energies and small momentum transfer the eikonal representation of the collision processes is natural, since in this regime the system accepts a geometrical description. After presenting the general properties, we present the basis of the scattering amplitudes in the framework of the Stochastic Vacuum Model (SVM), mentioning the main references.

2.1   S-matrix and transition amplitudes

In a quantum mechanical system, the transition amplitude from an initial to a final state ($|i\rangle \rightarrow |f\rangle$), is described by the S-Matrix, which is a unitary operator

containing all the dynamical information involved in the collision process,

$$|f\rangle = \hat{S}\,|i\rangle \; . \tag{2.1}$$

Given the initial state $|i\rangle$, the probability of finding a final state $|f\rangle$ is

$$P_{fi} = |\langle f|\hat{S}|i\rangle|^2 \; , \tag{2.2}$$

and the completeness relation summing over all possible final states is

$$\sum_f |f\rangle\langle f| = 1 \; . \tag{2.3}$$

The probability of finding any final state is 1, so that

$$\sum_f P_{fi} = \langle i|\hat{S}^{\dagger}\Big(\sum_f |f\rangle\langle f|\Big)\hat{S}|i\rangle = \langle i|\hat{S}^{\dagger}\hat{S}|i\rangle = 1 \; , \tag{2.4}$$

which implies $\hat{S}^{\dagger}\hat{S} = \hat{1}$, and, $\hat{S}$ is unitary matrix.

The S-matrix can be written in terms of non-interacting and interacting parts

$$\hat{S} = \hat{1} - i\hat{T} \; , \tag{2.5}$$

and the matrix elements are written

$$S_{fi} = \langle f|\hat{S}|i\rangle = \delta_{fi} - i\,(2\pi)^4\delta^4(P_f - P_i)\,T_{fi} \; , \tag{2.6}$$

with $\delta_{fi} = \langle f|i\rangle$ representing the absence of interaction and $(2\pi)^4\delta^4(P_f - P_i)T_{fi} = \langle f|\hat{T}|i\rangle$ is the non-trivial part representing the interaction term. The variables P_f and P_i are the final and initial total linear 4-momentum of the particles. The transition

rate per unity volume is defined by

$$R_{fi} = (2\pi)^4 \delta^4(P_f - P_i) \, |T_{fi}|^2. \tag{2.7}$$

The sum over all final states of the transition rate divided by the incident flux of particles gives the total cross section

$$\sigma_{\text{total}} = \frac{1}{j} \sum_f R_{fi}, \tag{2.8}$$

where the flux of incident particles is given by the relative velocity of incident beams multiplied by the volumetric density. The flux written

$$
\begin{aligned}
j &= |\vec{v}_1{}^* - \vec{v}_2{}^*| 2E_1^* \, 2E_2^* = \left| \frac{\vec{p}_1{}^*}{E_1^*} - \frac{\vec{p}_2{}^*}{E_2^*} \right| 2E_1^* \, 2E_2^* \\
&= |\vec{p}_i{}^*| \left[\frac{E_1^* + E_2^*}{E_1^* E_2^*} \right] 4E_1^* E_2^* = 4p_i^* \sqrt{s} \ ,
\end{aligned} \tag{2.9}
$$

is a quantity invariant under a Lorentz boost. The superscript * denotes the quantity in the CM frame as defined in Appendix A. Combining Eq.(2.9) and Eq. (2.8), the total cross section is written

$$\sigma_{\text{total}} = \frac{1}{4p_i^* \sqrt{s}} \sum_f R_{fi} \ . \tag{2.10}$$

Essentially, the total cross section represents the sum over all possible events observed in the final state per unit flux, unit volume and unit time.

2.1.1 Optical theorem

Using the unitarity condition we have

$$\langle k | \hat{S}^\dagger \hat{S} | i \rangle = \delta_{ki} \ , \tag{2.11}$$

and it follows

$$\langle k|\hat{T}|i\rangle - \langle k|\hat{T}^\dagger|i\rangle = i\sum_f (2\pi)^4 \delta^4(P_K - P_f)\langle k|\hat{T}^\dagger|f\rangle\langle f|\hat{T}|i\rangle \ . \qquad (2.12)$$

Considering the case where the final state is equal to the initial state $|k\rangle = |i\rangle$,

$$2\,\mathrm{Im}\langle i|\hat{T}|i\rangle = \sum_f R_{fi} \ . \qquad (2.13)$$

Eq. (2.10) then becomes

$$\sigma_{\text{total}} = \frac{\mathrm{Im}\langle i|\hat{T}|i\rangle}{2p_i^*\sqrt{s}} \ . \qquad (2.14)$$

The condition that the final state is equal the initial state, with the transferred momentum $t = 0$, gives

$$\sigma_{\text{total}} = \frac{\mathrm{Im}\ F(s, t=0)}{2p_i^*\sqrt{s}} \simeq \frac{\mathrm{Im}\ F(s, t=0)}{s} \ , \qquad (2.15)$$

where we define $F(s, t) \equiv \langle f|\hat{T}|i\rangle$ and have introduced the high energy approximation $\sqrt{s} \simeq 2p_i^*$. This expression is the optical theorem that relates the total cross section with the imaginary amplitude at $t = 0$ for a given energy.

2.1.2   Differential cross section

For the elastic channel, the scattering differential cross section describes the angular dependence of the probabilities of the scattered particles. An infinitesimal cross section element is written

$$d\sigma = \frac{|F(s, t)|^2}{4p_i^*\sqrt{s}}d\Gamma \ , \qquad (2.16)$$

where $d\Gamma$ is the relativistic invariant phase space

$$d\Gamma = \frac{1}{4\pi^2}\frac{p_f^*}{4\sqrt{s}}d\Omega \ , \qquad (2.17)$$

with $d\Omega = \sin(\theta_{\mathrm{cm}})d\theta_{\mathrm{cm}}d\phi$. The relation between the variables Ω and t is obtained using Eq. (A.19)

$$dt = -\frac{|\vec{p}_f^{\,*}|^2}{\pi}d\Omega \ , \tag{2.18}$$

and then

$$\frac{d\sigma}{d|t|} = \frac{1}{16\pi s(s - 4m^2)}|F(s,t)|^2 \simeq \frac{1}{16\pi s^2}|F(s,t)|^2 \ . \tag{2.19}$$

$F(s,t)$, is a complex function which must be studied in detail for the complete description of scattering dynamics. Part of our work is devoted to the study of the analytical properties of this amplitude and its behavior in s and t variables.

2.1.3 Analyticity and dispersion relations

The scattering amplitudes are described by a complex function of two variables, say E and t, where E is the incident particle energy in the lab system. In pp (p$\bar{\mathrm{p}}$) scattering at high energies we may use the relation with the cm energy $s \simeq 2\,m\,E$ where m is the proton mass. Relations are given in Appendix A. The basic assumptions usually made on the scattering amplitudes are that they are analytical and causal. In spite of the apparent distinction between these two features, they are related with each other. Another important assumption is that the singularities appearing in the complex energy plane are associated with properties of the dynamical processes, with the association of poles to bound states or resonances in the intermediate states. Cuts, connected with branching points, are associated with thresholds of n particle states in the final states. Under these assumptions, dispersion relations (DR) connecting the real and imaginary amplitudes in the forward direction can be written.

In Appendix B we derive the integral DR from first principles. For pp and p$\bar{\mathrm{p}}$ scattering we write the integral DR with one subtraction constant in terms of even

and odd amplitudes respectively

$$\mathrm{Re}\, F_+(s,u) = K + \frac{2}{\pi}s^2\mathbf{P}\int_{2m^2}^{\infty}\frac{\mathrm{Im}\,F_+(s')}{s'(s'^2-s^2)}\,ds'\ ,\qquad(2.20)$$

$$\mathrm{Re}\, F_-(s,u) = \frac{2}{\pi}s\mathbf{P}\int_{2m^2}^{\infty}\frac{\mathrm{Im}\,F_-(s')}{s'^2-s^2}\,ds'\ ,\qquad(2.21)$$

where m is proton mass and

$$F_+(s,u) \equiv [F(s,u)_{\mathrm{pp}\to\mathrm{pp}} + F(u,s)_{\mathrm{p\bar{p}}\to\mathrm{p\bar{p}}}]/2\qquad(2.22)$$

and

$$F_-(s,u) \equiv [F_{\mathrm{pp}\to\mathrm{pp}}(s,u) - F_{\mathrm{p\bar{p}}\to\mathrm{p\bar{p}}}(u,s)]/2\ .\qquad(2.23)$$

2.1.4 Derivative dispersion relations

The calculation of principal value integrals are usually treated by algorithms executing a large number of mathematical operations. One alternative to the usual integral DR are the Derivative Dispersion Relations (DDR) whose expressions were originally written in a very high energy approximation in terms of trigonometric functions, with spurious singularities for certain parameter values with divergent terms, and poor approximation with DR for low energies. For several years these forms were extensively used in the literature. In Ref. [35] the authors derived for the first time the exact forms for DDR representing the original integral dispersion relations (IDR). The new forms were expressed in terms with logarithm and trigonometric functions plus series of double sums of derivatives. The double sums are mathematically complicated to calculate and it is difficult to prove their convergence. This problem was solved in [36], where the double sums where reduced to single sum for appropriate forms of the imaginary amplitudes. Then, independent derivation of exact DDR forms was presented [37], with identification of reasons for

apparent singularities, and practical final forms written.

For practical applications in phenomenology the exact DDR are more efficient to treat the imaginary inputs. From the Froissart-Martin Theorem [12], the behavior of total cross section becomes simple at high energies, being limited asymptotically by a $\log^2(s)$ form. From the experimental data analysis one can obtain a parametrization for the total cross section and by the optical theorem we write the forward imaginary amplitude as function of s. Then, the DDR gives the real amplitude at $t = 0$. An extension of the DDR for the first derivative of the imaginary amplitude with respect to t close to $t = 0$ gives the real slope B_R [38], once the imaginary slope B_I is given as function of s. This second form of DDR depends on the input for the imaginary slope as function of the energy.

In the model discussed in this thesis the analytical forms of inputs are simple powers of $(s^\lambda \log^n s)$ with n being an integer number and λ a real number in the range $-1 < \lambda \le 0$. In Pomeron-like models, terms with $\lambda > 0$ occur.

For practical applications we define the Principal Value (PV) integrals

$$I(n, \lambda, x) = \mathbf{P} \int_1^{+\infty} \frac{x'^\lambda \ \log^n(x')}{[x'^2 - x^2]} dx' \ . \tag{2.24}$$

The phenomenology demands us to compute terms with $n = 0, 1, 2, 3, 4$ and $-1 < \lambda \le 0$. In Appendix B we consider the 5 cases of n and we show the mathematical properties of the exact forms of the DDR.

2.1.5 Eikonal framework

Many phenomenological models have been proposed to describe pp and p$\bar{\text{p}}$ elastic scattering. Some models are based on the exchange of particles in the t-channel, and others emphasize the energy dependences of the S-matrix poles and cuts. Following E. Predazzi and V. Barone [23], we refer to the first type as t-channel models and the second kind as s-channel models. The well-know approach of a t-channel model

is the Regge-pole theory, based on properties in the complex angular momentum plane, with association of singularities to reggeons (families of mesons, baryons) and Pomeron exchanged in the t-channel. These reggeons and Pomeron determine the behavior of the scattering amplitudes in the s-channel. No prescription is assumed for the t-dependence of the complex poles.

On the contrary, the eikonal approaches are examples of s-channel models. In this class of models the t dependence is obtained from the Fourier transform of amplitudes first written in geometric impact parameter space. In this framework, it is easy to impose the unitarity constraint. However, the energy dependence is usually not specified a priori, and must be incorporated by phenomenology or theoretical assumptions.

Both classes of models have merits and shortcomings in the description of experimental data. In spite of the large variety of attempts, so far, no model combines the s and t behavior in a satisfactory and complete way based only on fundamental principles.

In this thesis we work with a model first built in the eikonal framework. Through Fourier Transform we pass to the s, t space and construct the energy dependence of the model analysing experimental data of differential cross sections. We also compare our amplitudes with other models built using the same eikonal framework.

To introduce the eikonal formalism, we here mention its basic ingredients. We start with partial wave expansion scattering amplitude in s-channel

$$F(k^*, \theta_{k^*}) = 4 \sum_l (2l + 1) \, a_l(k^*) \, P_l(\cos \theta_k) \, , \qquad (2.25)$$

where k^* is the incident linear particle momentum, l is the angular momentum, P_l is the Legendre Polynomial of first kind, θ_{k^*} is the scattering angle between the incident and the scattered particles in the CM frame and $a_l(k^*)$ is the partial wave

amplitude, which can be written,

$$a_l(k^*) = i(1 - S_l) \ , \tag{2.26}$$

with $S_l = e^{2i\delta_l(k^*)}$ being the matrix element of S-Matrix in angular momentum representation, and $\delta_l(k^*)$ is the complex phase shift.[1]

At high energies (large k^*), and small scattering angles θ_{k^*}, large values of l become more important, with

$$P_l(\cos\theta_{k^*}) \simeq J_0(l\theta_{k^*}) \ . \tag{2.27}$$

Making an analytic extension of l, the sum in Eq.(2.25) is written as an integral

$$F(k^*, \theta_{k^*}) = 4 \int dl \ (2l + 1) \ a(k^*, l) \ J_0(l\theta_{k^*}) \ , \tag{2.28}$$

were $a(k^*, l) = a_l(k^*)$ for integer values of l. With the relation $k^* \ b = l + 1/2$ we write

$$
\begin{aligned}
F(k^*, \theta_{k^*}) &= 4 \ k^{*\ 2} \int db \ b \ a(k^*, b) \ J_0(k^* \ b \ \theta_{k^*}) \\
&= \frac{is}{2\pi} \int d^2\vec{b} \ e^{i\vec{q}.\vec{b}} \ (1 - e^{2i\delta(k^*, b)}) \ ,
\end{aligned} \tag{2.29}
$$

where we use the approximation $qb \simeq l\theta_{k^*}$, ($\vec{q}$ being the momentum transfer) and the Bessel function property

$$\frac{1}{2\pi} \int d\cos(\theta_{k^*}) e^{iqb\cos(\theta_{k^*})} = J_0(q \ b) \ . \tag{2.30}$$

---

[1]Note that, in the elastic channel, due to the rotational symmetry and associated with Schur's lemma the S-matrix elements should be diagonal in the energy and angular momentum basis, and independent of the angular momentum projection m.

With $-q^2 = t$, and at high energies $k^{*\,2} \simeq s/4$, we write

$$F(s,t) = \frac{is}{2\pi} \int d^2\vec{b}\; e^{i\vec{q}.\vec{b}} \left(1 - e^{2i\delta(s,b)}\right) . \qquad (2.31)$$

Theoretical models based on the eikonal framework provide the phase shift function $\delta(s,b)$, commonly presented as the eikonal function $\chi(s,b) = 2\delta(s,b)$.

In order to absorb the energy dependence in the amplitudes we define $\widetilde{F}(s,b) = s\, a(s,b) = is(1 - e^{i\chi(s,b)})$ and write

$$F(s,t) = \frac{1}{2\pi} \int d^2\vec{b}\; e^{i\vec{q}.\vec{b}}\; \widetilde{F}(s,b) . \qquad (2.32)$$

In the next section we motivate and present a b dependent scattering amplitude based on the Stochastic Vacuum Model. The energy dependence is constructed separately in another chapter. After the combination of s and b dependences we finally complete the interacting model arriving at an expression for the complex pp elastic scattering amplitude $\widetilde{F}(s,b)$.

2.2   b - dependence of pp amplitudes of the Stochastic Vacuum Model

The main point of this section is to motivate and explain the theoretical basis of our scattering amplitudes valid for all b, and consequently, for t space. Quantum Chromodynamics (QCD) is the fundamental theory that explains the strong interactions. However, in relativistic elastic scattering between hadrons the momentum transfer t is in general small. In this regime the QCD strong coupling constant $\alpha_s(t)$ becomes large, which makes impossible a perturbative treatment, such as in terms of Feynmann diagrams. A non-perturbative framework is needed to describe these peripheral collisions. In this section we explain the Stochastic Vacuum Model, a non-perturbative scheme based on QCD and the correlation functions extracted

from its assumptions.

2.2.1   Stochastic Vacuum Model

After the success of QCD sum rules [39] many effects of non-perturbative QCD could be properly described phenomenologically by the parameters of 'physical' vacuum (condensates, etc). A relatively simple model, called Stochastic Vacuum Model (SVM) uses these vacuum properties to treat several properties of hadronic interactions, as the linear rising of the confining potential between quarks [17].

In the framework of quantum field theory, Nachtmann calculated [40] the scattering amplitude of a quark/antiquark moving along a light-like path in an external colour field given in the eikonal approximation. These results were applied to quark-quark and quark-antiquark scattering by Dosch and Kramer [41], using the vacuum correlators (gluon condensates [42], introduced first in the spectroscopy of hadrons by Shifman-Zakharov-Vainshtein [39]) in order to compute the functional average over the background gluonic fields. However quark-quark scattering amplitudes are gauge dependent quantities, and in this sense, the Wegner-Wilson loops [8] defined in Minkowski space-time are more appropriate tools to deal with soft hadron-hadron problems, since they are gauge invariant quantities. The loops are formed by quarks and anti-quarks moving at high energies with anti-parallel trajectories along the light-like paths (see Fig. (2.1)) with the edges connected by Wilson lines.

Due to the first success of SVM, an extension was made and applied to describe high energy scattering of hadrons [43] using the Wilson loops. In these studies the main observation is that the gauge invariant background field correlator plays an important role. Using this model, Dosch, Ferreira and Kramer [44] calculated the total cross sections and the slope parameters of the elastic differential cross sections of meson-baryon and baryon-baryon systems for fixed energy ($\sqrt{s} = 20$ GeV). The basic ingredients to calculate the hadron-hadron amplitudes in the framework of SVM is the gluon condensate and the correlation length that is associated with the

vacuum interaction range.

In the following, we explain the correlation function coming from the average of Wilson loop over the background fields [40]. Wilson loop is defined by

$$W[C] \equiv \text{ tr } P e^{-ig \oint_{C(x,x)} dz^\mu A_\mu(z)} = \text{ tr } V[C(x,x)] \qquad (2.33)$$

where g is the strong coupling constant, $C(x,x)$ is a closed circuit, P is the path ordering and $A_\mu = \sum_i A_\mu^i \tau_i/2$ is the color field with τ_i being the Gell-Mann matrices of SU(3). The Wilson line $V[C(x,y)]$ is defined by

$$V[C(x,y)] = P e^{-ig \int_{C(x,y)} dz^\mu A_\mu(z)} , \qquad (2.34)$$

along the general circuit $C(x,y)$. Using the non-Abelian Stokes theorem [45] the closed line integral above is converted into a surface integral with $dS^{\mu\nu}$ being the infinitesimal area element surrounded by the circuit $C(x,x)$. Then the expectation value of the Wilson loop is

$$\langle W[C] \rangle = \langle \text{ tr } P e^{-ig \int_S dS^{\mu\nu} F_{\mu\nu}[z,C(w,z)]} \rangle, \qquad (2.35)$$

with

$$F_{\mu\nu}[z,C(w,z)] = V[C(w,z)] F_{\mu\nu}(z) V[C(z,w)] , \qquad (2.36)$$

where $F_{\mu\nu}(z)$ is the gluon strength tensor, which is parallel transported from the position w (chosen arbitrarily in order to define the correlator in a gauge invariant way) to the point z.

Using cumulant expansion one can write Eq.(2.35) as

$$\langle W[C] \rangle = P \exp \Big[\sum_n \frac{(-ig)^n}{2^n n!} \int_S dS^{\mu_1 \nu_1}(z_1)...dS^{\mu_n \nu_n}(z_n)$$
$$\langle\langle \text{ tr } F_{\mu_1 \nu_1}[z_1, C(w,z_1)]...F_{\mu_n \nu_n}[z_n, C(w,z_n)] \rangle\rangle \Big] , \qquad (2.37)$$

where $\langle\langle \, \text{tr} \, F_{\mu_1\nu_1}[z_1, C(w, z_1)]...F_{\mu_n\nu_n}[z_n, C(w, z_n)]\rangle\rangle$ are the cumulants of correlation functions. For a given function $f(z)$, the cumulant definition is

$$\langle\langle f(z)\rangle\rangle = \langle f(z)\rangle \tag{2.38}$$

$$\langle\langle f(z_1)f(z_2)\rangle\rangle = \langle f(z_1)f(z_2)\rangle - \langle f(z_1)\rangle\langle f(z_2)\rangle \tag{2.39}$$

$$\langle\langle f(z_1)f(z_2)f(z_3)\rangle\rangle = \langle f(z_1)f(z_2)f(z_3)\rangle - \langle f(z_1)\rangle\langle f(z_2)f(z_3)\rangle$$

$$-\langle f(z_2)\rangle\langle f(z_3)f(z_1)\rangle - \langle f(z_3)\rangle\langle f(z_1)f(z_2)\rangle \tag{2.40}$$

$$\langle\langle f(z_1)f(z_2)f(z_3)f(z_4)\rangle\rangle = \langle f(z_1)f(z_2)f(z_3)f(z_4)\rangle - \langle f(z_1)f(z_2)\rangle\langle f(z_3)f(z_4)\rangle$$

$$-\langle f(z_1)f(z_3)\rangle\langle f(z_2)f(z_4)\rangle - \langle f(z_1)f(z_4)\rangle\langle f(z_2)f(z_3)\rangle$$

$$... \tag{2.41}$$

Since the Gell-Mann matrices appearing in the gluon strength tensor $F_{\mu\nu}(x)$ are traceless, the lowest order approximation for the expected Wilson loop value is quadratic in the strength tensor. The first assumption of SVM is that higher order cumulants are zero, which means that only Gaussian correlators survive. This leads to

$$\langle W[C]\rangle \approx \exp\left[-\frac{g^2}{2^2 2!}\int_S dS^{\mu_1\nu_1}(z_1)dS^{\mu_2\nu_2}(z_2)\langle \, \text{tr} \, F_{\mu_1\nu_1}[z_1, C(w, z_1)]F_{\mu_2\nu_2}[z_2, C(w, z_2)]\rangle\right],$$

$$\tag{2.42}$$

and the path ordering is no longer important. The expansion of the above expression in terms of the correlation function appearing in the exponent is the starting point to obtain the hadron-hadron soft scattering amplitudes at high energies. The second assumption of SVM is the Lorentz invariance of the correlator. Obeying this

requirement the correlation function is written [41, 42]

$$
\langle g^2 F_{\mu\nu}^a[z_1, C(w, z_1)] F_{\alpha\beta}^b[z_2, C'(w, z_2)]\rangle =
$$

$$
\frac{\delta^{a,b}}{12(N_c^2 - 1)} \langle g^2 FF\rangle \Big[\kappa(g_{\mu\alpha}g_{\nu\beta} - g_{\mu\beta}g_{\nu\alpha})D(z^2)
$$

$$
+(1 - \kappa)\frac{1}{2}\big[\frac{\partial}{\partial z_\mu}(z_\alpha g_{\nu\beta} - z_\beta g_{\nu\alpha}) + \frac{\partial}{\partial z_\nu}(z_\beta g_{\nu\alpha} - z_\alpha g_{\nu\beta})D_1(z^2)\big]\Big] \quad (2.43)
$$

where $z = z_1 - z_2$, $\langle g^2 FF\rangle = \langle g^2 F_{\mu\nu}^a(0)F_{\alpha\beta}^a(0)\rangle$ being the gluon condensate [39], N_C is the number of colors and a, b are the color indexes. The third assumption of SVM establishes that the functions $D(z^2)$ and $D_1(z^2)$ must fall off with increasing z^2. These functions are related with the non-Abelian and Abelian contributions respectively and they are normalized such that $D(0) = D_1(0) = 1$. The constant κ measures the relation between these relative contributions and can take values from 0 to 1. The exponential fall of the functions $D(z^2)$ and $D_1(z^2)$ is motivated in the lattice QCD calculations in Euclidian space-time, and also, lattice QCD indicates large values to $\kappa/(1 - \kappa)$, ($\kappa = 0.75$) which means a dominance of non-Abelian contributions.

The correlation length is defined by

$$
\int_0^\infty dz\, D(z^2) \equiv a . \quad (2.44)
$$

Numerical study of D functions [46] shows an exponential decreasing behavior for $z^2 \to \infty$ and the correlation length $a \approx 1$ allowing to reach asymptotic forms for $D(z^2)$ and $D_1(z^2)$.

2.2.2 Eikonalyzed amplitudes

Now we describe the application of SVM in order to obtain the b dependence of hadron-hadron amplitudes within the eikonal framework.

The quark-quark scattering amplitude derived in [40] is

$$T_{\text{qq}}|_{s\to\infty} \to -i\bar{u}(p_3)\gamma^\mu u(p_1)\bar{u}(p_4)\gamma_\mu u(p_2)(Z_\psi^{-2}) \int d^2\vec{b}\, e^{i\vec{q}.\vec{b}}\, \langle [V[\Gamma_+]-1][V[\Gamma_-]-1]\rangle\ ,$$

$$(2.45)$$

where u and $\bar{u}$ are Dirac spinors associated with matrices γ_μ, $Z_\psi \equiv \langle\, \text{tr}\, V[0]\rangle/N_C$ is the wave function renormalisation constant determined from the eikonal approximation and $\Gamma_\pm$ are the quarks trajectories along light-like paths. In Fig.2.1 we show two quarks trajectories along light cone coordinates. In high energy limit the pre-factor in the above equation simplifies to

$$-i\bar{u}(p_3)\gamma^\mu u(p_1)\bar{u}(p_4)\gamma_\mu u(p_2) \to -2is\ \delta^{\lambda 3,\lambda 1}\delta^{\lambda 4,\lambda 2}\ ,\qquad (2.46)$$

where λ's are the helicity indices. This amplitude was extended to loop-loop scattering [41] replacing the trajectories $\Gamma_\pm$ by the closed rectangular circuit $C_\pm$ along the light-like directions $\pm$. In the following the helicities are no longer important. In this sense, the scattering profile function between two loops is

$$J(\vec{b}, \vec{R}_1, \vec{R}_2) = Z_\psi^{-2}\langle\, \text{tr}\, [V[C_+]-1]\, \text{tr}\, [V[C_-]-1]\rangle\ ,\qquad (2.47)$$

where

$$Z_\psi^{-2} = \left[\langle\frac{1}{N_C}\, \text{tr}\, V[0,\vec{R}_1]\rangle\langle\frac{1}{N_C}\, \text{tr}\, V[0,\vec{R}_2]\rangle\right]^{-1} = 1\ ,\qquad (2.48)$$

with $V[C_+] \equiv V[-b/2,\vec{R}_1]$ and $V[C_-] \equiv V[+b/2,\vec{R}_2]$. The vectors $\vec{R}_1$ and $\vec{R}_2$ are vectors connecting quarks/antiquarks inside the hadron in the plane transverse to the movement and the vector $\vec{b}$ is the impact parameter between two loops as shown in Fig. 2.2. The renormalization constant put equal 1 in expression (2.48) is related to the tensorial structure in Eq. (2.43).

Figure 2.1: Two quarks trajectories $\Gamma_\pm$ along light cone coordinates where $x_0 = t$, $x_3 = z$, x_t are the transverse coordinates. The transverse distance between the two lines defines the impact parameter.
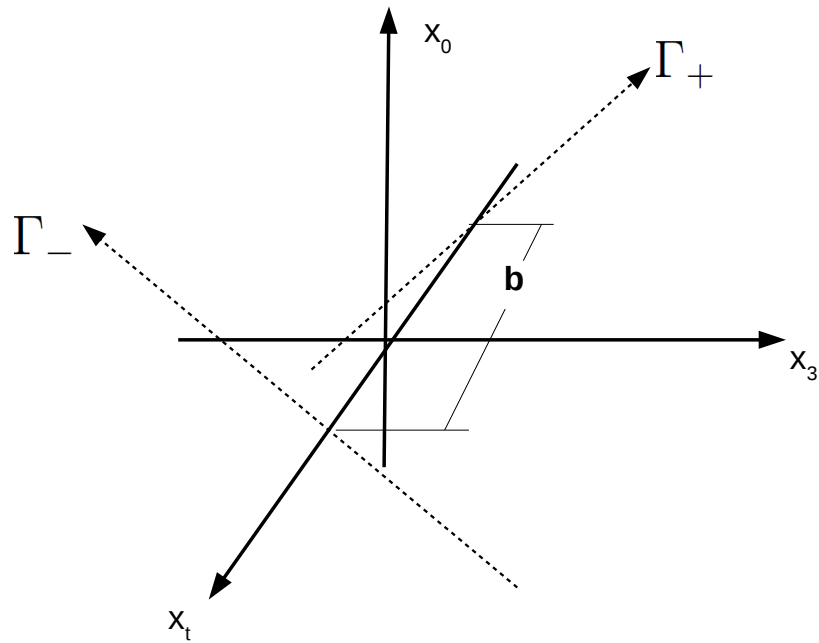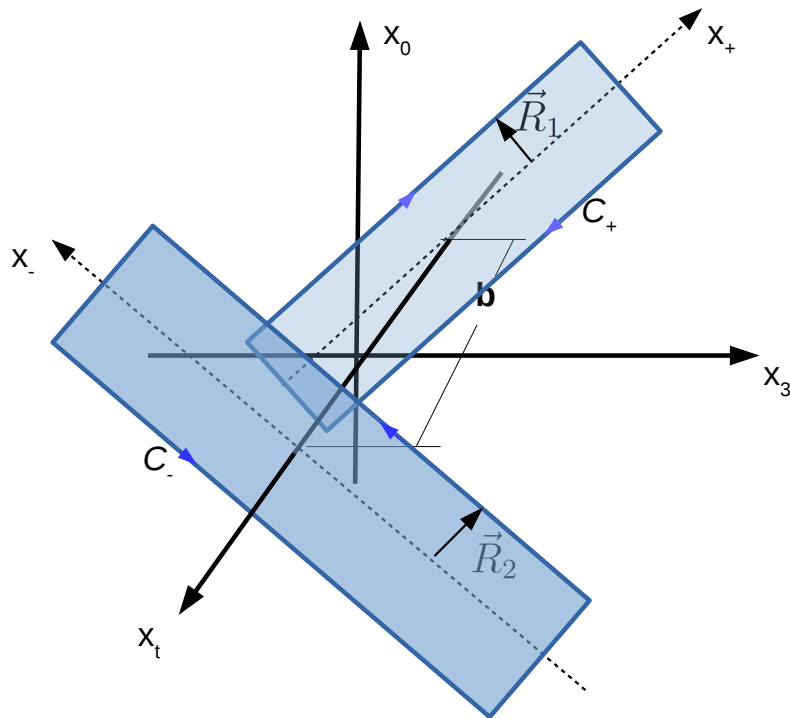
31

Figure 2.2: Analogously to Fig. 2.1 we show the loop-loop interaction in the light cone coordinates, where $\vec{R}_1$ and $\vec{R}_2$ being the quarks/antiquarks vectors within the hadrons and $\vec{b}$ is the impact parameter in the transverse plane. C_+ and C_- are the circuits of the Wilson loops over the coordinates $x_\pm = x_0 \pm x_3$.

After an expansion of the Wilson loops in Eq.(2.47), it follows

$$J(\vec{b}, \vec{R}_1, \vec{R}_2) = -(-ig)^4 (\frac{1}{2}!)^2 \, \text{tr} \, [\tau_{C_1} \tau_{C_2}] \, \text{tr} \, [\tau_{D_1} \tau_{D_2}] \int_{S_1} \prod_{i=1}^{2} dS^{\mu\nu}(x_i) \int_{S_2} \prod_{j=1}^{2} dS^{\alpha\beta}(y_j)$$

$$\times \frac{1}{N_C^2} \langle F^{C_1}_{\mu_1\nu_1}(x_1, w) F^{C_2}_{\mu_2\nu_2}(x_2, w) F^{D_1}_{\alpha_1\beta_1}(y_1, w) F^{D_2}_{\alpha_2\beta_2}(y_2, w) \rangle + \text{ (higher order) .} \quad (2.49)$$

The first assumption in SVM allows to factorize the correlation function of n points in 2-points correlation functions. This is the same factorization as the one provided by Wick theorem in quantum field theory,

$$\langle F^{C_1} F^{C_2} F^{D_1} F^{D_2} \rangle = \langle F^{C_1} F^{C_2} \rangle \langle F^{D_1} F^{D_2} \rangle + \langle F^{C_1} F^{D_1} \rangle \langle F^{C_2} F^{D_2} \rangle \quad (2.50)$$

$$+ \langle F^{C_1} F^{D_2} \rangle \langle F^{C_2} F^{D_1} \rangle.$$

The scattering amplitude for two hadrons is built with a convolution between two Wilson loops and the transverse distribution functions of quarks inside hadrons [41, 44],

$$T(s, -q^2) = 2is \int d^2b \; e^{-i\vec{q}.\vec{p}} \int d^2\vec{R}_1 \int d^2\vec{R}_2 |\psi_1(\vec{R}_1)|^2 |\psi_2(\vec{R}_2)|^2 \; J(b, \vec{R}_1, \vec{R}_2) ,(2.51)$$

where $\psi_1(\vec{R}_1)$ and $\psi_2(\vec{R}_2)$ are the quark/antiquark wave functions relative to the Wilson loops that represent the hadrons. An ansatz is given by [43, 44, 47]

$$\psi_H(R) = \sqrt{(2/\pi)} \frac{1}{S_H} e^{-R^2/S_H^2} \; , \quad (2.52)$$

S_H being a parameter associated with the hadron size, with distance dimension, and R is the absolute value of the position vector of quarks inside the hadron. The scattering amplitude for scattering of two hadrons is

$$J_{H_1H_2}(\vec{b}, S_{H_1}, S_{H_2}) = \int d^2\vec{R}_1 \int d^2\vec{R}_2 \; J(\vec{b}, \vec{R}_1, \vec{R}_2) \; |\psi_1(\vec{R}_1)|^2 \; |\psi_2(\vec{R}_2)|^2 \; , \quad (2.53)$$

which is dimensionless. For short we write $J_{H_1 H_2}(\vec{b}, S_{H_1}, S_{H_2}) = J(b/a)$. Taking into account the geometry of the interacting loops in light cone coordinates the asymptotic studies of profile function Ref. [47] showed that for large values of b/a (impact parameter greater than the correlation length) the function approximates to

$$J(b/a) = \exp\left(-\frac{3\pi}{8}\frac{b}{a}\right)\left[\frac{A_1}{b/a} + \frac{A_2}{(b/a)^2} + ...\right] \tag{2.54}$$

with $A_1, A_2, ...$ being functions of S_H/a, and the number $3\pi/8$ comes from the correlation function. For small and intermediate values of b/a, the phenomenology requires an additional Gaussian behavior for the function $J(b/a)$. The sum over all regions [44] is

$$J(b/a) \simeq J(0)\left[A_0\ e^{-P(b/a)^2} + \sum_{j=1}^{N}\frac{A_j}{1 + C_j(b/a)^j \exp[(3\pi/8)(b/a)]}\right], \tag{2.55}$$

where P, C_j and A_j are parameters depending on the ratio S_H/a.

In order to reproduce correctly the experimental data, a few changes are necessary in the profile function. The terms contributing for large b values are converted in a shape function with two terms and a relative negative sign in between, and the b variable is shifted with a parameter γ in order to avoid singularities in the denominator. With these changes the suggested form is

$$J(b/a) = J(0)\left[e^{-b^2/a_1} + a_2\ \widetilde{A}_\gamma(b)\right], \tag{2.56}$$

with $\widetilde{A}_\gamma(b)$ a function of the form

$$\widetilde{A}_\gamma(b) = \frac{e^{-\rho_4\sqrt{\gamma^2+b^2}}}{\sqrt{\gamma^2 + b^2}}(1 - e^{\rho_4\gamma - \rho_4\sqrt{\gamma^2+b^2}})\ , \tag{2.57}$$

with $\rho_4 = 3\pi/8$, and the parameters a_1 and a_2 depend on S_H/a. This form gives

$\widetilde{A}_\gamma(b = 0) = 0$. Finally, replacing the results above in the expression for the scattering between two hadrons, Eq. 2.51, in first order, the scattering amplitude becomes

$$T(s,t) = is[\langle g^2 FF \rangle a^4]^2 a^2 \int d^2\vec{b} \; e^{i\vec{q}.\vec{b}} \; J(b/a) \; . \tag{2.58}$$

The remaining integration is analytically soluble, giving

$$T(s,t) = is[\langle g^2 FF \rangle a^4]^2 a^2 \pi \left\{ J(0) \left[a_1 e^{-a^2|t|a_1/4} + 2a_2 \; A_\gamma(t) \right] \right\} \; , \tag{2.59}$$

with

$$A_\gamma(t) = \frac{e^{-\gamma\sqrt{\rho^2 + a^2|t|}}}{\sqrt{\rho^2 + a^2|t|}} - e^{\gamma\rho} \frac{e^{-\gamma\sqrt{4\rho^2 + a^2|t|}}}{\sqrt{4\rho^2 + a^2|t|}} \; . \tag{2.60}$$

To perform the integral of the shape function we made use of the formula [48]

$$\int_0^\infty J_0(\beta v) \; \frac{e^{-\lambda\sqrt{1+v^2}}}{\sqrt{1+v^2}} \; v \; dv \; = \; \frac{e^{-\sqrt{\lambda^2 + \beta^2}}}{\sqrt{\lambda^2 + \beta^2}} \; . \tag{2.61}$$

Note that $A_\gamma(t = 0) = 1$. Because of the correlation function is a real quantity it is important to remark that the amplitude have written is purely imaginary, and no energy dependence was taken into account. In [16] this was introduced through the effective hadronic size $S_H(s)$, taken as a linear form $a + b \log s$.

Based in the description above we express our imaginary amplitude as

$$T_I(s,t) = \alpha_I e^{-\beta_I|t|} + \lambda_I \Psi_I(\gamma_I, t) \; , \tag{2.62}$$

with

$$\Psi_I(\gamma_I, t) = 2 \; e^{\gamma_I} \left[\frac{e^{-\gamma_I\sqrt{1+a_0|t|}}}{\sqrt{1+a_0|t|}} - e^{\gamma_I} \frac{e^{-\gamma_I\sqrt{4+a_0|t|}}}{\sqrt{4+a_0|t|}} \right] \; , \tag{2.63}$$

where a_0 is associated with the correlation length and should be energy independent

and the parameters $\alpha_I(s)$, $\beta_I(s)$, $\gamma_I(s)$ and $\lambda_I(s)$ must be determined for each energy. In order to describe correctly the experimental data a real amplitude is necessary. We assume the same analytical form for the real amplitude, also with 4 real parameters to be determined. The complete forms of the amplitudes are

$$T_K(s,t) = \alpha_K(s)\mathrm{e}^{-\beta_K(s)|t|} + \lambda_K(s)\Psi_K(\gamma_K(s),t) \ , \tag{2.64}$$

with

$$\Psi_K(\gamma_K(s),t) = 2\ \mathrm{e}^{\gamma_K(s)} \left[\frac{\mathrm{e}^{-\gamma_K(s)\sqrt{1+a_0|t|}}}{\sqrt{1+a_0|t|}} - \mathrm{e}^{\gamma_K(s)}\ \frac{e^{-\gamma_K(s)\sqrt{4+a_0|t|}}}{\sqrt{4+a_0|t|}} \right] \ , \tag{2.65}$$

where $K = R, I$ characterize the real and imaginary amplitudes respectively.

In chapter 3 we use this complex amplitude for the analysis of pp scattering determining the energy dependence of the real and imaginary parameters.

Chapter 3

Description of forward elastic scattering

In this chapter we deal with the $|t|$ range below 0.02 GeV^2, where simple exponential behavior can be assumed for the imaginary and real amplitudes. Then the description of $d\sigma/dt$ is made with four energy dependent parameters: σ, ρ, B_I, B_R. Using the Particle Data Group representation for the total pp and p$\bar{\text{p}}$ cross sections we apply the exact expressions for DDR to obtain relations between the real and imaginary parts. We compare the exact results for the ρ parameter with the approximate forms used in PDG book [49] and with some experimental data. Using a form of energy dependence for the slope of the imaginary amplitude, we use DDR to obtain the slope B_R of the real part.

We stress the importance of the use of proper connections between real and imaginary amplitudes as fixed by DDR, particularly emphasizing the difference between B_I and B_R. The Coulomb interference must be used with proper account for the properties of the amplitudes, so that the parameters of cross sections, ratio ρ and slopes B_R and B_I, can be determined with accuracy. For this purpose, more general expressions for the Coulomb interference phase are obtained.

Some data from ISR (Cern) and Fermilab are analysed in the energy range where

the influence of these treatments is more dramatic.

3.1   Particle Data Group representation for the total cross section

In order to show that the constraints imposed by DDR must be obeyed in any model, we study the simple and direct representation of Particle Data Group of the total cross section. We apply the exact DDR to obtain the ρ parameter and we compare it with the simplified formula used by PDG. We criticize this formula specially at low energies.

The Particle Data Group (PDG) [49] gives a parametrization for the total cross section for pp and p$\bar{\text{p}}$ interaction in the well known form

$$\sigma^{\text{p}\mp\text{p}}(s) = P + H \log^2 \left(\frac{s}{s_0}\right) + R_1 \left(\frac{s}{s_0}\right)^{-\eta_1} \pm R_2 \left(\frac{s}{s_0}\right)^{-\eta_2} , \tag{3.1}$$

where the signs $\mp$ are related with pp and p$\bar{\text{p}}$ systems respectively.

Given quantities are: proton mass $m = 0.93827$mb, $s_0 = (2m + 2.076)^2 = 15.6223 \, \text{GeV}^2$, $\eta_1 = 0.412$, $\eta_2 = 0.5626$. The parameters $P = 33.73$ mb/0.3894, $H = 0.2838$ mb/0.3894, $R_1 = 13.67$ mb/0.3894, $R_2 = 7.77$ mb/0.3894 enter with GeV^{-2} units to produce dimensionless amplitudes described by Eqs. (2.20) and (2.21). The conversion constant is $(\hbar c)^2 = 0.3894$ mb GeV^2. We define $s_0 = 2mE_0$, and then $E_0 = 8.325 \, \text{GeV}$. Including the t dependence in the inputs, the dispersion relations are written

$$\text{Im} F_+(s,t) = s \left[P + H \log^2 \left(s/s_0\right) + R_1 \left(s/s_0\right)^{-\eta_1}\right] e^{B_I t/2} \tag{3.2}$$

and

$$\text{Im } F_-(s,t) = s \left[R_2 \left(s/s_0\right)^{-\eta_2}\right] e^{B_I t/2}. \tag{3.3}$$

For simplicity we have assumed that all terms of the imaginary amplitude have the same t dependence, given by the exponential slope $B_I(s)$, valid for very small $|t|$.

We introduce the variables $x = E/m \approx s/2m^2$, $x_0 = E_0/m \approx s_0/2m^2$, and it is always $x > 1$. Then DR's for the PDG form, Eq. (3.1), become

$$\text{Re}\, F_+(x,0) = K + \frac{2}{\pi}s\, x\mathbf{P} \int_1^{+\infty} \frac{[P + H\log^2(x'/x_0) + R_1(x'/x_0)^{-\eta_1}]}{[x'^2 - x^2]} \, dx' \quad (3.4)$$

and

$$\text{Re}\, F_-(x,0) = \frac{2}{\pi}\, s\, \mathbf{P} \int_1^{+\infty} \frac{x'[R_2(x'/x_0)^{-\eta_2}]}{[x'^2 - x^2]} \, dx' \;, \quad (3.5)$$

We identify inside the integrals, numerators of form $x'^\lambda \log^n(x')$, with n integer. We then define Principal Value (PV) integrals (see Eq.(2.24))

$$I(n, \lambda, x) = \mathbf{P} \int_1^{+\infty} \frac{x'^\lambda \, \log^n(x')}{[x'^2 - x^2]} dx' \;. \quad (3.6)$$

Collecting terms, we write

$$\text{Re}\, F_+(x,0) = K + \frac{2}{\pi}\, s\, x\, \Big[I(0,0,x)\big(P + H\log^2(x_0)\big) + I(1,0,x)\big(-2H\log(x_0)\big)$$
$$+I(2,0,x)\big(H\big) + I(0,-\eta_1,x)\big(R_1 x_0^{\eta_1}\big)\Big] \;, \quad (3.7)$$

and for the odd part

$$\text{Re}\, F_-(x,0) = \frac{2}{\pi}\, s\, \Big[I(0, 1-\eta_2, x)\big(R_2 x_0^{\eta_2}\big)\Big] \;. \quad (3.8)$$

The PV integrals can be written as local forms, that are exact representations, obtained in the study of Derivative Dispersion Relations Ref. [35–37]. We thus have

the general form (with $x > 1$, n zero or positive integer and $\Re(\lambda) \leq 1$)

$$I(n, \lambda, x) = \mathbf{P} \int_1^{+\infty} \frac{x'^\lambda \log^n(x)}{[x'^2 - x^2]} \, dx' \qquad (3.9)$$

$$= -\frac{\pi}{2x^2} \frac{\partial^n}{\partial \lambda^n} [x^{1+\lambda} \cot \left(\frac{\pi}{2}(1 + \lambda)\right)] + \frac{(-1)^n}{x^2} 2^{-(n+1)} n! \; \Phi(\frac{1}{x^2}, n+1, \frac{1+\lambda}{2}) \; .$$

The functions Φ in these expressions are the Hurwitz-Lerch transcendents, that have the series expansions

$$\frac{1}{2^N} \frac{1}{x} \; \Phi(\frac{1}{x^2}, N, \frac{1+\lambda}{2}) = \frac{x^{-1}}{(1+\lambda)^N} + \frac{x^{-3}}{(3+\lambda)^N} + \frac{x^{-5}}{(5+\lambda)^N} + \dots \qquad (3.10)$$

and the property used above

$$\frac{\partial}{\partial \lambda} \Phi(z, N, \frac{1+\lambda}{2}) = -\frac{N}{2} \; \Phi(z, N+1, \frac{1+\lambda}{2}) \; . \qquad (3.11)$$

The function Φ allows exact elegant representations of the PV integrals. Particular values used directly in this work and more complete information on the properties of the Φ transcendents and on the solutions of the PV integrals are given in Appendix B. The proof of Eq.(3.10) and a study of a new representation of the Lerch transcendents are given in a paper under preparation.

The sums converge rapidly for energies above 10 GeV, and are easily included in practical computations, requiring only one or a few terms of the series. The use of Eq.(3.10) is straightforward, except that care must be taken for odd negative integer values of λ, when singularities occur in both trigonometric and Φ function parts of the expression, with cancellation in a limit procedure. The details are given in the Appendix B.

A simple and interesting relation derived using properties of the transcendents is

$$\frac{\partial I(0, \lambda, x)}{\partial \log(x)} + (1 - \lambda)I(0, \lambda, x) = -\frac{1}{x^2 - 1} \; . \qquad (3.12)$$

Noting that

$$\frac{\partial I(n, \lambda, x)}{\partial \lambda} = I(n+1, \lambda, x) \ , \tag{3.13}$$

we obtain, taking successive derivatives of the above equation with respect to λ,

$$\frac{\partial I(n, \lambda, x)}{\partial \log(x)} + (1 - \lambda)I(n, \lambda, x) = nI(n-1, \lambda, x) \ . \tag{3.14}$$

We remark that $I(n = 0, \lambda = 0, x)$ can be written in terms of elementary functions

$$I(0, 0, x) = \mathbf{P} \int_{1}^{+\infty} \frac{[1]}{[x'^2 - x^2]} \, dx' = \frac{1}{2x^2} \ \Phi(\frac{1}{x^2}, 1, \frac{1}{2}) = \frac{1}{2x} \log \frac{x+1}{x-1} \tag{3.15}$$

The combinations of real parts, even and odd, at $t = 0$ are connected with the product of the $\rho_{\mathrm{pp}}^{\mathrm{p\bar{p}}}$ parameter and the total cross section given by

$$\sigma\rho\begin{pmatrix} \mathrm{pp} \\ \mathrm{p\bar{p}} \end{pmatrix} = \frac{\mathrm{Re} \ F_+(x, 0) \mp \mathrm{Re} \ F_-(x, 0)}{s} \ . \tag{3.16}$$

The subtraction dimensionless constant K is important at low energies. Its determination can be made using experimental information on the real part at one low energy for both pp and p$\bar{\mathrm{p}}$ systems (say at 52.8 GeV, where there are data). Values obtained for K are usually below 1000.

In Fig. 3.1 a) we plot the even and odd combinations of imaginary and real amplitudes given by the PDG input in Eq. 3.1. To show the influence of the subtraction constant K in the even combination $\mathrm{Re} \, F_+(E, t = 0)$, we plot lines with $K = 0$ (solid line) and $K = 1000$ (dashed line) against the energy. The even real amplitude increases fast, and the influence of K is comparatively small for energies above 100 GeV , becoming negligible in the use of DR at higher energies. At $\sqrt{s} = 50$ GeV the value of the even real amplitude is about 20000, so that the constant K can contribute with at most 5 % . We give in the next section a criterion for the

determination of K, that leads to $K = 935$.

To stress the importance of the use of the exact DDR forms, we compare in plot b) (not including K) the calculation of quantity $\frac{1}{2}[\sigma\rho(\mathrm{pp}) + \sigma\rho(\mathrm{p\bar{p}})]$ using exact DDR expressions with the simplified form written in the PDG book.

Exact expressions for the $\rho\sigma$ products from the PDG input

The equation written in PDG book for the ratio ρ is based on DDR, but it uses forms not valid for low energies. The form disagrees with the expressions given above for the real amplitudes and their consequences. Taking the low energy corrections up to first order, we write

$$\frac{1}{2}[\sigma\rho(\mathrm{p\bar{p}}) + \sigma\rho(\mathrm{pp})] = T_1 + T_2 + T_3, \tag{3.17}$$

with

$$T_1 = H\pi \log\left(\frac{s}{s_0}\right), \tag{3.18}$$

$$T_2 = \frac{K}{s} + \frac{4m^2}{s\pi}\left(P + H\left[\log^2\left(\frac{s_0}{2m^2}\right) + 2\log\left(\frac{s_0}{2m^2}\right) + 2\right]\right), \tag{3.19}$$

and

$$T_3 = R_1\left[-\left(\frac{s}{s_0}\right)^{-\eta_1}\tan\left(\frac{\pi\eta_1}{2}\right) + \left(\frac{s_0}{2m^2}\right)^{\eta_1}\frac{2m^2}{s}\left(\frac{2/\pi}{1-\eta_1}\right)\right]. \tag{3.20}$$

and the odd part,

$$\frac{1}{2}[\sigma\rho(\mathrm{p\bar{p}}) - \sigma\rho(\mathrm{pp})] = R_2\left(\frac{s}{s_0}\right)^{-\eta_2}\cot\left(\frac{\pi\eta_2}{2}\right) + R_2\left(\frac{s_0}{2m^2}\right)^{\eta_2}\left(\frac{2m^2}{s}\right)^2\left(\frac{2/\pi}{2-\eta_2}\right). \tag{3.21}$$

The influence of these changes are shown in the figures, comparing the PDG book forms with the correct DDR calculations.

Although we believe that the products $\sigma\rho$ are more adequate to present and analyse the data on the real part, we form the ratios ρ, that are less directly measured,

and consequently have larger error bars.

In Fig. 3.2 we show the ratios ρ (pp) and ρ (p$\bar{\text{p}}$) calculated with exact DDR and with the PDG expression [49]. We show also the analysis of data in an energy range where the effects here discussed are stronger. We stress that in this thesis we do not intend to present a final analysis of the low energy data. Actually, we point out that the determinations of the ρ parameter given in the literature should be revised, taking into account the behavior of the real amplitude, with $B_R > B_I$ and proper treatment of the Coulomb interference, discussed below. Numerical values are given in Table 3.1.

Eq. (3.12) can be applied to the odd combination. We obtain the exact relation

$$[\frac{\partial}{\partial \log x} + \eta_2]\left[\sigma\rho(\text{p}\bar{\text{p}}) - \sigma\rho(\text{pp})\right] = -\frac{2}{\pi} \, R_2 \, x_0^{\eta_2} \, \frac{1}{x^2 - 1} \, , \qquad (3.22)$$

that has a divergence in the low energy limit $x \to 1$. The approximate forms for $\rho(pp)$ and $\rho(\text{p}\bar{\text{p}})$ written in the PDG book give zero instead of the expression above.
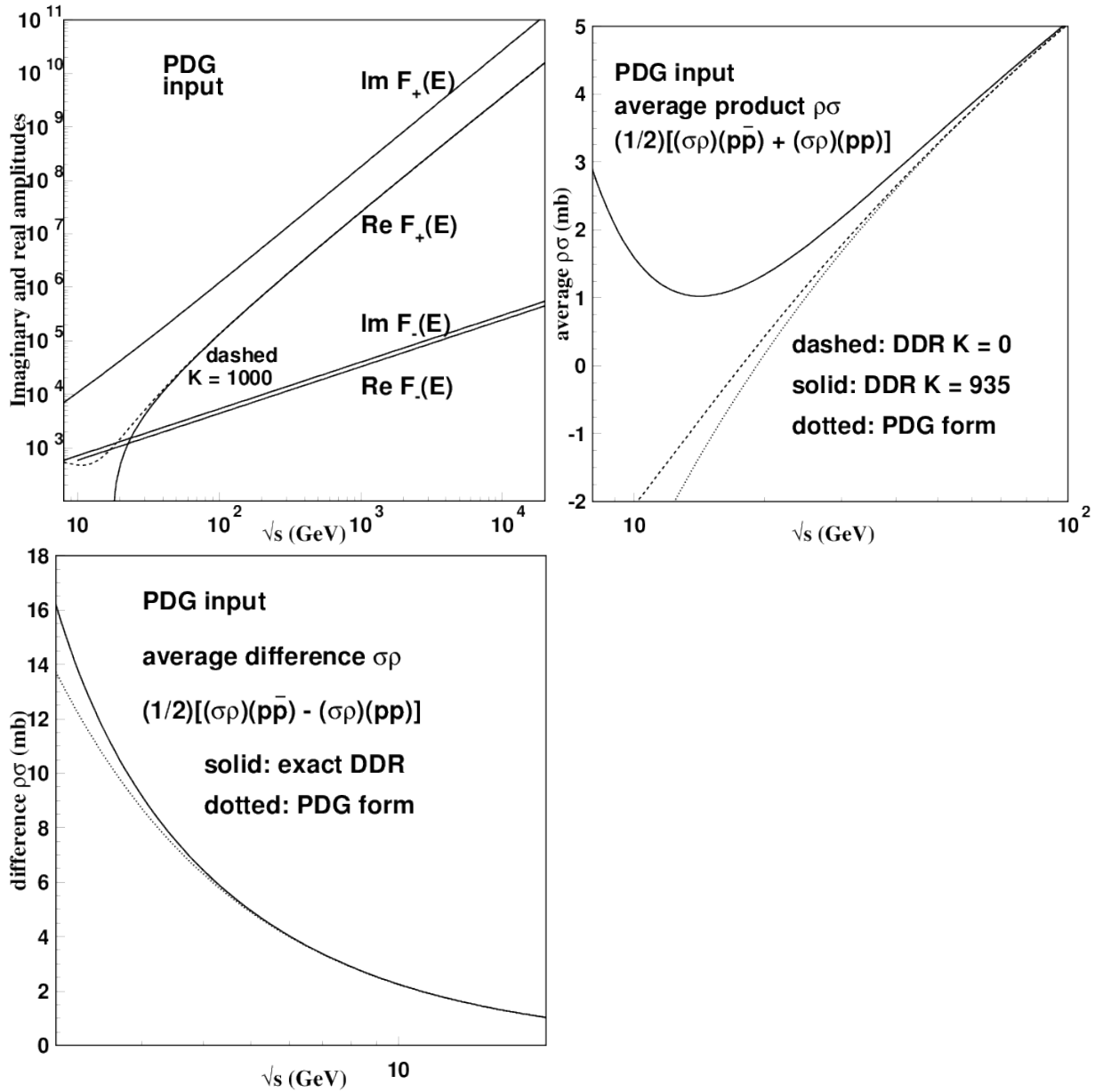
Figure 3.1:   a) (figure above and on the left) Input imaginary amplitudes $\mathrm{Im}\,F_+(E, t = 0)$ and $\mathrm{Im}\,F_-(E, t = 0)$ taken from the PDG representation, Eqs. (3.2, 3.3), and combined even and odd real amplitudes, $\mathrm{Re}\,F_+(E, t = 0)$ and $\mathrm{Re}\,F_-(E, t = 0)$, obtained with dispersion relations. The influence of the subtraction constant K is important only at low energies, as show by the dashed line, drawn with $K = 1000$, while the solid line corresponds to $K = 0$. The odd combinations are comparatively small, and can be neglected at high energies. In plots b) (figure above and on the right) and c) (figure bellow) even and odd combinations of the products $\sigma\rho$ obtained with exact DDR (with K=0), are compared with the proposed parametrization published by PDG.

$\sqrt{s}$(GeV)	system	ρ (PDG)	ρ(DDR)	Experimental Data
18.2	pp	-0.0349	0.0014	-0.011 ± 0.020^a
	p$\bar{\text{p}}$	0.0222	0.0562	0.067 ± 0.040^a
19.4	pp	-0.0260	0.0056	0.019 ± 0.018^a
	p$\bar{\text{p}}$	0.0268	0.0562	0.029 ± 0.032^a
23.5	pp	-0.0014	0.0199	0.022 ± 0.014^b
	p$\bar{\text{p}}$	0.0399	0.0600	
24.3	pp	0.0025	0.0222	0.014 ± 0.009^d
	p$\bar{\text{p}}$	0.0422	0.0608	0.045 ± 0.009^d
30.4	pp	0.0267	0.0387	0.034 ± 0.008^b
	p$\bar{\text{p}}$	0.0564	0.0679	0.055 ± 0.029^b
30.6	pp	0.0273	0.0393	0.042 ± 0.011^c
	p$\bar{\text{p}}$	0.0568	0.0682	
44.7	pp	0.0601	0.0650	0.062 ± 0.011^c
	p$\bar{\text{p}}$	0.0781	0.0828	
52.8	pp	0.0718	0.0751	0.077 ± 0.009^b
	p$\bar{\text{p}}$	0.0863	0.0894	0.106 ± 0.016^b
62.5	pp	0.0823	0.0843	0.095 ± 0.011^c
	p$\bar{\text{p}}$	0.0939	0.0959	
541	pp			
	p$\bar{\text{p}}$			0.135 ± 0.007^e
1800	pp			
	p$\bar{\text{p}}$			0.140 ± 0.070^f
7000	pp			0.145 ± 0.009^g
	p$\bar{\text{p}}$			

Table 3.1: Values of ρ from the PDG input, compared to experiments. The column $\rho(PDG)$ gives values from PDG book formula, that is wrong at low energies. The column $\rho(DDR)$ gives values obtained with same imaginary input, using exact DDR expressions. References : (a) $\sqrt{s}$ = 18.17 , 19.418 : L. A. Fajardo et al. , Phys. Rev. D24, 46 (1981) ; (b) $\sqrt{s}$ = 23.5 , 30.6 , 52.8 : N. A. Amos et al., Nucl. Phys. B262 , 689 (1985); (c) $\sqrt{s}$ = 30.6 , 44.7 , 62.5 : U. Amaldi et al., Phys. Lett. B66, 390 (1977) ; (d)$\sqrt{s}$ = 24.3 : R. E. Breedon et al., Phys. Lett. B216 , 459 (1989); (f) N. Amos et al., Phys. Rev. Lett. 68,2433 (1992) ; (g) G. Antchev et al., Totem Coll., Eur. Phys. Lett. 101, 21002 (2013); see Compilation by J. R. Cudell et al. , Phys. Rev. D73, 034008 (2006) , [arXiv:0511073];
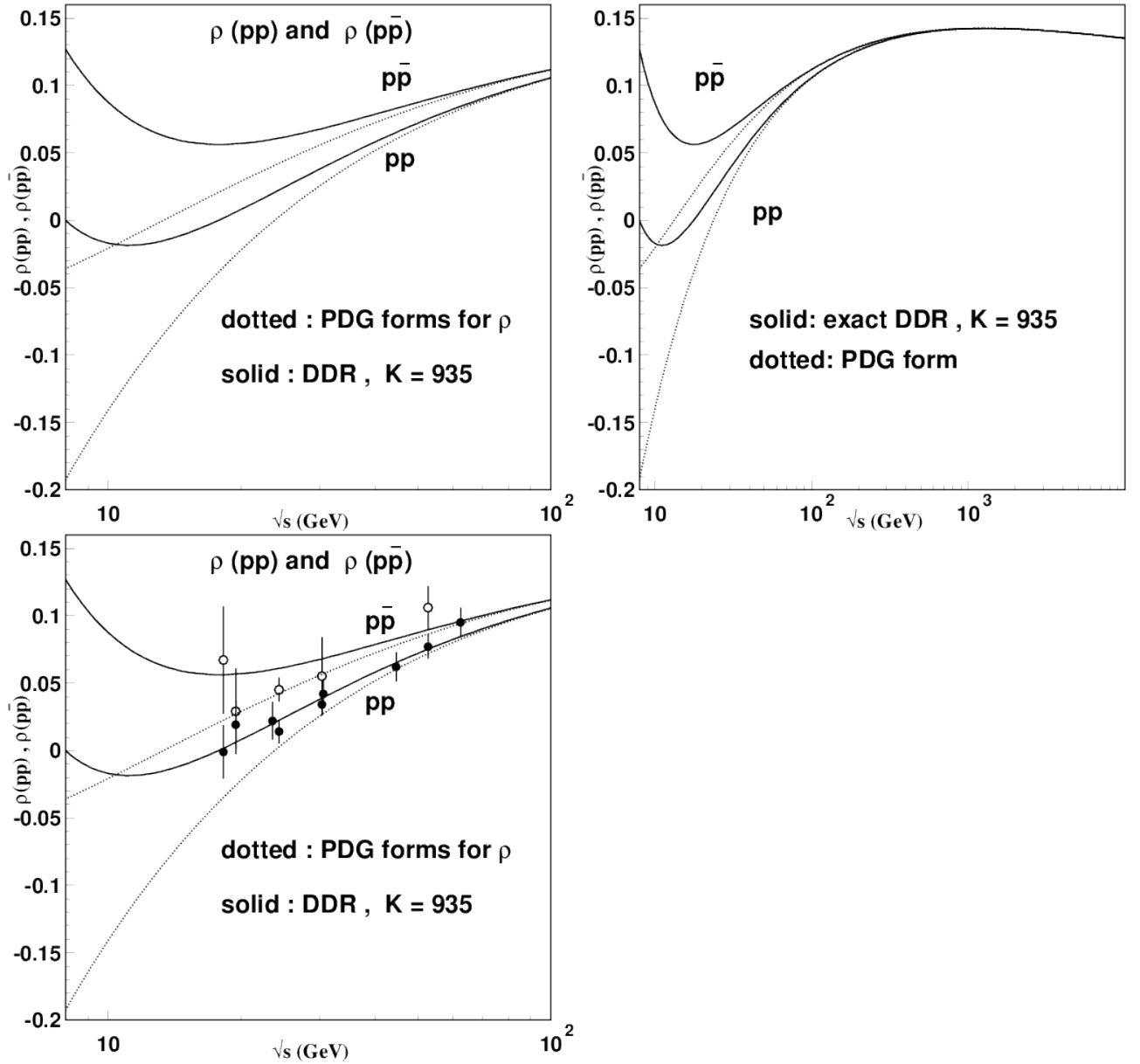
Figure 3.2:   Values of the ρ parameter for pp and p$\bar{\text{p}}$ scattering calculated with exact DDR and with the parametrization given in PDG book, in low and high energy ranges. The choice of the subtraction constant K = 935 is explained in the analysis of the DDR for slopes in the next section. Although this work has no purpose of analysing data at low energies, the plot below shows some data (see Table 3.1) in an energy range proper for comparison of calculations made with the PDG input.

3.1.1   Dispersion relations for slopes

For very small $|t|$ we extend the imaginary amplitude of the PDG representation introducing a factor $\exp[-B_I t/2]$, for all terms in the input form, as written above in Eqs. (3.2), (3.3). This is the simplest choice, in the absence of another specific model.

$B_I(s)$ is parametrized in the form

$$B_I(x) = b_0 + b_1 \log(x) + b_2 \log^2(x) \ . \tag{3.23}$$

Using as basis previous determinations at energies 19.4, 23.5, 33.6, 44.7, 546, 1800 and 7000 GeV , we obtain the parameter values for B_I in GeV^{-2}

$$b_0 \ = \ 12.11 \ , \ b_1 \ = \ -0.09033 \ , \ b_2 \ = \ 0.03081 \ . \tag{3.24}$$

Recalling $x = s/2m^2$, we write instead

$$B_I(s) = c_0 + c_1 \log(\sqrt{s}) + c_2 \log^2(\sqrt{s}) \ , \tag{3.25}$$

with $\sqrt{s}$ in GeV, and then

$$c_0 \ = \ 12.1710 \ , \ c_1 \ = \ -0.2504 \ , \ c_2 \ = \ 0.12324 \ . \tag{3.26}$$

Taking derivative with respect to t , we write the dispersion relations for the derivatives [36] of the even and odd combinations of amplitudes at the origin

$$\frac{\partial \mathrm{Re}\, F_+(x,t)}{\partial t}\bigg|_{t=0} = \frac{2}{\pi} \ s \ x \ \times \tag{3.27}$$
$$\mathbf{P} \int_1^{+\infty} \frac{[P + H \log^2(x'/x_0) + R_1(x'/x_0)^{-\eta_1}]}{[x'^2 - x^2]} \frac{1}{2}[b_0 + b_1 \log(x) + b_2 \log^2(x)] \ dx' \ ,$$

and

$$\frac{\partial \text{Re}\, F_-(x,t)}{\partial t}\Big|_{t=0} = \frac{2}{\pi}\, s\ \times \tag{3.28}$$
$$\mathbf{P}\int_1^{+\infty} \frac{x'[R_2(x'/x_0)^{-\eta_2}]}{[x'^2 - x^2]}\frac{1}{2}[b_0 + b_1 \log(x) + b_2 \log^2(x)]\ dx'\ .$$

The above equations control quantities observed in forward scattering and should be used as reference for any phenomenological or theoretical description of pp and p$\bar{\text{p}}$ forward scattering at high energies. The PV integrations can be performed, as before. Collecting terms, we write

$$\frac{\partial \text{Re}\, F_+(x,t)}{\partial t}\Big|_{t=0} = \frac{2}{\pi}\, s\, x\, \frac{1}{2}\ \times \tag{3.29}$$
$$\Big[I(0,0,x)\, \big(P + H \log^2 x_0\big)\, b_0 + I(1,0,x)\big[\big(- 2H \log x_0\big)\, b_0 + \big(P + H \log^2 x_0\big)\, b_1\big]$$
$$+ I(2,0,x)\, \big[H\, b_0 - 2H \log x_0\, b_1 + \big(P + H \log^2 x_0\big)\, b_2\big]$$
$$+ I(3,0,x)\, \big[- 2H \log x_0\, b_2 + H\, b_1\big] + I(4,0,x)\, H\, b_2 + I(0,-\eta_1,x)\big(R_1 x_0^{\eta_1}\big)\, b_0$$
$$+ I(1,-\eta_1,x)\big(R_1 x_0^{\eta_1}\big)\, b_1 + I(2,-\eta_1,x)\big(R_1 x_0^{\eta_1}\big)\, b_2\Big]\ ,$$

and for the odd part

$$\frac{\partial \text{Re}\, F_-(x,t)}{\partial t}\Big|_{t=0} = \frac{2}{\pi}\, s\, \frac{1}{2}\ \times \tag{3.30}$$
$$\Big[I(0,1-\eta_2,x)\big(R_2 x_0^{\eta_2}\big)\, b_0 + I(1,1-\eta_2,x)\big(R_2 x_0^{\eta_2}\big)\, b_1 + I(2,1-\eta_2,x)\big(R_2 x_0^{\eta_2}\big)\, b_2\Big]\ .$$

Fig. 3.3 a) gives the quantities $\partial \text{Re}\, F_+(x,t)/\partial t\big|_{t=0}$ and $\partial \text{Re}\, F_-(x,t)/\partial t\big|_{t=0}$ calculated by DDR using the extended PDG forms given in Eqs. (3.2, 3.3).

With the derivatives of the even and odd combinations calculated, we may separate the pp and p$\bar{\text{p}}$ channels. Assuming that the real amplitude in each system behaves with an exponential form $F(x,t) \approx F(x,0)\exp(B_R t/2)$ for small $|t|$, the derivatives can be factorized, leading to triple products $\sigma\rho B_R$ (pp) and $\sigma\rho B_R$ (p$\bar{\text{p}}$). These quantities are shown in Fig. 3.3, b) and c).

Explicit expressions for the triple products for energies above 200 GeV , including only the first term of the transcendents, are

$$
\frac{1}{s}\frac{\partial \mathrm{Re}\, F_+(x,t)}{\partial t}\Big|_{t=0} = \frac{1}{2}\big[(\sigma\rho B_R)\,(\mathrm{p\bar p}) + (\sigma\rho B_R)\,(\mathrm{pp})\big]
$$

$$
= \frac{2}{\pi}\frac{1}{2}\bigg[\big[(P + H\log^2 x_0)\,b_0\big]\frac{1}{x} + \big[\big(-2H\log x_0\big)\,b_0 + \big(P + H\log^2 x_0\big)\,b_1\big]\big[\frac{\pi^2}{4} - \frac{1}{x}\big]
$$

$$
+ \big[H\,b_0 - 2H\log x_0\,b_1 + \big(P + H\log^2 x_0\big)\,b_2\big]\big[\frac{\pi^2}{2}\log x + \frac{2}{x}\big]
$$

$$
+ \big[-2H\log x_0\,b_2 + H\,b_1\big]\Big(\frac{\pi^2}{4}[3\log^2 x + \frac{\pi^2}{2}] - \frac{6}{x}\Big) + H\,b_2\Big(\pi^2\log x\,[\log^2 x + \frac{\pi^2}{2}] + \frac{24}{x}\Big)
$$

$$
+ R_1 x_0^{\eta_1}\Big(\frac{\pi}{2}x^{-\eta_1}\big[-\tan(\frac{\pi}{2}\eta_1)\,b_0 + [-\log x\tan(\frac{\pi}{2}\eta_1) + \frac{\pi}{2}\sec^2(\frac{\pi}{2}\eta_1)]\,b_1
$$

$$
+[-\log^2 x\tan(\frac{\pi}{2}\eta_1) + \pi\sec^2(\frac{\pi}{2}\eta_1)\big(\log x - \frac{\pi}{2}\tan(\frac{\pi}{2}\eta_1)\big)]\,b_2\big]
$$

$$
+ \frac{1}{x}\Big[\frac{b_0}{(1-\eta_1)} - \frac{b_1}{(1-\eta_1)^2} + \frac{2\,b_2}{(1-\eta_1)^3}\Big]\Big)\bigg]
\tag{3.31}
$$

For the odd combination we have

$$
\frac{\partial \mathrm{Re}\, F_-(x,t)}{\partial t}\Big|_{t=0} = \frac{1}{2}\big[(\sigma\rho B_R)\,(\mathrm{p\bar p}) - (\sigma\rho B_R)\,(\mathrm{pp})\big]
$$

$$
= \frac{2}{\pi}\frac{1}{2}\,R_2 x_0^{\eta_2}\times\Big(\frac{\pi}{2}x^{-\eta_2}\big[\cot(\frac{\pi}{2}\eta_2)\,b_0 + [\log x\cot(\frac{\pi}{2}\eta_2) + \frac{\pi}{2}\csc^2(\frac{\pi}{2}\eta_2)]\,b_1
$$

$$
+[\log^2 x\cot(\frac{\pi}{2}\eta_2) + \pi\csc^2(\frac{\pi}{2}\eta_2)\big(\log x + \frac{\pi}{2}\cot(\frac{\pi}{2}\eta_2)\big)]\,b_2\big]
$$

$$
+ \frac{1}{x^2}\Big[\frac{b_0}{(2-\eta_2)} - \frac{b_1}{(2-\eta_2)^2} + \frac{2\,b_2}{(2-\eta_2)^3}\Big]\Big)
\tag{3.32}
$$

We remark that the subtraction constant K does not appear explicitly after the derivation in Eqs.(3.28, 3.29) (as it appears in Eq.(3.21)). Its influence is included in the values of the $\sigma\rho$ factors. It is very important that the triple factor for the pp system given by DDR from the PDG input has a zero, located at $\sqrt{s} = 17.7775\,\mathrm{GeV}$. If the factorization form is assumed, this requires that $\sigma\rho(\mathrm{pp})$ must be zero at the same energy. This requirement fixes the value of the subtraction constant, and we obtain $K = 935$, value that has been used in plots in Fig. 3.2.

Given the triple products, we can divide by the real amplitudes at $|t| = 0$, and obtain the real slopes. These quantities were shown before [38] to be very important

information for the study of forward pp and p$\bar{\text{p}}$ scattering.

It is important to remark that the derivatives depend on the t dependence in the inputs, as a characteristic feature of each model. In Chapter 4 we study the t dependence of the forward imaginary amplitude in the SVM model.

The values of the amplitudes and their slopes at $|t| = 0$ are connected by dispersion relations. We have given above the expressions for this connection. It is well known [36] that values determined from DDR for the slope B_R are larger than those of B_I. The remarkable difference between the slopes of imaginary and real amplitudes is shown by the ratio B_R/B_I, that is shown in Fig. 3.4.

In both cases the asymptotic value of the ratio is 2.

$$\frac{B_R}{B_I} \rightarrow 2 \ , \quad \text{as} \ \ \sqrt{s} \rightarrow \infty \ . \tag{3.33}$$

This is a consequence of DR if it is assumed that the input imaginary amplitude behaves like $\log^2(s)$ at high energies.

The strong real slope must be a characteristic feature of any realistic model. Neither phenomenological models nor analysis of data should ignore the basic properties of the amplitudes in elastic scattering. These are formal, unavoidable properties that connect the real and imaginary amplitudes at $|t|$=0. The calculations and figures presented above with the PDG form of total pp or p$\bar{\text{p}}$ cross section are a simplification of the reality, but they indicate universal properties.

Since the slopes B_I and B_R are different, the real and imaginary amplitudes do not run parallel in a plot against $|t|$ in the forward range, as if they were just connected by a constant quantity ρ. Each amplitude has its own slope at the origin, and vary differently in magnitude, each one looking for its zero [20, 50]. These facts are often ignored in the analysis of forward scattering for the determination of cross section [51]. They are of crucial importance for the study of Coulomb interference, and consequently for the determination of total cross section and of the ρ parameter.

With this fact, the determinations of ρ given in the literature (PDG) are doubtful, and should be revised.
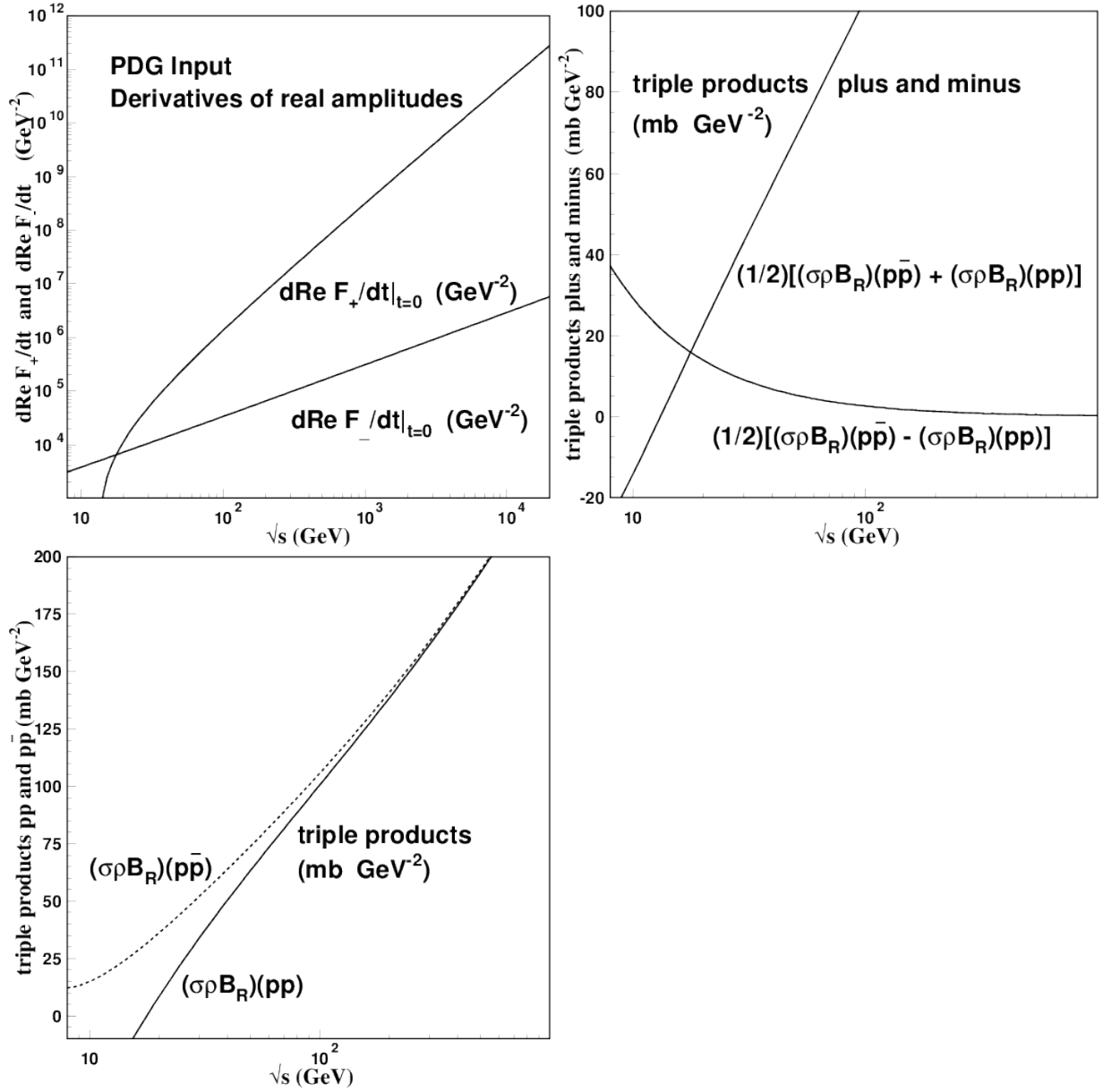
Figure 3.3: a) (figure above and on the left) Derivatives at $t = 0$ of the even imaginary and real amplitudes $d\mathrm{Re}\,F_+(x,t)/dt\big|_{t=0}$ and $d\mathrm{Re}\,F_-(x,t)/dt\big|_{t=0}$ as determined with the extended PDG input of Eqs. (3.2), (3.3), using exact DDR. The constant K disappears by derivation. Once the real amplitudes are assumed to have simple exponential t dependences, like $\sigma\rho\exp(B_R t/2)$ near the origin, the derivatives take the form of triple products $(1/2)\sigma\rho B_R$, which do not depend on the subtraction constant K. These triple products are shown in the b) (figure above and on the right) and c) (figure bellow) plots. These forms define the real slopes B_R for the pp and p$\bar{\text{p}}$ systems. It is important to observe that $\sigma\rho B_R$ (pp) has a zero, which is located at $\sqrt{s} = 17.7775\,\text{GeV}$, and $\sigma\rho$ (p$\bar{\text{p}}$) has no zero. With the assumption of the factorized form $(1/2)\sigma\rho B_R$ for the derivative at the origin, the product $\sigma\rho$ for pp must also have a zero at the same energy. This determines the value of the subtraction constant, that we find to be $K = 935$.

Figure 3.4: The slopes of real and imaginary amplitudes vary with the energy with a $\log^2$ dependence as given by Eqs. (3.25,3.30). Dispersion relations predict that at all (high) energies it is $B_R > B_I$. The ratio B_R/B_I is plotted as function of the energy, indicating the finite asymptotic limit 2.
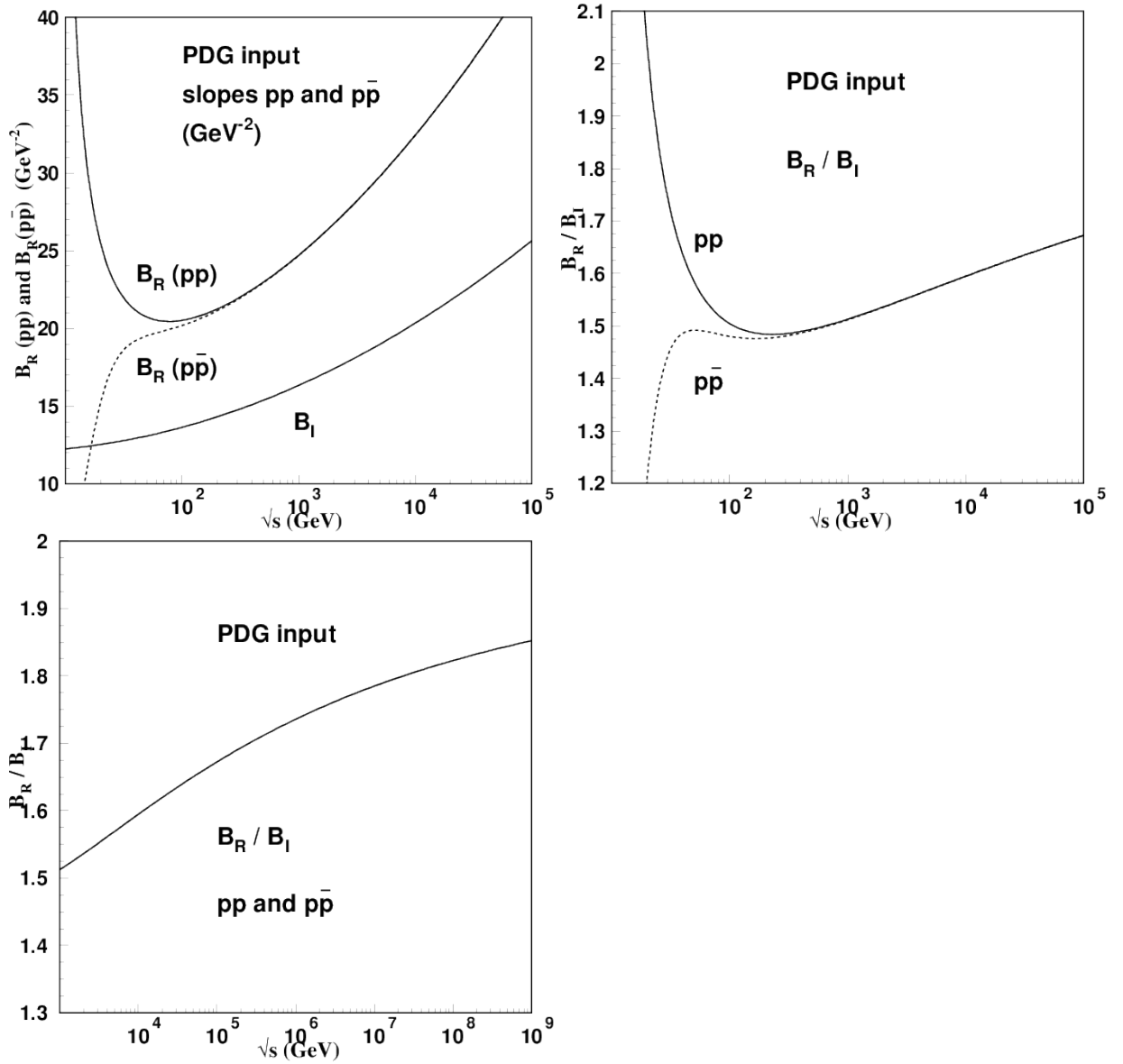
3.1.2 Remarks on behavior at high energies

For high energies, the even real part $\mathrm{Re}\,F_+(E, t = 0)$ behaves like $H\pi s \log(s/s_0)$ while the even imaginary goes like $Hs \log^2(s/s_0)$. The asymptotic behavior of the ratio of the even combinations is

$$\frac{\mathrm{Re}\,F_+(E, t = 0)}{\mathrm{Im}\,F_+(E, t = 0)} \approx \frac{\pi}{\log(s/s_0)} \ . \tag{3.34}$$

The imaginary and real odd combinations run parallel in the log plot, with

$$\frac{\mathrm{Re}\,F_-(E, t = 0)}{\mathrm{Im}\,F_-(E, t = 0)} \approx \cot\left(\frac{\pi\eta_2}{2}\right) \ . \tag{3.35}$$

In the real part we have $\mathrm{Re}\,F_+(E, t = 0) \approx H\pi s \log(s/s_0)$ and $\mathrm{Re}\,F_-(E, t = 0) \approx R_2 s (s/s_0)^{-\eta_2} \cot\left(\frac{\pi\eta_2}{2}\right)$ respectively for the even and odd combinations, with

$$\frac{\mathrm{Re}\,F_-(E, t = 0)}{\mathrm{Re}\,F_+(E, t = 0)} \approx \frac{R_2}{H\pi} \tan\left(\frac{\pi}{2}(1 - \eta_2)\right) \frac{(s/s_0)^{-\eta_2}}{\log(s/s_0)} \ . \tag{3.36}$$

We thus have in general that the odd combinations become negligible at high energies, putting pp and p$\bar{\mathrm{p}}$ identical in both imaginary and real amplitudes. In the phenomenological practice, within experimental errors, all possible differences between the two systems disappear for $\sqrt{s} \geq 500\,\mathrm{GeV}$.

The products $\sigma\rho$ are natural (more directly measured) quantities to represent properties of the real amplitudes in pp and p$\bar{\mathrm{p}}$ scattering. However, the ratio ρ is more commonly used, although forming the ratio implies in larger error bars. For high energies the pp and p$\bar{\mathrm{p}}$ cross sections and ρ approach common expressions. We can verify that for large s the PDG parametrization gives that the difference, $\rho(\mathrm{p}\bar{\mathrm{p}}) - \rho(\mathrm{pp})$ goes to zero very fast,

$$\rho(\mathrm{p}\bar{\mathrm{p}}) - \rho(\mathrm{pp}) \approx 2\cot(\eta_2\pi/2)\,\frac{R_2\,(s/s_0)^{-\eta_2}}{H \log^2[s/s_0]} \ . \tag{3.37}$$

Comparing with the difference between cross sections

$$\sigma(\mathrm{p\bar{p}}) - \sigma(\mathrm{pp}) \approx 2R_2\left(\frac{s}{s_0}\right)^{-\eta_2} , \tag{3.38}$$

we conclude that the difference of ρ's falls much faster.

Thus we have that at high energies the differences between p$\bar{\mathrm{p}}$ and pp can be neglected, for both imaginary and real forward amplitudes, and the information from DR for energies larger than, say, $\sqrt{s} = 500$ GeV , valid for any phenomenological description of pp and p$\bar{\mathrm{p}}$ scattering is given by Eq.(2.20) only.

Froissart-Martin bound

In the introduction of this thesis we presented the theorem of Froissart-Martin bound. This bound guides theoretical and phenomenological models on the description of the rising of the total cross section. Considering the PDG description of pp scattering, with the high energy behavior in the PDG representation

$$\sigma_{\mathrm{tot}}(s) \approx H \log^2(\frac{s}{s_0}) \tag{3.39}$$

we obtain the average in the Martin-Roy definition, Eq.(1.9),

$$\bar{\sigma}_{\mathrm{tot}}(s, \infty) = H\left[1 + [1 + \log(s/s_0)]^2\right] \tag{3.40}$$

and the theorem becomes

$$H\left[1 + [1 + \log(s/s_0)]^2\right] \leq \frac{4\pi}{t_0}[\log(s/s_{\mathrm{sc}}) + (1/2)\log\log(s/s_{\mathrm{sc}})]^2 . \tag{3.41}$$

Taking only the dominant terms at high energies, and assuming for s_{sc} the same

as the PDG scale s_0, we obtain the bound

$$H \leq \frac{4\pi}{|t|_0}. \tag{3.42}$$

Using $|t|_0 = 4m_\pi^2$ the bound becomes, numerically

$$H \leq \frac{4\pi}{m_\pi^2} = 160.28 \text{ GeV}^{-2} = 62.41 \text{ mb}, \tag{3.43}$$

that is enormously distant from the experimental value H=0.2838 mb .

In QCD the dynamical basis for the proof of a bound relation is affected by the existence of glueballs [52]. Results from lattice theory and models of nonperturbative QCD [53] seem to confirm the $\log^2(s)$ behavior of the total cross section at high energies, giving the external multiplicative constant with a value close to the experimental reality. We may note that in the external factor π/m_π^2 obtained in the theorem for $\pi\pi$ scattering, if we change from pion to gluonium mass (say 1.6 GeV) the external factor changes by 1/130.6 and the bound becomes $H \leq 0.478$ mb. This is not much higher than 0.2838 mb, and seems interesting as a reference bound for pp scattering to stimulate further studies.

3.2 Differential cross section and Coulomb interference

In the region of small momentum transfer $|t|$, the intense Coulomb amplitude added to the nuclear interaction creates an interference that is observable in the $|t|$ distribution in $d\sigma/dt$. This Coulomb interference region of low $|t|$ values goes typically up to $|t| = 0.01$ GeV^2, but (in view of present data) we show that the form of $d\sigma/dt$ in general can actually be described in terms of simple exponential real and imaginary nuclear amplitudes well beyond this range.

In previous analyses of pp and p$\bar{\text{p}}$ data, the real and imaginary nuclear amplitudes were considered as having the same exponential dependence $\exp{(Bt/2)}$, where B is the slope of $d\sigma/dt$. This simplifying assumption is not adequate, according to dispersion relations [38] and according to the theorem of A. Martin [54] that says that the position of the first zero of the real amplitude is closer and approaches $t = 0$ as the energy increases. Both results indicate that the slope of the real amplitude should be larger than that of the imaginary one, and in the present work we investigate the description of the Coulomb interference region allowing for different real and imaginary slopes. We review the scattering data in cases where this kind of information can be investigated.

We present the forward quantities σ, ρ and the slope B frequently measured by the experiments.

In elastic pp and p$\bar{\text{p}}$ collisions, the combined nuclear and coulomb amplitudes is written

$$T(s,t) = T^N(s,t) + T^C(t) \; , \tag{3.44}$$

where $T^N(s,t)$ is the complex nuclear amplitude

$$T^N(s,t) = T_R^N(s,t) + iT_I^N(s,t) \; , \tag{3.45}$$

and $F_C(t)$ is the real Coulomb amplitude

$$T^C(t) = \mp \frac{2\alpha}{|t|} F^2_{\text{proton}}(t) e^{i\alpha\Phi(s,t)} \ , \tag{3.46}$$

with the proton electromagnetic form factor

$$F_{\text{proton}} = (0.71/(0.71 + |t|))^2 \tag{3.47}$$

associated to a relative phase Φ. The phase Φ was initially considered by H.A. Bethe [55] and then by West and Yennie [56], followed by different evaluations worked out by several authors [57–59]. In the present work we extend these investigations in the very low $|t|$ range, considering the possibility of different slopes for the real and imaginary amplitudes following the West and Yennie phase.

In the normalization that we use [60] the differential cross section is written

$$\frac{d\sigma}{dt} = \pi \left(\hbar c\right)^2 \left\{ \left[\frac{\rho\sigma}{4\pi \left(\hbar c\right)^2} \, e^{B_R t/2} + F^C(t) \cos\left(\alpha\Phi\right) \right]^2 + \left[\frac{\sigma}{4\pi \left(\hbar c\right)^2} \, e^{B_I t/2} + F^C(t) \sin\left(\alpha\Phi\right) \right]^2 \right\} \tag{3.48}$$

For small angles we can approximate

$$T^N(s,t) \approx T_R^N(s,0)e^{B_R t/2} + iT_I^N(s,0)e^{B_I t/2} \ . \tag{3.49}$$

We emphasize that the difference between slopes B_R and B_I must be respected. The parameter

$$\rho = \frac{T_R^N(s,0)}{T_I^N(s,0)} \ , \tag{3.50}$$

the optical theorem

$$\sigma = 4\pi(\hbar c)^2 T_I^N(s,0) \ , \tag{3.51}$$

and the slopes B_R, B_I are used to parametrize the differential cross section for small $|t|$. In these expressions, σ is in milibarns and the amplitudes T_R, T_I are in GeV^{-2}.

For low $|t|$, many authors approximate Eq. 3.48 to a wrong form

$$\frac{d\sigma}{dt} = \left|\frac{d\sigma}{dt}\right|_{t=0} e^{Bt} \ ,$$

(3.52)

where

$$B = \frac{\rho^2 B_R + B_I}{1 + \rho^2}$$

(3.53)

is the usual slope observed in the data of $d\sigma/dt$.

3.2.1 Coulomb phase

Here we present a prescription of the phase we made use, to connect the hadronic amplitudes with the coulomb amplitude described by the proton electromagnetic form factor. We use as a framework the West Yennie phase [56] making an extension in order to contain the real slope concept. The starting point is the expression

$$\Phi(s,t) = \mp\left[\ln\left(-\frac{t}{s}\right) + \int_{-4p^2}^{0} \frac{dt'}{|t'-t|}\left[1 - \frac{T^N(s,t')}{T^N(s,t)}\right]\right]$$

(3.54)

where the signs $\mp$ are applied to the choices pp/p$\bar{\text{p}}$ respectively. The quantity p is the proton momentum in center of mass system, and at high energies $4p^2 \approx s$. For small $|t|$, assuming that $T^N(s,t')$ keeps the same form for large $|t'|$ (this approximation should not have practical importance for the results), we have

$$\begin{aligned}\frac{T^N(s,t')}{T^N(s,t)} &= \frac{T_R^N(s,0)\ e^{B_R t'/2} + iT_I^N(s,0)\ e^{B_I t'/2}}{T_R^N(s,0)\ e^{B_R t/2} + iT_I^N(s,0)\ e^{B_I t/2}} \\ &= \frac{c}{c+i}e^{B_R(t'-t)/2} + \frac{i}{c+i}e^{B_I(t'-t)/2} \ ,\end{aligned}$$

(3.55)

where

$$c \equiv \rho e^{B_R - B_I} t/2 \ .$$

(3.56)

The calculation is explained in detail in the Appendix C. The integrals that

appear in the evaluation of Eq. (3.54) are reduced to the form [59]

$$I(B) = \int_{-4p^2}^{0} \frac{dt'}{|t'-t|}[1 - e^{B(t'-t)/2}] \tag{3.57}$$

that is solved in terms of exponential integrals [61] as

$$I(B) = E_1\left[\frac{B}{2}(4p^2 + t)\right] - E_i\left[-\frac{Bt}{2}\right] + \ln\left[\frac{B}{2}(4p^2 + t)\right] - \ln\left[-\frac{Bt}{2}\right] + 2\gamma . \tag{3.58}$$

The real part of the phase is then written

$$\Phi(s,t) = \mp\left[\ln\left(-\frac{t}{s}\right) + \frac{1}{c^2+1}[c^2I(B_R) + I(B_I)]\right] , \tag{3.59}$$

and this expression is introduced into Eq. (3.46).

With this fact, the determinations of ρ given in the literature (PDG) are doubtful, and should be revised.

The properties of the real part must be respected. The analysis of the Coulomb interference without account for the behavior of the real strong amplitude represents a violation of Quantum Mechanics. Eq.(3.48) should not be used to obtain σ, ρ.

Considering elastic pp and p$\bar{\text{p}}$ scattering at energies above $\sqrt{s} = 19$ GeV, the real and imaginary amplitudes have zeros located in ranges $|t| \approx (0.1 \sim 0.3)$ GeV^2 and $|t| = (0.5 \sim 1.5)$ GeV^2 respectively, and the use of exponential forms beyond a limited forward range leads to inaccurate determination of the characteristic forward scattering parameters σ, ρ, B_I and B_R. For a precise description of the elastic amplitudes we need to use more general expressions valid for all t that are connected with the exponential behavior as limits.

A program of description of the elastic differential cross sections by unified analytical forms of the amplitudes in the full t range is important for the identification of the amplitudes (disentanglement), necessary for the understanding of the involved dynamics. We have made effort in this direction [20, 21, 51].

The data are not rich and uniform enough for this purpose in the whole energy range of the ISR, Fermlab, SPS experiments, and sometimes it is not possible to show that the results are model dependent.

We present below an analysis of data for $\sqrt{s} \geq 19\,\mathrm{GeV}$ in the forward range , using pure exponential forms for the real and imaginary parts. The analysis is made using Eq. (3.48), with full expression for the Coulomb phase.

3.3 Analysis of experiments at ISR and Fermilab energies

In this section we discuss data at energies from 19 to 540 GeV, including the slope B_R and proper Coulomb phase in the analysis.

An extensive analysis has been done in the Master Degree Thesis [62] with a determination of the forward parameters for ISR/FERMILAB until LHC energies, treating both pp and p$\bar{\text{p}}$ scattering. We here do not intend to present the whole analysis again but summarize the main points and show modified results.

The published data [49] for $d\sigma/dt$ are used to determine σ and rho, and are treated with equation for $d\sigma/dt$ different from Eq.(3.48), or sometimes take some parameter values (such as the total cross section or ρ) from other experiments. Independent real and imaginary amplitudes are not always consistently with DR. To have an independent evaluation of the absolute normalization we analyse the published data considered as event rate dN/dt, using a free normalization factor a_5. In other words we write the publish data as

$$\left[\frac{dN}{dt}\right]_{\text{data}} = a_5 \, \frac{d\sigma}{dt} \; , \tag{3.60}$$

with $d\sigma/dt$ written as in Eq.(3.48), and a_5 is determined for each experiment. We understand that a_5 adjusts the data to the Coulomb amplitude that is dominant

at low $|t|$, in interference with the strong real amplitude constrained by DDR. We have used fitting programs (Cern Minuit-PAW, Cern-Root, and Numerical Recipes) to obtain correlations for the parameters (σ, ρ, B_R, B_I and a_5), for values of energy where the data seem have more quality. We first concentrate on the low energy range of ISR and Fermlab, where, due to the small magnitude of the real ratio ρ, there are discrepancies and non-regularities. We find that results obtained for the four amplitude parameters may be sensitive to the determination of a_5, although this factor is always nearly 1. At 19.4 GeV the correction of normalization by a_5 is essential, leading to a new value of ρ and matching the data from two experiments.

Below we present some cases, explaining our determination of parameters.

It is important to remark that in some cases the results obtained in the fittings depend on the set of data of low $|t|$ selected for the analysis of the Coulomb interference region. We indicate the number N of fitted points in the description below.

In the region from 19.4 to 30.6 GeV , ρ is small, with little influence of the real amplitude, and it is difficult to determine ρ and B_R, while σ and B_I are more stable. For obvious reasons, there is strong correlation between the extracted values of ρ and B_R, and the use of DDR is important to resolve ambiguities.

We may consider that B_I should be the best determined parameter at the energies up to 30 GeV, as it is less dependent of normalization and of influence of the real amplitude. We have attempted to control the arbitrariness that occurs at some energies, assuming for B_I a dependence on $\log s$ as given in Eq. (3.25).

The whole situation shows that the data collected in these experiments are not detailed and regular enough to allow precise determination of the amplitudes in the forward direction. There is ample freedom in the parameters, with correlated ranges leading to the same χ^2. The analysis shows the need for DR and additional tools (models, or external inputs) to help in ambiguities.

We stress that this thesis does not intend to give the best final values for the

scattering parameters. We rather wish to call attention to details that must be taken into account in the treatment of future data from LHC, and we suggest that a complete revision of the published data be made by experts.

3.3.1 Analysis in the energy range from 19.4 to 30.6 GeV

The energy range from 19.4 to 30.6 GeV is particularly critical for the determination of parameters, with discrepancies in the information from the experiments.

Measurements at Fermilab explored the region of low $|t|$ at energies from 19.4 to 27.36 [63–66]. The 19.4 GeV and 27 GeV energies were also studied in detail at higher $|t|$ [67, 68].

Cern measurements [66, 69, 70] were taken at 23.542 , 30.632 , 30.7 and 24.3 GeV for pp and 30.4 and 24.3 GeV for p$\bar{\text{p}}$.

For p$\bar{\text{p}}$ there are data [64] at 19.4 GeV on ρ, but not on $d\sigma/dt$, and at 24.3 GeV there are $d\sigma/dt$ data in the thesis by Breedon [66].

We discuss below some of the data, namely those that are more accessible to the intended analysis, that requires a regular set of points with $|t| \leq 0.01$ GeV^2.

Results are compiled in Table 3.2.

The 19.4 GeV discrepancy case

Measurements at $\sqrt{s}$=19.4 GeV have lead to 69 points at very low $|t|$ (from 0.00066 to 0.03 GeV^2) by Kuznetsov et al. [63] and 134 points (from $|t| = 0.02$ to 0.66 GeV^2) by Fajardo et al [64] and Schiz et al. [67]. Other measurements, which we do not analyse here, cover higher $|t|$ ranges and are not adquate for the analysis. The two experiments give ρ with opposite signs: $\rho = -0.0034 \pm 0.009$ for Kuznetsov et al [63] and $\rho = 0.019 \pm 0.018$ for Fajardo et al and Schiz et al [64, 67]. The discrepancy can be eliminated with the introduction of a free normalization factor a_5, writing Eq.(3.61) with $a_5 \neq 1$ for one or both datasets. The normalization factor a_5 is fixed by checking the Coulomb interference at low $|t|$. Using the

first 52 points of Kuznetsov data, extended up to $|t| = 0.01309 \, \text{GeV}^2$, we find best fitting with $a_5 = 1.0063 \pm 0.0216$, $\rho_{\text{pp}} = 0.014 \pm 0.017$, $\sigma_{\text{pp}} = 39.09 \pm 0.32$ mb, $B_I = 12.51 \pm 0.56 \, \text{GeV}^{-2}$, $B_R = 23.53 \pm 1.42 \, \text{GeV}^{-2}$ (five parameters) and $\chi^2 = 0.8597$, With the same amplitude parameters and $a_5 = 1.0$, the lowest $|t|$ part of the Fajardo and Schiz data (that do not reach very small $|t|$) are compatibly well reproduced. The Fajardo/Schiz data do not cover the low $|t|$ range necessary for the precise evaluation of forward parameters with Coulomb interference, so that we here only test compatibility extending the solution obtained in the low $|t|$ range. This is shown in Fig. 6.9 , where the Kuznetsov data are shown with corrected normalization, representing then the true cross sections. The figure shows then a very good matching with the other experiment. It is remarkable that this matching is purely a result of the Coulomb interference condition. This gives support to the method of using the Coulomb interference structure to check data at low $|t|$ to obtain correct normalization and determine forward scattering parameters.

The 23.542 - 23.882 GeV case

At 23.542 GeV(CERN ISR experiment) there are 31 experimental points [70], with $0.00037 \leq |t| \leq 0.0102 \, \text{GeV}^2$. The Fermilab data at 23.882 GeV [63] consist of 61 points in the interval $0.00066000 \leq |t| \leq 0.031600 \text{GeV}^2$. The reported ρ values for the very close energies present strong discrepancy. In order to obtain smaller values of χ^2 and stable values for the parameters, our fitting procedure uses 24 points, with $|t|$ limited to $|t| \leq 0.00671 \, \text{GeV}^2$ and 40 points with $|t| \leq 0.00804 \, \text{GeV}^2$ respectively for the two experiments.

We look for a unified description, allowing for a free normalization a_5 in each experiment. The most favorable datasets use the first N = 24 ($|t| \leq 0.00543$) and N = 40 ($|t| \leq 0.00804$) points respectively. We find that the Cern dataset has a best fitting with $a_5 = 1$, namely without change, while for the Fermilab data our result is $a_5 = 1.0169 \pm 0.0034$. The ρ values become compatible with the DDR predictions,
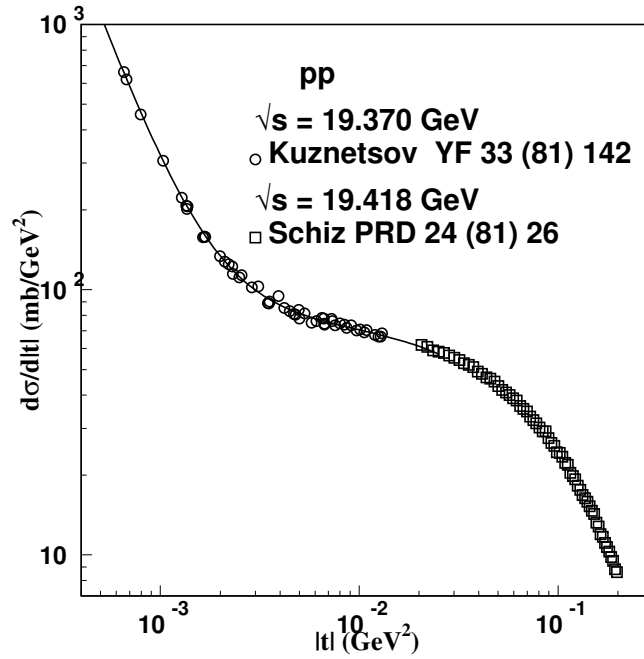
Figure 3.5: Data from Kuznetsov et al [63] and Fajardo/Schiz et al [64, 67] at 19.4 GeV. The figure shows the 69 Kuznetsov points (normalized with $1/1.0063$) together with Schiz first 61 points up to $|t| = 0.2$ GeV^2. The amplitude parameters are $\sigma = 39.09$ mb, $\rho = 0.014$, $B_I = 12.51$ GeV^{-2}, $B_R = 23.53$ GeV^{-2}. The log horizontal scale helps to expand and show in detail the low $|t|$ behavior, and it is remarkable that the description works very well up to $|t| = 0.02$, beyond the range of the fitted data and after the range of the representation of the amplitudes by pure exponential forms .

with a slight rise with the energy.

The numbers are

$$\sqrt{s} = 23.542 \text{ GeV} \, , \ B_I = 12.61 \text{ GeV}^{-2}, \ \rho = 0.0199 \pm 0.003,$$

$$N = 24, \ a_5 = 1, \chi^2 = 0.3193,$$

$$\sigma = 39.73 \pm 0.08 \text{ mb}, B_R = 22.15 \text{ GeV}^{-2}$$

and

$$\sqrt{s} = 23.882 \text{ GeV} \, , \ B_I = 12.62 \text{ GeV}^{-2} \, , \ \rho = 0.020 \pm 0.003 \, ,$$

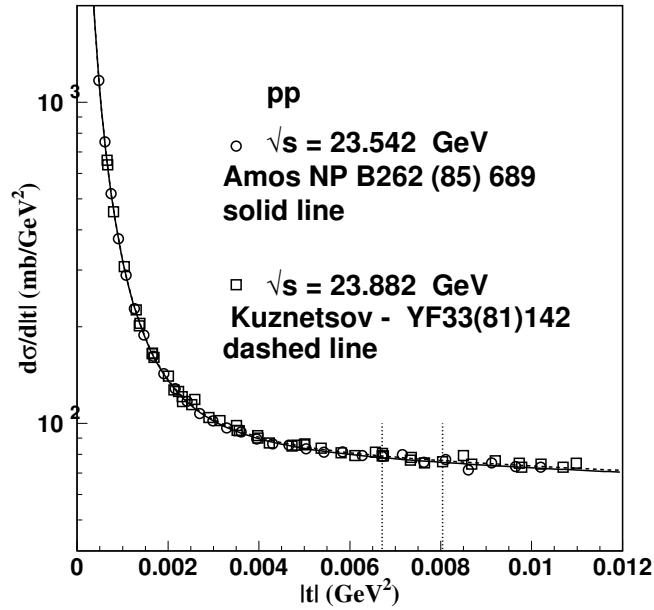$$N = 40 \, , \ a_5 = 1.0169 \pm 0.0034 \, , \ \chi^2 = 0.7694,$$

Figure 3.6:   Data at 23.542 and 23.882 GeV, with the lines fitting respectively the first 24 points up to $|t| = 0.00671\text{GeV}^2$ and the first 40 points up to $|t| = 0.00804\text{GeV}^2$ (ranges indicated by vertical dotted lines) using expressions of Coulomb interference and exponential forms for the amplitudes. The parameters are given in the text. The 23.882 GeV data is shown multiplied by 1/1.0169.

$$\sigma = 39.99 \pm 0.10 \text{ mb}, B_R = 22.10 \text{ GeV}^{-2} .$$

The data (with normalization factor in the 23.882 case) and the lines fitting the forward points are shown in Fig. (3.6).

24.3 GeV data on pp and p$\bar{\text{p}}$ scattering [66]

This was the CERN UA6 experiment, and the $d\sigma/dt$ data are taken from R. Breedon PhD thesis. For pp there are N = 31 points, with $0.00108 \le |t|(\text{GeV}^2) \le 0.01313$. Good fitting with correct Coulomb interference contribution requires $a_5 = 1.024 \pm 0.002$. Parameters are

$$\sigma = 39.30 \pm 0.05 \text{ mb} , \ \rho = 0.022 \pm 0.012 , \ B_I = 12.63 \, \text{GeV}^{-2}, B_R = 23.55 \, \text{GeV}^{-2}$$

$$N = 31 , \ a_5 = 1.024 \pm 0.002, \ \chi^2 = 0.5590 .$$

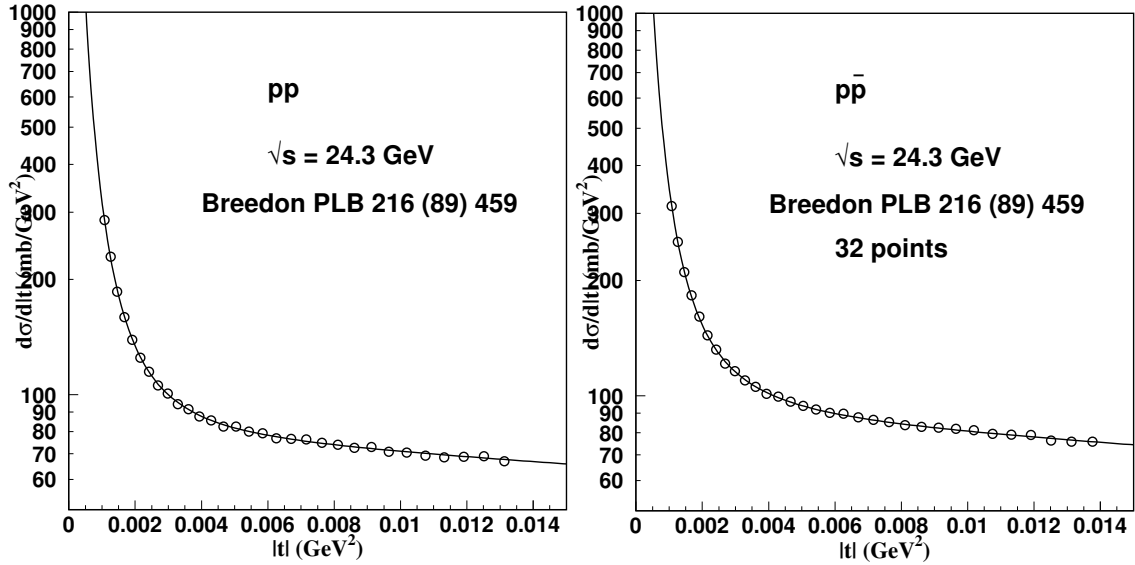The ρ and B_R parameters obey DDR requirements.

Figure 3.7:   Data at 24.3 GeV, for pp corrected with factor $1/1.024$, and for p$\bar{\text{p}}$, and calculated $d\sigma/dt$. The parameters are given in the text.

For p$\bar{\text{p}}$ there are N $= 32$ points, with $0.00108 \leq |t|(\text{GeV}^2) \leq 0.01376$. The fitting with Coulomb interference does not require change of normalization, and leads to

$$\sigma = 41.41 \pm 0.04 \text{ mb} \;,\; \rho = 0.052 \pm 0.002 \;,\; B_I = 12.63 \text{ GeV}^{-2},\; B_R = 18.20 \text{ GeV}^{-2}$$

$$N = 32 \;, a_5 = 1 \;,\; \chi^2 = 0.4787 \;.$$

The plots with the data for pp and p$\bar{\text{p}}$ at 24.3 GeV are shown in Fig. (3.7).

pp scattering at $\sqrt{s} = $ 30.632 and 30.7 GeV and p$\bar{\text{p}}$ at 30.4 GeV

Two compatible datasets are available at about 30 GeV from ISR/CERN. At 30.632 GeV there are 32 points [70] in the interval $|t| = 0.0005 - 0.0176$ GeV^2 and at 30.7 GeV there are 181 measured points [69] in the large $|t|$ interval from 0.00106 to 5.75 GeV^2. We treat the dataset of lower $|t|$ with 32 points [70] at 30.632 GeV, obtaining parameters

$$\sigma = 40.24 \pm 0.05 \text{ mb} \;,\; \rho = 0.034 \pm 0.003 \;,\; B_I = 12.76 \pm 0.24 \;,$$
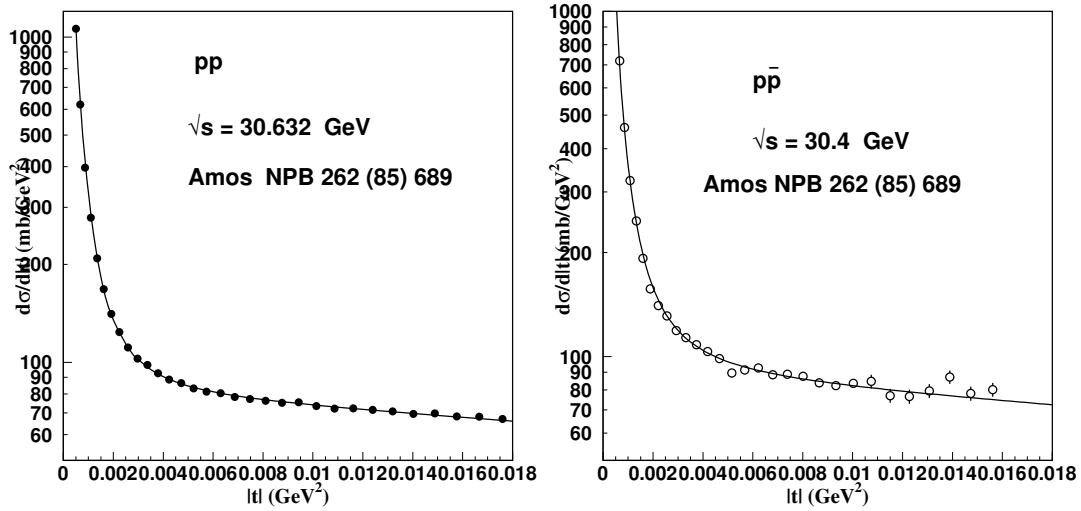
Figure 3.8: The 32 points, of the 30.632 GeV measurements and the 29 points of the $p\bar{p}$ for 30.4 GeV are fitted with expressions of Coulomb interference and exponential forms for the amplitudes. The parameters are given in the text.

$$B_R = 22.11 \text{GeV}^{-2} \text{ , } N = 32 \text{ , } a_5 = 1, \text{ } \chi2 = 0.6038 \text{ .}$$

The data, with the fitting curve, based on the Coulomb interference expressions and exponential amplitudes, are shown in Fig. 3.8. The parameters satisfy our parametrization and the predictions from DDR.

Now for $p\bar{p}$ at 30.4 GeV, where there are N=29 points for $0.00067 \leq |t| \leq 0.01561$ GeV^2. The parameters are

$$\sigma = 41.43 \pm 0.15 \text{ mb , } B_I = 12.23 \pm 1.08 \text{ GeV}^{-2} \text{ , } B_R = 18.45 \text{ GeV}^{-2} \text{ ,}$$

$$\rho = 0.086 \pm 0.006, a_5 = 1 \text{ , } \chi^2 = 1.436$$

Our suggestions for the low energy range

Table 3.2 shows data [63–66, 70], predictions from DDR, and results of our analysis of differential cross-section for energies in the range from 19.4 to 30.7 GeV.

Table 3.2: Our suggestions for forward scattering parameters

|	$\sqrt{s}$ (GeV)	σ (mb)	ρ	B_I (GeV^{-2})	B_R (GeV^{-2})	a_5	χ^2	N
pp	19.4	39.09	0.014	12.51	23.53	1.0063	0.8597	52
	23.542	39.73	0.0199	12.61	22.15	1	0.3193	24
	23.882	39.99	0.020	12.62	22.10	1.0169	0.7694	40
	24.3	39.30	0.022	12.63	23.55	1.024	0.5590	31
	30.632	40.24	0.034	12.76	22.11	1	0.6038	32
p$\bar{\text{p}}$	24.3	41.41	0.052	12.63	18.20	1	0.4787	32
	30.4	41.43	0.086	12.23	18.45	1	1.436	29

3.3.2 Energy range from 44.7 to 62.5 GeV

This is an important range to analyse because it has a good statistics (large number of points) and the experiments reach since very small values of t until large t values, which permits a better investigation of the forward regime and the transition from simple exponential forms to a more complete amplitude description in t. Despite of the large amount of data it is not easy to determine the forward quantities from the data. Another feature of this region is that in 52 GeV both pp and p$\bar{\text{p}}$ $d\sigma/dt$ were measured, allowing to compare both processes at equal footing. The determination of ρ at this energy becomes important to determine the subtraction constant in the dispersion relations.

At $\sqrt{s} = 44.699$ GeV the dataset is presented in the report by Amaldi and Schubert [69]. They published 230 data points extending up to $|t| = 7.25$ GeV^2. The first 40 points of the forward part, up to $|t| = 0.01856$ GeV^2, are well represented by the Coulomb interference formula, as shown in Fig. 3.9. With amplitude parameters fixed as suggested by our parameterization of the total cross section and by DDR predictions.

The plot in the LHS of the figure 3.9 shows data points up to $|t| = 0.29$ GeV^2, and it is remarkable that the calculation with simple exponential amplitudes reproduces well the data much beyond the forward fitting range. The plot in the RHS shows the deviation from the pure exponential form for large momentum transferred.

Fig. (3.10) shows the forward data [70] at $\sqrt{s} \approx 52.8$ GeV for pp (34 points

Figure 3.9: Forward scattering data at 44.699 GeV . The line is obtained using amplitude parameters suggested by derivative dispersion relations, given in the text, and the normalization constant is fitted as $a_5 = 1.0146$ using the 40 points with lowest $|t|$. In the RHS we plot together the large $|t|$ data exhibiting the peculiar behavior of the data with of the amplitudes deviating from the simple exponential dependence.
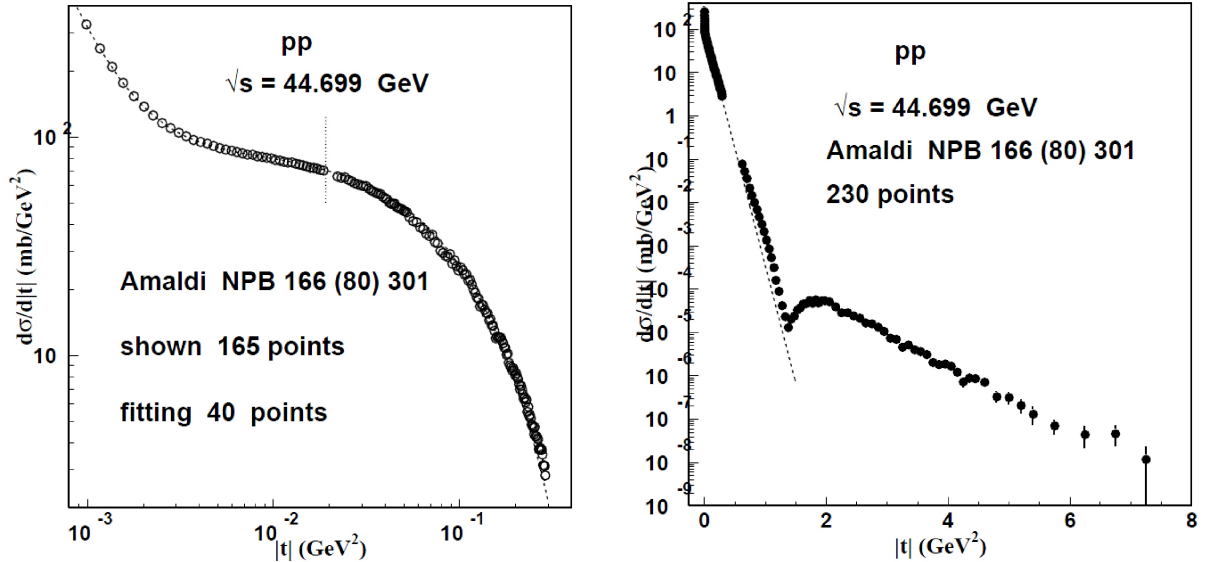

for $0.00107 \leq |t| \leq 0.05546$) and for p$\bar{\text{p}}$ (28 points for $0.00097 \leq |t| \leq 0.03866$) scattering and the lines obtained using amplitude parameters from DDR predictions and the Coulomb interference expressions. It's important to remark that fittings with free parameters do not converge here. We need to fix parameters according the assumptions above.

For the p$\bar{\text{p}}$ case it is important to introduce a normalization constant $a_5 = 1.0113$ that leads to a minimun average $\chi^2 = 1.080$ for the whole dataset of 28 points.

It is important to remark that the calculations with $B_R = B_I$ lead to larger χ^2 values in both pp and p$\bar{\text{p}}$ cases. Thus we here confirm the indication for $B_R > B_I$.

Fig. 3.11 shows the data at 62.5 GeV (138 points) [70] and the line representing the calculation with the forward exponential amplitudes, with $0.00167 \leq |t| \leq 6.25$. We present also a plot of the 64 points with lowest $|t|$, with $0.00167 \leq |t| \leq 0.099$ with a vertical dotted line indicating the first 29 points , with $0.00167 \leq |t| \leq 0.02931$ that lead to a calculated average $\langle \chi^2 \rangle = 1.058$. We remark that there is free parameters

Figure 3.10: Data of pp and p$\bar{\text{p}}$ scattering at 52.8 GeV described by exponential amplitudes, with parameters fixed by the DDR expressions, and Coulomb interference. The p$\bar{\text{p}}$ data are modified with a fitted normalization factor $a_5 = 1.0113$.
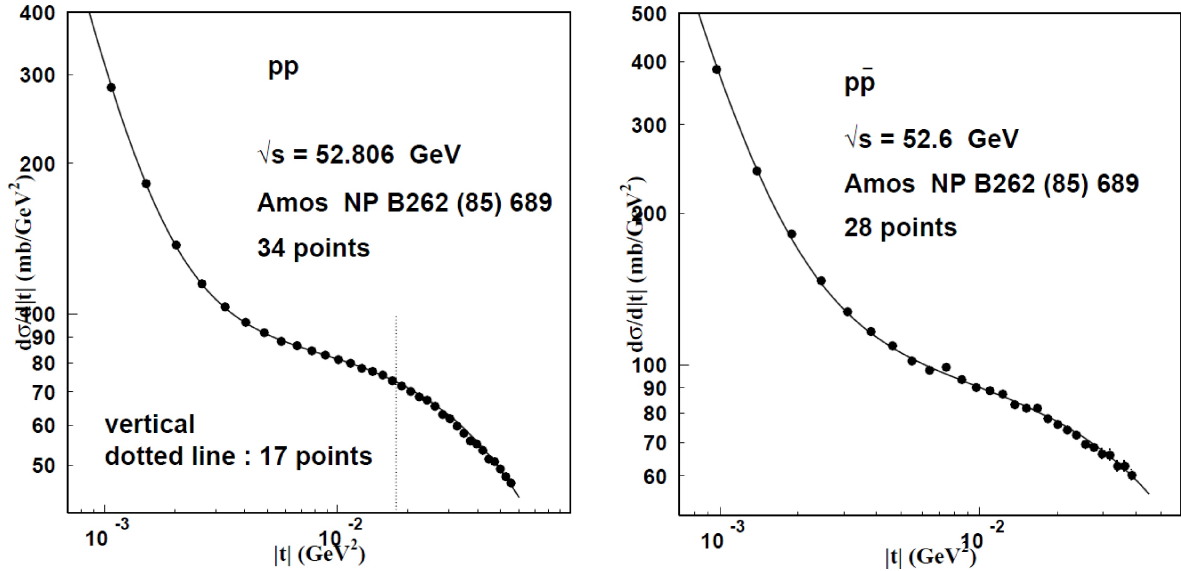
in the determination of the forward quantities. The parameters were provided by DR.

With the same fixed quantities for the amplitudes, we may introduce a free normalization constant for the data, obtaining $a_5 = 0.9976$ and $\chi^2 = 0.8922$ with the same N = 29 points.

Table 3.3: Our suggestions for forward scattering parameters

	$\sqrt{s}$ (GeV)	σ (mb)	ρ	B^I (GeV^{-2})	B^R (GeV^{-2})	a_5	χ^2	N
pp	44.699	41.59	0.066	12.49	18.69	1.0146	0.9029	40
	52.8	42.40	0.077	12.67	21.00	1	1.322	34
	62.5	43.32	0.089	12.85	21	0.9976	0.8922	
p$\bar{\text{p}}$	52.6	43.21	0.092	12.67	21.14	1.0113	1.080	28
	62.3	43.98	0.10	12.85	21	1	1.7	17

Figure 3.11: Data (138 points) and forward 64 points of pp scattering at $\sqrt{s} = 62.5$ GeV [70] shown together with the line representing the calculation with amplitude parameters taken from DDR expressions. It is interesting that the simple exponential amplitudes and the Coulomb interaction designed for very small $|t|$ describe (visually) very well the data much beyond this range.
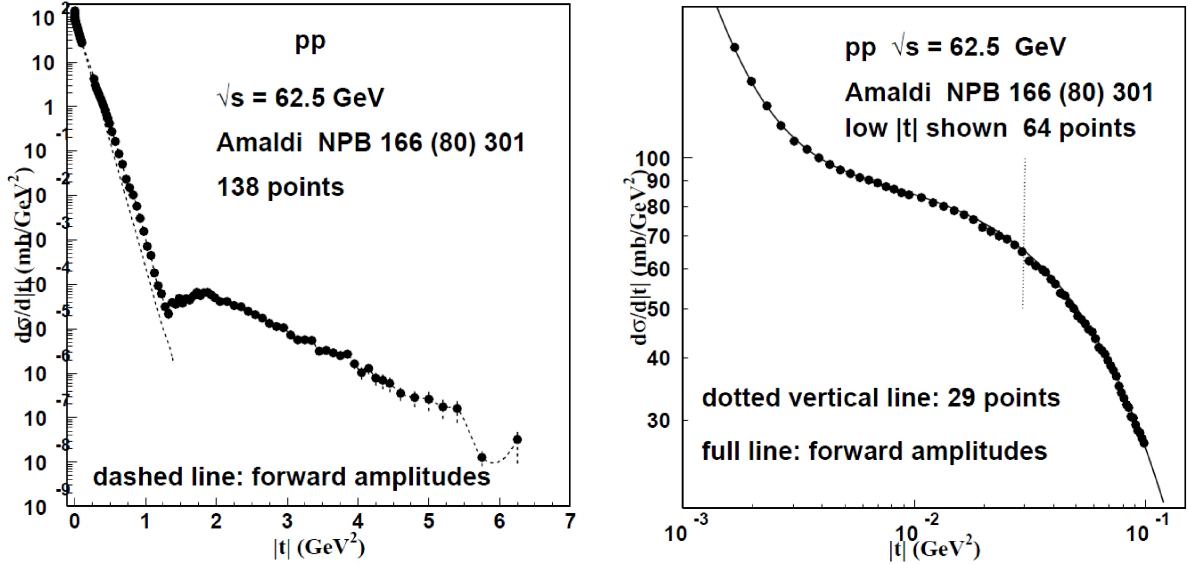
3.3.3 Energy 540 GeV

This is an interesting energy to analyse, first, because at about 540 GeV the total cross section of pp and p$\bar{\text{p}}$ are expected to be the same, according to Pomerochuk theorem and second at these energies the ρ parameter are the same for both processes.

At 541 GeV, the lowest $|t|$ values reached in measurements of p$\bar{\text{p}}$ elastic scattering are reported with event rates [71] only, with many (99) points in a range of low $|t|$ values, $0.000875 \leq |t| \leq 0.11875$. According to Durham HEP data basis, the cross-section values have not been determined otherwise in this low $|t|$ range. To make use of these valuable data, we made use of our method of finding a normalization factor by the Coulomb interference, connecting event rate and differential cross-section, finding a very clear and precise connection.

Our procedure is to describe the dN/dt data with the expression for the Coulomb interference region, with the parameter a_5 explained before, and the four quantities

Figure 3.12: Differential cross section at 541 GeV obtained from the event rate [71]. The vertical dotted line indicates the set of 84 points used in the fit to determine the normalization constant
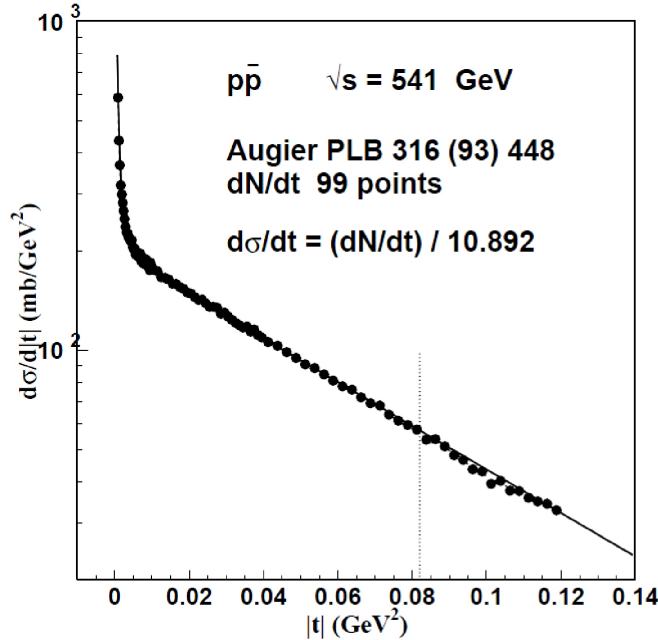
that describe forward p$\bar{\text{p}}$ scattering according to our parametrization of the total cross section and to the DDR expressions that determine ρ and the slopes.

These fixed parameters are

$$\sigma = 61.78 \text{ mb} , \ \rho = 0.142 , \ B_I = 15.15 \text{ GeV}^{-2} , \ B_R = 21.20 \text{ GeV}^{-2}$$

Then, given the event rate dN/dt we need to determine by fit only a normalization factor a_5 to obtain the cross sections $d\sigma/dt$. We define the best set in the sample of 99 points by looking for the smallest χ^2 . The selected set takes the first 84 points, with $000875 \leq |t| \leq 0.08125$, leading to $a_5 = 10.892 \pm 0.0126$, namely

$$\frac{d\sigma}{dt} = \frac{dN}{dt} \times \frac{1}{10.892 \pm 0.0126} \qquad (3.61)$$

Fig. 3.12 shows the 99 points of the calculated $d\sigma/dt$.

In Fig. 3.13 we show the good agreement of $d\sigma/dt$ at low $|t|$, obtained from dN/dt

Figure 3.13: The normalized event rate data at 541 GeV are in good agreement with the $d\sigma/dt$ data [72–74] at the same energy and higher $|t|$ values.
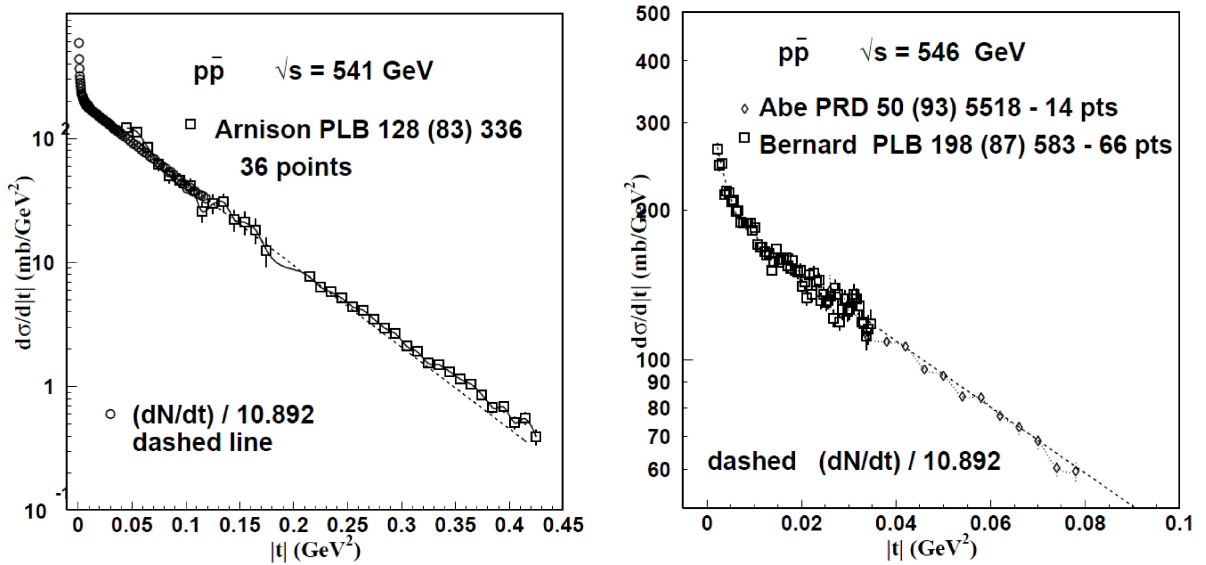
by adjustment of the coulomb interference, with the data of G. Arnison et al. [72], of Bernard et al. [73] and of Abe et al. [74] in $|t|$ ranges that partially superpose with the dN/dt event rate data. These results give confidence in our method that converts the event rate into absolute cross sections. We extend the comparison of different $d\sigma/dt$ measurements examining the data by Bozzo et al. [75, 76]. We observe in Fig. 3.14 that the normalized event rate data at 541 GeV are in good agreement with the $d\sigma/dt$ data [72, 75, 76] at the same energy. We draw also high $|t|$ data to remark the meaning of the forward scattering amplitudes in relation to higher $|t|$ values.

As a test of consistency of this method of connection between event rate and absolute cross section we compare values of $d\sigma/dt$ at the Cern/ISR energies, multiplied by an arbitrary normalization factor, with the Coulomb interference amplitudes. We find that this normalization factor is actually equal to one in all investigated cases.

To show the influence of value of the ratio B_R/B_I beyond these limits , we have studied values with fixed $\beta = B_R/B_I = 2$ obtaining χ^2 values that do not vary strongly, showing that the data can be described, within errors, by scattering parameters in different ranges.

Figure 3.14: Looking closely at the normalized cross section obtained from the low $|t|$ data, represented by continuous dashed line, in confront with the Bozzo et al. data [75, 76], we observe very good agreement. In the RHS we plot higher $|t|$ data to point out the meaning of the forward scattering solution by amplitudes with simple exponential dependences compared to a full $|t|$ shapes that require appropriate models.
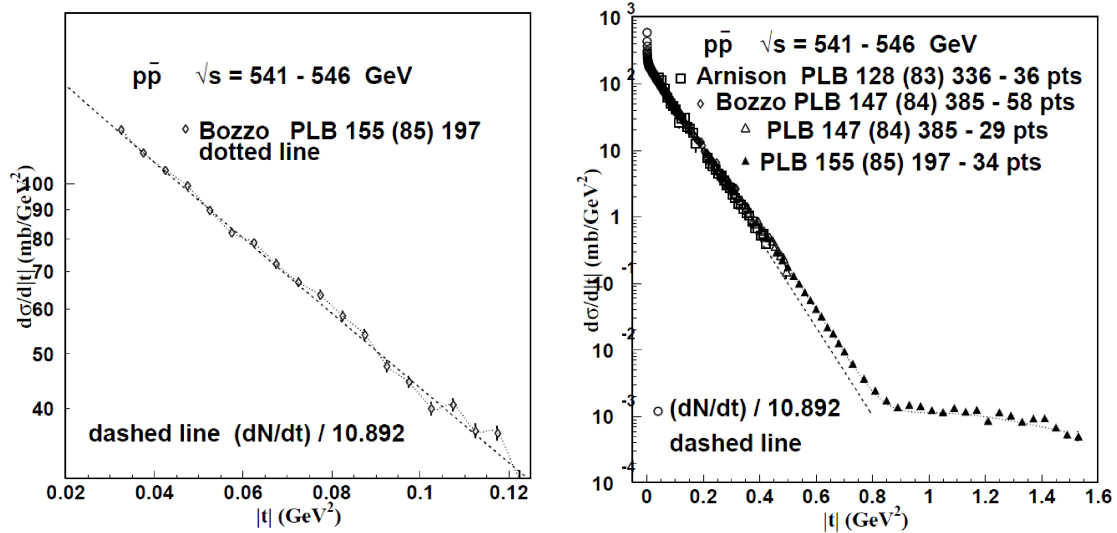
Correlations among parameters are shown in Fig. 3.15 with drawing of level lines determined for low χ^2 values.

We have built a file with a continuous and non superposing set of points, being the first 59 points from normalized dN/dt (with normalization factor 10.6) and 121 points from Bozzo et al. The 180 points form a regular $|t|$ distribution, which we fit with formulae from our previous work [48]. The results are shown in Fig. 3.16. The parameter values obtained in this fitting are $\sigma = 63.06 \pm 1.90$ mb , $\rho = 0.124 \pm 0.005$, $B_I = 13.88 \pm 0.42$ GeV^{-2}, $B_R = 25.79 \pm 0.77$ GeV^{-2}, with $\chi^2 = 1.32$.

Figure 3.15: Correlations between the parameters ρ and $\beta = B_R/B_I$ and between σ and β that lead to low values of χ^2. In each case the other two parameters are let free while tables of χ^2 are built with specified values for the two plotted parameters. Also the normalization factor 10.083 is taken as fixed independently from PAW fitting program.
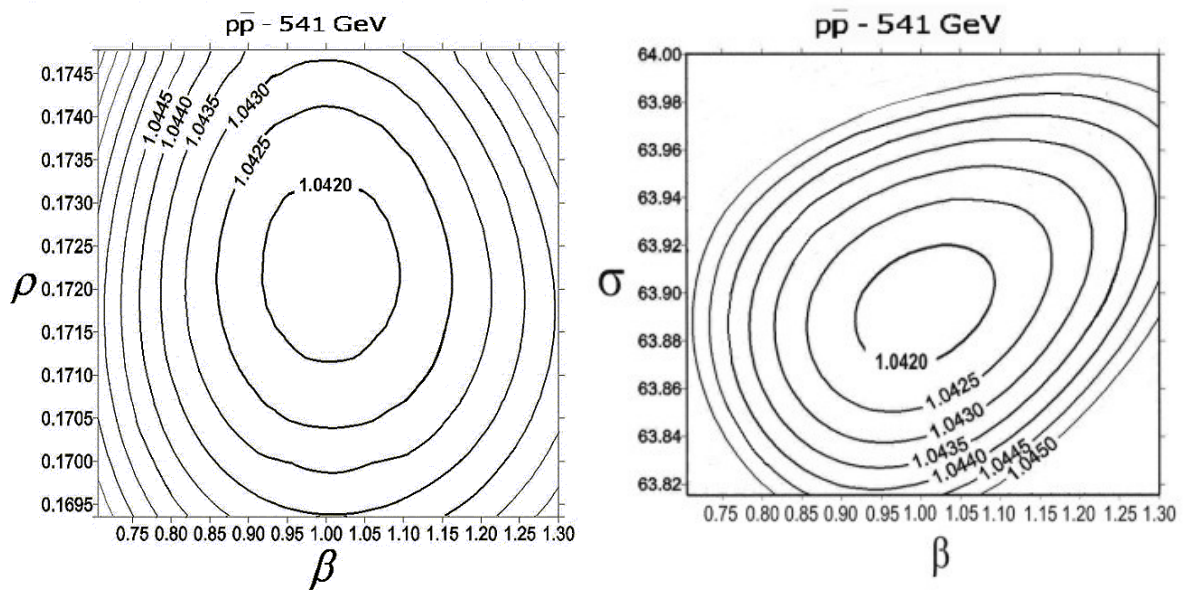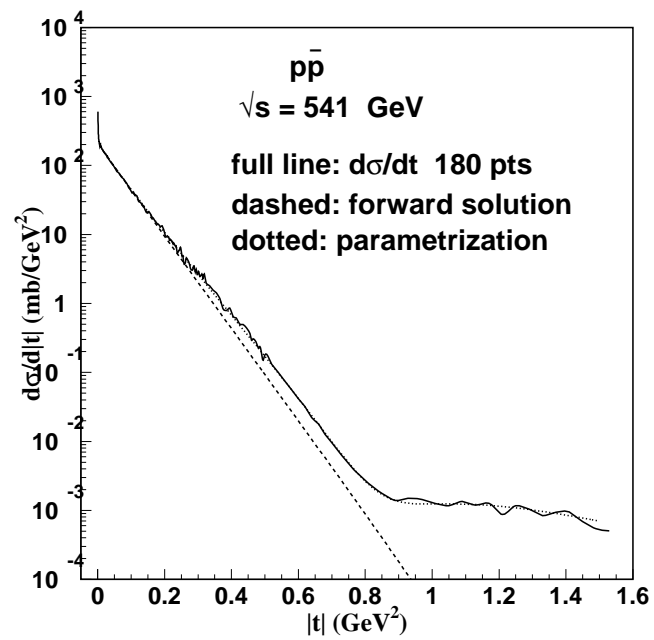
Figure 3.16: Data at 541 GeV selected and organized. The dotted line is a fit described in our previous work [48].

Chapter 4

Energy dependence of KFK scattering amplitudes

In Chapter 2 the pp elastic scattering amplitudes based on SVM were written with complete t dependence. Up to now, the s dependence is still missing. In this chapter we analyse differential cross sections for pp and p$\bar{\text{p}}$ with our amplitudes (called KFK from now on) determining the energy behavior of the real and imaginary parameters. Originally [48] the s behavior of the pp cross section was constructed through energy dependence of the effective proton radius. More than a decade ago, Ferreira and Pereira analysed all available elastic scattering data for energies above 20 GeV [48] and all $|t|$, identifying properties of the amplitudes (zeros, signs, magnitudes), with proper attention given to the real part, which plays a critical role in differential cross sections at mid and large $|t|$ range. Recently, we extended this analysis [20, 21] to the LHC-Totem elastic scattering at 7 TeV and 8 TeV data [80], [81], and also the behavior of proposed amplitudes was re-examined in the whole energy region from 20 GeV to 14 TeV, including the cosmic energy domain, to determine the precise energy dependence of the model parameters [21]. We gave special treatment for p$\bar{\text{p}}$ at 1800/1960 GeV [51] where the experimental information presents strong discrepancies. From these analyses, an analytic representation of

the amplitudes as function of s and t was established.

We also analyse the data with an additional term in the real amplitude dominates for large t values, where phenomenological contributions of non-perturbative origin becomes small, and the perturbative calculations due to tri-gluon exchange becomes relevant [82]. It is remarkable that this tail term does not depend strongly on s. It is also important to stress that the sign of the tri-gluon exchange amplitude may have influence on the structure of the dip and the bump for pp and p$\bar{\text{p}}$. Depending on the sign of the real non-perturbative part for large $|t|$, the sign of the three gluon exchange may cause a second dip in $d\sigma/dt$ (Ref. [51]).

After the extensive analysis including a wide energy range we obtain a complete s dependence of the model, which allows us to interpolate and extrapolate the results to regions where the experimental information is poorer or does not exist.

An application of the dispersion relation was made to KFK amplitudes and we show that the constraints between the real and imaginary parameters comming from the exact DDR are independently confirmed by free fittings of the amplitudes with the experimental data.

4.1 Analytic representation of amplitudes of pp elastic scattering

The differential cross section is written

$$\frac{d\sigma}{dt} = (\hbar c)^2 \; |T_R(s,t) + iT_I(s,t)|^2 \; . \tag{4.1}$$

In the following discussion, we use the unit system where σ is in mb (milibarns) and the energy in GeV, so that $(\hbar c)^2 = 0.3894$ mb GeV^2. T_R and T_I, with dimensions

GeV^{-2}, contain the nuclear and the Coulomb parts in the forms

$$T_R(s,t) = T_R^N(s,t) + \sqrt{\pi}F^C(t)\cos(\alpha\Phi) \, , \qquad (4.2)$$

and

$$T_I(s,t) = T_I^N(s,t) + \sqrt{\pi}F^C(t)\sin(\alpha\Phi) \, . \qquad (4.3)$$

The Coulomb scattering amplitude $F^C(s,t)$ enters in the pp/p$\bar{\text{p}}$ amplitudes with the form given by Eq.(3.46) in terms of proton electromagnetic form factor.

The total cross section is given by

$$\sigma = 4\sqrt{\pi}\,(\hbar c)^2\ T_I^N(s,t=0) \, . \qquad (4.4)$$

Using the same notation as used in the forward scattering chapter, $T_R^N(s,t)$ and $T_I^N(s,t)$ are respectively the real and imaginary parts of the properly normalized scattering amplitude of the strong interaction. The Coulomb amplitude is relevant in the very forward range $|t| < 10^{-2}$ GeV^2. We neglect spin effects.

Nuclear amplitudes for all-t values

To obtain precise description of the elastic $d\sigma/dt$ data for all $|t|$, we use the forms that were introduced in chapter 2 and shown to be successful with ISR and Fermilab data [48], together with the assumption of the perturbative three-gluon exchange amplitude [82], writing

$$T_K^N(s,t) = \alpha_K(s)e^{-\beta_K(s)|t|} + \lambda_K(s)\Psi_K(\gamma_K(s),t) + \delta_{K,R}R_{ggg}(t) \, , \qquad (4.5)$$

where $\Psi_K(\gamma_K(s),t)$ are shape functions already described in Chap. 2, and $R_{ggg}(t)$ represents the contribution from the perturbative three-gluon exchange amplitude. The label K means either $K = R$ for the real amplitude or $K = I$ for the imaginary amplitude, and $\delta_{K,R}$ is the Kronecker's delta symbol, that is, the last term only

contributes for the real part.

The dimensions parameters of the real and imaginary amplitudes introduced in Eqs.(2.64,2.65) are: γ_K dimensionless, α_K, λ_K and β_K are in GeV^{-2}. The fixed quantity $a_0 = 1.39$ GeV^{-2} is related to the square of the correlation length a of the gluon vacuum condensate value, with $a = (0.2 \sim 0.3)$ fm [42–44].

These expressions are planned to represent the non-perturbative dynamics of scattering for all $|t|$ and the perturbative term R_{ggg} is built to vanish for small $|t|$.

The limits at $|t| = 0$ lead to the values for the total cross section σ, the ratio ρ of the real to imaginary amplitudes, and the slopes $B_{R,I}$ at $t = 0$ through

$$\sigma(s) = 4\sqrt{\pi} \, (\hbar c)^2 \, [\alpha_I(s) + \lambda_I(s)] \, , \tag{4.6}$$

$$\rho(s) = \frac{T_R^N(s, t = 0)}{T_I^N(s, t = 0)} = \frac{\alpha_R(s) + \lambda_R(s)}{\alpha_I(s) + \lambda_I(s)} \, , \tag{4.7}$$

$$\begin{aligned} B_K(s) &= \left. \frac{2}{T_K^N(s,t)} \frac{dT_K^N(s,t)}{dt} \right|_{t=0} \\ &= \frac{2}{\alpha_K(s) + \lambda_K(s)} \left[\alpha_K(s)\beta_K(s) + \frac{3}{4}\lambda_K(s)a_0\left(\gamma_K(s) + \frac{7}{6}\right) \right] \, . \end{aligned} \tag{4.8}$$

The determination of each amplitude starts with four energy dependent parameters that must be obtained from the data. However, well established s dependence of the imaginary slope B_I (with typical Regge model behavior), connections between $\lambda_R + \alpha_R$ and $\lambda_I + \alpha_I$ and B_R with B_I constrained by dispersion relations for amplitudes and for slopes [38] help to control the parameter values.

As discussed before [48], the shape functions in Eq. (2.65) are very convenient choices for all values of $|t|$, determining consistently for all energies the zeros, the formation of dips and bumps, the signs and magnitudes of the two amplitudes and are able to reproduce with good accuracy all $d\sigma/dt$ behavior. This description represents the non-perturbative QCD dynamics that is responsible for soft elastic

hadronic scattering. They account effectively for the terms of Regge and/or eikonal phenomenology that determine the process for $|t|$ ranges up to about $|t| \approx 2.5 \text{ GeV}^2$. For higher $|t|$, perturbative contributions as the three-gluon exchange may become important.

Universal behavior for large $|t|$: Faissler measurements at 27.4 GeV

For $|t|$ values beyond the dip and bump characteristic of the differential cross sections at ISR/CERN and Fermilab energies, namely for $|t| > 1.5 \text{ GeV}^2$, the differential cross sections become increasingly independent of the energy. The measurements of pp scattering at $\sqrt{s} = 27.4 \text{ GeV}$ [68] provides the only large $|t|$ data, covering the interval from 5.5 to 14.2 GeV^2. It is known that the points are smoothly and naturally connected with the lower $|t|$ points at all energies [48]. As shown by Donnachie and Landshoff [82] this tail corresponds to a perturbative three-gluon exchange mechanism, with real amplitude positive for pp and negative for p$\bar{\text{p}}$ scattering, and $d\sigma/dt$ falling as $|t|^{-8}$. The most remarkable example is given by the data of pp scattering at $\sqrt{s} = 52.8 \text{ GeV}$ [83] , with measurements up to $|t| = 9.75 \text{ GeV}^2$ that superpose well with the 27.4 GeV tail. This indicates that in this region the non-perturbative real part is indeed positive, and also that the magnitude of the imaginary part is small compared to the real part. At high energies in p$\bar{\text{p}}$ scattering the negative sign of the perturbative tail may lead to a marked dip in the transition region from 3 to 4 GeV^2 [51].

Based on this expectation for the perturbative tail, we introduce a simple form of the universal three-gluon contribution amplitude $R_{ggg}(t)$ at large $|t|$, parametrizing the Landshoff term of the amplitude as

$$R_{ggg}(t) \equiv \pm 0.45 \; t^{-4}(1 - e^{-0.005|t|^4})(1 - e^{-0.1|t|^2}) \; , \qquad (4.9)$$

where the last two factors cut-off this term smoothly in the non-perturbative domain,

and the signs $\pm$ refer to the pp and p$\bar{\text{p}}$ amplitudes respectively.

Although the cut-off factors written in Eq. (4.9) have been adequate for all cases that were examined, their detailed forms in the transition range $(2.5 < |t| < 4)$ GeV^2 must be examined with data in detail.

4.2   Analysis of elastic p$\bar{\text{p}}$ data at 1.8 TeV

There are strong discrepancies on the reported values of total cross section measured at Fermilab at 1.8-1.96 TeV. We have analyse directly the differential cross sections data in terms of KFK amplitudes. Our aim is the determination of the energy dependent parameters, and obtain predictions for the total cross section based on the non-uniform data.

The available experimental data on differential cross section of p$\bar{\text{p}}$ elastic scattering at 1.8 TeV are

- N = 51 points in the interval $0.00339 \leq |t| \leq 0.627$ (in GeV^2) from the Fermilab E-710 experiment published by N. Amos et al [77] in 1990.

- N = 26 points in the interval $0.0035 \leq |t| \leq 0.285$ (in GeV^2) from the Fermilab CDF experiment published by F. Abe et al [78] in 1994.

To these data we may now add the results of a more recent experiment at 1.96 TeV

- N = 17 points in the interval $0.26 \leq |t| \leq 1.20$ (in GeV^2) from the Fermilab D0 experiment published by V. M. Abazov et al [84] in 2012.

In order to compatibilize the last set together with the former two sets, we we use the reduction factor $(1.8/1.96)^{0.3232} = 0.973$ obtained as correction of energy effect from 1.96 to 1.8 TeV according to Regge phenomenology [23]. As the $|t|$ range involved is small we can safely neglect the $|t|$ dependence of this factor. In the following, we refer to these converted data as "1.96 TeV data".
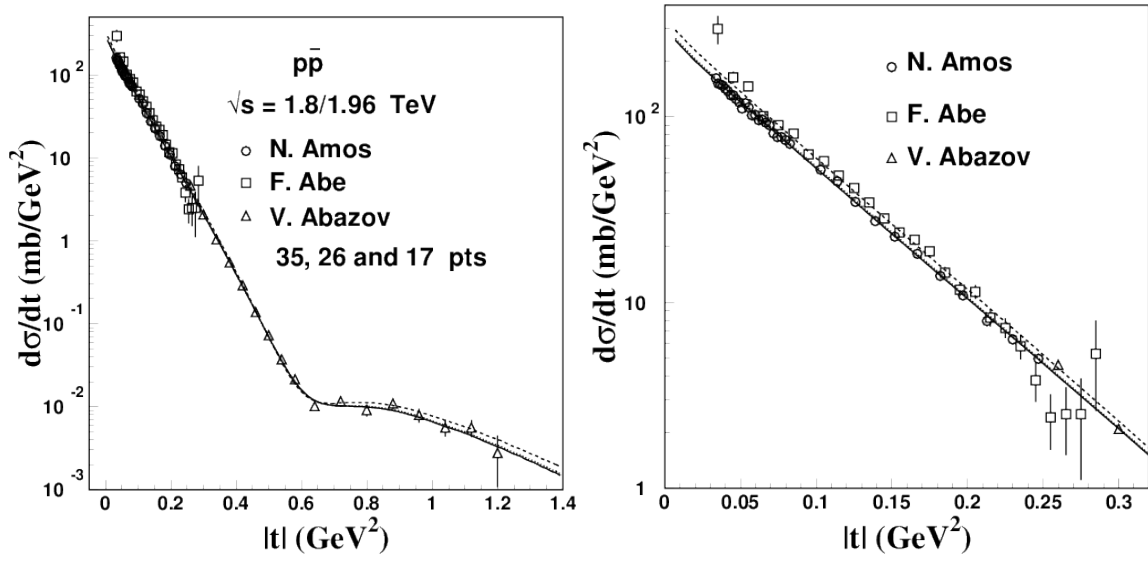
Figure 4.1:   Data of p$\bar{\text{p}}$ scattering at 1.8 and 1.96 TeV [77,78,84], taken in the E-710, CDF and D0 experiments in Fermilab. The D0 data are multiplied by a reducing factor 0.973 to take into account the energy difference (see the text). The E-710 data [77] are restricted to the first 35 points (open circles) due to superposition with the recent D0 data (open triangles) of the same experimental group. The plot in the RHS, concentrated in the forward part, exhibits clearly the known discrepancy between the two experiments in the low $|t|$ region. The solid, dashed and dotted lines represent respectively our best descriptions for datasets I, II and III constructed from the combination of three data points available, as described in the text. The dotted line is hidden under the solid line.

The data are shown in Fig. 4.1. They do not cover a low enough $|t|$ range for a precise treatment in terms of exponential forms for the amplitudes, or, even less, for the differential cross section. Besides, there is a discrepancy of values in the data from the two independent experiments, exhibited in Fig. 4.1, that has lead to a 20 year old duplicity of values for the total cross section, which has seriously affected the efforts for a global description of the energy dependence of the total cross section.

We recall values of the scattering parameters that are found in original papers by experimental groups:

- E-710 experiment [85]: $\rho = 0.140 \pm 0.069$, $B = 16.99 \pm 0.47$ GeV^2 , $\sigma = 72.8 \pm 3.1$ mb

- CDF experiment [86]: $B = 16.98 \pm 0.25$ GeV^2 , $\sigma = 80.03 \pm 2.24$ mb

In this thesis we analyse carefully this ambiguity using KFK amplitudes with help of the new large $|t|$ data from the 1.96 TeV experiment. As much as possible, we deal with all experimental information together in a unified analysis. For this purpose, we group the data in three different sets.

- SET I - The 1.96 TeV data (converted) give a natural and smooth connection with the E-710 data (basically they come from the same experimental group); there is some superposition in the extreme ends, where we select the more recent data, that have smaller error bars. We thus join 35 points with $3.39 \times 10^{-2} \leq |t| \leq 0.247$ GeV^2 from E-710 with 17 points from D0, to form a combined data SET I (called STANDARD), with N = 52 points in the range $0.00339 \leq |t| \leq 1.2$ GeV^2.

- SET II - We observe that there is a good convergence of the large $|t|$ end points of the CDF spectrum with the beginning of the recent D0 points. This is a welcome surprise, and suggests the consistent construction of a combined set from the two groups, with N = 26 and the N = 17 points, respectively. Actually, to select points in the range where there is superposition, and simultaneously to obtain a clearer smooth connection, we exclude the last 5 CDF points, that present a rather scattered behavior (observe Fig. 1). We thus build SET II here (called HYBRID), with N = 21 + 17 = 38 points. The assemblage is shown in Fig. 4.2. The construction of this HYBRID SET II is motivated by the consideration that the apparently irreconcilable discrepancy between the E-710 and CDF experiments that exists in the low and mid $|t|$ range need not imply that they are incompatible for larger $|t|$. Our description aims at representations of $d\sigma/dt$ covering all $|t|$ spectrum, and this hybrid connection is very important.

- SET III - In a third construction, we investigate what comes out from our

full-$|t|$ description if we put all data together on the same footing, merging the N = 52 points of SET I with the N = 26 CDF basis. We thus form a GLOBAL SET III, with N=78 points.

We fit $d\sigma/dt$ for the three datasets described above, using Eqs. (4.1),(4.2), (4.3), (2.64) of our representation. In the fitting procedure, in principle all 8 parameters are treated independently to minimize χ^2, but we find that some parameters can be chosen with common values to all datasets without sensitive changes in the solutions. They are :

$$\alpha_I = 11.620 \pm 0.024 \text{ GeV}^{-2}, \ \beta_R = 1.10 \text{ GeV}^{-2} \ , \ \rho = 0.141 \pm 0.002 \ ,$$

$$B_I = 16.76 \pm 0.04 \text{ GeV}^{-2}, \ B_R = 26.24 \pm 0.39 \text{ GeV}^{-2} \ . \quad (4.10)$$

We remark that the usual quantity B (slope of $d\sigma/dt$) is not the same as B_I. The relation is

$$B = \frac{B_I + \rho^2 B_R}{1 + \rho^2} \quad (4.11)$$

and we then obtain $B = 16.94 \text{ GeV}^{-2}$, remarkably close to the values of the experimental groups (16.99 ± 0.47 and 16.98 ± 0.25 GeV^{-2} for the E-710 [85] and CDF [86] groups respectively).

The results of the fittings with respect to the other free parameters are given in Table 4.1, together with some characteristic features of the solutions. The corresponding curves representing these fittings of $d\sigma/dt$ are shown in Figs. 4.1,4.2, 4.3.

It is important to observe that the discrepancy between the CDF and E-710 data shown in the RHS of Fig. 4.1 becomes smaller as $|t|$ increases and both sets of data seem to connect smoothly to the D0 data, as seen in 4.3. That is, the well-known contradiction between E-710 and CDF data becomes less serious as $|t|$ increases, and the D0 data helps to point out the connection. Our global $|t|$ analysis helps to describe this connection.

Table 4.1: Characteristic quantities of the all-t representation for the amplitudes. Common values for all sets: $\rho = 0.141 \pm 0.002$, $B_I = 16.76 \pm 0.04$ GeV^{-2} , $B_R = 26.24 \pm 0.39$ GeV^{-2} , $\alpha_I = 11.620 \pm 0.024$ GeV^{-2}, and choice of $\beta_R = 1.10$ GeV^{-2}. The remaining free parameters are $\beta_I, \lambda_R, \sigma$. The error bars are given by the CERN Minuit Program. SET I (N=52 points) is built with E-710 (35 points) and D0 (17 points) data. SET II (N=35 points)is built joining CDF (21 points) and D0 (17 points). The complete SET III (N=78 points) puts together CDF (26 points), E-710 (35 points) and D0 (17 points) data. $|t|_{\text{infl}}$ is the position of the inflection point in $d\sigma/dt$. $\langle \chi^2 \rangle$ is the average value of the squared relative theoretical/experimental deviations.

SET	N points	β_I GeV^{-2}	λ_R GeV^{-2}	$|t|_{\text{infl}}$ GeV^2	$(d\sigma/dt)_{\text{infl}}$ mb/GeV^2	$\sigma(\text{el})$ mb	σ mb	$\langle \chi^2 \rangle$
I	52	3.7785 ± 0.0078	3.6443 ± 0.0093	0.745	0.01013	16.67	72.76 ± 0.13	0.7661
II	38	3.5686 ± 0.0186	3.8645 ± 0.0093	0.727	0.01114	18.92	77.63 ± 0.44	1.4961
III	78	3.7441 ± 0.0080	3.6784 ± 0.0096	0.741	0.01029	17.02	73.54 ± 0.20	2.6591
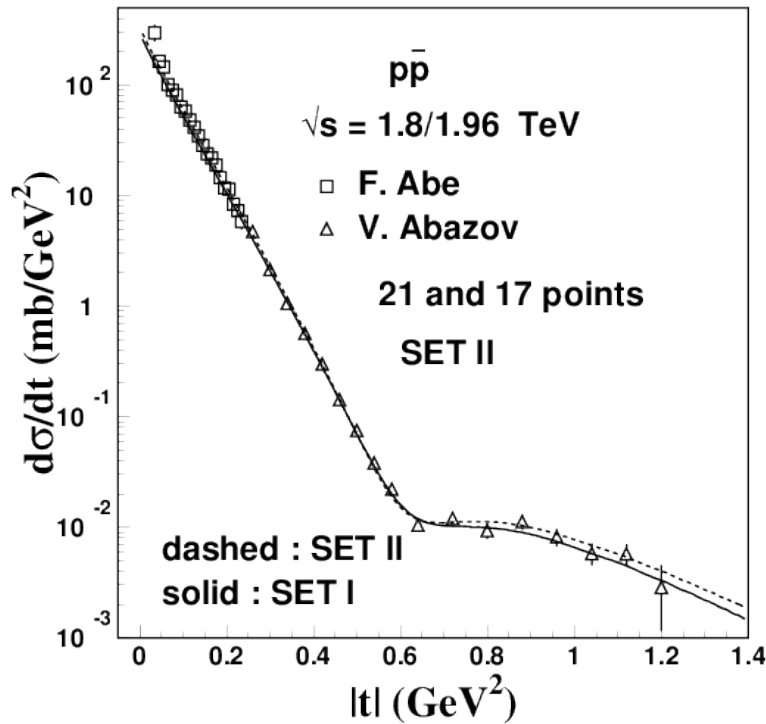
Figure 4.2: Hybrid SET . Combination of N=21 points from CDF (open squares) with 17 points from D0 (open triangles). The last 5 points of CDF data (see Fig. 4.1) are excluded, to exhibit more clearly a smooth connection, and this is done also numerically in fittings with SET II (38 points). The E-710 points do not enter in this SET II. Solid line: fit of SET I, for comparison; dashed line: fit of SET II. Although the lines of the two solutions are visually very close, the limits $|t| \to 0$ lead to different values of σ, given in Table 4.1 and shown in closeup in Fig. 4.3.

Figure 4.3: Data of SET II (21 points from CDF and 17 points from D0 experiment), with plots that enhance the forward range. Note the smooth connection of the highest $|t|$ CDF points with the recent D0 data. The solid and dashed lines refer to the fitting solutions obtained with sets I and II respectively, with parameters given in Table 4.1. In spite of the apparent proximity, the lines lead to remarkably different values for the total cross section. The solution for SET III falls between these two drawn lines (see dotted line in Fig. 4.1) and is not included here to keep clarity.
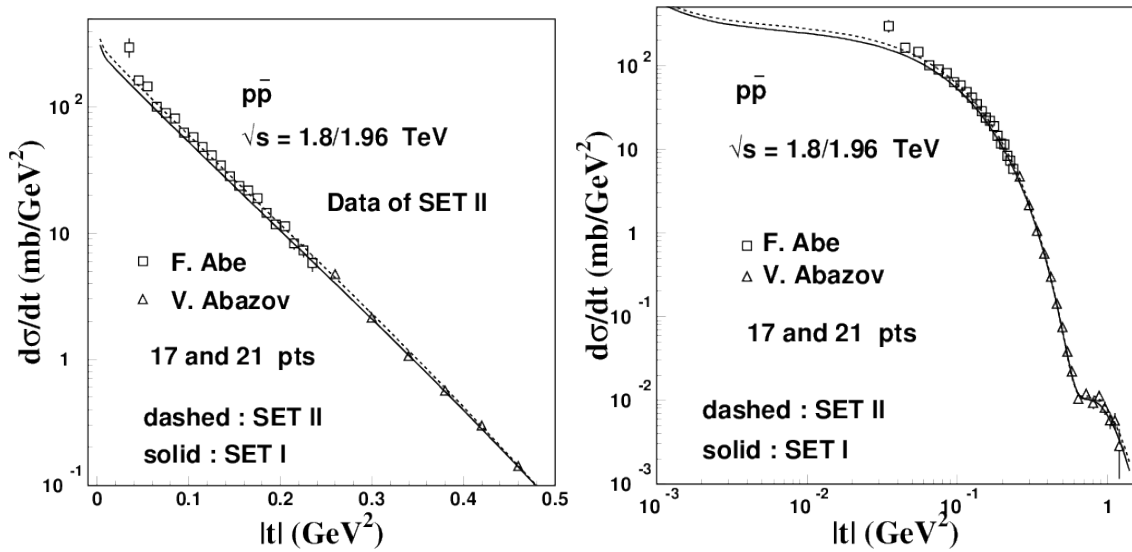
We recall that the above analysis is based on analytical expressions for the scattering amplitudes applied to all $|t|$. In the present 1.8 TeV case, the integrated use of all-$|t|$ data is crucial since there are no data points in the very forward range, 10^{-3} to 10^{-2} GeV^2, and the pure exponential forms are not at all reliable. Due to the very large energy gaps in the experimental data, this energy region $\sqrt{s} = 1.8/1.96$ TeV is extremely important for the determination of the energy dependence of the total cross section, $\sigma(s)$ and hence for its extrapolation for ultra-high energies treated by fundamental theorems.

To show the importance of the use of the full-$|t|$ amplitudes and full-$|t|$ data together, we test toy fits of the forward data of E-710 (35 points) and CDF (21 points) experiments. The E-710 data are fitted with essentially the same parameters as the full SET I, and this shows their nearly perfect coherence, with the E-710 and D0 data matching very well when described by our full-$|t|$ amplitudes. However,

the separate treatment of the 21 points of the CDF data leads to values of $\beta_I = 3.7280$ GeV^{-2}, $\lambda_R = 3.3060$ GeV^{-2} and $\sigma = 79.00 \pm 0.57$ mb that are different from those of SET II in Table 4.1, and this solution has a disastrous behavior for large $|t|$. Thus, we conclude that, in our model, the use of the pure CDF points for the determination of the very forward quantities seems not reliable, if it is not controlled by the D0 points of the larger $|t|$ domain. Thus in our analysis the construction of SET II is essential for the treatment of the CDF data.

Properties of 1.8 TeV Amplitudes

It is general property of our approach that the non-perturbative amplitudes fall-off rapidly after $|t| \approx 1.5$ GeV^2, with the magnitude of the positive real part becoming dominant over the negative imaginary part for $|t|$ larger than about 2.5 GeV^2. The imaginary amplitude has only one zero, located near the inflection point of $d\sigma/dt$, while the real part has a first zero at small $|t|$, obeying Martin's theorem [54], and a second zero located after the imaginary zero. As the non-perturbative real part decreases, the perturbative tail remains, giving to the differential cross section the characteristic shape $1/|t|^8$, discussed by Donnachie and Landshoff [82]. Such a general aspect of the scattering amplitudes have been well verified at ISR and LHC energies [20, 48]. The present analysis at 1.8 TeV data repeats this general behavior, as exhibited in Fig. 4.4.

Role of Perturbative Tail in p$\bar{\text{p}}$ scattering

The universal (energy independent) perturbative 3-gluon exchange process [82], given by Eq. (4.9), contributes in p$\bar{\text{p}}$ scattering with a negative sign, which leads to an interesting prediction. As mentioned above, the non-perturbative real amplitude is positive in the transition region, and the inclusion of the negative tail amplitude leads eventually to its cancellation and the creation of a third real zero (see Table 4.2). This mechanism is shown in the RHS of Fig. 4.4, where we draw two curves
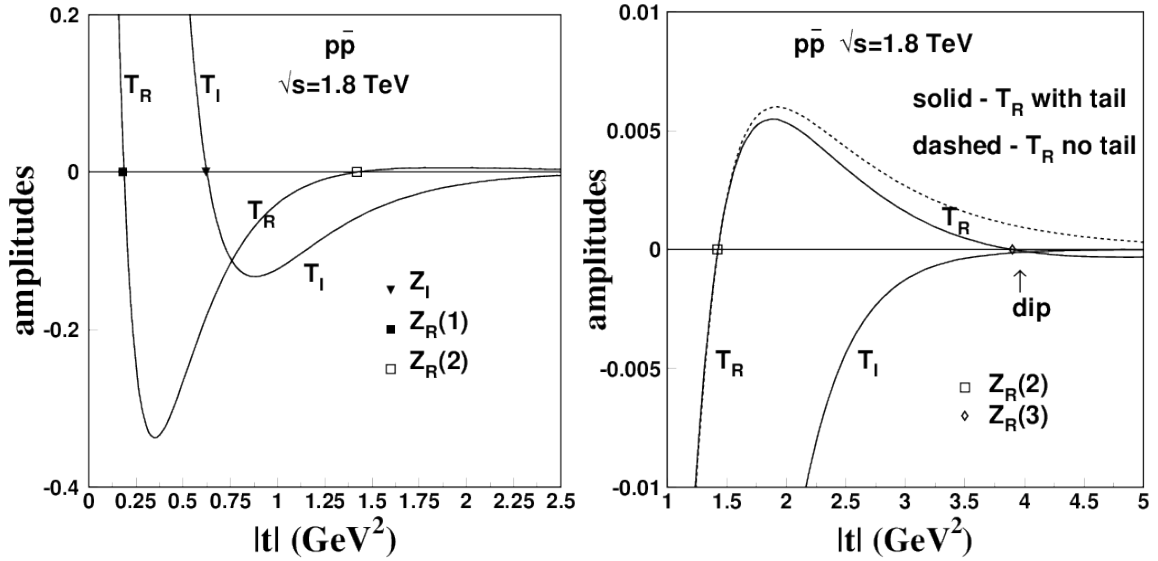
Figure 4.4: Amplitudes in p$\bar{\text{p}}$ elastic scattering at $\sqrt{s} = 1.8$ TeV shown in different ranges and scales, described by Eqs. (4.2), (4.3), (2.63) with parameters determined by phenomenology. The solid lines drawn refer to the solutions for T_R and T_I obtained for SET I. In the $|t|$ range up to about 2 GeV^2 the amplitudes are governed by non-perturbative dynamics and are qualitativelly similar for pp and p$\bar{\text{p}}$, with one zero for T_I and two zeros for T_R. T_I remains negative and goes fast to zero, while at $|t| \approx 3$ GeV^2 the non-perturbative T_R is positive and dominates. In p$\bar{\text{p}}$ scattering the negative contribution of the 3-gluon exchange term inverts the sign of T_R, forming a third zero and a marked dip in $d\sigma/dt$, with locations and depths dependent on the detail of the β_R parameter, as shown in Table 4.2.

for the real amplitude, with solid line and dashed line, corresponding respectively to presence and absence of perturbative contribution.

As the imaginary part is not dominant in this region, a marked dip may be observed in $d\sigma/dt$. This is shown in Fig. 4.5. In this figure (RHS), we also show in dotted line the behavior of cross section with non-pertubative amplitudes only, without the effect of pertubative tail.

The precise form of this dip-bump structure created by the perturbative tail depends sensitively on the values of model parameters (such as β_R) that govern the properties of the transition domain. Unfortunately, the existing data stops at about $|t| = 1.2$ GeV^2, leaving the higher $|t|$ region without information to fix the connection with the range of the perturbative tail. Thus the parameter β_R cannot

SET	β_R GeV^{-2}	λ_R GeV^{-2}	Z_I GeV^2	$Z_R(1)$ GeV^2	$Z_R(2)$ GeV^2	$Z_R(3)$ GeV^2	$|t|_{\text{dip}}$ GeV^2	$|t|_{\text{bump}}$ GeV^2	ratio
I	1.10	3.6443	0.6253	0.1771	1.4336	3.8827	3.9456	4.8631	5.4567
I	1.40	3.6328	0.6253	0.1776	1.5884	3.0605	3.4839	4.1212	1.3086
II	1.10	3.8645	0.6156	0.1792	1.2986	4.3159	4.3520	5.3314	8.4118
II	1.40	3.8492	0.6156	0.1799	1.4217	3.3047	3.6434	4.2920	1.3761
III	1.10	3.6784	0.6231	0.1776	1.3987	3.9781	4.0312	4.9580	6.2212
III	1.40	3.6662	0.6231	0.1781	1.5452	3.1181	3.5111	4.1609	1.3442

Table 4.2: Positions of zeros of the real and imaginary amplitudes, locations of the dip and bump at large $|t|$ predicted by the introduction of the perturbative tail of negative sign, and the ratio characterizing the shape of this structure. The parameter β_R, that determines the behavior of the real part at the end of the non-perturbative region, is not tightly determined by the data (that ends at 1.2 GeV^2), and has important role for the location and depth of the large $|t|$ dip. We present results for two choices of β_R. The parameter λ_R varies in the fits, following the choice of β_R. The quantities ρ, B_I, B_R, α_I are universal, as in Table 4.1. The quantity ratio is $[d\sigma/dt]_{\text{bump}}/[d\sigma/dt]_{\text{dip}}$.

be fixed accurately, and as its value is crucial for the prediction of the position and depth of a dip in the transition region for p$\bar{\text{p}}$ scattering at 1.8 TeV, we present in Table 4.2 two alternative choices, with $\beta_R = 1.10$ and 1.40 GeV^{-2}.

In Table 4.2 are given the values of $|t|$ at the zeros of the amplitudes, and the locations of the dip and bump in $d\sigma/dt$ at large $|t|$ that are due to the contribution of the three-gluon exchange term. The quantity ratio $= (\text{d}\sigma/\text{dt})_{\text{bump}}/(\text{d}\sigma/\text{dt})_{\text{dip}}$ that informs about the shape of the structure depends strongly on the values of the parameter β_R, that must be determined by experiment, necessarily with extension of the measured range to higher $|t|$ values. The common parameters are given in Eq. (4.10). The fitting of each solution is needed only to evaluate λ_R.
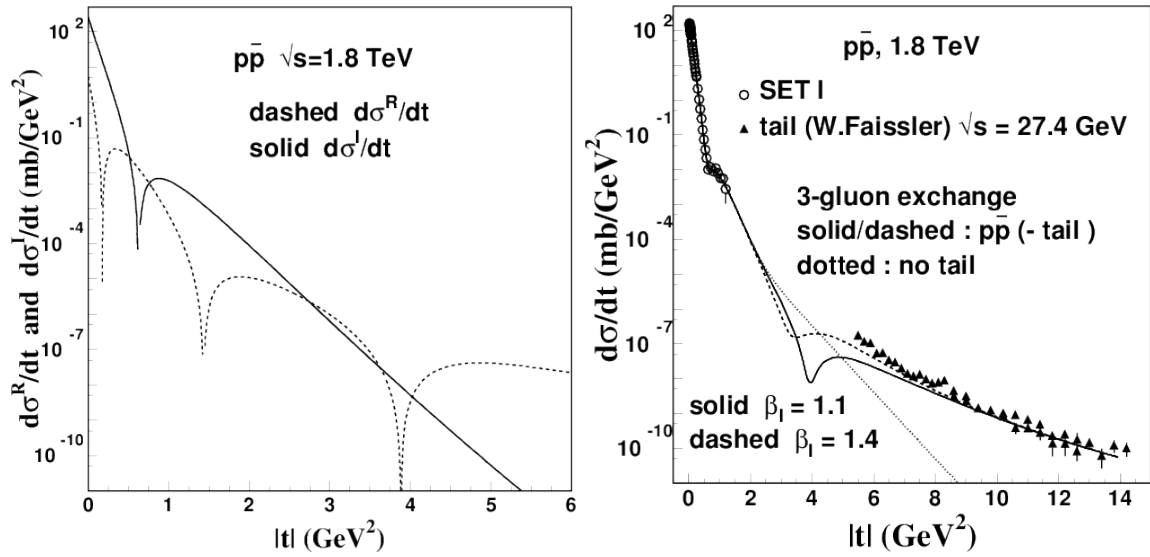
Figure 4.5:   The plots show the predictions for the contributions of real $d\sigma^R/dt$ and imaginary $d\sigma^I/dt$ parts of $d\sigma/dt$ in the presence of the real perturbative tail due to 3 gluon exchange. In p$\bar{\text{p}}$ scattering the negative sign of the tail causes a zero in $d\sigma^R/dt$ and a dip in $d\sigma/dt$ located in the range 3-5 GeV^2. The RHS figure shows two examples of the dip structure, formed with $\beta_R = 1.10$ GeV^{-2} (solid) and $\beta_R = 1.40$ GeV^{-2} (dashed) as given in Table 4.2. We suggest that the analysis of data from the Fermilab experiment at 1.96 TeV be extended to investigate this dip region.
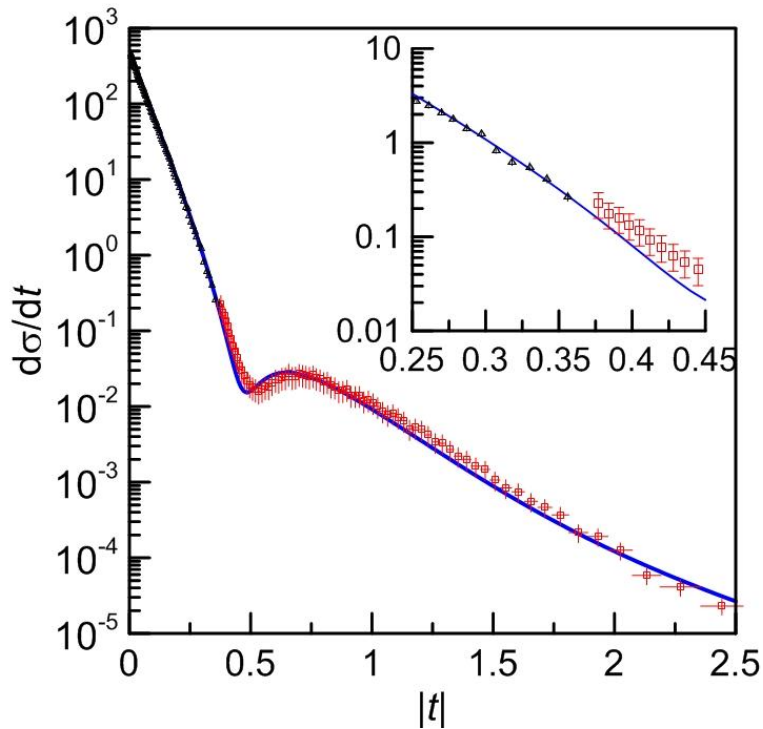
Figure 4.6: Analytic representation for the data on $d\sigma/dt$ for elastic pp scattering at 7 TeV, together with the experimental data [79]; triangles are for subset A and open squares for subset B. The values of the parameters are given in Eqs. (4.12), (4.13). The inset at the up-right corner shows in close up a gap between the datasets A and B, that seems to be at the limit of the error bars.

4.3   Analysis of elastic pp data at 7 TeV

The Totem Collaboration has published data of differential elastic cross section [79] in two separate tables, in the ranges $0.00515 \leq |t| \leq 0.371$ (referred to as dataset A) and $0.377 \leq |t| \leq 2.443$ (referred to as dataset B) GeV^2, with 87 and 78 points respectively. Rather large systematic errors are informed in the dataset B. The representation of these data with the analytical forms of Eqs. (4.5) and (2.63) is shown in Fig. 4.6. The averaged square deviation for the datasets $A + B$ (165 points) is $\langle \chi^2 \rangle = 0.3105$.

The values of the quantities that also enter in the forward scattering amplitudes

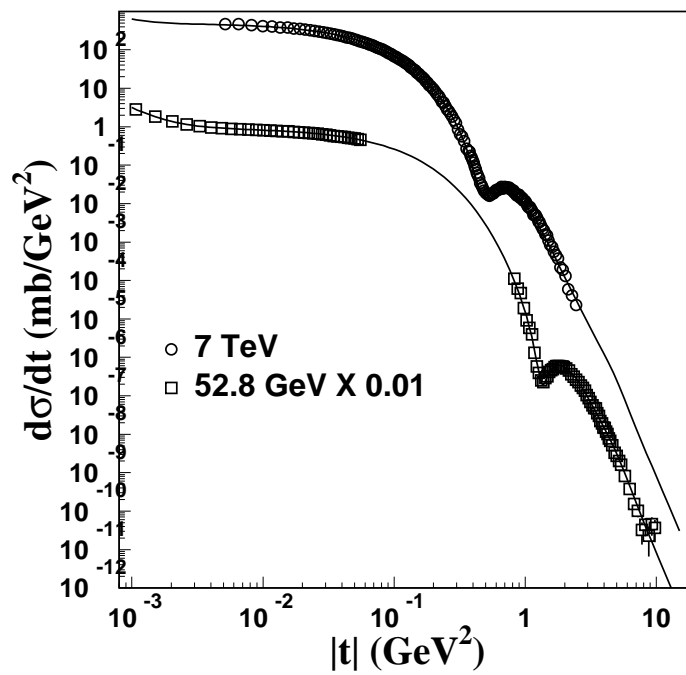Figure 4.7: Data for elastic pp scattering at 7 TeV ([79], 165 points) and 52.8 GeV ([83], 97 points). The lines represent the parameterizations with Eqs. (4.5) and (2.63), with average squared deviations $\langle \chi^2 \rangle = 0.3105$ and 0.8328 respectively. Numerical characteristic values and description of features of the data and of the amplitudes are given in the text and in Tables 4.3 and 4.4 .

Table 4.3: Amplitude parameters for the 52.8 GeV and 7 TeV data.

$\sqrt{s}$ GeV	N points	σ mb	ρ –	B_I GeV^{-2}	B_R GeV^{-2}	α_I GeV^{-2}	β_I GeV^{-2}	λ_R GeV^{-2}	β_R GeV^{-2}	$\langle\chi^2\rangle$
52.8	97	42.49	0.078	13.04	19.07	5.9561	2.3477	1.1307	1.1436	0.8328
7000	165	98.65	0.141	19.77	30.20	13.730	4.0826	4.7525	1.4851	0.3105

treated with exponential functions as in Eq.(3.48) are

$$\sigma = 98.65 \pm 0.26 \text{ mb} , \ \rho = 0.141 \pm 0.001 ,$$

$$B_I = 19.77 \pm 0.03 \text{ GeV}^{-2}, \ B_R = 30.2 \pm 0.7 \text{ GeV}^{-2} , \tag{4.12}$$

and the other independent quantities that enter in the full-t forms are (in GeV^{-2})

$$\alpha_I = 13.730 \pm 0.030 , \ \beta_I = 4.0826 \pm 0.0093 ,$$

$$\lambda_R = 4.7525 \pm 0.0155 , \ \beta_R = 1.4851 \pm 0.0318 . \tag{4.13}$$

Here we have 8 independent values, that are collected in Table 4.3. [1] Other quantities are related to these through Eqs. (4.6, 4.7, 4.8). Plots and features of the amplitudes are given in the next section.

Characteristic values of the differential and integrated cross sections for the 7 TeV data given by this representation are

$$\sigma_{\text{el.}} = 25.5418 \text{ mb} ; \ \sigma_{\text{inel.}} = 73.1082 \text{ mb} ; \ \sigma_{\text{el.}}/\sigma = 0.2589 ;$$

$$|t|_{\text{dip}} = 0.4847 \text{ GeV}^2 ; \ (d\sigma/dt)_{\text{dip}} = 0.01532 \text{ mb GeV}^{-2};$$

$$|t|_{\text{bump}} = 0.6488 \text{ GeV}^2; (d\sigma/dt)_{\text{bump}} = 0.02816 \text{ mb GeV}^{-2} ;$$

$$\text{ratio(bump/dip)} = 1.8383. \tag{4.14}$$

In a closeup examination of the graph, shown in the inset in Fig. 4.6, we observe

---

[1] Because the present data stops at about 2.5 GeV^2, the quantity β_R is difficult to fix uniquely.

a discontinuity in the magnitudes of $d\sigma/dt$ in the junction of the two sets of data. We estimate that a renormalization factor 0.86 would adjust the higher $|t|$ to the more forward data in this region.

It is very interesting to compare the 7 TeV data with the similar behavior of the 52.8 GeV data [83], that are available in the ranges $0.107 \times 10^{-2} \leq |t| \leq 0.5546 \times 10^{-2}$ GeV^2 with 34 points and $0.825 \leq |t| \leq 9.75$ GeV^2 with 63 points. This comparison is shown in Fig. 4.7 and in Tables 4.3 and 4.4, and the behavior of the amplitudes is discussed in Sec. 4.3

Properties of the 7 TeV amplitudes

The amplitudes obtained in the analysis of the data, based on Eq. (4.5), are shown in Fig. 4.8 and numerical information is given in Tables 4.3 and 4.4. Their general features are common to the lower energies from ISR and the Tevatron, with regular variation of the parameters. The results agree with requirements from dispersion relations for amplitudes and for slopes [38], as we will see in the end of this chapter, and the Coulomb interference accounts for the necessary generalization of the Coulomb phase, presented in the Appendix A. Near $t \simeq 0$, the real part obeys the theorem by A. Martin [54] about its first zero, decreasing quickly and crossing zero at small $|t|$, before the imaginary part becomes small. The $|t|$ dependence of the amplitudes for all $|t|$ is shown in part (b) of Fig. 4.8.
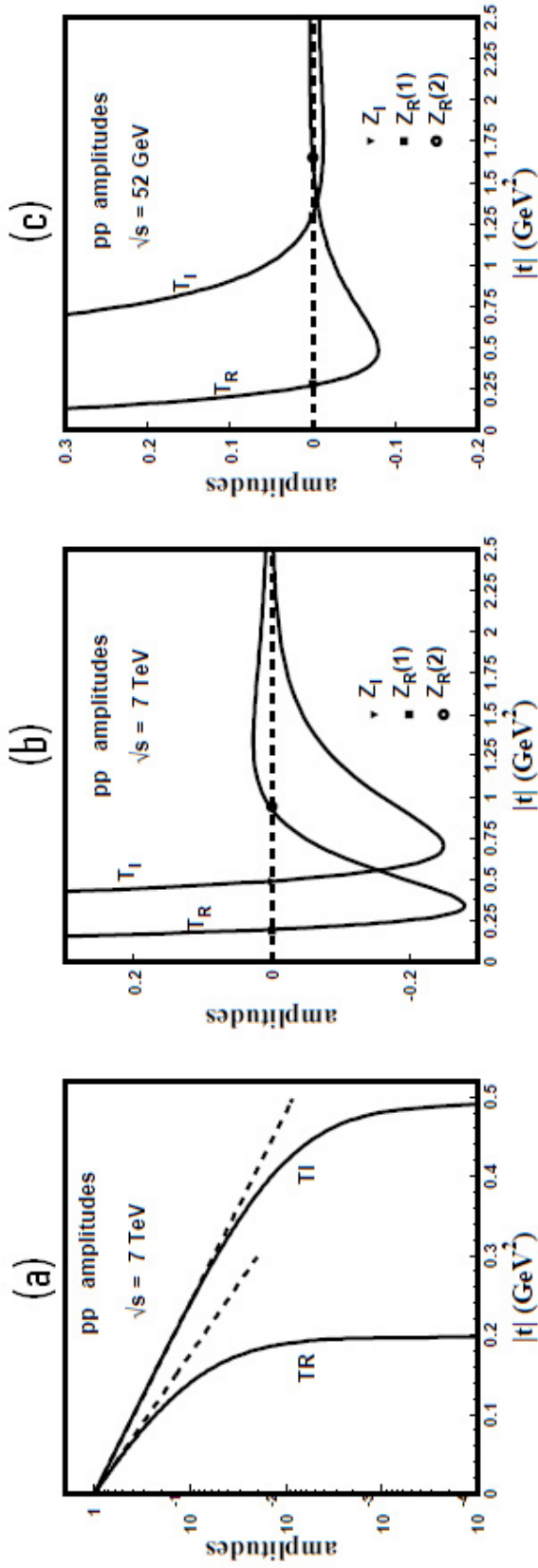
Figure 4.8: (a) Forward scattering amplitudes T_R and T_I at $\sqrt{s} = 7$ TeV in log scale, normalized to one at $|t| = 0$, showing their slopes, $B_I = 19.77$ and $B_R = 30.2\,\mathrm{GeV^{-2}}$, and their curvatures; (b) Long t dependence of the real and imaginary scattering amplitudes showing the complete set of zeros; (c) t dependence of the real and imaginary scattering amplitudes at $\sqrt{s} = 52.8$ GeV. Comparing with the figure for 7 TeV, we observe that all zeros move towards smaller $|t|$ values as the energy increases.

The imaginary part starts dominant over the real part, crosses zero at higher $|t|$, then remains negative and asymptotically tends to zero from the negative side, while the real part crosses zero again near $|t| = 0.8$ GeV^2 , becoming positive. After the second real zero, namely for $|t|$ larger than about 1.0 GeV^2 , the real amplitude stays positive, without further oscillation, and for $|t| \geq 2$ GeV^2 becomes increasingly dominant over the imaginary part. Important qualitative feature of our description of the data is that for large $|t|$ the magnitude of the imaginary part is smaller than the positive real part.

This behavior is consistent with a regular continuation of the results obtained for the ISR energies, and as an example we show in part (c) of Fig. 4.8 the amplitudes for 52.8 GeV. At this and higher energies [48] the Z_I zero occurs between $Z_R(1)$ and $Z_R(2)$. The magnitude of $T_I(s,t)$ is in general dominant over the real part between $Z_R(1)$ and $Z_R(2)$, so that the dip is located near Z_I. As the energy varies, while the first zero of $T_R(s,t)$ stays almost constant in the $|t|$ range from 0.15 to 0.3 GeV^2, the positions of both Z_I and $Z_R(2)$ move to the left. The relative proximity of real and imaginary zeros influences the shape and depth of the dip. At 540 and 1800 GeV the imaginary zero is distant from both real zeros, so that no dip is formed, and only an inflection is observed.

Table 4.4 gives the positions of the zeros of the amplitudes and the characteristic observable quantities in pp elastic scattering at 7 TeV and 52.8 GeV.

Table 4.4: Positions of zeros of the amplitudes, locations of the predicted dip and bump, and ratio characterizing the shape of this structure. For comparison that shows the regularity, we give the same information for $\sqrt{s} = 52.8$ GeV. We observe that as the energy increases all zeros move towards smaller $|t|$, with the imaginary zero moving faster, becoming more distant from the the second real zero $Z_R(2)$ and closer to the first one $Z_R(1)$.

$\sqrt{s}$ GeV	$Z_{\rm I}$ GeV^2	$Z_{\rm R}(1)$ GeV^2	$Z_{\rm R}(2)$ GeV^2	$|t|_{\rm dip}$ GeV^2	$|t|_{\rm bp}$ GeV^2	$(d\sigma/dt)_{\rm dip}$ mb/GeV^2	$(d\sigma/dt)_{\rm bp}$ mb/GeV^2	ratio bp/dip	$\sigma_{\rm el}$ mb	$\sigma_{\rm inel}$ mb	$\sigma_{\rm el}/\sigma$
52.8	1.3083	0.2710	1.6157	1.3560	1.7947	1.9×10^{-5}	6.3×10^{-5}	3.2805	7.4308	35.0591	0.1749
7000	0.4671	0.1641	0.8235	0.4847	0.6488	0.0153	0.0282	1.8383	25.54	73.11	0.26

The details of the dip-bump structure carry information on the scattering amplitudes, and are particularly sensitive to their relative behavior near their zeros [48]. Thus, a marked dip appears when one of the amplitudes (real or imaginary) crosses the zero in the interval where the other amplitude stays nearly constant with magnitude small compared to the variation of the former. In a domain where one of the amplitudes is dominant, the zero of the amplitude with smaller magnitude does not affect the observable differential cross section, as happens in the region of the first real zero ($\approx 0.15 - 0.3$ GeV^2).

The parts $d\sigma^R/dt$ and $d\sigma^I/dt$ of the differential cross section due to the real and imaginary amplitudes are shown in Fig. 4.9.

Differently from lower energies, the dip at $|t| \approx 0.5$ GeV^2 is more influenced by the proximity of the imaginary zero (≈ 0.5 GeV^2) and the first real zero $Z_R(1)$ (at 0.2 GeV^2). Due to the increasing proximity of the imaginary and real zeros at higher energies, the dip/bump structure becomes more marked, and this is expected to happen at 14 TeV.

At 7 TeV the bump that follows the dip is formed by the T_I and the T_R amplitude that have there similar magnitudes, with T_I becoming more strongly negative while T_R quickly becomes zero. This explains the ratio nearly 2 (actually 1.838) between bump and dip heights. After the bump the fall is faster because it is only determined by the dominant magnitude of the imaginary amplitude, that decreases fast in $|t|$. T_R is small positive, but of long range, surviving until it meets the expected perturbative tail after $|t| = 2$ GeV^2.
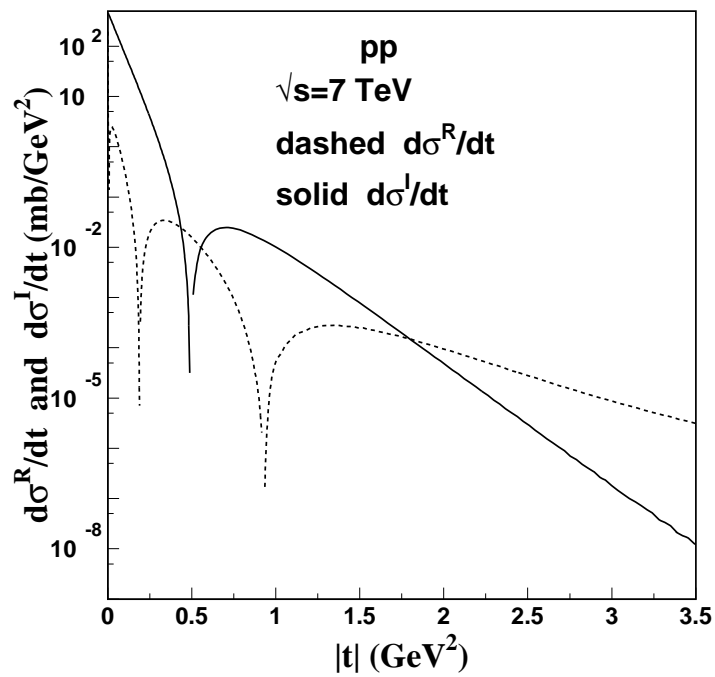
Figure 4.9: Partial cross sections $d\sigma^I/dt$ and $d\sigma^R/dt$ as functions of $|t|$ as calculated with the analytic forms of Eqs. (4.5) and (2.63). The dip in the sum $d\sigma/dt$ (at 0.485 GeV^2) is close to the zero of the imaginary part (at 0.467 GeV^2).

4.4 Full energy dependence

An extensive analysis of all pp elastic scattering data for $\sqrt{s}$ from 20 GeV to 7 TeV leads to a separate identification of the real and imaginary parts contributing to Eq. (4.1). We made use also of the p$\bar{\text{p}}$ data at 540 and 1800 GeV. At these energies pp and p$\bar{\text{p}}$ cross sections are the same obeying the Pomeranchuck theorem and the ρ parameter also converges to the same value as shown before. The energy dependence of the eight parameters is given below, with $\sqrt{s}$ in TeV, and GeV^{-2} in the units of the parameters α_K, β_K and λ_K, (γ_K are dimensionless)

$$\alpha_I(s) = 11.0935 + 1.35479 \log \sqrt{s}, \tag{4.15}$$

$$\beta_I(s) = 4.44606586 + 0.3208411 \log \left(\sqrt{s}/30.4469 \right)$$
$$+ 0.0613381 \left[\log^2 \left(\sqrt{s}/30.4469 \right) + 0.5 \right]^{1/2}, \tag{4.16}$$

$$\alpha_R(s) = 0.208528 + 0.0419028 \log \sqrt{s}, \tag{4.17}$$

$$\beta_R(s) = 1.1506 + 0.12584 \log \sqrt{s} + 0.017002 \log^2 \sqrt{s}, \tag{4.18}$$

$$\gamma_I(s) = 10.025 + 0.79097 \log \sqrt{s} + 0.088 \log^2 \sqrt{s}, \tag{4.19}$$

$$\gamma_R(s) = 10.401 + 1.4408 \log(\sqrt{s}) + 0.16659 \log^2(\sqrt{s}), \tag{4.20}$$

$$\lambda_I(s) = 14.02008 + 3.23842 \log \sqrt{s} + 0.444594 \log^2 \sqrt{s}, \tag{4.21}$$

$$\lambda_R(s) = 3.31949 + 0.743706 \log \sqrt{s}. \tag{4.22}$$

In fig. 4.4 we show the real and imaginary parameters in GeV^{-2} unit as function of the center of mass energy. In fig. 4.4 we show the imaginary and real dimensionless parameters γ_K with their energy dependence.

The peculiar (not so simple) expression for $\beta_I(s)$ is constructed in order to satisfy both the low-energy phenomenology and unitarity constraints at all energies. For very high energy and considerations for asymptotic behavior, it is useful to use

Figure 4.10: In the left figure we show the imaginary parameters in units of GeV^{-2} as function of the energy. The figure in the right shows the corresponding real parameters. It is remarkable the soft energy dependence of these set of parameters.
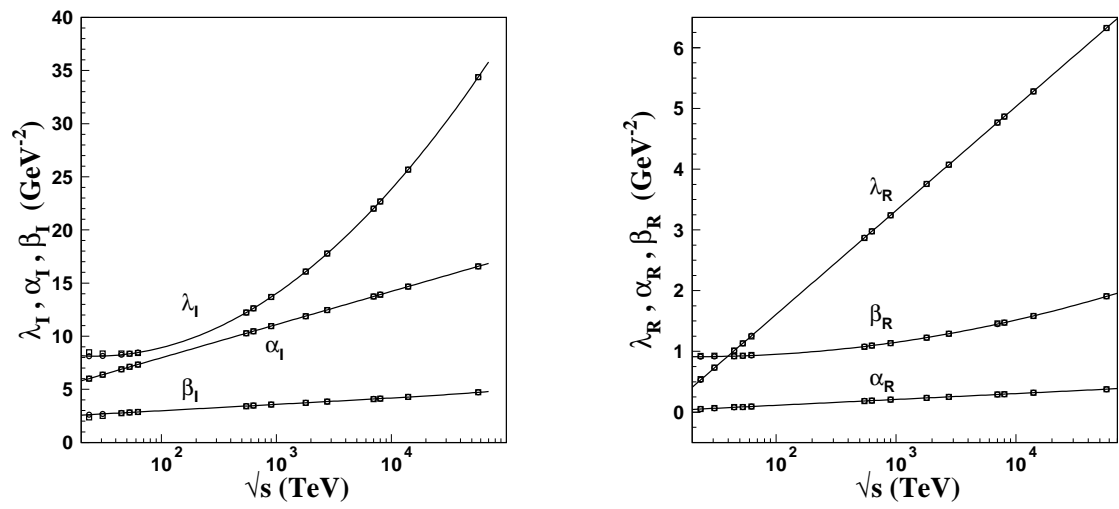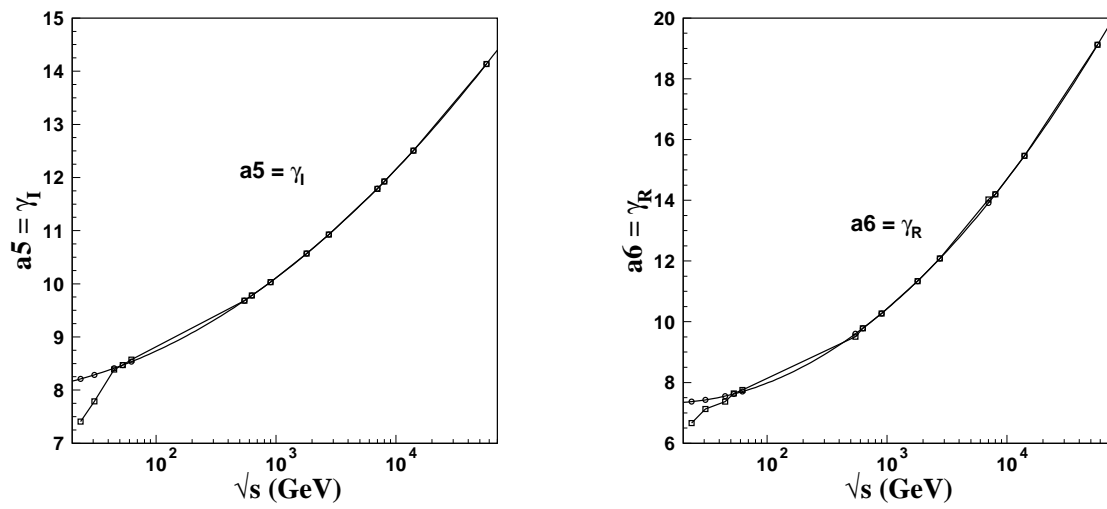
Figure 4.11: In the left figure we show the imaginary parameter $\gamma_I s$ as function of the energy. The figure in the right shows the corresponding real parameter. Notice that both curves increases as $\log^2 s$. This rising has important consequences in the determination of the real and imaginary slopes.

simpler form for $\beta_I(s)$.

$$\beta_I(s) = 3.14055 + 0.382179 \, \log \sqrt{s} \, . \tag{4.23}$$

Using the energy dependence given by Eqs. (4.15-4.19) and the forward expression Eqs.(4.6,4.7,4.8) we can write the practical formulas for the four quantities

$$\sigma(s) = 69.3286 + 12.6800 \log \sqrt{s} + 1.2273 \log^2 \sqrt{s} \, , \tag{4.24}$$

$$B_I(s) = 16.2472 + 1.53921 \log \sqrt{s} + 0.174759 \log^2 \sqrt{s} \, , \tag{4.25}$$

$$B_R(s) = 22.835 + 2.862 \log \sqrt{s} + 0.329721 \log^2 \sqrt{s} \, , \tag{4.26}$$

and

$$\rho(s) = \frac{3.528018 + 0.7856088 \log \sqrt{s}}{25.11358 + 4.59321 \log \sqrt{s} + 0.444594 \log^2 \sqrt{s}} \, , \tag{4.27}$$

where $\sqrt{s}$ is in TeV, σ in milibarns, B_I and B_R are in GeV^{-2}; ρ is dimensionless, passes through a maximum at about 1.8 TeV, and decreases at higher energies, with asymptotic value zero. The parameters σ , B_I and B_R are shown in Fig. (4.12). The ratio B_R/B_I is always larger than one, as expected from dispersion relations [38]. The ratio B_R/B_I as function of the energy is shown in Fig. (4.13). There is a finite asymptotic value $B_R/B_I \rightarrow 1.887$.

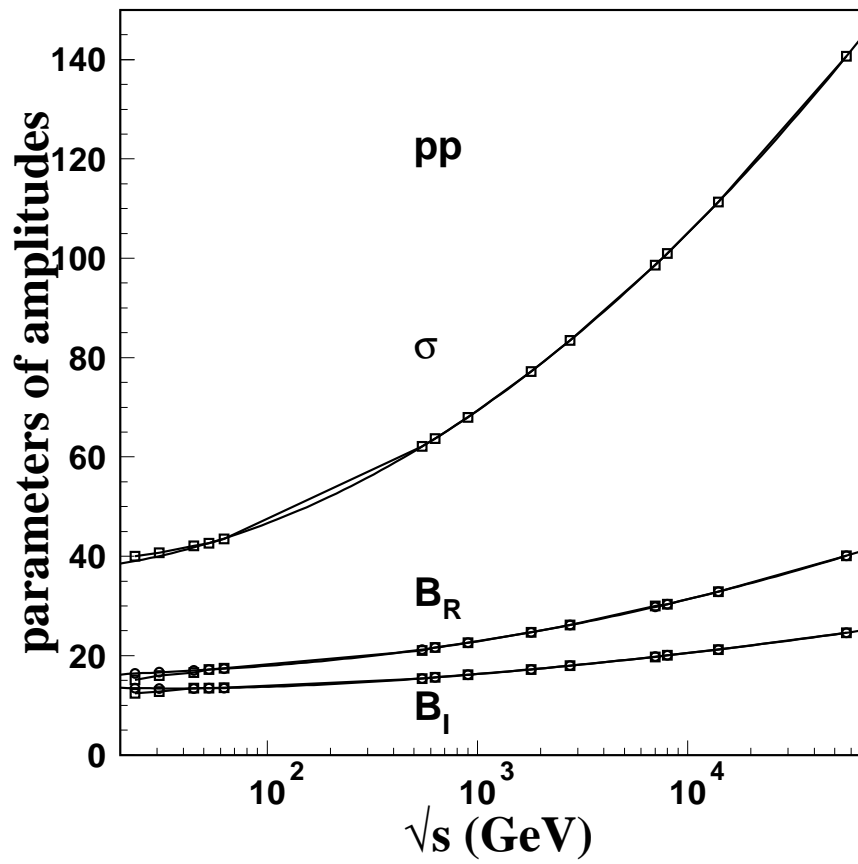Figure 4.12: The total cross section and real and imaginary slopes are shown as function of energy.
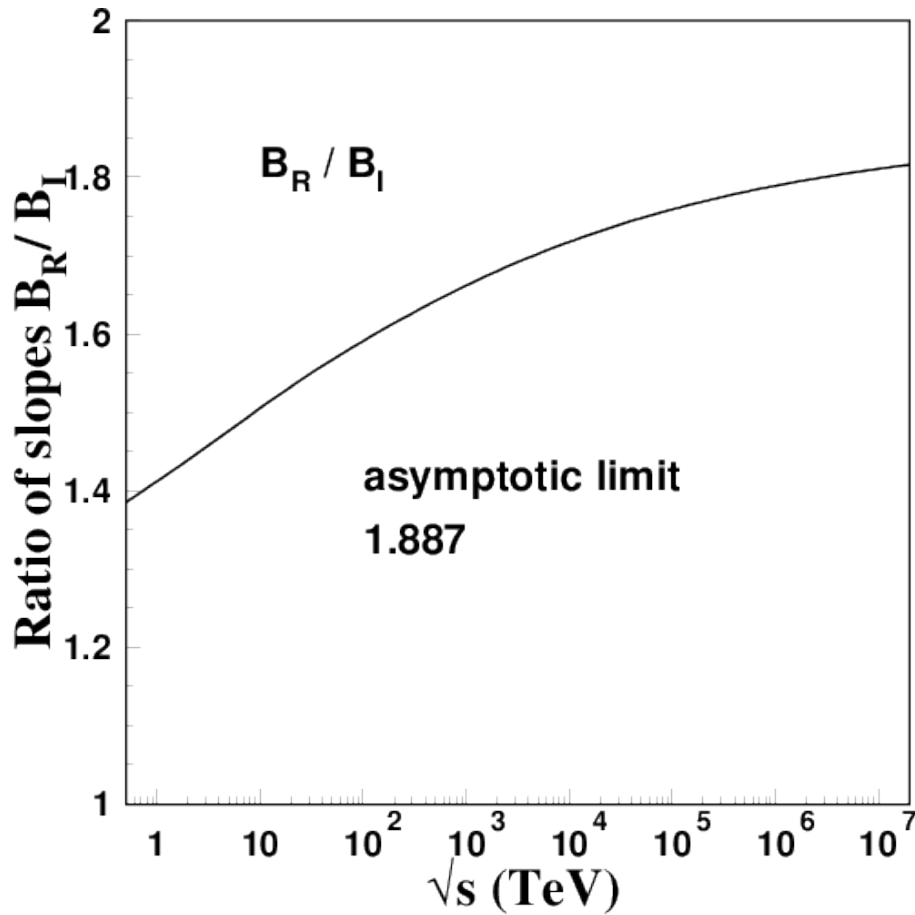
Figure 4.13: The slopes of real and imaginary amplitudes vary with the energy with a $\log^2$ dependence as given by Eqs. (4.25,4.26). At all energies it is $B_R > B_I$, as predicted by dispersion relations [38]. In the figure, the ratio B_R/B_I is plotted as function of the energy, indicating the finite asymptotic limit.

Table 4.5: Values of parameters that build the amplitudes for all $|t|$, for the energies of LHC pp collisions.

$\sqrt{s}$	imaginary amplitude				real amplitude			
	σ	B_I	α_I	β_I	ρ	B_R	λ_R	β_R
TeV	mb	GeV^{-2}	GeV^{-2}	GeV^{-2}		GeV^{-2}	GeV^{-2}	GeV^{-2}
1.8	77.21	17.17	11.8898	3.7175	0.1427	24.63	3.7566	1.2304
2.76	83.47	17.96	12.4689	3.8293	0.1431	26.08	4.0745	1.2959
7	98.65	19.90	13.7298	4.0745	0.1415	29.65	4.7667	1.4599
8	101.00	20.21	13.9107	4.1100	0.1411	30.21	4.8660	1.4858
13	109.93	21.35	14.5685	4.2409	0.1392	32.35	5.2271	1.5852
14	111.34	21.53	14.6689	4.2612	0.1389	32.68	5.2822	1.6011

4.5   Observables in the range from 1.8 to 14 TeV

In Fig. 4.14 we show the predictions for $d\sigma/dt$ for the LHC energies 2.76 , 8 , 13 and 14 TeV. We first observe that the dip and the bump peak displace to the left as the energy increases and in this figure these displacements follow almost straight lines, as indicated by marks with black circles and open squares. For the sake of convenience, we list the values of parameters for these energies in Table 4.5, where $\gamma_I, \lambda_I, \alpha_R$ and γ_R are substituted by more commonly used quantities σ, ρ together with the slope parameters B_I and B_R. In Table 4.6 we show the values of several quantities obtained in the numerical calculation of the amplitudes and of observables in the elastic process. Some characteristic features are exhibited below in plots.
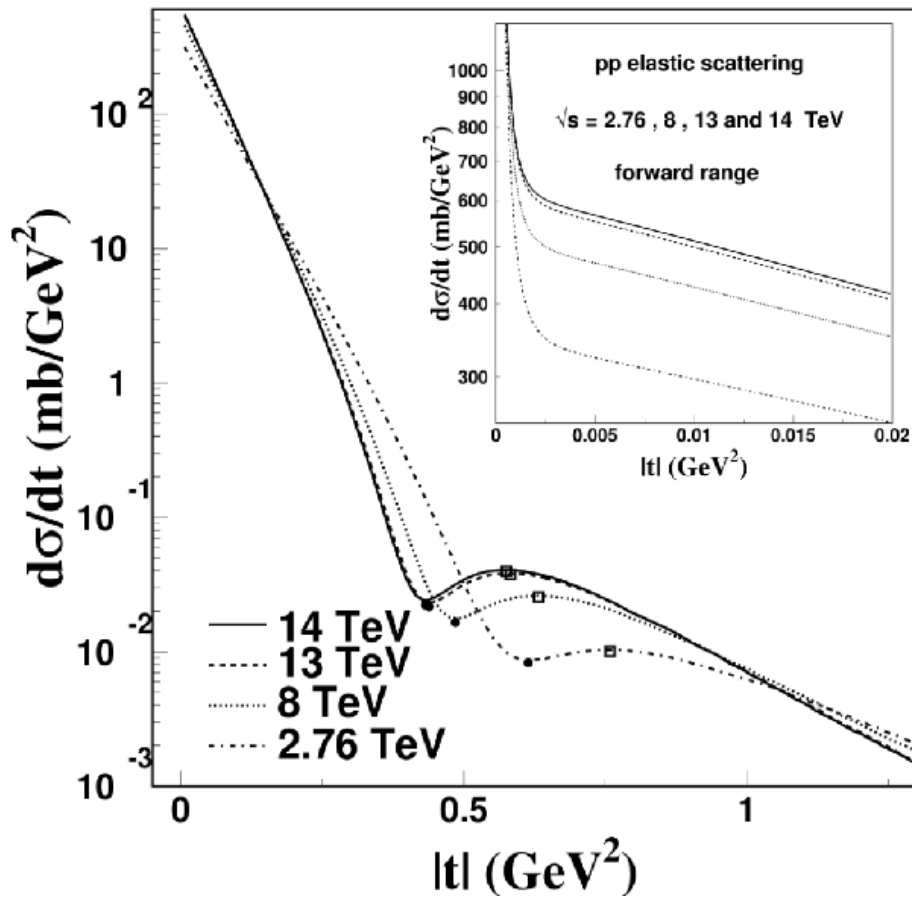
Figure 4.14: The lines show the values of $d\sigma/dt$ obtained for energies of LHC experiments. The 7 TeV case, presented before [20], is obviously very close to the 8 TeV curve. The positions of dips and bump peaks at different energies, marked with dots and squares, can be connected with straight lines. The inset shows the low $|t|$ range, with Coulomb interaction effects included.

Table 4.6: Some associated quantities that characterize the structure of amplitudes and cross sections : positions of zeros, dip, and $|t|_{\text{peak}}$ at highest point of bump in $d\sigma/dt$; ratio R of values of $d\sigma/dt$ at $|t|_{\text{peak}}$ and $|t|_{\text{dip}}$; position and height of the inflection ; inelastic and integrated elastic cross sections.

$\sqrt{s}$ TeV	Z_{I} GeV²	$Z_{\text{R}}(1)$ GeV²	$Z_{\text{R}}(2)$ GeV²	$|t|_{\text{dip}}$ GeV²	$d\sigma/dt|_{\text{dip}}$ mb/GeV²	$|t|_{\text{peak}}$ GeV²	$d\sigma/dt|_{\text{peak}}$ mb/GeV²	ratio R	$|t|_{\text{infl}}$ GeV²	$d\sigma/dt|_{\text{infl}}$ mb/GeV²	σ_{inel} mb	σ_{el} mb	σ_{el}^{I} mb	σ_{el}^{R} mb	$\sigma_{\text{el}}/\sigma$
1.8	0.6250	0.2052	1.0464	0.6798	0.00583	0.8170	0.00663	1.1362	0.7289	0.00615	58.89	18.31	18.07	0.24	0.237
2.76	0.5723	0.1925	0.9788	0.6138	0.00825	0.7587	0.01009	1.2221	0.6633	0.00896	63.11	20.35	20.09	0.27	0.244
7	0.4757	0.1673	0.8445	0.4989	0.01535	0.6465	0.02286	1.4891	0.5459	0.01812	73.26	25.39	25.07	0.32	0.257
8	0.4635	0.1639	0.8267	0.4850	0.01659	0.6319	0.02549	1.5368	0.5314	0.01985	74.82	26.18	25.86	0.33	0.259
13	0.4225	0.1522	0.7654	0.4385	0.02158	0.5816	0.03742	1.7338	0.4827	0.02732	80.79	29.20	28.85	0.35	0.266
14	0.4166	0.1505	0.7565	0.4319	0.02242	0.5743	0.03963	1.7678	0.4758	0.02864	81.66	29.68	29.32	0.35	0.267

In Fig. 4.15 we use the energy $\sqrt{s} = 8$ TeV as an example to show the imaginary and real amplitudes $T_I^N(s,t)$, $T_R^N(s,t)$ as functions of $|t|$ as predicted by Eq.(4.5). For all energies the characteristic features are the two zeros of the real part, and the single zero of the imaginary part appearing in the plotted range (a second zero of T_I^N would appear in a much larger $|t|$, outside experimental visibility). The interplay of the imaginary and real amplitudes at mid values of $|t|$ is responsible for the dip-bump structure of the differential cross section, that was shown before [20] for $\sqrt{s} = 7$ TeV, and is shown for 8 TeV in the next section, with accurate description of the preliminary data in the whole $|t|$ range. For $|t| \geq 1.5\,\mathrm{GeV}^2$ the real part becomes dominant, with positive sign. The inset shows the small $|t|$ range, in log scale, normalized to one at $|t| = 0$. The straight exponential slopes are shown in dashed lines, with the dramatic difference between the real and imaginary amplitudes. Soon the amplitudes leave the straight line and curve down, searching for their respective zeros. The consequence to the behavior of $d\sigma/dt$ is observed at 8 TeV for $|t|$ larger than about $0.15\,\mathrm{GeV}^2$.

The difference in slopes B_R and B_I that is required by dispersion relations [38], is often neglected. The real part is small for small $|t|$, due to the small value of ρ, but becomes influential or dominant for mid and large $|t|$. The amplitudes must be treated as functions for the whole $|t|$ range. Our unique analytical form connects all regions and controls the behaviour both at small and large $|t|$. Thus, for example, the value of ρ is very important for the shape of the dip-bump structure.

The regular energy dependence of the positions of the zeros and of dips and peaks of bumps is shown in Fig. 4.16. We see that all these characteristic quantities move towards smaller $|t|$ with increasing energy, following forms like

$$A + \frac{1}{a + b \log \sqrt{s} + c \log^2 \sqrt{s}} \,, \qquad (4.28)$$

possibly with finite asymptotic limits A. Particularly interesting is the displacement

of the first real zero $Z_R^{(1)}$, that at very high energies behaves as above, with $A = 0$ and $c = 0$, according to a theorem by A. Martin [54]. This behaviour is obviously connected with a fast increase of the slope B_R.

It is interesting to observe the relative positions of the dip and the peak of the bump in $d\sigma/dt$ and the zeros of the imaginary and real parts, shown in Fig. 4.16. This question has been discussed a long time ago [48]. The figure shows that Z_I and the dip position tend to the (apparently) common finite limit. Dips and peaks are always located between Z_I and $Z_R^{(2)}$. All energy dependences are simple and can be easily parameterized.

It is interesting to note that the ratio between the maximum of the mid-$|t|$ bump (called peak) and the dip minimum

$$R = [d\sigma/dt]_{\text{peak}}/[d\sigma/dt]_{\text{dip}} \tag{4.29}$$

increases with energy rather rapidly (see Fig. 4.16-b) like $\sim \ln^2 \sqrt{s}$, while the distance $|t|_{\text{peak}} - |t|_{\text{dip}}$ remains practically constant (Fig. 4.16-a).

In Fig. 4.17 we plot $d\sigma/dt$ for 2.76 and 8 TeV, showing that the characteristic dip/bump structure of $d\sigma/dt$ occurs in the interval between the imaginary zero and the second real zero.
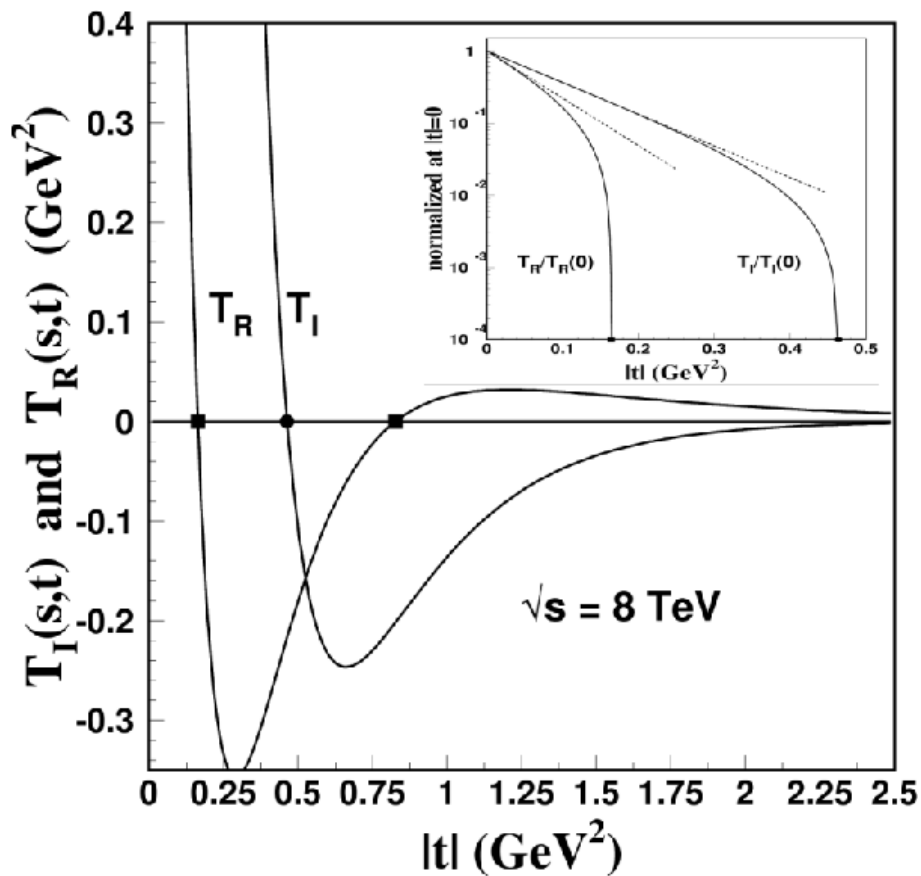
Figure 4.15: Plots of the real and imaginary parts of elastic pp scattering amplitude at 8 TeV, as functions of $|t|$. The general behaviour is the same for all energies, with one and two zeros respectively for the imaginary and real parts. The behaviour for small $|t|$ is shown in the inset, indicating the difference of slopes B_R and B_I at the origin, and the deviations of the exponential forms that occur as $|t|$ increases, each amplitude going towards its zero. A second zero of the imaginary part occurs at much higher $|t|$.
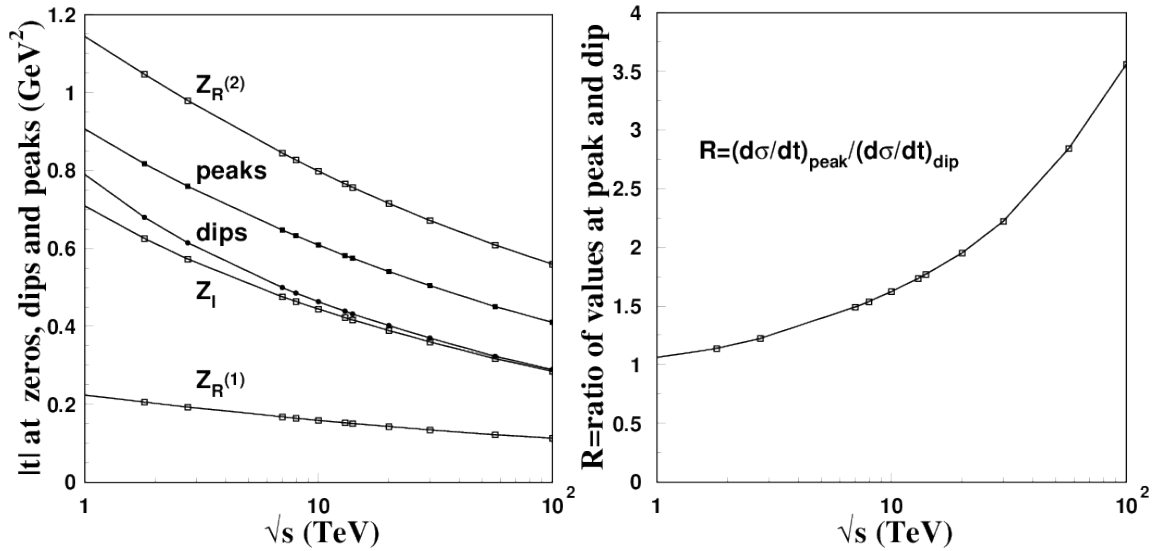
Figure 4.16:   a) Positions of the zeros of the amplitudes, and of the dip and peak at the bump of $d\sigma/dt$. There appears one zero in the imaginary and two in the real amplitude. A second imaginary zero occurring at very large $|t|$ is outside the physically accessible range. All quantities move towards small values with increasing energies. The dips tend to coincide with the imaginary zero at high energies. The remarkable dip/bump structure in pp scattering occurs in the interval between the imaginary zero and the second real zero. The first real and the imaginary zero move towards smaller $|t|$, indicating the $\log^2 \sqrt{s}$ increase of the real and imaginary slopes. The dots are put to help the connection of values of the quantities for different energies. b) There is a regular and fast increase of the ratio $R = [d\sigma/dt]$peak$/[d\sigma/dt]$dip, with increasing sharpness of the dip/bump structure although the distance $|t|_{\mathrm{peak}} - |t|_{\mathrm{dip}}$ between them varies very little. These symptoms come from the increasing proximity of $|t|_{\mathrm{dip}}$ and Z_I, and to the convergence to finite asymptotic limits of both $|t|_{\mathrm{peak}}$ and $|t|_{\mathrm{dip}}$.

3

114
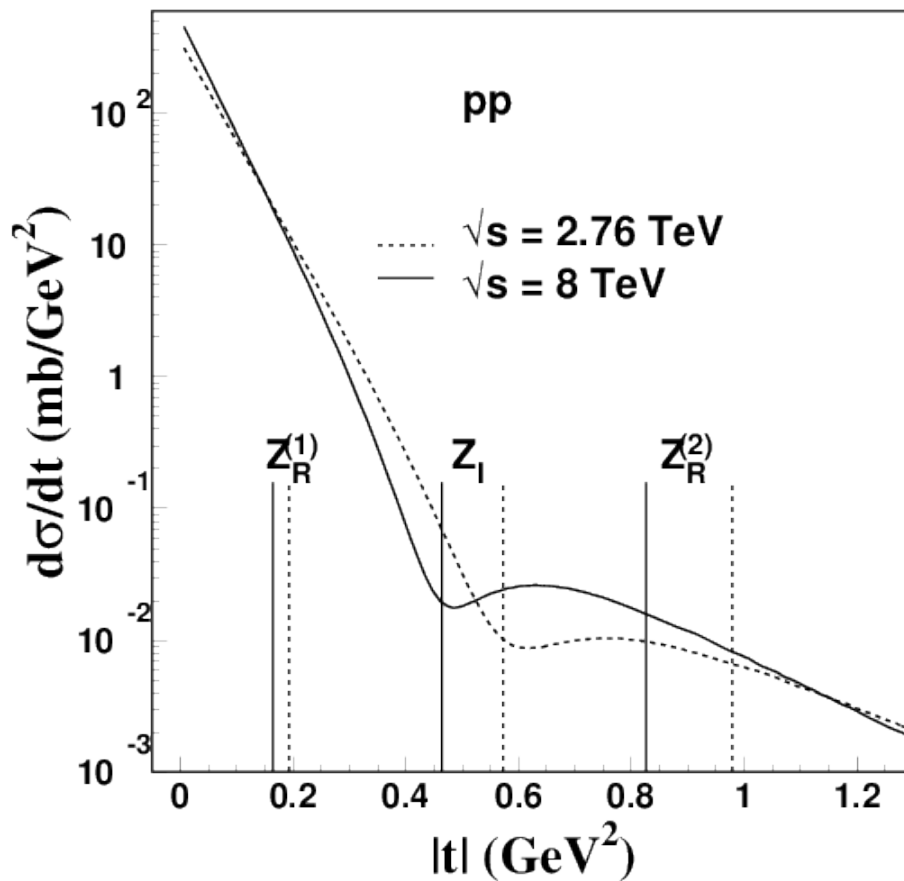
Figure 4.17: The dip-bump structure in the differential cross section is determined by the interplay of the regularly increasing modulus (magnitude) of the imaginary part and the regularly decreasing modulus (magnitude) of the real part. At all energies both dip and peak of the bump are located between Z_I and $Z_R^{(2)}$. This behaviour is shown in this figure for the energies 2.76 and 8 TeV. As the energy increases $|t|_{\text{dip}}$ approaches Z_I from the right to the left. Fig. 4.16 illustrates these properties again, in another way.

Comparison with data and predictions for 8 TeV

Our description [20] of the elastic scattering data at 7 TeV from the Totem Collaboration [80] reproduces N=165 points in $d\sigma/dt$ with an impressive squared average relative deviation $\langle \chi^2 \rangle = 0.31$. Characteristic quantities at this energy, shown in Tables 4.5 and 4.6 are $\sigma = 98.65$ mb, $\sigma_{\mathrm{el}} = 25.39$ mb , $B = 19.90$ GeV^{-2}, that compare extremely well with the values published by Totem [80], $\sigma = 98.6 \pm 2.2$ mb, $\sigma_{\mathrm{el}} = 25.4 \pm 1.1$ mb , $B = 19.9 \pm 0.3$ GeV^{-2}.

After the successful description of the 7 TeV data [20], we now present comparison and predictions for other LHC energies.

For the inelastic cross section we assume the difference $\sigma_{\mathrm{inel}} = \sigma - \sigma_{\mathrm{el}}$ and then we have 73.26 mb at 7 TeV.. Published values of the Totem Coll. using different methods are 73.15 ± 1.26 [80], 73.7 ± 3.4 [87] and 72.9 ± 1.5 [88]. Alice Coll. [89] gives $\sigma_{\mathrm{inel}} = 73.2 \pm 5.3$ mb , and Atlas Coll. $\sigma_{\mathrm{inel}} = 69.4 \pm 2.4 \pm 6.9$ mb [90]. We are not able to understand the CMS results [91] in terms of pure σ_{inel} due to non-informed missing contributions. In these measurements there are extrapolations to using Monte Carlo models to include diffractive events of low mass. Of course all these results are compatible with our calculations.

A measurement to be compared with our predictions is the $\sqrt{s} = 2.76$ TeV value of Alice Coll., that gives $\sigma_{\mathrm{inel}} = 62.8 \pm 4.2$ mb , while our tables give the compatible value 63.11 mb.

The analysis of compatibility for the 1.8 TeV measurements of σ_{inel} by CDF and E811 in Fermilab [92] suggests the value $(1 + \rho^2)\sigma_{\mathrm{inel}} = (60.3 \pm 2.3$ mb, that with with our ρ value gives $\sigma_{\mathrm{inel}} = (59.1 \pm 2.3$ mb. Our table gives 58.89 mb for 1.8 TeV, once more in very good agreement.

Finally, at 57 TeV the Auger Cosmic Ray experiment [27], using other models for the pp input, evaluates $\sigma_{\mathrm{inel}} = 92 \pm 14.8$ mb , while our extrapolation gives 101 mb. We have discussed this measurement [93] together with other CR Extended Air Showers (EAS) experiments, using our amplitudes as inputs and a basic Glauber

method to connect pp and p-air processes. Our calculation reproduces well all CR data for p-air cross sections with $\sqrt{s}$ (in the pp system) up to 100 TeV.

For 8 TeV we have predictions $\sigma = 101.00$ mb , $\sigma_{\mathrm{el}} = 26.18$ mb , $\sigma_{\mathrm{inel}} = 74.82$ mb , $\sigma_{\mathrm{el}}/\sigma = 0.26$ shown in the tables. The measurements by Totem [94] give for the same quantities $\sigma = 101.7 \pm 2.9$ mb , $\sigma_{\mathrm{el}} = 27.1 \pm 1.4$ mb, $\sigma_{\mathrm{inel}} = 74.7 \pm 1.7$ mb , $\sigma_{\mathrm{el}}/\sigma = 0.266 \pm 0.006$. Of course these numbers are very encouraging, indicating also good expectations for $d\sigma/dt$ at this energy.

The data and our curve for $\sigma_{\mathrm{inel}}(s)$ are shown in Fig. 4.18. All this information shows that our formulae for the energy dependence of $\sigma(s)$ and $\sigma_{\mathrm{inel}}(s)$ in pp scattering work very well.

Expected data for $d\sigma/dt$ at 8 TeV

The preliminary data for $d\sigma/dt$ at 8 TeV, shown in talks by members of the Totem Collaboration [95], are encouraging for the application of our method of analysis. We recall that in the treatment of the 7 TeV data, we obtained precise description, with average $\langle \chi^2 \rangle = 0.34$ for 165 data points in the whole $|t|$ interval of measurements.

If Fig. 4.19 we shown our calculation for $d\sigma/dt$ covering the whole $|t|$ range of the preliminary information, using the amplitudes defined in Sec. 4.5. The characteristic features of the forward peak and of the dip/bump structure are expected to represent accurately the angular dependence. Numerical values for characteristic features are given in Tables 4.5 and 4.6.

This is the description of the global $d\sigma/dt$ data at 8 TeV, that promises to be more complete and regular than the 7 TeV data, except for not reaching larger $|t|$ values. In the following we discuss the forward region in more detail.

In Fig. 4.20 we plot the calculations in the small $|t|$ range , including the influence of the Coulomb phase [20]. The calculation with Coulomb phase put equal to zero is represented by the dashed line, showing that its influence is small. Our specific

calculation of the Coulomb phase takes into account the difference in values of the B_R and B_I slopes. Other calculations for the interference phase [96] also show that its influence is small, reducing $d\sigma/dt$ by a few percent.

Our values for B_I and B_R given in Table 4.5 lead to the $d\sigma/dt$ effective slope at 8 TeV equal to $B = 20.405$ GeV^{-2}.

Our predictions seem to be in accordance with the eye-guided reading of the preliminary data of $d\sigma/dt$ that appear in presentations of the Totem group in workshops, at least at the qualitative level. At 7 TeV our expressions perform extremely well when compared to the published experimental information, and we expect that the same will happen at 8, 13 and 14 TeV .
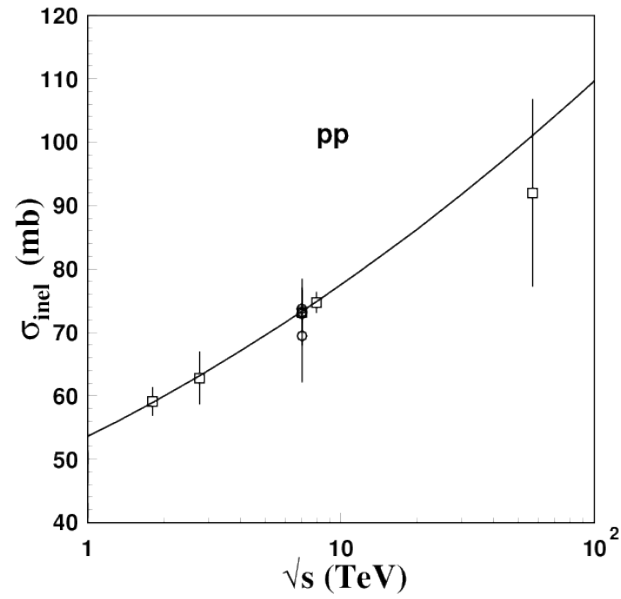
Figure 4.18: Our calculations for pp inelastic cross sections and the data above $\sqrt{s} = 1$ TeV , that cover the energies 1.8 TeV [92], 2.76 TeV [89], 7 TeV [80, 87–90], 8 TeV [94] and 57 TeV [27].
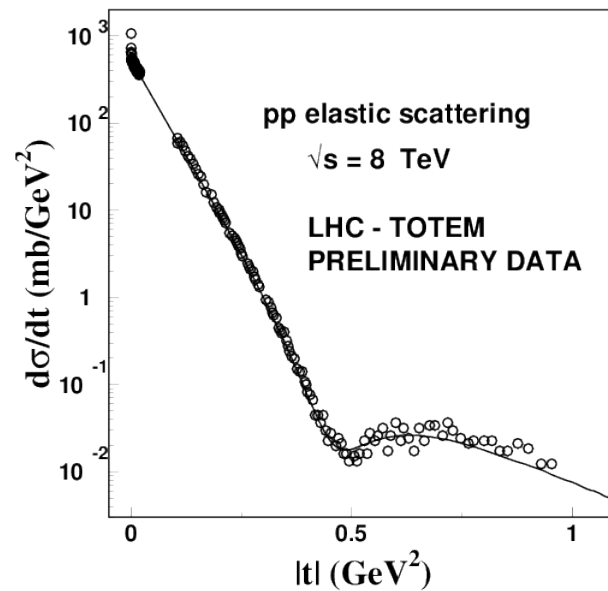
Figure 4.19: Preliminary experimental data and predicted representation for $d\sigma/dt$ in the whole $|t|$ range of observations at 8 TeV made in LHC by the Totem Collaboration [95].
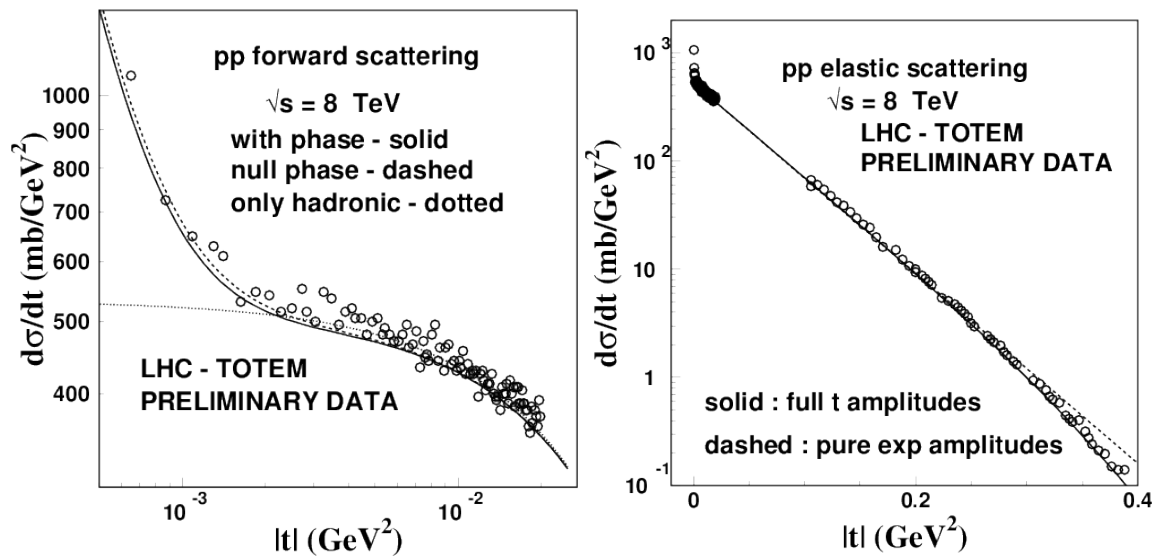
Figure 4.20: Calculation of $d\sigma/dt$ in the forward range at 8 TeV. The solid lines correspond to the full calculation with our amplitudes. a) In the LHS a log $|t|$ scale is used to represent in detail the forward range; the dashed line is obtained with Coulomb phase put equal to zero; the dotted line represents the hadronic interaction. b) In the RHS The dashed line represents the calculation with pure exponential amplitudes, with the real and imaginary parts entering with their corresponding slopes; the dotted line shows the usual description of the foreword peak in the form $d\sigma/dt = d\sigma/dt|_{t=0}\ \exp\left(-B|t|\right)$.

4.6 Use of dispersion relations in KFK

Once we have the proposed s dependence of KFK we are able to apply the DDR to the scattering amplitudes and study the connections between the real and imaginary parameters. The amplitudes in t space are written as in Eq.(4.5)

As we mentioned before, the explicit t dependence of the amplitudes, that is characteristic of this model, is able to describe with precision the differential cross sections in the whole t range in high energy scattering (above 19 GeV).

The normalization of the $T_K^N(s,t)$ amplitude is defined by the optical theorem in Eq.(4.6), and the differential elastic cross section

$$\frac{d\sigma(s,t)}{dt} = (\hbar c)^2 [T_I^2(s,t) + T_R^2(s,t)] = \frac{d\sigma^I(s,t)}{dt} + \frac{d\sigma^R(s,t)}{dt} \ . \tag{4.30}$$

At $|t| = 0$ we define the ρ parameter through the product

$$\sigma\rho = (\hbar c)^2 4\sqrt{\pi} T_R^N(s,0) = (\hbar c)^2 4\sqrt{\pi} [\alpha_R(s) + \lambda_R(s)] \ , \tag{4.31}$$

corresponding to the real amplitude at $t = 0$, with $[\alpha_R(s) + \lambda_R(s)]$ related to $[\alpha_I(s) + \lambda_I(s)]$ by dispersion relations.

Attention must be given to a conversion factor to use σ in mb , as the amplitudes T_I^N, T_R^N and parameters are given in GeV^{-2}.

The non-trivial t dependence of the amplitudes is characteristic fundamental of the model, entering as variables in two different functions that build the amplitudes. As mentioned before, for small $|t|$ the imaginary an real slopes, B_I and B_R are given by

$$\begin{aligned} B_K(s) &= \frac{2}{T_K^N(s,t)} \frac{\partial T_K^N(s,t)}{\partial t}\Big|_{t=0} \\ &= \frac{2}{\alpha_K(s) + \lambda_K(s)} \left[\alpha_K(s)\beta_K(s) + \frac{3a_0}{4}\lambda_K(s)\left(\gamma_K(s) + \frac{7}{6}\right)\right] \ . \end{aligned} \tag{4.32}$$

The products

$$
\begin{aligned}
\sigma B_I &= 2 \times 4\sqrt{\pi}\,(\hbar c)^2\, \frac{\partial T_I^N}{\partial t}\Big|_{t=0} \\
&= 2 \times 4\sqrt{\pi}\,(\hbar c)^2\, \left[\alpha_I(s)\beta_I(s) + \frac{3a_0}{4}\lambda_I(s)\Big(\gamma_I(s) + \frac{7}{6}\Big)\right]
\end{aligned}
\tag{4.33}
$$

and

$$
\begin{aligned}
\sigma\rho B_R &= 2 \times 4\sqrt{\pi}\,(\hbar c)^2\, \frac{\partial T_R^N}{\partial t}\Big|_{t=0} \\
&= 2 \times 4\sqrt{\pi}\,(\hbar c)^2\, \left[\alpha_R(s)\beta_R(s) + \frac{3a_0}{4}\lambda_R(s)\Big(\gamma_R(s) + \frac{7}{6}\Big)\right]
\end{aligned}
\tag{4.34}
$$

are connected by dispersion relations, as explained below.

The energy dependence of the parameters is given by simple forms in terms of $\log s$ as [20, 21]

$$
\alpha_K(s) = \alpha_{K0} + \alpha_{K1}\log\sqrt{s}\ ,
\tag{4.35}
$$

$$
\beta_K(s) = \beta_{K0} + \beta_{K1}\log\sqrt{s} + \beta_{K2}\log^2\sqrt{s}\ ,
$$

$$
\lambda_K(s) = \lambda_{K0} + \lambda_{K1}\ \log\sqrt{s} + \lambda_{K2}\ \log^2\sqrt{s}\ ,
$$

$$
\gamma_K(s) = \gamma_{K0} + \gamma_{K1}\ \log\sqrt{s} + \gamma_{K2}\ \log^2\sqrt{s}\ .
$$

To apply DDR we use the imaginary amplitude in the low $|t|$ rangeas an input, with parameters extracted from data. We show below the constraints imposed on the real part by DDR.

In this chapter we are concerned only with higher energies, above 500 GeV, in phase with the present importance of the analysis of LHC experiments. Thus we do not deal with distinction between pp and p$\bar{\text{p}}$ amplitudes (Pomeranchuk Theorem). Also, we use $s \approx 2mE$ and $x = s/(2m^2)$. Correspondingly, the term with the subtraction constant K, that is not important at high energies, will be excluded.

The correspondence between the scattering amplitude in DDR expressions and

the amplitudes in our model is

$$\frac{\text{Im } F(s,0)}{s} = 4\sqrt{\pi} \ T_I(s,0) \ . \tag{4.36}$$

In order to work with simpler mathematical expressions for dispersion relations we define the variable $x = s/2m^2$ and change notation $T_K^N(s,t) \to T_K^N(x,t)$. Then the energy dependence of the parameters is written in a generic mathematical expression

$$\bar{\eta}_K(x) = \bar{\eta}_{K0} + \bar{\eta}_{K1} \log + \bar{\eta}_{K2} \log^2 x \ , \tag{4.37}$$

where $\bar{\eta}_K = \{\bar{\alpha}_K, \bar{\beta}_K, \bar{\gamma}_K, \bar{\lambda}_K\}$ with the obvious correspondence of parameters

$$\begin{aligned}
\bar{\eta}_{K0} &\equiv \eta_{K0} + \frac{\eta_{K1}}{2} \log(2m^2) + \frac{\eta_{K2}}{4} \log^2(2m^2) \ , \\
\bar{\eta}_{K1} &\equiv \frac{\eta_{K1}}{2} + \frac{\eta_{K2}}{2} \log(2m^2) \ , \\
\bar{\eta}_{K2} &\equiv \frac{\eta_{K2}}{4} \ .
\end{aligned} \tag{4.38}$$

The values of the parameters on the right side of equations above are given in Eq.(4.15).The numerical values of the parameters of the imaginary part, that serve as input for the dispersion relations, and were obtained in the analysis of data, are

$$\bar{\alpha}_I(x) = 2.063762 + 0.681500 \ \log x \ , \tag{4.39}$$

$$\bar{\beta}_I(x) = 0.608653 + 0.191089 \ \log x \ ,$$

$$\bar{\lambda}_I(x) = 14.905103 - 1.790311 \ \log x + 0.128825 \ \log^2 x \ ,$$

$$\bar{\gamma}_I(x) = 9.408298 - 0.134066 \ \log x + 0.020195 \ \log^2 x \ .$$

The DR of the amplitudes is written

$$
\begin{aligned}
\frac{\text{Re } F(x, t=0)}{2m^2\, x} &= 4\sqrt{\pi}\frac{2}{\pi}\, x\, \mathbf{P} \int_1^{+\infty} \frac{T_I^N(x', t)}{x'^2 - x^2}dx' \\
&= 4\sqrt{\pi}\,\frac{2}{\pi}\, x\, \mathbf{P} \int_1^{+\infty} \frac{\bar{\alpha}_I(x') + \bar{\lambda}_I(x')}{x'^2 - x^2}dx' \quad .
\end{aligned}
\tag{4.40}
$$

Since the parameters are in GeV^{-2}, to obtain the product $\sigma\rho$ in mb units we multiply the above equation by the factor $(\hbar c)^2 = 0.3894$. Then $(\hbar c)^2\text{Re } F_+/s = \sigma\rho$, and we writte

$$
\sigma\rho = (\hbar c)^2 \Big[4\sqrt{\pi}\frac{2}{\pi}x[(\bar{\alpha}_{I0} + \bar{\lambda}_{I0})I(0, 0, x) + (\bar{\alpha}_{I1} + \bar{\lambda}_{I1})I(1, 0, x) + \bar{\lambda}_{I2}I(2, 0, x)]\Big]
\tag{4.41}
$$

where the function $I(n, \lambda, x)$ is defined in Eq.(2.24). Taking only the first contribution of the Lerch transcendent terms Φ we have the result

$$
\begin{aligned}
\sigma\rho = (\hbar c)^2 \Big\{ & 4\sqrt{\pi}\Big[(\bar{\alpha}_{I1} + \bar{\lambda}_{I1})\frac{\pi}{2} + \bar{\lambda}_{I2}\pi \log x\Big] \\
& + \frac{1}{x}\Big[4\sqrt{\pi}\frac{2}{\pi}(\bar{\alpha}_{I0} + \bar{\lambda}_{I0} - \bar{\alpha}_{I1} - \bar{\lambda}_{I1} + 2\bar{\lambda}_{I2})\Big]\Big\}
\end{aligned}
\tag{4.42}
$$

For $\sqrt{s} \geq 100\,\text{GeV}$, with x of the order 10^4 , the term in $1/x$ is less than 1% of the first part. We can neglect this term for the energies of our interest. The expression for the $\sigma\rho$ product then becomes

$$
\sigma\rho = (\hbar c)^2 4\pi^{3/2}\Big[\frac{\bar{\alpha}_{I1} + \bar{\lambda}_{I1}}{2} + \bar{\lambda}_{I2} \log x\Big] \quad .
\tag{4.43}
$$

Figures 4.21 show the $\sigma\rho$ product and the parameter ρ . Experimental data are included for comparison.

In the LHS of the DR, Eq. (4.41), the form of the real amplitude $T_R(s, 0)$ gives

$$
\sigma\rho = 4\sqrt{\pi}\,(\hbar c)^2 \Big[\bar{\alpha}_{R0} + \bar{\lambda}_{R0} + \big(\bar{\alpha}_{R1} + \bar{\lambda}_{R1}\big) \log x\Big]
\tag{4.44}
$$

Table 4.7: Comparison of parameters between DDR calculations applied to T_I amplitudes and direct fitting results for all examined energies.

DDR	KFK
-1.741716	-1.676787
0.404716	0.392804

Comparing this expression with with the DDR results obtained above, collecting coefficients with the same x dependence in the expressions Eqs. (4.43,4.44) we have:

$$\left(\bar{\alpha}_{I1} + \bar{\lambda}_{I1}\right)\frac{\pi}{2} \Longleftrightarrow \bar{\alpha}_{R0} + \bar{\lambda}_{R0} \tag{4.45}$$

$$\pi \ \bar{\lambda}_{I2} \Longleftrightarrow \bar{\alpha}_{R1} + \bar{\lambda}_{R1} \tag{4.46}$$

In table 4.7 we present the numerical comparison between the DDR results and the real part parameters obtained in fittings of $d\sigma/dt$.

Dispersion Relation for the slopes

We now use the explicit t dependence of the KFK amplitudes. Here we have important difference with the t dependence used in chap 3, whose simple extension of the PDG form is introduced. Taking the derivative of the real amplitude we obtain

$$\frac{\partial \text{Re } F(x,t)}{\partial t}\Big|_{t=0} = 4\sqrt{\pi} \ \frac{2}{\pi} \ s \ x \ \mathbf{P} \int_1^{+\infty} \frac{|\partial T_I^N(x',t)/\partial t|_0}{x'^2 - x^2} dx' \quad . \tag{4.47}$$

Substituting the expressions for the inputs, we have

$$
\begin{aligned}
\frac{\partial \mathrm{Re}\ F(x,t)}{\partial t}\bigg|_{t=0} = 4\sqrt{\pi}\ \frac{2}{\pi}\ s\ x\bigg\{ &\Big[\bar{\alpha}_{I0}\bar{\beta}_{I0} + \frac{3a_0}{4}\bar{\lambda}_{I0}\Big(\bar{\gamma}_{I0} + \frac{7}{6}\Big)\Big] I(0,0,x) \\
&+\Big[\bar{\alpha}_{I0}\bar{\beta}_{I1} + \bar{\alpha}_{I1}\bar{\beta}_{I0} + \frac{3a_0}{4}\Big(\bar{\lambda}_{I0}\bar{\gamma}_{I1} + \bar{\lambda}_{I1}(\bar{\gamma}_{I0} + \frac{7}{6})\Big)\Big] I(1,0,x) \\
&+\Big[\bar{\alpha}_{I1}\bar{\beta}_{I1} + \frac{3a_0}{4}\Big(\bar{\lambda}_{I0}\bar{\gamma}_{I2} + \bar{\lambda}_{I1}\bar{\gamma}_{I1} + \bar{\lambda}_{I2}(\bar{\gamma}_{I0} + \frac{7}{6})\Big)\Big] I(2,0,x) \\
&+\frac{3a_0}{4}\Big[\bar{\lambda}_{I1}\bar{\gamma}_{I2} + \bar{\lambda}_{I2}\bar{\gamma}_{I1}\Big]\ I(3,0,x) + \frac{3a_0}{4}\bar{\lambda}_{I2}\bar{\gamma}_{I2}\ I(4,0,x)\bigg\} \,.
\end{aligned} \tag{4.48}
$$

The contributions from the Φ functions in exact solutions of the PV integrals are very small for large x and the above expression becomes

$$
\begin{aligned}
\frac{\partial \mathrm{Re}\ F_+}{\partial t}\bigg|_{t=0} = 4\sqrt{\pi}\ s\bigg\{ &\Big[\bar{\alpha}_{I0}\bar{\beta}_{I1} + \bar{\alpha}_{I1}\bar{\beta}_{I0} + \frac{3\ a_0}{4}\Big(\bar{\lambda}_{I0}\bar{\gamma}_{I1} + \bar{\lambda}_{I1}(\bar{\gamma}_{I0} + \frac{7}{6})\Big)\Big]\frac{\pi}{2} \\
&+\Big[\bar{\alpha}_{I1}\bar{\beta}_{I1} + \frac{3a_0}{4}\Big(\bar{\lambda}_{I0}\bar{\gamma}_{I2} + \bar{\lambda}_{I1}\bar{\gamma}_{I1} + \bar{\lambda}_{I2}(\bar{\gamma}_{I0} + \frac{7}{6})\Big)\Big]\pi \log x \\
&+\frac{3a_0}{4}\Big[\bar{\lambda}_{I1}\bar{\gamma}_{I2} + \bar{\lambda}_{I2}\bar{\gamma}_{I1}\Big]\frac{\pi}{2}\Big(3\log^2 x + \frac{\pi^2}{2}\Big) + \frac{3a_0}{4}\bar{\lambda}_{I2}\bar{\gamma}_{I2}\ 2\pi\ \log x\Big(\log^2 x + \frac{\pi^2}{2}\Big)\bigg\} \,.
\end{aligned} \tag{4.49}
$$

For the real slope we use the definition

$$
B_R = \frac{2}{\mathrm{Re}\ F(s,0)}\frac{\partial \mathrm{Re}\ F(s,t)}{\partial t}\bigg|_{t=0} \,. \tag{4.50}
$$

To obtain the physical quantities from the second DDR in units of mb GeV^{-2} we multiply the previous equation by $2(\hbar c)^2$ and $(1/s)$. We have

$$
B_R\ \sigma\ \rho = 2\ (\hbar c)^2\ \frac{1}{s}\frac{\partial \mathrm{Re}\ F}{\partial t}\bigg|_{t=0} \tag{4.51}
$$

As the first DDR, the second DDR provide constraint equations between the real and imaginary parameters. To obtain the relations, we write the derivative of the

real amplitude at $t = 0$

$$
\frac{\partial \mathrm{Re}\, F(x,t)}{\partial t}\Big|_{t=0} = 4\sqrt{\pi}\ s\ \left[\alpha_R\ \beta_R + \frac{3a_0}{4}\lambda_R\left(\gamma_R + \frac{7}{6}\right)\right]
$$

$$
= 4\sqrt{\pi}\ s\ \left\{ \bar\alpha_{R0}\bar\beta_{R0} + \frac{3a_0}{4}\lambda_{R0}\left(\bar\gamma_{R0} + \frac{7}{6}\right) \right.
$$

$$
+ \left[\bar\alpha_{R0}\bar\beta_{R1} + \bar\alpha_{R1}\bar\beta_{R0} + \frac{3a_0}{4}\left(\bar\lambda_{R0}\bar\gamma_{R1} + \bar\lambda_{R1}(\bar\gamma_{R0} + \frac{7}{6})\right)\right]\log x
$$

$$
+ \left[\bar\alpha_{R1}\bar\beta_{R1} + \bar\alpha_{R0}\bar\beta_{R2} + \frac{3a_0}{4}\left(\bar\lambda_{R0}\bar\gamma_{R2} + \bar\lambda_{R1}\bar\gamma_{R1}\right)\right]\log^2 x
$$

$$
\left. + \left[\bar\alpha_{R1}\bar\beta_{R2} + \frac{3a_0}{4}\bar\lambda_{R1}\bar\gamma_{R2}\right]\log^3 x \right\}\ , \tag{4.52}
$$

and we follow the same procedure of collecting terms of x dependence

The several terms give

1) constant term

$$
\left[\bar\alpha_{I0}\bar\beta_{I1} + \bar\alpha_{I1}\bar\beta_{I0}\ +\ \frac{3a_0}{4}\left(\bar\lambda_{I0}\bar\gamma_{I1} + \bar\lambda_{I1}\bar\gamma_{I0} + \frac{7}{6}\bar\lambda_{I1}\right)\right]\frac{\pi}{2} + \frac{3a_0}{4}\left[\bar\lambda_{I1}\bar\gamma_{I2} + \bar\lambda_{I2}\bar\gamma_{I1}\right]\frac{\pi^3}{4}
$$

$$
\Updownarrow
$$

$$
\bar\alpha_{R0}\bar\beta_{R0} + \frac{3a_0\lambda_0}{4}\left(\bar\gamma_{R0} + \frac{7}{6}\right))\ , \tag{4.53}
$$

2) $\log x$ term

$$
\pi\left[\bar\alpha_{I1}\bar\beta_{I1} + \frac{3a_0}{4}\left(\bar\lambda_{I0}\bar\gamma_{I2} + \bar\lambda_{I1}\bar\gamma_{I1} + \bar\lambda_{I2}(\bar\gamma_{I0} + \frac{7}{6}) + \bar\lambda_{I2}\bar\gamma_{I2}\pi^2\right)\right] \tag{4.54}
$$

$$
\Updownarrow
$$

$$
\left[\bar\alpha_{R0}\bar\beta_{R1} + \bar\alpha_{R1}\bar\beta_{R0} + \frac{3a_0}{4}\left(\bar\lambda_{R0}\bar\gamma_{R1} + \bar\lambda_{R1}(\bar\gamma_{R0} + \frac{7}{6})\right)\right]\ ,
$$

3) $\log^2 x$ term

$$
\frac{9\pi\, a_0}{8}\left[\bar\lambda_{I1}\bar\gamma_{I2} + \bar\lambda_{I2}\bar\gamma_{I1}\right]
$$

$$
\Updownarrow
$$

$$
\left[\bar\alpha_{R1}\bar\beta_{R1} + \bar\alpha_{R0}\bar\beta_{R2} + \frac{3a_0}{4}\left(\bar\lambda_{R0}\bar\gamma_{R2} + \bar\lambda_{R1}\bar\gamma_{R1}\right)\right] \tag{4.55}
$$

Table 4.8: Comparison of parameters between DDR calculations applied to KFK $\partial T_I/\partial t$ amplitude and direct fitting results for all examined energies.

DDR	KFK
-18.897808	-15.715451
6.726881	4.286346
-0.262464	-0.292835
0.017041	0.016234

4) $\log^3 x$ term

$$\frac{3a_0}{4}2\pi\bar{\lambda}_{I2}\bar{\gamma}_{I2} \Longleftrightarrow \bar{\alpha}_{R1}\bar{\beta}_{R2} + \frac{3a_0}{4}\bar{\lambda}_{R1}\bar{\gamma}_{R2} \ . \tag{4.56}$$

For the second DDR we have 4 equations of constraints for the real and imaginary parameters. In table 4.8 we compare numbers of the real amplitude from fittings with the above DDR calculations. We observe that for high powers of $\log x$ the constraint equations are more approximately obeyed.
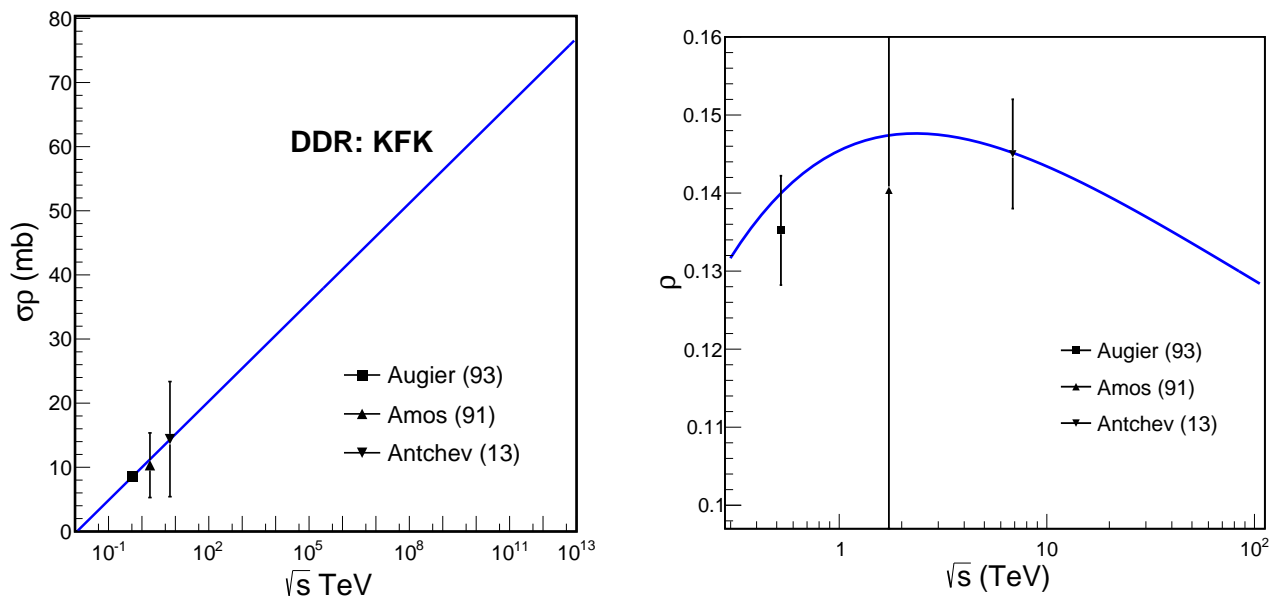
Figure 4.21: The figure on the left shows the product $\sigma\rho$ obtained by exact form of DDR applied to KFK amplitude. The experimental points at 0.546, 1.8 and 7 TeV are show with the respective error bars. The figure on the right show the ratio ρ compared with the experimental points at the same energy as the figure on the left.

4.7   Connection with Pomeron framework

A characteristic aspect in our approach is that there is no explicit use of Pomeron-type phenomenology. In Pomeron framework the total cross section is written [22] as

$$\sigma_{\text{Pom}} = A + B \ (s/s_0)^{0.096}. \tag{4.57}$$

where $\sqrt{s_0}$ is the unit of energy used in determining the coefficients.

On the other hand, the energy dependence of the total cross section obtained from KFK amplitude has the form

$$\sigma = C_0 + C_1 \ln \sqrt{\frac{s}{s_0}} + C_2 \ln^2 \sqrt{\frac{s}{s_0}}, \tag{4.58}$$

and for $\sqrt{s_0} = 1$ TeV, we have

$$C_0 = 69.3286, \quad C_1 = 12.6800, \quad C_2 = 1.2273.$$

After a short algebra, we can rewrite Eq.(4.58) as

$$\sigma = C_0 - \frac{1}{2}\frac{C_1}{C_2} + \frac{1}{2}\frac{C_1^2}{C_2}\left(1 + x + \frac{1}{2}x^2\right) \tag{4.59}$$

where

$$x = \frac{C_2}{C_1} \ln \frac{s}{s_0}. \tag{4.60}$$

As far as $x \ll 1$ (in our case, $\sqrt{s} < 10^4$ TeV), we can write in a limited energy range

$$\sigma \simeq C_0 - \frac{1}{2}\frac{C_1^2}{C_2} + \frac{1}{2}\frac{C_1^2}{C_2}\left(\frac{s}{s_0}\right)^{C_2/C_1}, \tag{4.61}$$

where we have used $e^x \sim 1 + x + x^2/2$ for $x \ll 1$. Inserting the numbers, we get the

Pomeron type expression for our total cross section as

$$\sigma(s) \simeq 3.8259 + 65.5026 \, (s/s_0)^{0.09679}, \tag{4.62}$$

From this, we identify the correspondence of our amplitude with that of Pomeron phenomenology as $A = 3.8259$ and $B = 65.5026$ in Eq.(4.57). The power exponent 0.096 obtained from KFK total cross section agrees with the Pomeron model (4.57) remarkably well.

The above analysis shows that, numerically speaking, the two approaches are perfectly compatible. However, there are few caveats. First of all, the Pomeron amplitude in the power form violates the unitarity, in contrast to our amplitude (that is not power like, but of $\log^2 s$ form). Next, the numerical values of the coefficients in Eq.(4.58) depends on the unit of the energy. If we change the value of s_0, the total cross section has the same energy dependence as the second order polynomial in $\ln s/s_0$, with different values of C_i 's. Thus. the condition $x \ll 1$ leads to the different energy domain, and also the parameters in Eq.(4.62) change. In other words, we always can obtain the Pomeron-like structure for the energy dependence of the total cross section as an effective expansion around certain energy scale.

In Regge phenomenology, in addition to the energy dependence of the total cross section, the Pomeron trajectory specifies also the t dependence, that is the differential cross section. In our case, this is related to the parameters of the forward scattering amplitudes. For sake of simplicity, we neglect the real part, writing

$$T_I(s,t) \simeq T_I(s,0) \, e^{B_{\text{eff}}(s)t/2}, \tag{4.63}$$

where

$$B_{\text{eff}}(s) = 2 \left. \frac{\partial}{\partial t} \ln T_I(s,t) \right|_{t=0}. \tag{4.64}$$

Using the same technique to convert the polynomial in $\ln s/s_0$ into a power form,

we can estimate the Pomeron trajectory, in an approximate way. We will not enter in detain into this, but we find that the Pomeron feature in our amplitude as an effective expression, obtained from an expansion of the amplitude around certain energy scale. Unfortuntely, the domain where there appear evidences of deviation of the power behavior with a fixed exponent from the quadratic polynomical in $\ln s$ is not yet reachable in the present accelerators (10^4 TeV). Perhaps measurements of pp from future cosmic rays experiments can go beyond the energy limit of validity of Pomeron-like models and shows aspects of what is the dynamics of strong interactions due to the 'physical' vacuum.

Chapter 5

Amplitudes in geometric space

In this chapter we describe the b-space amplitudes, discussing their energy dependence. The eikonal representation of KFK amplitudes simplifies the interpretation of the unitarity constraints. We also show that the ratios of integrated cross sections (elastic, inelastic, total) are consequences of the large b behavior of the imaginary amplitude in this space. The behavior depends on the asymptotic form of the SVM which behaves like an Yukawa term. We show that the interpretation of the interaction range is naturally related with the imaginary slope.

5.1   Amplitudes in b-space

The Fourier transform of the momentum transfer $\vec{q}$ amplitudes to the b-space defines the impact parameter (or simply b-space representation). Since the impact parameter variable $\vec{b}$ is not observable, the treatments of data are made in (s, t) space, except for integrated cross sections. However the b-space description gives insight in geometric aspects of the collision, since in the classical limit the variable b reduces to the physical impact parameter. Besides, it plays an important role in the eikonal representation, where unitarity constraints become simpler. On the other hand, the dispersion relation (causality) constraint is properly dealt in t-space. In the following discussion, we do not consider effects of spin or polarization.

As mentioned before the analytic representation of our nuclear amplitude (except for the perturbative three-gluon exchange contribution for large $|t|$ range) has a simpler form in terms of impact parameter space through the Fourier transform,

$$\tilde{T}_K(s,b) = \frac{1}{2\pi} \int d^2\vec{q}\, e^{-i\vec{q}.\vec{b}}\, T_K^N(s,t=-q^2),$$

which is given in closed form as

$$\widetilde{T}_K(s,\vec{b}) = \frac{\alpha_K}{2\beta_K} e^{-b^2/4\beta_K} + \lambda_K \widetilde{\psi}_K(s,b) , \tag{5.1}$$

with the characteristic shape function

$$\widetilde{\psi}_K(s,b) = \frac{2e^{\gamma_K - \sqrt{\gamma_K^2 + b^2/a_0}}}{a_0 \sqrt{\gamma_K^2 + b^2/a_0}} \left[1 - e^{\gamma_K - \sqrt{\gamma_K^2 + b^2/a_0}}\right] . \tag{5.2}$$

Once again, the label $K = R, I$ in Eqs.(5.1,5.2) indicates either the real or the imaginary part of the complex amplitude.

The first term in Eq. (5.1) is like the usual Regge-like term [23]. The second term, referred to as shape function represents contributions from the perturbed vacuum structure around the protons. The shape function $\tilde{\psi}$ normalized as

$$\frac{1}{2\pi} \int d^2\vec{q}\, \tilde{\psi}_K (s,b) = 1 . \tag{5.3}$$

Although b is not exactly the physical impact parameter, the b-space representation permits a geometrical interpretation of the behavior of the amplitude. For large b, which corresponds to peripheral collisions, the amplitudes fall down with a Yukawa-like tail,

$$\sim \frac{1}{b} e^{-b/b_0} , \tag{5.4}$$

that reflects the effects of virtual partons (the modified gluon field) at large distance in the Stochastic Vacuum Model. Another feature of the b-space representation is

that it can be directly related to the eikonal formalism, as shown in another section.

In Figs 5.1 we show the complete and separate contributions (Gaussian and shape) to the real and imaginary amplitudes in b-space. It is remarkable the soft and continuous behavior with the energy. As the energy increases the imaginary amplitude at $b = 0$ approaches the unitarity boundary $\sqrt{\pi}$,reaching saturation. We can observe that this displacement to the unitary boundary is due to the Gaussian contributions. This fact constrain the parameters α_I and β_I with the relation $\sqrt{\pi} = \alpha_I/(2\beta_I)$, which is needed to extrapolate our model to extremely high energies. However, with increasing energy the shape contributions tend to diffuse in impact parameter space. The saturation limit also requires additional constraints between the shape function parameters γ_I and λ_I, but this bound appears in a more involved way. The real part also presents a regular behavior with the energy, but no restriction from unitarity is made.
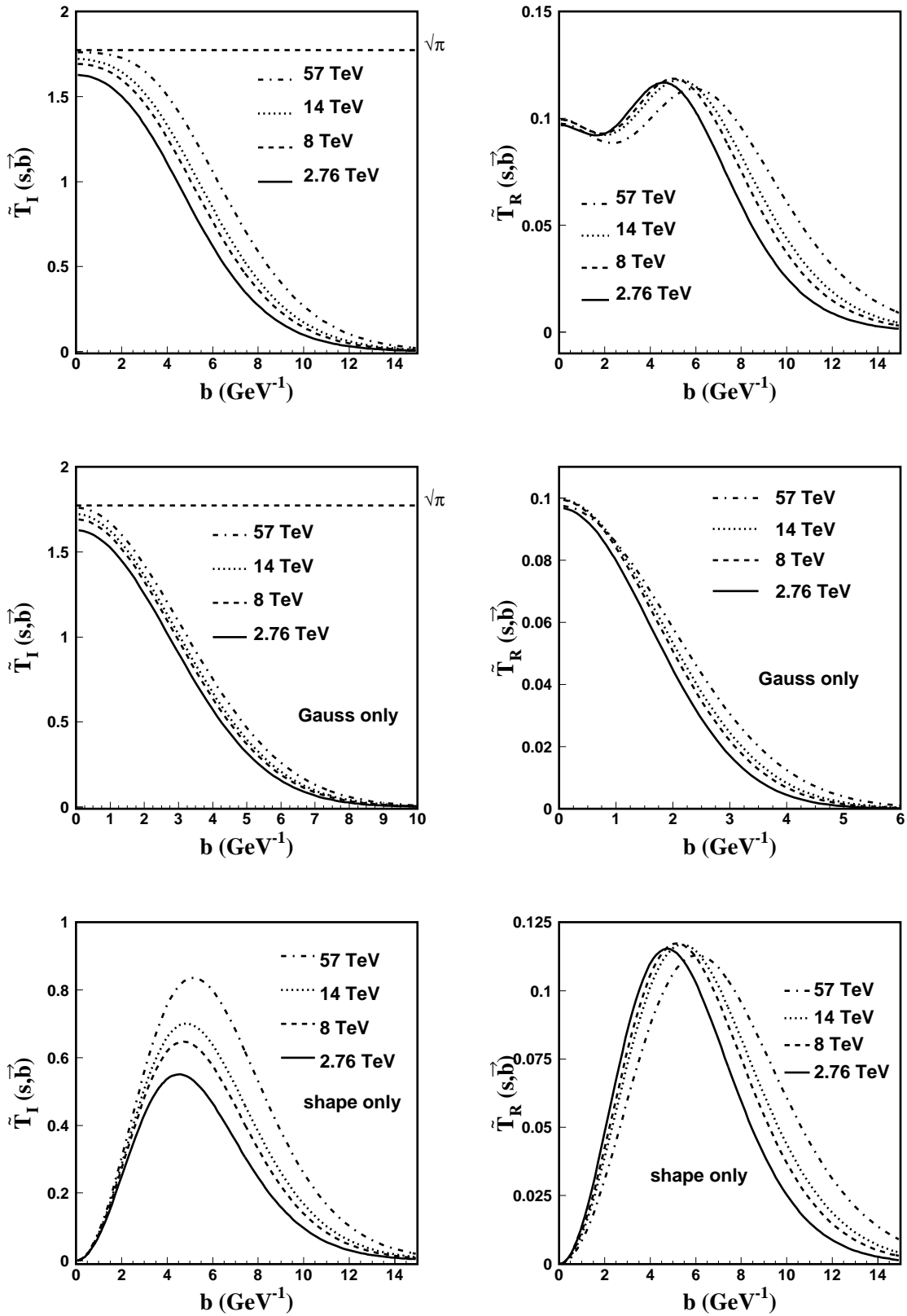
Figure 5.1: The figures on the left show the imaginary amplitude in b-space. The first figure shows the complete imaginary function and the last two show the gaussian and shape contributions respectively. The figures on the right show the real parts, with the first figure being the total contribution and the last two the gaussian and shape respectively.

5.2   Profile functions

The integrated elastic cross section is obtained by integration of elastic differential cross section

$$\sigma_{\text{el}} = \int dt \, \frac{d\sigma_{\text{el}}}{dt} = (\hbar c)^2 \int |T(s,t)|^2 \, dt \; . \tag{5.5}$$

The momentum transfer integration variable is written

$$c^2 d^2\vec{q} \;\; \rightarrow \;\; 2\pi c^2 q dq = \pi c^2 dq^2 = \pi dt \; . \tag{5.6}$$

Using the above equation and writing the Fourier transform of the complex amplitude the elastic cross section is

$$
\begin{aligned}
\sigma_{\text{el}} &= (\hbar c)^2 \frac{1}{\pi} \int c^2 d^2\vec{q} \left| \frac{1}{2\pi} \int d^2\vec{b} \, e^{ic\vec{q}.\vec{b}} \, \tilde{T}(s,\vec{b}) \right|^2 \\
&= (\hbar c)^2 \frac{c^2}{\pi} \frac{1}{(2\pi)^2} \int d^2\vec{b} \, d^2\vec{b}' \int d^2\vec{q} \, e^{ic\vec{q}.(\vec{b}-\vec{b}')} \tilde{T}(s,\vec{b}) \tilde{T}^*(s,\vec{b}') \\
&= \frac{(\hbar c)^2}{\pi} \int d^2\vec{b} \, |\tilde{T}(s,\vec{b})|^2 \\
&= \int d^2\vec{b} \, \frac{d^2\widetilde{\sigma}_{\text{el}}}{d\vec{b}^2} \; ,
\end{aligned}
\tag{5.7}
$$

where we have changed the order of integration between $d^2\vec{q}$ and $d^2\vec{b}$ and made use of the identity $\int d^2\vec{q} \, e^{ic\vec{q}.(\vec{b}-\vec{b}')} = (2\pi/c)^2 \delta^2(\vec{b}-\vec{b}')$. It is then natural to identify the integrands and write

$$\frac{d^2\widetilde{\sigma}_{\text{el}}}{d\vec{b}^2} = \frac{(\hbar c)^2}{\pi} |T(s,\vec{b})|^2 \; . \tag{5.8}$$

($\vec{b}$ is expressed in GeV^{-1}). Using the same procedure to write the total cross section, we write Fourier transform of the imaginary amplitude writing σ_{tot} as

$$\sigma_{\text{tot}} = 4\sqrt{\pi}(\hbar c)^2 \, T_I(s, t = 0) \tag{5.9}$$

$$= \frac{2}{\sqrt{\pi}}(\hbar c)^2 \int d^2\vec{b} \, \tilde{T}_I(s, \vec{b})$$

$$= \int d^2\vec{b} \, \frac{d\widetilde{\sigma}_{\text{tot}}}{d\vec{b}^2} \quad ,$$

and the equality between the integrands gives

$$\frac{d^2\widetilde{\sigma}_{\text{tot}}}{d\vec{b}^2} = \frac{2(\hbar c)^2}{\sqrt{\pi}}\tilde{T}_I(s, \vec{b}) \quad . \tag{5.10}$$

The inelastic cross section is obtained simply by the subtraction

$$\sigma_{\text{inel}} = \sigma_{\text{tot}} - \sigma_{\text{elas}} \tag{5.11}$$

$$= (\hbar c)^2 \int d^2\vec{b} \left(\frac{2}{\sqrt{\pi}}\tilde{T}_I(s, \vec{b}) - \frac{1}{\pi}|\tilde{T}(s, \vec{b})|^2 \right)$$

$$= \int d^2\vec{b} \, \frac{d^2\widetilde{\sigma}_{\text{inel}}}{d\vec{b}^2} \quad ,$$

with

$$\frac{1}{(\hbar c)^2}\frac{d^2\widetilde{\sigma}_{\text{inel}}}{d\vec{b}^2} = \left(\frac{2}{\sqrt{\pi}}\tilde{T}_I(s, \vec{b}) - \frac{1}{\pi}|\tilde{T}(s, \vec{b})|^2 \right) \quad . \tag{5.12}$$

The above equation commonly defines the inelastic profile function

$$G(s, \vec{b}) = \frac{2}{\sqrt{\pi}}\tilde{T}_I(s, \vec{b}) - \frac{1}{\pi}|\tilde{T}(s, \vec{b})|^2 \quad . \tag{5.13}$$

There is no fundamental basis to define $d^2\widetilde{\sigma}/d\vec{b}^2$ functions as genuine differential cross sections in b-space, but, since they behave monotonically and continuously in b, it is natural to relate these profile functions with the geometric dependence of the interaction. In Fig. 5.2 we show the profile functions for a few energies in the LHC domain and up to 57 TeV.
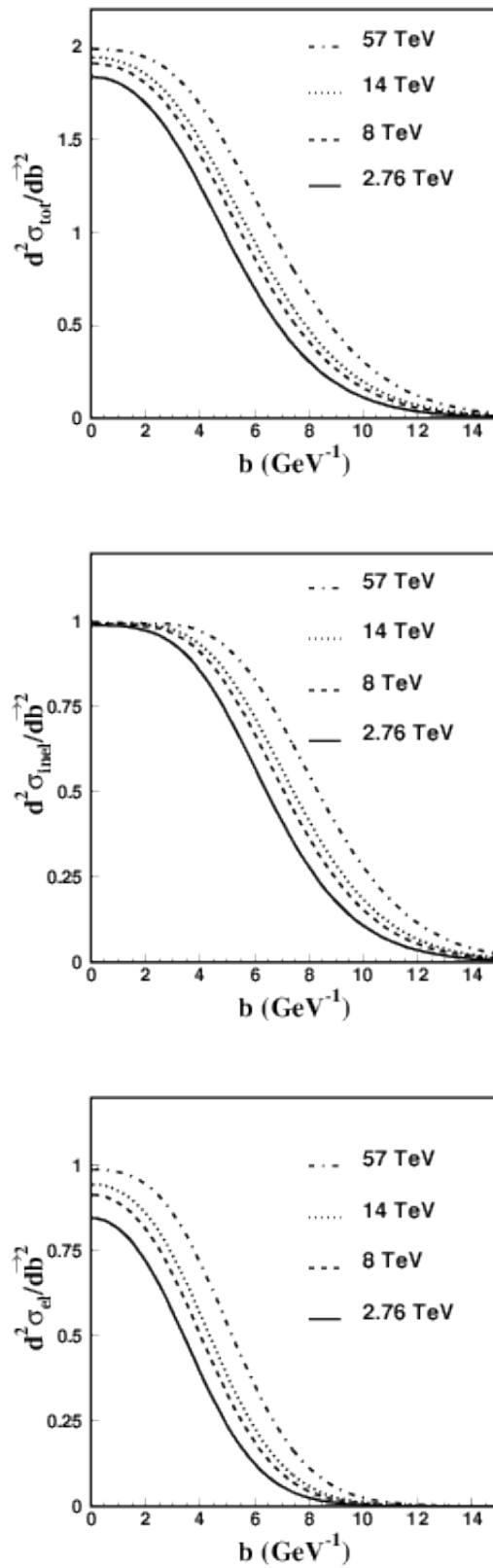
Figure 5.2: In these figures we show the energy evolution of the profile functions, from LHC energy range up to cosmic ray energies. Notice that, as the energy increases, the profile functions tends to saturate. This saturation limit is imposed by unitarity.

5.3 Eikonals

The eikonal treatment is useful for processes involving small scattering angles and very large incoming momentum. This approach is useful because it simplifies the analysis of unitarity as we will see shortly. Another aspect is that many microscopic dynamical models for hadronic scattering are built using this framework. In this sense we can extract the eikonal function from our amplitude in b-space.

We introduce the eikonal function $\chi(s, b)$ through

$$i\sqrt{\pi}\,(1 - e^{i\chi(s,\vec{b})}) \equiv \widetilde{T}(s, \vec{b}) = \widetilde{T}_R(s, \vec{b}) + i\widetilde{T}_I(s, \vec{b}), \tag{5.14}$$

where $\sqrt{\pi}$ is our normalization and the complex function χ is

$$\chi(s, \vec{b}) = \chi_R(s, \vec{b}) + i\chi_I(s, \vec{b}) . \tag{5.15}$$

Separating real and imaginary parts, we have

$$1 - \cos\chi_R\, e^{-\chi_I} = \frac{1}{\sqrt{\pi}}\widetilde{T}_I(s, \vec{b}), \tag{5.16}$$

$$\sin\chi_R\, e^{-\chi_I} = \frac{1}{\sqrt{\pi}}\widetilde{T}_R(s, \vec{b}). \tag{5.17}$$

From Eq. (5.17) we have immediately the inequality

$$e^{-2\chi_I} \geq \frac{1}{\pi}\widetilde{T}_R^2(s, \vec{b}), \tag{5.18}$$

and thus the general unitarity constraint is written as

$$\frac{\widetilde{T}_R^2}{\pi} \leq e^{-2\chi_I(s,\vec{b})} \leq 1 , \tag{5.19}$$

or

$$0 \leq \chi_I \leq -\frac{1}{2}\log(\widetilde{T}_R^2/\pi) .$$

Models with only imaginary amplitude have no superior limit for the imaginary eikonal. In our case, as can be seen in Fig.5.3, our solutions for all energies, obey the bound condition imposed by the real part. Satisfying a monotonic behavior of the scattering amplitudes, our solutions are restricted to the branch where $\chi_R \geq 0$, and thus, in turn, we have

$$0 \; \leq \; \widetilde{T}_I(s, \vec{b}) \leq \sqrt{\pi} \;\; , \;\; \forall \; s, b \; . \tag{5.20}$$

Under these conditions, our analysis shows that for a fixed $\sqrt{s}$, the function $\widetilde{T}_I(s, \vec{b})$ is monotonically decreasing in b. As mentioned before, the maximum of the imaginary amplitude, $\widetilde{T}_I(s, \vec{b} = 0)$ tends to its limiting value $\sqrt{\pi}$ for asymptotic large energies [21]. In Table 5.1 we present characteristic values of amplitudes and eikonals at $b = 0$ for different energies.

In terms of the eikonal function, we write

$$\frac{d^2\widetilde{\sigma}_{\text{el}}}{d\vec{b}^2}(s, \vec{b}) \;\; = \;\; 1 - 2\cos\chi_R e^{-\chi_I} + e^{-2\chi_I}, \tag{5.21}$$

$$\frac{d^2\widetilde{\sigma}_{\text{tot}}}{d\vec{b}^2}(s, \vec{b}) \;\; = \;\; 2\left(1 - \cos\chi_R e^{-\chi_I}\right) \tag{5.22}$$

$$\frac{d^2\widetilde{\sigma}_{\text{inel}}}{d\vec{b}^2}(s, \vec{b}) \;\; = \;\; 1 - e^{-2\chi_I}. \tag{5.23}$$

The functions above are useful because of its soft evolution with the energy and the simplicity of the analytical forms. They do not present complicated structures of dips or bumps as the amplitudes in t-space do, as can be seen in Fig. 5.2. We will see in the next section that the way these functions go to zero for large b is directly associated with the asymptotic behavior of the integrated cross sections.
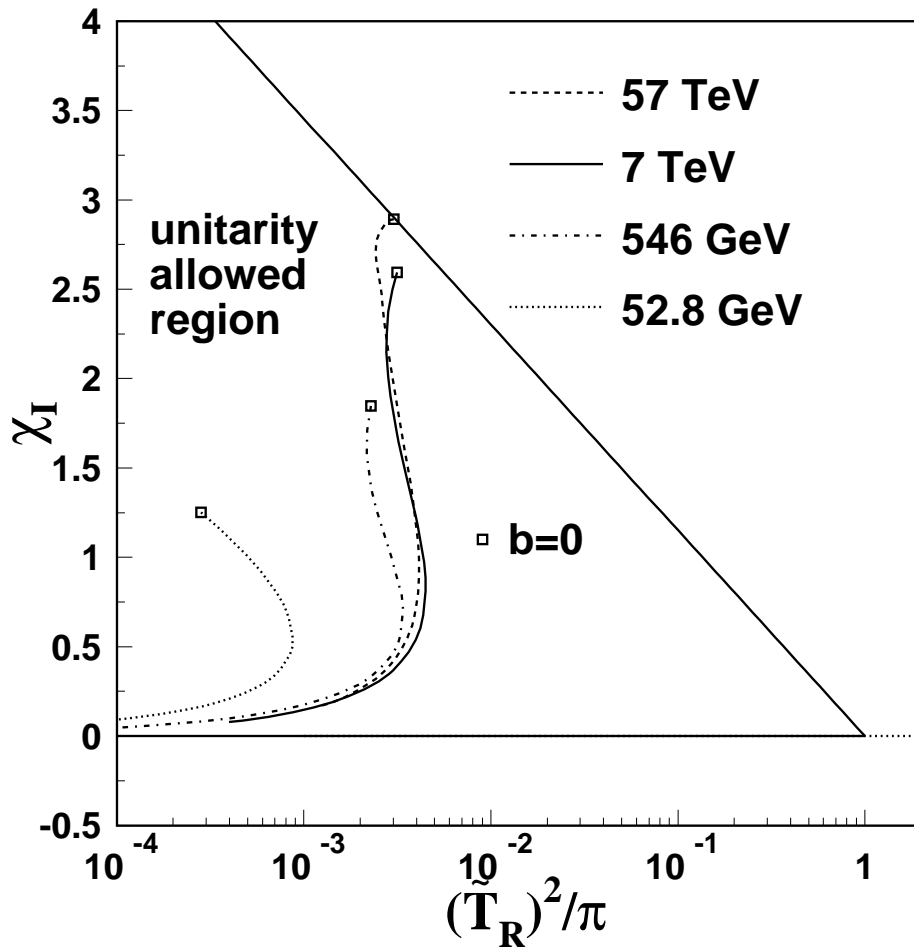
Figure 5.3: We introduce a new map of unitarity constraint of the amplitudes. This bound is shown in eikonal representation taking into account the presence of the real amplitude. Notice that at 57 TeV the amplitudes begin to saturate the unitary bound.

Table 5.1: Characteristic values of b-space amplitudes and eikonal functions. These quantities are related to the saturation of unitarity bounds. Thus $\widetilde{T}_I(b = 0)$ approaches the bound $\sqrt{\pi} = 1.77$ as $\sqrt{s}$ increases.

$\sqrt{s}$ (TeV)	$\widetilde{T}_I(b=0)$	$\widetilde{T}_R(b=0)$	$\chi_I(b=0)$	$\chi_R(b=0)$
1.8	1.5992	0.0947	2.1945	0.5004
2.76	1.6281	0.0969	2.3219	0.5910
7	1.6849	0.0993	2.5939	0.8482
8	1.6923	0.0995	2.6299	0.8927
13	1.7176	0.0997	2.7460	1.0678
14	1.7212	0.0997	2.7611	1.0958

5.4 Geometric scaling and ratio of cross sections

In Fig. 5.4-a, we plot $d^2\sigma_{\text{inel}}/d\vec{b}^2$ defined in Eq. (5.23) as function of b for $\sqrt{s} = 2.76$ and 14 TeV. The behavior at very high energies ($\sqrt{s} = 10^4, 10^5$ and 10^6 TeV) is also shown. We clearly see the increase of effective radius of the interaction range with increasing energy. One can observe that for extremely high energies the profile functions keep form unchanged. This is the scaling behavior advocated by J. Dias de Deus [97] long time ago. In Fig. 5.4-b, we plot the same quantities with respect to the combined variable

$$x \equiv \frac{b}{\sqrt{\sigma\left(s\right)/2\pi}} \; , \qquad (5.24)$$

which we call scale variable. This figure shows clearly that there exist a universal function $\xi\left(x\right)$ such that

$$\frac{d^2\sigma_{\text{inel}}}{d\vec{b}^2}(s,b) \to \xi\left(x\right) \qquad (5.25)$$

for $\sqrt{s} \gg 10^4$ TeV. An important point is that $\xi\left(x\right)$ is far from the Heaviside step function, rather possessing a diffused skin. In this asymptotic limit, we can safely set $\cos\chi_R \to 1$ so that the 'partial' total cross section is [21]

$$\frac{d^2\sigma}{d\vec{b}^2}\left(s,b\right) \to 2\left(1 - \sqrt{1 - \xi(x)}\right). \qquad (5.26)$$

Note that $0 \le \xi \le 1$ means $(1 - \xi) \le \sqrt{1 - \xi}$, so that $\xi\left(x\right) \ge 1 - \sqrt{1 - \xi\left(x\right)}$ for all x where the equality sign holds if and only if $\xi = 0$ or $\xi = 1$. Therefore, whenever the function ξ is different from a sharp-cut Heaviside theta function $\theta\left(1 - x\right)$, we have

$$\frac{\int_0^\infty x \; \xi(x) \; dx}{2\int_0^\infty x \; \left(1 - \sqrt{1 - \xi(x)}\right) \; dx} > \frac{1}{2} \; . \qquad (5.27)$$

For our amplitudes, as shown in Fig. 5.4, ξ clearly does not converge to a sharp-cut θ function, preserving an appreciable diffused surface for asymptotic energies.

Therefore, we have

$$\frac{\sigma_{\text{inel}}(s)}{\sigma(s)} > \frac{1}{2}, \qquad (5.28)$$

or

$$\frac{\sigma_{\text{el}}(s)}{\sigma(s)} < \frac{1}{2}. \qquad (5.29)$$

This means that our amplitudes do not show the black disk behavior at very large energies, deviating from the result for a black disk $\sigma_{\text{el}}(s)/\sigma(s) \to 1/2$. From the above discussion, we can also easily see that the more extended the diffused surface $\xi(x)$ is, the smaller the ratio $\sigma_{\text{el}}(s)/\sigma(s)$ becomes. In fact, in our case this ratio is close to $1/3$ (see also [25]). Note that this is somewhat different scenario compared to [97], where $\xi(x)$ does not have surface diffuseness.

Analytical scaled form of KFK amplitude at high energies

Above, we made use of KFK scaled form to analyse the ratio of integrated cross sections for asymptotic energies. In order to work with an analytical scaled form at high energies we need to make a few approximations. It is know that the integrated quantities are dominated by the forward part of the scattering amplitudes. From Eq.(2.65) we can approximate the imaginary part as

$$
\begin{aligned}
\Psi_I(\gamma_I(s), t) &= 2 \, e^{\gamma_I(s)} \left[\frac{e^{-\gamma_I(s)\sqrt{1+a_0|t|}}}{\sqrt{1+a_0|t|}} - e^{\gamma_I(s)} \frac{e^{-\gamma_I(s)\sqrt{4+a_0|t|}}}{\sqrt{4+a_0|t|}} \right] \\
&\simeq 2 \, e^{\gamma_I(s)} \left[\frac{e^{-\gamma_I(s)(1+\frac{a_0}{2}|t|)}}{(1+\frac{a_0}{2}|t|)} - e^{\gamma_I(s)} \frac{e^{-\gamma_I(s) \, 2 \, (1+\frac{a_0}{8}|t|)}}{2(1+\frac{a_0}{8}|t|)} \right], \quad (5.30)
\end{aligned}
$$

where we expand the square root terms for small $a_0|t|$. In the denominators in Eq.(5.30) we approximate respectively $(1+a_0|t|/2) \simeq \exp(a_0|t|/2)$ and $(1+a_0|t|/8) \simeq \exp(a_0|t|/8)$ and we re-write the shape function as

$$\Psi_I(\gamma_I(s), t) \simeq 2 \, e^{-[\gamma_I(s)+1] \, \frac{a_0}{2}|t|} - e^{-[2\gamma_I(s)+1] \, \frac{a_0}{8}|t|}. \qquad (5.31)$$

Besides the shape function, the imaginary amplitude given by Eq.(2.64) has a Gaussian term and we write the approximated forward form of Eq.(5.1) in b-space as

$$\widetilde{T}_I(s,\vec{b}) \simeq \frac{\alpha_I}{2\beta_I} e^{-b^2/4\beta_I} + \frac{2\lambda_I}{a_0} \left[\frac{e^{-b^2/[2(\gamma_I+1)a_0]}}{\gamma_I+1} - 2\frac{e^{-2b^2/[(2\gamma_I+1)a_0]}}{2\gamma_I+1} \right] . \qquad (5.32)$$

In order to treat very high energies we use only the highest powers in $\log s$ of the parameters $\alpha_I(s)$, $\beta_I(s)$, $\lambda_I(s)$ and $\gamma_I(s)$ given by Eqs.(4.15), (4.16), (4.21) and (4.19), and write

$$\begin{aligned}\widetilde{T}_I(s,\vec{b}) &\approx \frac{\alpha_{I1}}{2\beta_{I1}} e^{-b^2/(4\beta_{I1}\log(\sqrt{s}))} \\ &+ \frac{2}{a_0}\frac{\lambda_{I2}}{\gamma_{I2}} \left[e^{-b^2/[2\gamma_{I2}\log^2(\sqrt{s})a_0]} - e^{-b^2/[\gamma_{I2}\log^2(\sqrt{s})a_0]} \right] ,\end{aligned} \qquad (5.33)$$

with $\sqrt{s}$ in TeV. Defining the scaling variable

$$y \equiv \frac{b}{\sqrt{2\gamma_{I2}a_0}\log\sqrt{s}} , \qquad (5.34)$$

(which is proportional to the variable x at high energies) we re-write Eq.(5.33)

$$\widetilde{T}_I(s,y) \approx \frac{\alpha_{I1}}{2\beta_{I1}} e^{-\frac{a_0\gamma_{I2}}{2\beta_{I1}}\log\sqrt{s}\ y^2} + \frac{2}{a_0}\frac{\lambda_{I2}}{\gamma_{I2}} \left[e^{-y^2} - e^{-2y^2} \right] . \qquad (5.35)$$

We still have an energy dependent term in Eq.(5.35), but the shape contribution part coming from SVM is completely scaled. For very high energies, say $s > \bar{s}_0$ (where $\bar{s}_0$ is a very high energy value to be chosen), the first part of Eq.(5.35) becomes stable. In this sense we write the above equation

$$\widetilde{T}_I(y) \approx \frac{\alpha_{I1}}{2\beta_{I1}} e^{-\frac{a_0\gamma_{I2}}{2\beta_{I1}}\log\sqrt{s_0}\ y^2} + \frac{2}{a_0}\frac{\lambda_{I2}}{\gamma_{I2}} \left[e^{-y^2} - e^{-2y^2} \right] , \qquad (5.36)$$

as a completely scaled function. In Fig. 5.5 we show $d^2\sigma_{\text{inel}}/d\vec{b}^2(s,y)$ function given by Eq. (5.23) obtained by the replacement of Eq.(5.35) in Eqs.(5.16) and (5.17). It is clear that for very high energies Eq.(5.36) becomes exact.
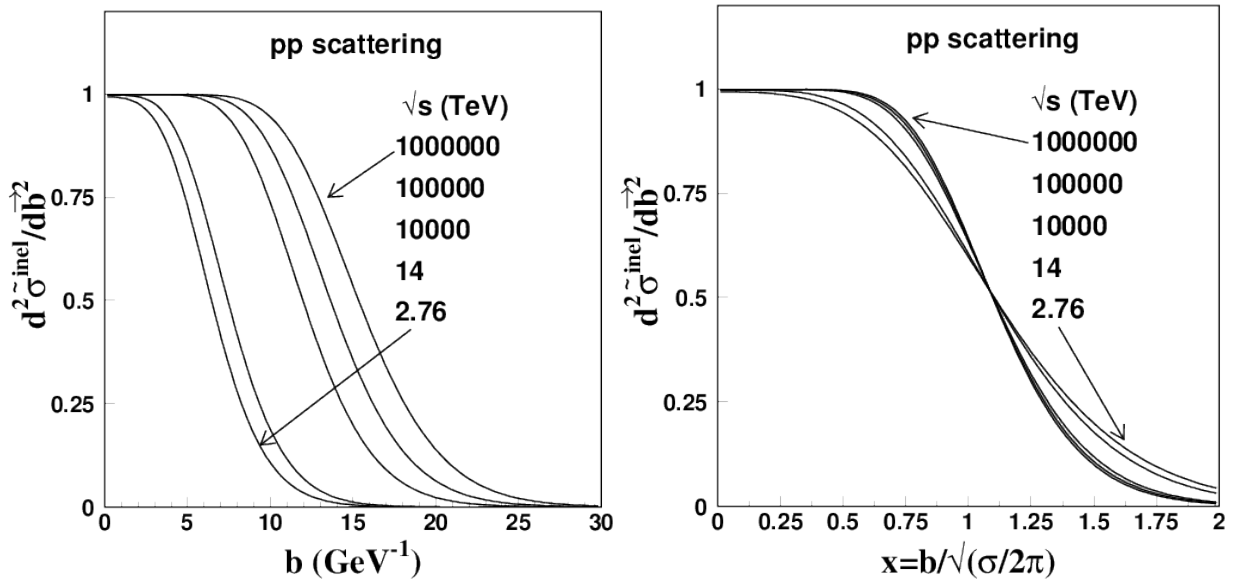
Figure 5.4:   a) Plots of $d^2\sigma_{\text{inel}}/d\vec{b}^2$ as function of b for $\sqrt{s} = 2.76$, 14 TeV and for three very high energies; b) the same functions plotted with scaled variable $x = b/\sqrt{\sigma(s)/2\pi}$, showing the convergence to a unique function, $\xi(x)$ which has a finite surface diffuseness.
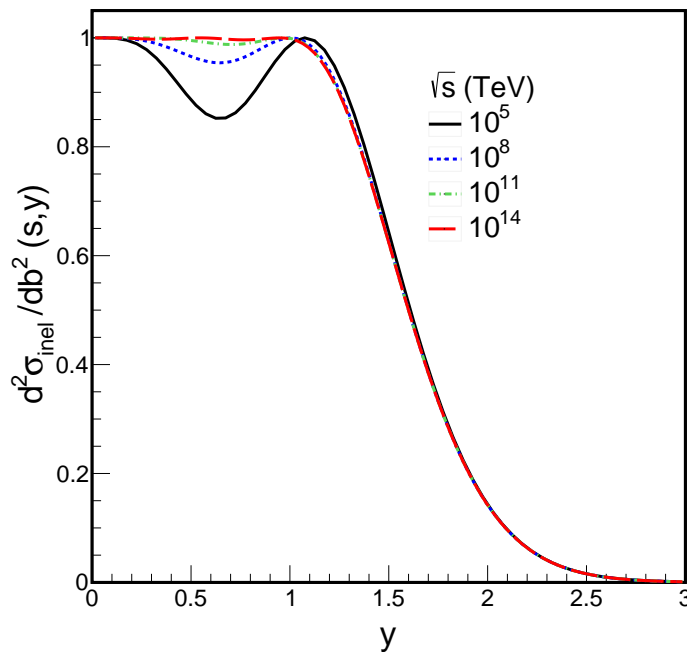
Figure 5.5:   Plots of $d^2\sigma_{\text{inel}}/d\vec{b}^2(s,y)$ analytical form as function of the scaled variable y. It is remarkable that as the energy increases the function approaches the universal scaling form, and for extremely high energies we can safely write $d^2\sigma_{\text{inel}}/d\vec{b}^2(y)$ as an analytical function of a single variable defined as $y \equiv b/(\sqrt{2\gamma_{I2}a_0}\log\sqrt{s})$.

5.4.1 Integrated quantities, ratios and asymptotic limits

In the forward regime, we write the differential cross section in terms of real and imaginary contributions separately as

$$\frac{d\sigma_{\text{el}}^R}{d|t|} \simeq \frac{\sigma^2 \rho^2}{16\pi} e^{-B_R|t|} \qquad , \qquad \frac{d\sigma_{\text{el}}^I}{d|t|} \simeq \frac{\sigma^2}{16\pi} e^{-B_I|t|} \ . \tag{5.37}$$

Although these formulas are valid only in limited range in t, they account for most of the integrated contributions when we integrate them from 0 to infinity. Dividing the results by the total cross section, we obtain:

$$\frac{\sigma_{\text{el}}^R}{\sigma} \simeq \frac{\sigma \rho^2}{16\pi B_R} \qquad , \qquad \frac{\sigma_{\text{el}}^I}{\sigma} \simeq \frac{\sigma}{16\pi B_I} \ . \tag{5.38}$$

The integrated elastic cross section due to the imaginary amplitude can be represented by

$$\sigma_{\text{el}}^I(s) = \int_0^\infty dt\, T_I(s,t)^2 \ dt = 15.3366 + 4.15903 \log \sqrt{s} + 0.43405 \log^2 \sqrt{s} \ , \tag{5.39}$$

with $\sqrt{s}$ in TeV and $\sigma_{\text{el}}^I(s)$ in mb. The accuracy of this representation is very good, particularly for energies equal and above 7 TeV . The ratio with the total cross section has a finite asymptotic limit at high energies

$$\sigma_{\text{el}}^I/\sigma \rightarrow 0.354 \ . \tag{5.40}$$

This result is very important for a geometrical description of pp scattering, as it means that pp collision does not follows a black disk form at high energies (see below).

For the contribution of the real part to the elastic cross section the quantity that is related to the exponential behavior in the forward direction, and that presents a finite asymptotic ratio with σ, requires an extra factor $1/\rho^2$. We have the represen-

tation

$$\frac{1}{\rho^2}\sigma_{\text{el}}^R(s) = \frac{1}{\rho^2}\int_0^\infty dt \; T_R(s,t)^2 \; dt = 10.2037 + 2.47691\log\sqrt{s} + 0.23108\log^2\sqrt{s} \; .$$

$$(5.41)$$

The asymptotic ratio is now

$$(1/\rho^2)(\sigma_{\text{el}}^R/\sigma) \to 0.188 \; . \tag{5.42}$$

These ratios participate in the geometric interpretation in b-space representations.

The ratio of the imaginary part $\sigma/(16\pi B_I)$ is studied to investigate the occurrence of black disk behavior (assuming zero real part), where the ratios $\sigma_{\text{el}}^I/\sigma$ and $\sigma/(16\pi B_I)$ are both equal to 1/2. As shown in Fig. 5.6 our solutions lead to values about 1/3 for the imaginary part case, which is a more realistic expectation [25] than the black disk hypothesis.
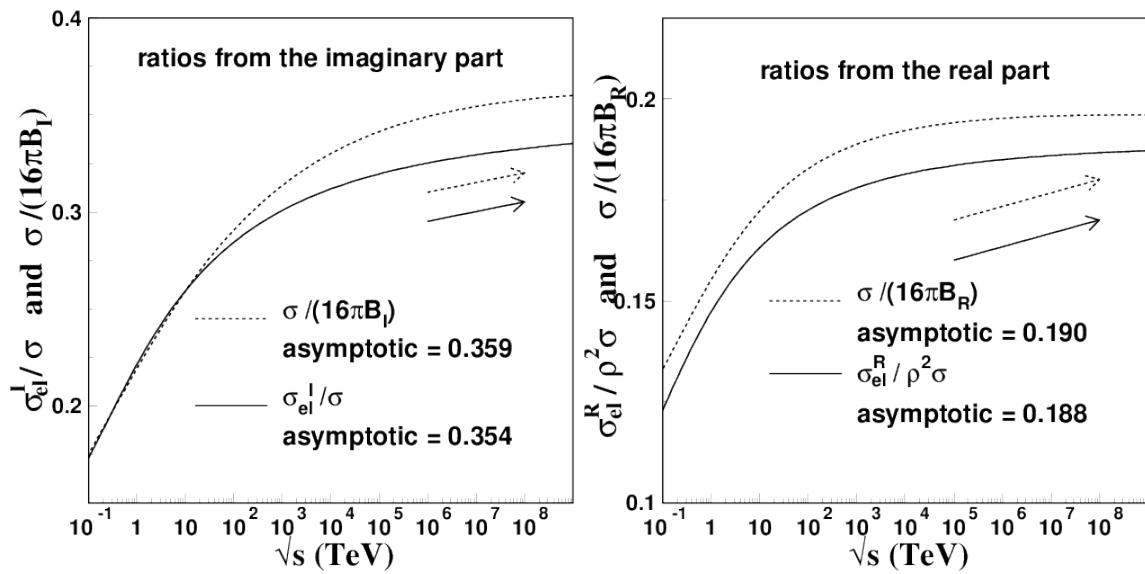
Figure 5.6: Ratio between integrated (imaginary part) elastic cross section and total cross section and ratio between total cross section and imaginary slope as function of energy. On the RHS, the same for the real sector. The asymptotic limits are approached very slowly : observe the extended energy scale. For each part (Imaginary or Real) the two kinds of ratio would be the equal if the amplitudes were of purely exponential form. We may observe that the ratio of ratios in each sector (I or R) ir about the same, namely $0.359/0.354 \approx 0.190/0.188 \approx 1.01$.

5.5   Interaction range and slope $B_I(s,t)$

In impact parameter representation th imaginary slope plays an important role in the interpretation of the interaction range. The imaginary slope is defined as

$$B_I(s) = - \left[\frac{2}{T_I(s,t)} \frac{d}{dt} T_I(s,t) \right]_{t=0} . \qquad (5.43)$$

The corresponding amplitude is written as Fourier transform in b space

$$T_I(s,t) = \int b \; db \; J_0(\sqrt{t}b) \; \tilde{T}_I(s,\vec{b}) . \qquad (5.44)$$

Taking the first derivative with respect to the momentum transfered we obtain

$$\begin{aligned} \frac{d}{dt} T_I(s,t) &= \int b \; db \; \frac{d}{dt} J_0(\sqrt{t}b) \; \tilde{T}_I(s,\vec{b}) \qquad (5.45) \\ &= \int bdb \frac{-b}{2\sqrt{t}} J_1(\sqrt{t}b) \; \tilde{T}_I(s,\vec{b}) . \end{aligned}$$

The Eq. (5.43) needs to be calculated at $t = 0$, so we approximate $J_1(\sqrt{t}b)$ to first order in t

$$\begin{aligned} \frac{d}{dt} T_I(s,t) &= \int b \; db \; \frac{-b}{2\sqrt{t}} \left(\frac{b\sqrt{t}}{2} \right) \tilde{T}_I(s,\vec{b}) \qquad (5.46) \\ &= -\frac{1}{4} \int db^2 \; b^2 \; \tilde{T}_I(s,\vec{b}) . \end{aligned}$$

Inserting the Eq. (5.46) into Eq. (5.43) we have

$$B_I(s) = \frac{1}{2} \frac{1}{T_I(s,t=0)} \int db^2 \; b^2 \; \tilde{T}_I(s,\vec{b}) . \qquad (5.47)$$

On the other side by Eq. (5.10) we can identify $\tilde{T}_I(s,\vec{b})$ as a kind of distribution of total cross section in b-space. So, Eq. (5.47) can be interpreted as a average of b^2 with weight function $\frac{1}{(\hbar c)^2} \frac{d\sigma_{tot}}{d^2\vec{b}}$.

Using Eq. (5.9) we can write Eq.(5.47) as

$$
\begin{aligned}
B_I(s) &= \frac{1}{2}\left(\int db^2\, b^2\, \frac{d\sigma_{tot}}{d^2\vec{b}}\right)\Bigg/\left(\int db^2\, \frac{d\sigma_{tot}}{d^2\vec{b}}\right) \\
&= \frac{1}{2}\langle b^2\rangle.
\end{aligned}
\tag{5.48}
$$

In other words, we can identify the imaginary slope as a measurement of the average impact parameter squared, which is related with the interaction range. The total cross section grows with $\log^2\sqrt{s}$ and by geometric arguments $\sigma_{\text{tot}}(\sqrt{s})$ should be proportional to $\langle b^2\rangle$ what means that $\langle b^2\rangle$ should also be proportional to $\log^2\sqrt{s}$ at high energies. So, it is natural to expect for large energies the behavior $B_I(s)\sim\log^2\sqrt{s}$. This behavior will be important for cosmic ray energies where one can estimate the pp total cross section by extracting the information from p-air collisions using the Glauber formalism. This formalism uses as an input the total cross section and the slopes. In general this slope is assumed to behave as $B_I(s)\sim\log\sqrt{s}$ which clearly will provide a wrong estimation for the pp total cross section.

Chapter 6

Proton-air scattering

Proton-nucleus collisions occurs when extremely energetic particles coming from somewhere in the universe enter in the atmosphere. It is well known that the atmosphere is composed of 70% nitrogen and 20% oxygen approximately. We focus this chapter in the collisions between protons and these abundant elements. The collision between protons and nuclei at high energies gives rise to an Extensive Air Shower (EAS) of hadrons and leptons that reach the ground, being observed by the detectors of the experiments [27–34] . From these measurements the forward inelastic p-air cross sections are estimated.

Previously we have established a full $F(s, t)$ elastic scattering amplitude of pp that allows safe interpolations and extrapolations required in the present era of expansion of the energy frontier. After successful reproduction of the data in the energy frontier of accelerator physics at the $\sqrt{s} = 7$ TeV and 8 TeV energies of LHC, we direct our efforts to the examination of the cosmic ray data extracted from studies of EAS, where there is access to pp center of mass energies of up to 100 TeV. We feel that we start to approach the asymptotic regime where we hope to find the simplified dynamical description of elastic and diffractive processes in which the proton enters as a global object, determining the main features of the observables through its size and the modification of the QCD vacuum around it. In this high

energy regime we may find the ideal conditions for the application of our amplitudes.

We want to compare the p-air production cross section, calculated by Glauber model, with our representation of pp scattering as input, to the experimental values obtained from the available cosmic ray data. We are mainly concerned with the energies beyond the LHC experiments but also present results for EAS experiments in the region below 1 TeV.

We also study the behavior expected for the p-air interaction at ultra-high energies, both as continuous extrapolation based on the region of the present data and as consequence of the known properties of the pp amplitudes in b-space.

As mentioned above, our proton-proton scattering amplitudes have been carefully determined, permitting identification of the properties of the real part which is often neglected in calculations at high energies. We here stress again the importance of the difference between the slopes B_I and B_R of the imaginary and real parts. In the present work this detail enters in the application of Glauber formalism to evaluate the connection between p-air and pp cross sections.

Our analysis of energy dependence of amplitudes and observables in pp collisions shows that the total cross section has a neat $\log^2 s$ form [21], as already indicated in several analyses [49]. As an important feature of our results, we obtain for the slopes, both for B_I and B_R, also a $\log^2 s$ dependence. This is new and important finding. Generally accepted idea is that the slope of the differential cross sections varies like simple linear $\log s$, as in Regge phenomenology. Our new result has a crucial effect for the use of Glauber formalism in the analysis of p-air extended showers at the high energies of our concern, since the value of the slope B_I, together with the value of the total cross section, are the basic and strongly influent inputs of the calculation.

For the application of Glauber approach, we basically require information on the amplitudes in forward scattering. In our model these features are easily obtained taking small t limit [20, 21] in our full-$|t|$ treatment. In these conditions the am-

plitudes take simpler exponential forms, and the relevant parameters are confined only to the total cross section σ, the ratio ρ between real and imaginary parts at $t = 0$, and the slopes B_I and B_R of each of the two parts. We provide the energy dependence of these quantities with simple analytical forms that are appropriate for the whole energy range from 50 GeV to 100 TeV. With these forms at hand, we investigate the behavior of quantities that are meaningful for the investigation of important features of the interaction in the forward region, and can make predictions for asymptotic energies.

6.1 Glauber formalism

Glauber method [98] provides the basic principles for the calculation of strong interactions with composite systems. It assumes the collision hadron-nucleus as an incoherent sum of individual hadron-hadron scattering. The method first introduced in the treatment of scattering by deuterons was extended to more general nuclei, where the complexity of rescattering processes lead to considerations about the importance of intermediate diffracted states [99] not given as known external inputs. The application of the method to the analysis of proton-air collisions in the EAS [100] gives the basic connection between the cosmic ray data and the hadronic scattering properties. As the basis of Glauber formalism is well know in its standard form, we present here the essential points giving the connection between pp and p-air processes, emphasizing the new features that arise from our treatment of pp amplitudes.

The information on the parameters given in the previous section for the pp interaction enters in the calculation of production cross section $\sigma_{\mathrm{p-air}}^{\mathrm{prod}}$ that is obtained from the analysis of EAS.

Our forward amplitudes $T(s,t)$ show different t behavior in the imaginary and real parts, with different slopes B_I and B_R. By Fourier transform the amplitudes in

b space are

$$\widehat{T}_{\mathrm{pp}}(s,\vec{b}) = \widehat{T}_R(s,\vec{b}) + i\widehat{T}_I(s,\vec{b}) = \frac{\sigma_{\mathrm{pp}}^{\mathrm{tot}}}{4\pi(\hbar c)^2}\left[\frac{\rho}{B_R}e^{-\frac{b^2}{2B_R}} + i\frac{1}{B_I}e^{-\frac{b^2}{2B_I}}\right] . \qquad (6.1)$$

In terms of the eikonal function $\chi(s,\vec{b})$ this is written

$$-i\,\widehat{T}_{\mathrm{pp}}(s,\vec{b}) = 1 - e^{i\chi_{\mathrm{PP}}(s,\vec{b})} \equiv \Gamma_{\mathrm{pp}}(s,\vec{b}) . \qquad (6.2)$$

The term $e^{i\chi_{\mathrm{PP}}(s,\vec{b})}$ represents the S-matrix function in b-space. The optical theorem for pp scattering appears as

$$\sigma_{\mathrm{pp}}^{\mathrm{tot}}(s) = 2\,(\hbar c)^2\,\mathrm{Re}\,\int d^2\vec{b}\,\Gamma_{\mathrm{pp}}(s,\vec{b}) . \qquad (6.3)$$

Analogously, for elastic scattering in the p-air system, we define a quantity $\Gamma_{\mathrm{p-air}}(s,\vec{b})$ that satisfies the optical theorem for the p-air total cross section

$$\sigma_{\mathrm{p-air}}^{\mathrm{tot}}(s) = 2\,(\hbar c)^2\,\mathrm{Re}\,\int d^2\vec{b}\,\Gamma_{\mathrm{p-air}}(s,\vec{b}) . \qquad (6.4)$$

Glauber theory introduces a structure to express $\Gamma_{\mathrm{p-air}}(s,\vec{b})$ in terms of pp scattering amplitudes and reaction matrix elements.

To describe the phenomena in the EAS in Cosmic Ray (CR) observations we need to evaluate the quantity

$$\sigma_{\mathrm{p-air}}^{\mathrm{prod}} = \sigma_{\mathrm{p-air}}^{\mathrm{tot}} - (\sigma_{\mathrm{p-air}}^{\mathrm{el}} + \sigma_{\mathrm{p-air}}^{\mathrm{q-el}}) \qquad (6.5)$$

that is determined experimentally.

For elastic and quasi-elastic processes characterized by momentum transfer $|t|$, a transition matrix element between states i and f, defined with nucleon coordinates

$(\vec{r_1}, ..., \vec{r_A})$ is written

$$T^{fi}_{\text{p-air}}(s, q^2) = \frac{1}{2\pi} \int d^2\vec{b} \, e^{ic\vec{q}.\vec{b}} \int \psi^*_f(\vec{r_1}, ..., \vec{r_A}) \times \tag{6.6}$$

$$\Gamma_{\text{p-air}}(s, \vec{b}, \vec{s_1}, ..., \vec{s_A}) \, \psi_i(\vec{r_1}, ..., \vec{r_A}) \prod_{j=1}^{A} d^3\vec{r_j} \, ,$$

with $\vec{b}$ the p-A impact parameter, $\vec{r_i}$ the position of the nucleon inside the nucleus, $\vec{s_i}$ the projection of $\vec{r_i}$ in the perpendicular collision plane.

Assuming that the i and f states are similar bound nuclei with nucleon densities $\rho_j(\vec{r_j})$, and that there is no correlation between the nucleons in the collision process, we write

$$\psi^*_i(\vec{r_1}, ..., \vec{r_A})\psi_i(\vec{r_1}, ..., \vec{r_A}) = \prod_{j=1}^{A} \rho_j(\vec{r_j}) \, , \tag{6.7}$$

where $\rho_j(\vec{r_j})$ is the density of the nucleon i in the nucleus.

For atoms with atomic numbers A less than or equal 18 typically present in the atmosphere the nuclear densities can be described by harmonic potentials with s and p orbitals $\rho_s(\vec{b})$ and $\rho_p(\vec{b})$ that are introduced explicitly [101] as

$$\rho_s(\vec{r}) = \frac{1}{\pi^{3/2}b_0^3} e^{-r^2/b_0^2} \tag{6.8}$$

$$\rho_p(\vec{r}) = \frac{2r^2}{3\pi^{3/2}b_0^5} e^{-r^2/b_0^2} \, ,$$

normalized to unity

$$\int d^3\vec{r} \, \rho_{s,p}(\vec{r}) = 1 \, . \tag{6.9}$$

The b_0 quantity is related with the averaged radius of the Nucleus target. In this work, for nitrogen and oxigen atoms the parameters are $b_0 = 1.7069$ fm and $b_0 = 1.8133$ fm respectively.

Glauber method introduces for p-A scattering the expression based on product

of S-matrix factors of A independent elementary scattering processes

$$\Gamma_{\text{p-air}}(s, \vec{b}, \vec{s}_1, ..., \vec{s}_A) = 1 - \prod_{j=1}^{A} \left[1 - \Gamma_{\text{pp}}(s, |\vec{b} - \vec{s}_j|)\right] . \qquad (6.10)$$

This is the assumption of a factorization property for the p-A system..

Then the expression for the transition matrix element becomes

$$T^{fi}_{\text{p-air}}(s, q^2) = \frac{1}{2\pi} \int d^2\vec{b} \; e^{ic\vec{q}.\vec{b}} \int \psi_f^*(\vec{r_1}, ..., \vec{r_A}) \times \qquad (6.11)$$

$$\left[1 - \prod_{j=1}^{A} \left[1 - \Gamma_{\text{pp}}(s, |\vec{b} - \vec{s}_j|)\right]\right] \psi_i(\vec{r_1}, ..., \vec{r_A}) \prod_{j=1}^{A} d^3\vec{r_j}$$

The quantity that enters Eq. (6.4) for the evaluation of the total p-air cross section is

$$\Gamma_{\text{p-air}}(s, \vec{b}) = 1 - \prod_{j=1}^{A} \int d^3\vec{r_j} \; \rho_j(\vec{r_j}) \left[1 - \Gamma_{\text{pp}}(s, |\vec{b} - \vec{s}_j|)\right] . \qquad (6.12)$$

The sum of elastic and quasi-elastic processes is given by

$$\sigma^{\text{el}}_{\text{p-air}} + \sigma^{\text{q-el}}_{\text{p-air}} = (\hbar c)^2 \int \sum_f |T^{fi}_{\text{p-air}}(s, q^2)|^2 \; d^2\vec{q} \qquad (6.13)$$

$$= (\hbar c)^2 \int d^2\vec{b} \int \left|1 - \prod_{j=1}^{A}(1 - \Gamma_{\text{pp}}(s, |\vec{b} - \vec{s}_j|))\right|^2 \prod_{k=1}^{A} \rho_k(\vec{r_k}) \; d^3\vec{r_k} .$$

The last line of Eq. (6.13) makes use of the orthogonality condition

$$\int \psi_f^*(\vec{r_1}, ..., \vec{r_A}) \psi_i(\vec{r_1}, ..., \vec{r_A}) \prod_{j=1}^{A} d^3\vec{r_j} = 0 , \qquad (6.14)$$

and the completeness relation

$$\sum_f \psi_f^*(\vec{r_1}, ..., \vec{r_A}) \psi_f(\vec{r_1}, ..., \vec{r_A}) \prod_{j=1}^{A} d^3\vec{r_j} = 1 . \qquad (6.15)$$

Taking the product of Eq.(6.13) over the nuclear densities, with 4 nucleons in s shell and A-4 in p shell, we have

$$\sigma_{\mathrm{p-air}}^{\mathrm{el}} + \sigma_{\mathrm{p-air}}^{\mathrm{q-el}} = (\hbar c)^2 \int d^2\vec{b} \ \times \qquad (6.16)$$

$$\left\{ 1 - 2\mathrm{Re} \left[\left[\int d^3\vec{r}(1 - \Gamma_{\mathrm{pp}}(\vec{b} - \vec{s}))\rho_s(r) \right]^4 \left[\int d^3\vec{r}(1 - \Gamma_{\mathrm{pp}}(\vec{b} - \vec{s}))\rho_p(r) \right]^{A-4} \right] \right.$$

$$+ \ \left[\int d^3\vec{r}(1 - 2\mathrm{Re} \ \Gamma_{\mathrm{pp}}(\vec{b} - \vec{s}) + |\Gamma_{\mathrm{pp}}(\vec{b} - \vec{s})|^2)\rho_s(\vec{r}) \right]^4 \ \times$$

$$\left. \left[\int d^3\vec{r}(1 - 2\mathrm{Re} \ \Gamma_{\mathrm{pp}}(\vec{b} - \vec{s}) + |\Gamma_{\mathrm{pp}}(\vec{b} - \vec{s})|^2)\rho_p(\vec{r}) \right]^{A-4} \right\} \ .$$

We thus follow Glauber formalism [98] in general lines, extended with the inclusion of the real part of pp amplitude, where the slopes B_R and B_I are independent. We consider also the effect of the contributions of intermediate diffractive states according to Good-Walker [99], taking to account only the single diffractive channel as the simplest source of inelastic screening as in [27]. The assumption is made that the single diffractive amplitude squared, normalized by the single diffractive integrated cross section is equal the elastic scattering amplitude squared, divided by the integrated elastic cross section,

$$\frac{1}{\sigma_{\mathrm{pX}}^{\mathrm{SD}}(s, M^2)}|\Gamma_{\mathrm{pX}}(s, \vec{b})|^2 = \frac{1}{\sigma_{\mathrm{pp}}^{\mathrm{elas}}(s)}|\Gamma_{\mathrm{pp}}(s, \vec{b})|^2 \ , \qquad (6.17)$$

with $\Gamma_{\mathrm{pX}}(s, \vec{b})$ the single diffractive scattering amplitude, $\sigma_{\mathrm{pX}}^{\mathrm{SD}}(s, M^2)$ the single difractive cross section and M^2 is the upper mass limit of the single particle dissociated from the proton. The ratio between single diffractive and elastic cross sections defines the parameter $\lambda^2 \equiv \sigma_{\mathrm{pX}}^{\mathrm{SD}}(s, M^2)/\sigma_{\mathrm{pp}}^{\mathrm{elas}}(s)$ which will be usefull to characterize the diffractive states contribution. In spite that the elastic profile function is different from diffractive profile function especially for high energies, the assumption that they are equal is justified when we consider only the low mass diffractive states. To

incorporate the diffractive states one can consider the nucleon states

$$|\mathrm{p}\rangle = \begin{pmatrix} 1 \\ 0 \end{pmatrix} \quad , \quad |\mathrm{p}^*\rangle = \begin{pmatrix} 0 \\ 1 \end{pmatrix} , \tag{6.18}$$

corresponding to proton state and proton excited intermediate state respectively. The elastic scattering amplitude is promoted to a matrix of the form

$$\hat{\Gamma}_{\mathrm{pp}}(s, \vec{b}) = \begin{bmatrix} 1 & \lambda \\ \lambda & 1 \end{bmatrix} \Gamma_{\mathrm{pp}}(s, \vec{b}) . \tag{6.19}$$

To apply this expression in the p-air amplitude we diagonalize it and replace the result in Eq.(6.10) and we obtain

$$\Gamma_{\mathrm{p-air}}(s, \vec{b}, \vec{s}_1, ..., \vec{s}_A) = \tag{6.20}$$
$$1 - \frac{1}{2} \prod_{j=1}^{A} \left[1 - (1 + \lambda)\Gamma_{\mathrm{pp}}(\vec{b} - \vec{s}_j) \right] - \frac{1}{2} \prod_{j=1}^{A} \left[1 - (1 - \lambda)\Gamma_{\mathrm{pp}}(\vec{b} - \vec{s}_j) \right] ,$$

and consequently modify Eqs.(6.4) and (6.16).

The parameter λ is tested with values 0 and 0.5 [27]. The effects of both are not very large, and are compared in Table 6.1 where values obtained at 57 TeV are presented.

Fig. 6.1 shows the influences of the difference of values $B_R \neq B_I$ and of the quantity λ that represents the presence of diffractive intermediate states. As we see, the effects do not appear as large in the plots, increase with the energy, and may become more important as experimental errors and oscillations decrease.

Table 6.1 shows comparative numbers for several cases at the energy 57 TeV, where we see that the effects on values of the p-air cross section are under 1 percent. In the B_R case the weak influence is due to the small ρ value.

Stressing that we provide reliable information on cross sections and amplitude slopes for the pp scattering input, and a proper, although simple, treatment of

Table 6.1: Influences of the quantities λ and B_R in Glauber calculations of $\sigma_{\text{p}-\text{air}}$ at $\sqrt{s} = 57$ TeV. The input parameters are $\sigma = 140.66$ mb, $B_I = 25.33$ GeV^{-2} , $B_R = 39.80$ GeV^{-2} and $\rho = 0.132$. Some data points are included to provide a scale for the importance of the effects in comparison to experimental errors. The effects increase with the energy, and may become important as experimental errors decrease.

λ	B_I	B_R	$\sigma_{\text{p}-\text{air}}^{\text{prod}}$
0.5	25.329	39.796	539.225
0.5	25.329	25.329	536.617
0.0	25.329	39.796	537.547
0.0	25.329	25.329	537.333

Glauber strategy, we believe that our calculations of $\sigma_{\text{p}-\text{air}}^{\text{prod}}$ are worth as a study of the EAS data. Actually, we show in the next section that there is very good coherence between our calculations and the data.
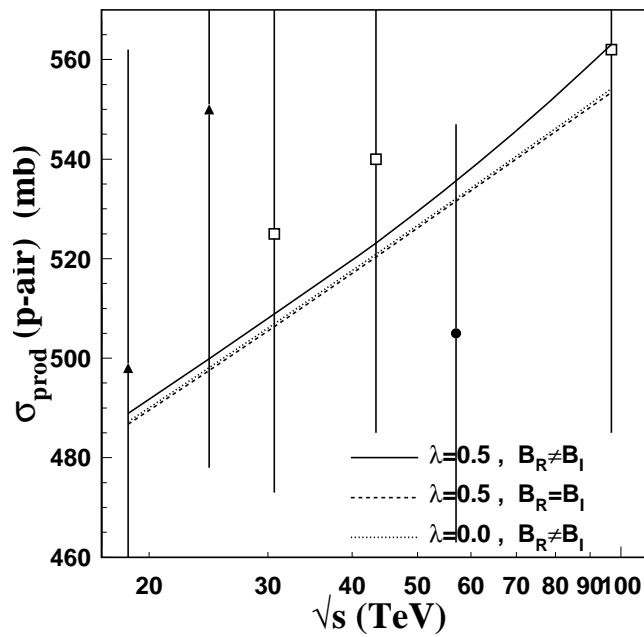
Figure 6.1: Effects of the values of the parameter λ of the Good-Walker concerns with intermediate states and of the difference of values between imaginary and real slopes in Glauber calculation. The solid line represents the standard, supposed to be the best calculation, with $\lambda = 0.5$. The dashed and dotted lines, very close to each other, represent modified calculations putting $\lambda = 0$, in dotted line, and putting $B_R = B_I$, in dashed line. Some data points are shown together to help the information on the magnitude of the effects.

6.2   Comparison with data

Fig. 6.2 shows our calculation of $\sigma^{\mathrm{prod}}_{\mathrm{p-air}}$ with a solid line, together with the data points from experiments with Extensive Air Showers [27–34] . We stress that the calculation is straightforward and unique, without free parameters, made with inputs given by Eqs. (4.24-4.27), that are determined by the elastic differential cross sections at the energies from 20 GeV to 7 TeV. The theoretical curve follows Eq.(6.21) that gives a simple and convenient representation for the calculations and a good reproduction of the data at all energies

$$\sigma^{\mathrm{prod}}_{\mathrm{p-air}} = 383.474 + 33.158 \log \sqrt{s} + 1.3363 \log^2 \sqrt{s} \, , \qquad (6.21)$$

with $\sqrt{s}$ in GeV.

We observe that the data and our calculations of $\sigma^{\mathrm{prod}}_{\mathrm{p-air}}$ increase with the energy with $\log^2 \sqrt{s}$ dependence as the pp cross sections , but more slowly than the pp total cross section. Looking for the comparison of the two rates and for more evidence of regularity in the behavior of the data, we show in Fig. 6.2 the ratio $\sigma^{\mathrm{prod}}_{\mathrm{p-air}}/\sigma$ for a set of selected data (chosen by regularity reasons) together with the energy dependence of our calculations. We observe a regular decrease in the ratio, with a tendency to a finite and distant asymptotic limit, $1.3363/1.2273 = 1.089$ (see Eqs.(6.21) and (4.24)). The importance of the existence of a finite asymptotic limit for this ratio and its numerical value are discussed in a geometric approach in the next section.

We hope that this observation of regularity and interesting energy dependence will estimulates more measurements to identify properties of the hadronic interactions in cosmic ray experiments.
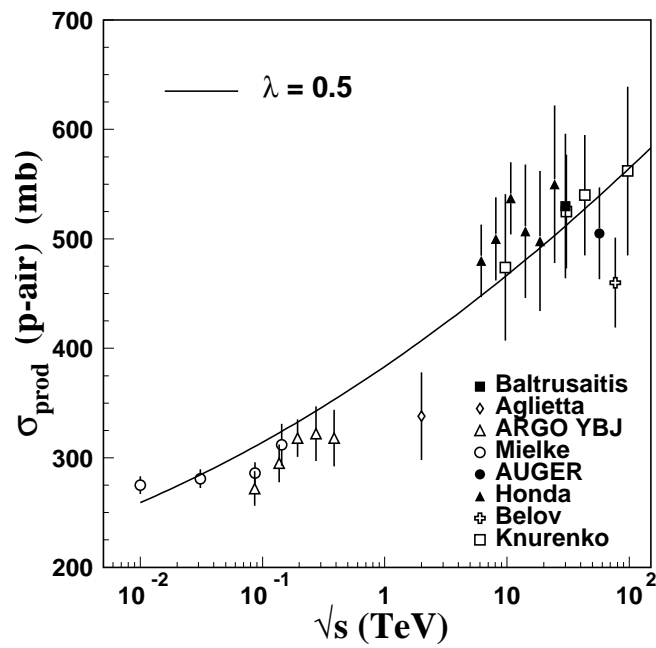
Figure 6.2: Our calculation of the p-air production cross section is represented by the solid line that folows Eq. (6.21). Details are given in the text. The data are from several experiments [27–34]. Both data and calculations increase with the energy with a $\log^2 \sqrt{s}$ form.
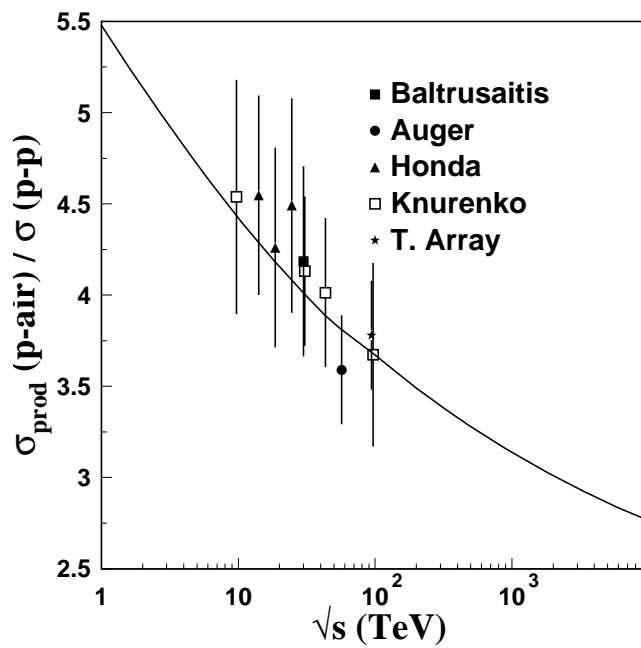
Figure 6.3: Ratio of p-air and pp cross sections. We show our calculation in solid line and open circles together with selected data. We observe regular behavior in the data and variation with the energy, with slow approach towards a finite asymptotic limit. The measured points by the recent Telescope Array experiment [130] comes as a prediction of our calculation.

6.3 Geometric view and asymptotic approach

One of the interesting questions of pA collision cross section is its energy dependence compared to that of pp collision. In this section we use our knowledge of pp amplitudes in $b-$space [21] to estimate this relation. The elastic pp scattering amplitude is

$$-i \, \widehat{T}_{\text{pN}}(s, \vec{b}) = 1 - e^{i\chi(s, \vec{b})} \, , \tag{6.22}$$

where χ is the eikonal function, and the last term is essentially the $S-$matrix in b space. For high energies, b represents essentially the angular momentum, so that χ is (a twice of) the phase shift. In the presence of inelastic channels, χ becomes complex, $\chi = \chi_R + i\chi_I$, and we can define the impact parameter representation of partial cross sections in terms of these functions as

$$\frac{d^2 \sigma_{pp}^{\text{el}}}{d^2 \vec{b}} = 1 - 2 \cos \chi_R e^{-\chi_I} + e^{-2\chi_I}, \tag{6.23}$$

$$\frac{d^2 \sigma_{pp}^{\text{inel}}}{d^2 \vec{b}} = 1 - e^{-2\chi_I}, \tag{6.24}$$

$$\frac{d^2 \sigma_{pp}^{\text{tot}}}{d^2 \vec{b}} = 2 \left(1 - \cos \chi_R e^{-\chi_I} \right). \tag{6.25}$$

At high energies, for the calculation of total and integrated cross sections, we can safely take $\chi_R \to 0$, so that

$$\sigma_{pp}^{\text{el}}(s) \to \int d^2 \vec{b} \left(1 - e^{-\chi_I} \right)^2, \tag{6.26}$$

$$\sigma_{pp}^{\text{inel}}(s) \to \int d^2 \vec{b} \left(1 - e^{-2\chi_I} \right), \tag{6.27}$$

$$\sigma_{pp}^{\text{tot}}(s) \to 2 \int d^2 \vec{b} \left(1 - e^{-\chi_I} \right). \tag{6.28}$$

The Glauber approximation writes the pA S-matrix as a simple product of inde-

pendent scattering centers inside the nucleus,

$$e^{i\chi_{pA}} \simeq \left\langle \prod_{j=1}^{A} e^{i\chi_{pN_j}} \right\rangle \qquad (6.29)$$

where $\langle \rangle$ denotes the average over all nucleon states inside the nucleus and the product $\prod_i$ is taken over the nucleons N_j. Thus, the pA scattering amplitude is

$$-i\widehat{T}_{\mathrm{pA}}(\vec{b}) = 1 - e^{i\chi_{pA}} \simeq 1 - \left\langle \prod_{j=1}^{A} e^{i\chi_{pN_j}} \right\rangle = 1 - \left\langle \prod_{j=1}^{A} \left(1 + i\widehat{T}_{\mathrm{pN}}(\vec{b}) \right) \right\rangle, \qquad (6.30)$$

that leads to equations of last section. Glauber approach gives essentially

$$\frac{1}{2} \frac{d^2 \sigma_{pA}^{\mathrm{tot}}}{d^2\vec{b}}(s,\vec{b}) = \left\langle 1 - \prod_{i=1}^{A} \left(1 - \frac{1}{2} \frac{d^2 \sigma_{pp}^{\mathrm{tot}}}{d^2\vec{b}_i}(s,\vec{b} - \vec{b}_i) \right) \right\rangle, \qquad (6.31)$$

and

$$\frac{d^2 \sigma_{pA}^{\mathrm{el}}}{d^2\vec{b}}(s,\vec{b}) = \left\langle \left[1 - \prod_{i=1}^{A} (1 - \frac{d^2 \sigma_{pp}^{\mathrm{tot}}}{d^2\vec{b}_i}(s,\vec{b} - \vec{b}_i)) \right]^2 \right\rangle. \qquad (6.32)$$

At extremely high energies, where $\sigma_{pp}^{\mathrm{tot}}$ becomes much larger than the target nucleus, geometrical cross section $\sigma_A^{\mathrm{geo}} \equiv \pi R_A^2$, where R_A is the nuclear radius, for example with $\sigma_{pp}^{\mathrm{tot}} \geq 5 \, \sigma_A^{\mathrm{geo}}$, we may neglect the variation in position of each nucleon, so that

$$\frac{1}{2} \frac{d^2 \sigma_{pA}^{\mathrm{tot}}}{d^2\vec{b}}(s,\vec{b}) \simeq 1 - \left(1 - \frac{1}{2} \frac{d^2 \sigma_{pp}^{\mathrm{tot}}}{d^2\vec{b}} \left(s,\vec{b} \right) \right)^A, \qquad (6.33)$$

and

$$\frac{d^2 \sigma_{pA}^{\mathrm{el}}}{d^2\vec{b}} \left(s,\vec{b} \right) \simeq \left[1 - \left(1 - \frac{d^2 \sigma_{pp}^{\mathrm{tot}}}{d^2\vec{b}} \left(s,\vec{b} \right) \right)^A \right]^2. \qquad (6.34)$$

Such situation occurs in our case, for example, at $\sqrt{s} \sim 10^{12}$ TeV, that corresponds the highest energy observed in cosmic ray experiments. In our study of the pp amplitudes in b-space space, we have found for very large energies an approximate

geometric scaling law

$$\frac{1}{2}\frac{d\sigma_{pp}^{\text{tot}}}{d^2\vec{b}}(s,\vec{b}) \rightarrow \zeta(x) ,$$ (6.35)

where

$$x \equiv \frac{b}{b_{\text{eff}}(\sqrt{s})} ,$$ (6.36)

valid for all b at large s, so that

$$\sigma_{pp}^{\text{tot}}(s) \rightarrow 4\pi b_{eff}^2(\sqrt{s})\int_0^\infty x\ \zeta(x)\ dx .$$ (6.37)

If we introduce another function

$$\xi(x) = 1 - [1 - \zeta(x)]^2 ,$$ (6.38)

we obtain

$$\sigma_{pp}^{\text{inel}}(s) \rightarrow 2\pi b_{\text{eff}}^2(\sqrt{s})\int_0^\infty x\ \xi(x)\ dx ,$$ (6.39)

where we have used Eqs. (6.27, 6.28). From Eqs.(6.37, 6.39), we obtain

$$\frac{\sigma_{pp}^{\text{inel}}(s)}{\sigma_{pp}^{\text{tot}}(s)} \rightarrow \frac{\int_0^\infty x\ \xi(x)\ dx}{2\int_0^\infty x\ \zeta(x)\ dx} = \text{const.}$$ (6.40)

Usually, ζ and ξ are functions having a common property,

$$\zeta(x) , \ \xi(x) \rightarrow \begin{cases} 1, & x \rightarrow 0 \\ 0, & x \rightarrow \infty \end{cases} ,$$ (6.41)

When we have the case of a tail as in a black disk

$$\zeta(x) = \theta(1-x) ,$$ (6.42)

then $\xi(x)$ becomes identical with $\zeta(x)$, and we have the ratio

$$\lim_{s\to\infty}\frac{\sigma_{pp}^{\text{inel}}(s)}{\sigma_{pp}^{\text{tot}}(s)}=\frac{1}{2}\,, \tag{6.43}$$

that is a well known result for the black disk.

Generally, $\zeta(x)$ is not a sharp-cut theta function as in Eq. (6.42) but stays unity up to a certain value of x (that is $x=1$, $b=b_{eff}(\sqrt{s})$), then monotonically decreases to zero with a tail form. We can then choose to write

$$\zeta(x)=\begin{cases} 1, & x\leq 1 \\ \Phi(x), & x>1 \end{cases}\,, \tag{6.44}$$

where $\Phi(x)$ is a positive and monotonically decreasing function with $\Phi(1)=1$.

Let us now turn to the pA case. From Eqs. (6.33, 6.34), we have

$$\frac{1}{2}\sigma_{pA}^{\text{tot}}(s)=2\pi b_{eff}^{2}\left(\sqrt{s}\right)\int_{0}^{\infty}x\,dx\left[1-(1-\zeta(x))^{A}\right]\,, \tag{6.45}$$

and

$$\sigma_{pA}^{\text{el}}(s)=2\pi b_{eff}^{2}\left(\sqrt{s}\right)\int_{0}^{\infty}x\,dx\left[1-(1-\zeta(x))^{A}\right]^{2}\,, \tag{6.46}$$

so that, taking the difference $\sigma_{pA}^{\text{tot}}-\sigma_{pA}^{\text{el}}$,

$$\begin{aligned}\sigma_{pA}^{\text{inel}}(s)&=2\pi b_{eff}^{2}\left(\sqrt{s}\right)\int_{0}^{\infty}x\,dx\left[1-(1-\zeta(x))^{2A}\right] \\ &=2\pi b_{eff}^{2}\left(\sqrt{s}\right)\left(1+\int_{1}^{\infty}x\,dx\left[1-(1-\Phi(x))^{2A}\right]\right)\,.\end{aligned} \tag{6.47}$$

Since $0\leq 1-\Phi\leq 1$ for all x, we have $(1-\Phi)^{2A}\leq 1-\Phi$, for $A\geq 1$. Thus we have the inequality

$$\int_{1}^{\infty}x\,dx\left(1-(1-\Phi(x))^{2A}\right)\geq\int_{1}^{\infty}x\,dx\,\Phi(x)\,. \tag{6.48}$$

From this consideration, we arrive at the conclusion that

$$\frac{\sigma_{pA}^{\text{inel}}}{\sigma_{pp}^{\text{tot}}}(s) = \int_0^\infty x \, dx \left[1 - (1 - \zeta(x))^{2A}\right] / \int_0^\infty x \, \zeta(x) \, dx$$

$$\geq 1/2 \,, \tag{6.49}$$

for $\sqrt{s} \to \infty$. Note that in the black disk case $\zeta(x) = \theta(1-x)$, we obtain the well defined limit

$$\sigma_{pA}^{\text{inel}}(s)/\sigma_{pp}^{\text{tot}}(s) \to 1/2 \,.$$

As mentioned before, our phenomenological pp solution does not correspond to the black disk , and the actual pp ratio is $\sigma_{pp}^{\text{inel}}/\sigma_{pp}^{\text{tot}} \to 2/3$. With this information at hand, we look for the value of

$$\sigma_{pA}^{\text{inel}}(s)/\sigma_{pp}^{\text{tot}}(s)$$

using a tail form proper for the realistic pp amplitudes.

6.3.1 Yukawa and exponential tail

The asymptotic behavior of stochastic vacuum model predicts the tail as that of Yukawa type. So, we may choose

$$\zeta(x) = \begin{cases} 1, & x \leq 1 \\ \exp(-\alpha(x-1))/x, & x > 1 \end{cases} \tag{6.50}$$

so that

$$\frac{1}{2}\sigma_{\text{pp}}^{\text{tot}} = 2\pi b_{eff}^2 \left(\sqrt{s}\right) \left(\frac{1}{2} + \frac{1}{\alpha}\right), \tag{6.51}$$

and

$$\xi(x) = \begin{cases} 1, & x \leq 1 \\ 2e^{-\alpha(x-1)}/x - e^{-2\alpha(x-1)}/x^2, & x > 1 \end{cases} \tag{6.52}$$

to obtain

$$\sigma_{\text{pp}}^{\text{inel}} = 2\pi b_{eff}^2 \left(\sqrt{s}\right) \left(\frac{1}{2} + \frac{2}{\alpha} - \int_0^\infty \frac{e^{-2\alpha x}}{x+1} dx\right) \tag{6.53}$$

The relation $\sigma_{\text{pp}}^{\text{inel}}/\sigma_{\text{pp}}^{\text{tot}} = 2/3$ that determines the value of α is then

$$4\left(\frac{1}{2} + \frac{1}{\alpha}\right) = 3\left(1 + \frac{2}{\alpha} - \int_0^\infty \frac{e^{-2\alpha x}}{x+1} dx\right) , \tag{6.54}$$

leading to

$$\alpha \simeq 1.61073 . \tag{6.55}$$

With this, for $A = 15$, for example, we obtain

$$\begin{aligned}
\sigma_{\text{pA}}^{\text{inel}} &= 2\pi b_{\text{eff}}^2 \left(\sqrt{s}\right) \left(1 + \int_1^\infty x \, dx \left(1 - \frac{e^{-\alpha(x-1)}}{x}\right)^{2A}\right) \\
&\simeq 2\pi b_{\text{eff}}^2 \left(\sqrt{s}\right) \times 2.30764 ,
\end{aligned} \tag{6.56}$$

giving

$$\left.\frac{\sigma_{\text{pA}}^{\text{inel}}}{\sigma_{\text{pp}}^{\text{tot}}}\right|_{\text{Yukawa}} \simeq 1.1858 \tag{6.57}$$

for very large s.

This value depends sensitively on the choice of the tail function Φ. The slower the decay of the tail, the bigger the ratio becomes. If we choose Φ as a pure exponential

$$\Phi = e^{-\alpha(x-1)} , \tag{6.58}$$

which has longer tail than the Yukawa type, then using the same procedure we get $\alpha \simeq 2.1583$ and the corresponding value of the ratio becomes

$$\left.\frac{\sigma_{\text{pA}}^{\text{inel}}}{\sigma_{\text{pp}}^{\text{tot}}}\right|_{\text{Exponential}} \simeq 1.798 \tag{6.59}$$

This value can be compared with the energy dependence of the ratio shown in Fig. 6.4

We remark that the quantity b_{eff} that determines the interaction range drops off in the calculated ratios.

6.3.2 Asymptotics is far away

To show how the asymptotic range is approached, Fig. 6.4 shows the calculated (p-air)/pp ratio at extremely high energies, up to $\sqrt{s} = 10^{20}$ TeV, where the values are still decreasing. To see the tendency, we use the values of $\sigma_{\text{p-air}}^{\text{inel}}$ at 10^{12}, 10^{16} and 10^{20} to obtain the form

$$\sigma_{\text{p-air}}^{\text{inel}}(s) = 490.883 + 19.7119 \log \sqrt{s} + 1.8178 \log^2 \sqrt{s} \ . \qquad (6.60)$$

Dividing this function by the $\log^2$ form of the pp total cross section in Eq. (4.24), we obtain the dashed line shown in the figure. We see that the representation of the ratio looks very good above 10^6 TeV. In this parametrization the predicted asymptotic limit is $1.8178/1.2273 = 1.4811$. We would obtain somewhat different limit, had we taken a different set of three energies to construct the form in Eq. (6.60), but the result would remain in the interval 1.4 - 1.5 . The slow convergence of the ratio towards a finite limit at high energies is an important fact.

It is remarkable that there is an impressive confirmation of the limit 1.1858 given in Eq. (6.57), that was determined using as input the 2/3 ratio of inelastic to total pp cross sections and assumption of the Yukawa-like shape in the b dependence of the pp amplitudes.

Eq. (6.60) gives a proper representation of $\sigma_{\text{p-air}}^{\text{inel}}(s)$ to be used for energies higher than $\sqrt{s} \approx 10^6$ TeV. Used at the highest CR experimental energy $\sqrt{s} = 96.85$ TeV it gives a value 10% too high : thus not too bad.

On the other hand, the form given for $\sigma_{\text{p-air}}^{\text{inel}}(s)$ in Eq. (6.21) is based on the three points $\sqrt{s} = 96.85$, 10^3 and 10^4 TeV , and gives very good representation of the exact values from 10 GeV to 10^6 TeV. However, this form is not adequate for

the asymptotic limit.

The good coherence of different evaluations of these finite asymptotic ratios is remarkable. They point out to what can be expected for CR experiments at ultra high energies.
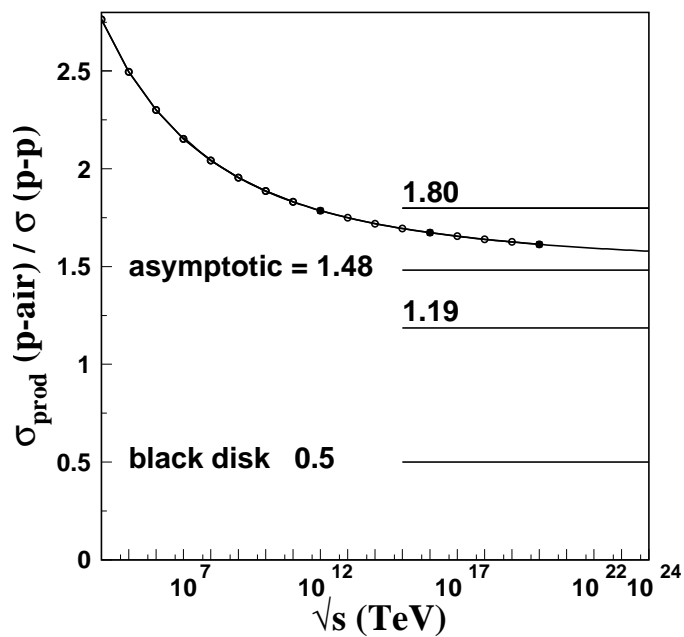
Figure 6.4: Ratio of p-air and pp cross sections at ultra-high energies. Calculations are marked with dots and connected with a continuous line. The line is given analytically by the fraction of $\log^2$ forms for $\sigma_{\mathrm{p-air}}^{\mathrm{inel}}(s)$ and $\sigma_{\mathrm{pp}}^{\mathrm{tot}}(s)$, given in the text. It gives good representation of the points for energies above 10^6 TeV and tends to the asymptotic limit 1.48, as explained in the text.

Chapter 7

Comparative analysis of models

In this chapter we present different models in comparison with our calculations through the point of view of the predictions for the amplitudes, showing similarities and differences.

7.1 BSW

The Bourrely, Soffer and Wu model (BSW model) [102–104] (introduced more than 30 years ago) is an s-channel model built in the geometric b-space within the eikonal framework. The scattering amplitude is written as

$$\mathcal{M}(s,t) = \frac{is}{2\pi} \int d^2\vec{b}\, e^{-i\vec{q}\cdot\vec{b}} \left(1 - e^{-\Omega(s,\vec{b})} \right) \ , \tag{7.1}$$

where Ω is the opacity function (eikonal χ) defined in term of phase shift, Eq.(2.26) as $\Omega(s,\vec{b}) = 2i\delta(s,\vec{b})$. The main feature of the model is the factorization between the energy and the geometric dependence in the eikonal function for high energies

$$\Omega(s,\vec{b}) = \mathcal{S}(s)\, F(b) \ . \tag{7.2}$$

174

For low energies (ISR energy range) the Regge background contributions must be taken into account, and the eikonal is no longer factorized. The s dependence of $\mathcal{S}(s)$ comes from the perturbative field theoretical calculation studies by Cheng-Wu. Working in a massive quantum electrodynamics framework they found that the asymptotic behavior of the scattering amplitude is

$$s^{1+\epsilon}(\ln s)^{-3/2} \; , \tag{7.3}$$

where ϵ is a positive quantity depending on the coupling constant of the theory. Motivated by this result, BSW incorporate this form in the opacity function using the crossing symmetry of quantum field theory, and write the s dependence term as

$$\mathcal{S}(s) = \frac{s^c}{(\log s)^{c'}} + \frac{u^c}{(\log u)^{c'}} \; , \tag{7.4}$$

where s and u are in GeV^2 and the approximation $\log u = \log s - i\pi$ is valid for high energies.

The geometric function is obtained by Fourier transform of the modified eletro-magnetic form factor of proton

$$F(b) = \int_0^\infty dq\, q\tilde{F}(-q^2) J_0(q\,b) \; , \tag{7.5}$$

with

$$\tilde{F}(t) = fG^2(t)\frac{a^2+t}{a^2-t} \qquad \text{and} \qquad G(t) = \frac{1}{(1-t/m_1^2)(1-t/m_2^2)} \; . \tag{7.6}$$

The BSW model assumes the charge distribution inside the proton as proportional to the matter distribution and the interaction term is due to the $\mathcal{S}(s)$ function which gives the real and imaginary amplitudes.

This model uses small number of parameters. There are six energy independent quantities c, c', m_1, m_2, a and f that are given in Table 7.1.

$c = 0.167$	$m_1 = 0.577 \text{GeV}$	$a = 1.858 \text{GeV}$
$c' = 0.748$	$m_2 = 1.719 \text{GeV}$	$f = 6.971 \text{GeV}^{-2}$

Table 7.1: Parameters for the BSW model. Extracted from reference [103].

7.2 HEGS model

The High Energy General Structure (HEGS) model was developed by O. V. Selyugin [105–107] for the description of elastic pp and p$\bar{\text{p}}$ scattering, giving a quantitative description of the data in a wide energy range $9.8 \leq \sqrt{s} \leq 8000 \text{GeV}$ using a small number of fitting parameters. It uses the proton electromagnetic form factors calculated from the General Parton Distributions (GPDs) and assumes, similarly to the BSW model, that the matter distribution is proportional to the charge distribution on the proton.

The hadronic amplitudes are calculated through a unitarization procedure and are written, similarly to Eq. 2.31 and 7.1, in the form

$$F_H(s,t) = \frac{is}{2\pi} \int d^2\vec{b}\, e^{-i\vec{q}\cdot\vec{b}} \left(1 - e^{\chi(s,\vec{b})} \right) \ , \tag{7.7}$$

with the correspondence $\Omega(s,\vec{b}) = -\chi(s,\vec{b})$ (see Eq. 7.2). The microscopic contributions are taken into account in t-space through so-called Born terms $F_h^{\text{Born}}(s,t)$, which are used to form the complex quantity

$$\chi(s,b) = \frac{i}{2\pi} \int d^2\vec{q}\, e^{i\vec{b}\cdot\vec{q}} F_h^{\text{Born}}(s, -q^2) \ . \tag{7.8}$$

The Born amplitude, in the extended version [106] of the model, is written as the sum of three main contributions, two cross-even parts and one possible Odderon term

$$\begin{aligned} F_h^{\text{Born}}(s,t) &= h_1 F_1^2(t) F_a(s,t) \left(1 + \frac{R_1}{\hat{s}^{0.5}} \right) + h_2 A^2(t) F_b(s,t) \\ &\pm h_{\text{odd}}(t) A^2(t) F_b(s,t) \left(1 + \frac{R_2}{\hat{s}^{0.5}} \right) \end{aligned} \tag{7.9}$$

where the $+(-)$ sign is used to compute pp (p$\bar{\text{p}}$) scattering and

$$h_{\text{odd}}(t) = i\,h_3\,t/(1 - r_0^2\,t)^{\cdot}. \tag{7.10}$$

The first two terms in Eq. (7.9) are interpreted by the author, respectively, as a possible Pomeron and a cross-even part of non-pertubative three gluon exchange. There may also be added a fourth contribution due to spin-flip, which is not relevant in the high-energy domain and is not included here. $F_1(t)$ and $A(t)$ are hadronic form factors, parametrized as

$$\begin{aligned} F_1(-q^2) &= \frac{4m_p^2 + \mu\,q^2}{4m_p^2 + q^2}\left(\frac{1}{1 + q/a_1 + q^2/a_2^2 + q^3/a_3^3}\right)^2\,, \\ A(-q^2) &= \frac{\Lambda^4}{(\Lambda^2 + q^2)^2}\,, \end{aligned} \tag{7.11}$$

where $m_p = 0.93827\text{GeV}$ is the proton mass; $F_a(s,t)$ and $F_b(s,t)$ are Regge-like terms

$$F_a(s,t) = \hat{s}^\epsilon\,e^{B(s,t)\,t}, \qquad F_b(s,t) = \hat{s}^\epsilon\,e^{B(s,t)\,t/4} \tag{7.12}$$

with the slope [1]

$$B(s,-q^2) = \left(\alpha + k\frac{q}{q_0}e^{-k\,q^2\,\log\hat{s}}\right)\log\hat{s} \tag{7.13}$$

where $q_0 = 1\text{GeV}$ and $s_0 = 4m_p^2$ set the momentum and energy scale.

The energy dependence appears here and in Eq. (7.9) through the complex quantity

$$\hat{s} = s\,e^{-i\pi/2}/s_0\,. \tag{7.14}$$

This last version of the HEGS model contains seven energy-independent fitting parameters, given in Table 7.2. The parameters kept fixed are given in the same table. The fit is performed simultaneously with the data in the energy range of

---

[1] The slope here does not refer to the traditional definition of the slope in the final hadronic amplitude responsible for the exponential behavior at small$-t$. Here, it accounts for non-linear aspects in the Regge-like terms $F_a(s,t)$ and $F_b(s,t)$ present in the Born amplitude.

$9.8 \leq \sqrt{s} \leq 8000 \text{GeV}.$

fitted parameters			
$h_1 = 3.67 \text{ GeV}^{-2}$	$h_2 = 1.39 \text{ GeV}^{-2}$	$h_3 = 7.51 \text{ GeV}^{-4}$	$k = 0.16 \text{GeV}^{-2}$
$R_1 = 4.45$	$R_2 = 53.7$	$r_0^2 = 3.82 \text{ GeV}^{-2}$	
fixed parameters			
$a_1 = 16.7 \text{ GeV}$	$a_2^2 = 0.78 \text{ GeV}^2$	$a_3^3 = 12.5 \text{ GeV}^3$	$\mu = 2.79$
$\epsilon = 0.11$	$\Lambda^2 = 1.6 \text{ GeV}^2$	$\alpha = 0.24 \text{ GeV}^2$	

Table 7.2: The first two rows show fitting parameters for the extended version of HEGS model. The second two rows give the fixed parameters in data fit of the extended version of HEGS model. These parameters are extracted from reference [106].

7.3 Dynamical Gluon Mass - DGM

Dynamical Gluon Mass [108] is an eikonal model that incorporates semi-hard interaction ingredients as, the microscopic $gg \rightarrow gg$ cross section

$$\hat{\sigma}_{gg}(\hat{s}) = \qquad (7.15)$$
$$\left(\frac{3\pi\bar{\alpha}_s^2}{\hat{s}}\right)\left[\frac{12\hat{s}^4 - 55M_g^2\hat{s}^3 + 12M_g^4\hat{s}^2 + 66M_g^6\hat{s} - 8M_g^8}{4M_g^2\hat{s}[\hat{s} - M_g^2]^2} - 3\ln\left(\frac{\hat{s} - 3M_g^2}{M_g^2}\right)\right],$$

where $\hat{s}$ is the energy fraction of the proton carried by the gluon and

$$\hat{\alpha}_s(\hat{s}) = \frac{4\pi}{\beta_0 \ln[(\hat{s} + 4M_g^2(\hat{s}))/\Lambda^2]} \qquad (7.16)$$

is the running coupling constant (derived by Cornwall [109]) with $\beta_0 = 11 - \frac{2}{3}n_f$ (n_f is the number of flavours) and $\Lambda = \Lambda_{\text{QCD}} = 284$ MeV. The dynamical gluon mass is written

$$M_g^2(\hat{s}) = m_g^2\left[\frac{\ln((\hat{s} + 4m_g^2)/\Lambda^2)}{\ln(4m_g^2/\Lambda^2)}\right]^{-12/11}, \qquad (7.17)$$

where m_g is the mass scale that regularizes the infra-red sector of the gluon propagator. The above formulas transit in two regimes, perturbative and non-perturbative. For large energies $\hat{s} \gg \Lambda$ the mass M_g goes to zero.

The pp and p$\bar{\text{p}}$ elastic scattering eikonals are described in terms of even and odd complex functions

$$\chi_{\text{p}\bar{\text{p}}} = \frac{1}{2}(\chi_{\text{even}} + \chi_{\text{odd}}) \quad , \quad \chi_{\text{pp}} = \frac{1}{2}(\chi_{\text{even}} - \chi_{\text{odd}}) \tag{7.18}$$

composed by the microscopic sub-processes, quark-quark, quark-gluon and gluon-gluon contributions, each of them with the associated overlap function coming from the proton dipole form factor. The even and odd eikonals are respectively

$$
\begin{aligned}
\chi_{\text{even}}(s, b) &= \chi_{qq}(s, b) + \chi_{qg}(s, b) + \chi_{gg}(s, b) \\
&= i[\sigma_{qq}(s)W(b; \mu_{qq}) + \sigma_{qg}(s)W(b; \mu_{qg}) + \sigma_{gg}(s)W(b; \mu_{gg})] \, ,
\end{aligned} \tag{7.19}
$$

and

$$\chi_{\text{odd}}(s, b) = \kappa C_{\text{odd}} \frac{m_g}{\sqrt{s}} e^{i\pi/4} W(b; \mu_{\text{odd}}) \, , \tag{7.20}$$

with the overlap function

$$W(b; \mu) = \frac{\mu^2}{96\pi}(\mu b)^3 K_3(\mu b) \, , \tag{7.21}$$

where μ and C_{odd} are free fit parameters and K_3 is the modified Bessel function of second kind. The constant κ is defined as $\kappa \equiv 9\pi\bar{\alpha}_s^2(0)/m_g^2$.

The quark-quark and quark-gluon energy dependent contributions are respectively

$$\sigma_{qq}(s) = \kappa C_{qq} \frac{m_g}{\sqrt{s}} e^{i\pi/4} \tag{7.22}$$

and

$$\sigma_{qg}(s) = \kappa \left\{ C_{qg} + C'_{qg} \left[\ln\left(\frac{s}{m_g^2}\right) - i\frac{\pi}{2} \right] \right\} , \tag{7.23}$$

where C_{qq}, C_{qg} and C'_{qg} are the free fit parameters. The gluon-gluon contribution σ_{gg} in the eikonal is obtained by the convolution of the gluon distribution function and the partonic gluon-gluon cross section

$$\sigma_{gg}(s) = C_{gg} \int_{4m_g^2/s}^{1} d\tau\, F_{gg}(\tau)\hat{\sigma}_{gg}(\hat{s}) , \tag{7.24}$$

where $\tau = \hat{s}/s$, C_{gg} is a fit parameter and F_{gg} is the convoluted gluon distribution function

$$F_{gg}(\tau) = [g \otimes g](\tau) = \int_{\tau}^{1} \frac{dx}{x} g(x)g(\tau/x) , \tag{7.25}$$

where $g(x)$ is written in a phenomenological parametrized form

$$g(x) = N_g \frac{(1-x)^5}{x^J} , \tag{7.26}$$

where $N_g = (6-\epsilon)(5-\epsilon)...(1-\epsilon)/240$, $\epsilon = 0.08$ is associated with the Pomeron intercept and $J = 1+\epsilon$. The dispersion relation is applied to σ_{gg} to obtain the real part in order to work with an analytical closed form for gg amplitude. In this sense it is written as

$$\mathrm{Re}\,\sigma_{gg}(s) \simeq \frac{\pi}{2}\frac{d}{d\ln s}\sigma_{gg}(s) . \tag{7.27}$$

Combining all the ingredients above the scattering amplitude is written

$$A(s,q) = \frac{i}{2\pi} \int d^2\vec{b}\, e^{-i\vec{q}\cdot\vec{b}}(1 - e^{i\chi_{DGM}(s,b)}) , \tag{7.28}$$

where χ_{DGM} represents either pp or p$\bar{\text{p}}$ processes. In table 7.3 we present the fit parameters that describe the model obtained with $m_g = 400$ MeV and $\epsilon = 0.08$.

m_g (MeV)	400
C_{odd}	3.03 ± 0.4
C_{qq}	10.07 ± 1.4
C_{qg}	0.874 ± 0.059
C'_{qg}	0.0451 ± 0.0062
C_{gg}	0.00379 ± 0.00017
μ_{odd}	0.41 ± 0.17
μ_{gg}	0.651 ± 0.066
μ_{qq}	1.32 ± 0.16
μ_{qg}	0.838 ± 0.044

Table 7.3: We show the dimensionless fit parameters C_{odd}, C_{qg}, C_{qq} and C_{gg} together with μ_{odd}, μ_{qg}, μ_{qq} and μ_{gg} that are in GeV (see [108]).

7.4 Comparison of the models

The three models, BSW, HEGS and DGM, calculate the (s,t)-amplitudes by Fourier transform of the eikonal functions $\Omega(s,\vec{b})$, $\chi(s,\vec{b})$ and $\chi_{DGM}(s,\vec{b})$, as shown in Eqs. (7.1), (7.7) and (7.28) respectively. The eikonals are related to the amplitude in the impact parameter representation of the KFK model (Eq. 5.14) through

$$1 - e^{-\Omega(s,\vec{b})} = 1 - e^{\chi(s,\vec{b})} = 1 - e^{i\chi_{DGM}(s,\vec{b})} = -\frac{i}{\sqrt{\pi}}\left[\tilde{T}_R(s,\vec{b}) + i\,\tilde{T}_I(s,\vec{b})\right] \qquad (7.29)$$

A comparison of the t-amplitudes is shown for 7 TeV in Fig. 7.1. Their normalizations are defined by differential cross-section $d\sigma/dt$ and the total cross section $\sigma(s)$ through

$$\frac{1}{(\hbar c)^2}\frac{d\sigma}{dt} = |T(s,t)|^2 = \frac{\pi}{s^2}|\mathcal{M}(s,t)|^2 = \frac{\pi}{s^2}|F_H(s,t)|^2 = \pi|A(s,t)|^2 \qquad (7.30)$$

and

$$\frac{\sigma_{\text{tot}}(s)}{(\hbar c)^2} = 4\sqrt{\pi}\, T_I(s,0) = \frac{4\pi}{s}\mathcal{M}_I(s,0) = \frac{4\pi}{s}(F_H)_I(s,0) = 4\pi\, A_I(s,0) \ . \qquad (7.31)$$
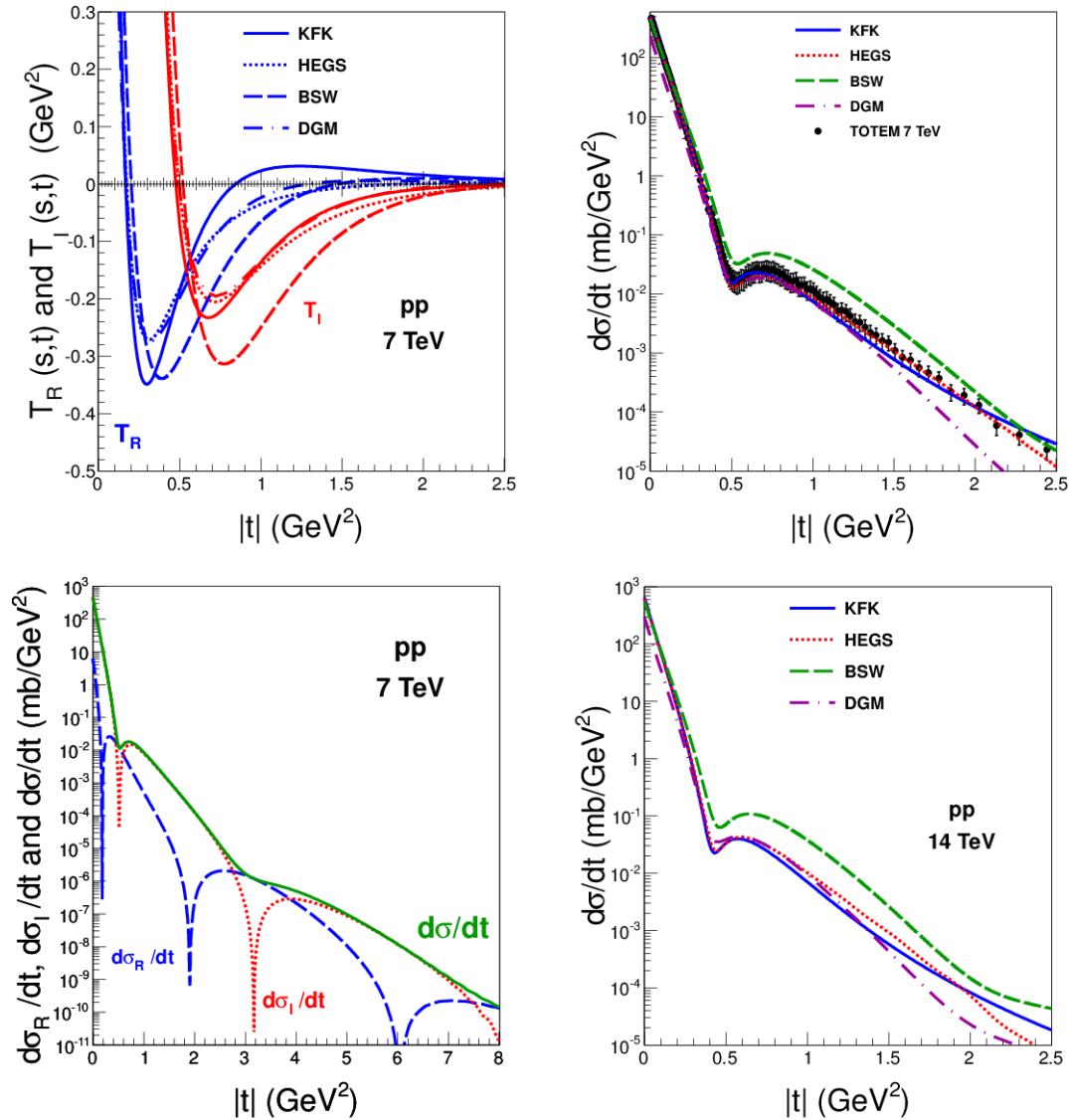

Figure 7.1: a) Real and imaginary amplitudes (top left) and b) differential cross-section (top right) of KFK (solid), BSW (dotted), HEGS (dashed) and DGM (dashed-dotted) models for $\sqrt{s} = 7$ TeV; c) differential cross-section for HEGS model with imaginary and real contribution for $\sqrt{s} = 7$ TeV (bottom left), indicating the presence of a second zero in the imaginary amplitude, that does not occur in KFK; d) the differential cross-section predictions for $\sqrt{s} = 14$ TeV (bottom right).

The Coulomb interaction is not included here. Fig. 7.1 displays the differential

cross-section of the four models for $\sqrt{s} =$7 TeV compared to Totem data, and shows the predictions for 14 TeV. In spite quite different microscopic construction, HEGS and KFK models describe well the available data since the forward region until large t values and it is not possible to discriminate which one agrees better with the data. DGM has a good agreement with both KFK and HEGS models in the region around the dip. Although BSW fairly disagrees with the others for almost the whole t range, it gives a consistent energy dependence of the forward quantities. BSW has an historical importance as being one of the first elastic scattering hadron-hadron model that predicts the rise of the total cross sections. This rise was predicted first by Wu, who calculated microscopic reactions in a massive quantum electrodynamics.

As shown in Fig. 7.1 for the HEGS model, the magnitude of imaginary amplitudes in the plots between zeros are larger than the real magnitudes in the four models. These amplitudes oscillate in $d\sigma/dt$ producing dips near T_I zeros. It is difficult to confirm the oscillatory behavior beyond the first imaginary zero as they occur for larger $-|t|$. In KFK model, the amplitudes $T_R(s,t)$ and $T_I(s,t)$ in t-space have simple analytical forms, with only one imaginary zero and two real zeros (at least for $|t| < 30$ GeV^2).

The similarities of KFK, BSW, HEGS and DGM models only occur up to the location of the second real zero, namely up to $|t| \leq 3$ GeV^2 at $\sqrt{s} =$7 TeV. Fig. 7.2 shows the zeros of the real and imaginary amplitudes in the four models. We observe that the first real zero and the first imaginary zero are in good agreement among the four models. This teaches us that t values beyond the dip should be measured with high precision in order to locate better signs and zeros of the amplitudes.

A common feature of these four models with full $|t|$-description of the amplitudes is that they all agree that $B_R \neq B_I$, in particular, with $B_R > B_I$ at all energies above. This behavior is shown in Fig. 7.2 and must be taken into account in the analysis of the forward scattering data for the estimates of the total cross-sections $\sigma_{\text{tot}}(s)$ and of the $\rho(s) = T_R(s,t=0)/T_I(s,t=0)$ paramteres [107].
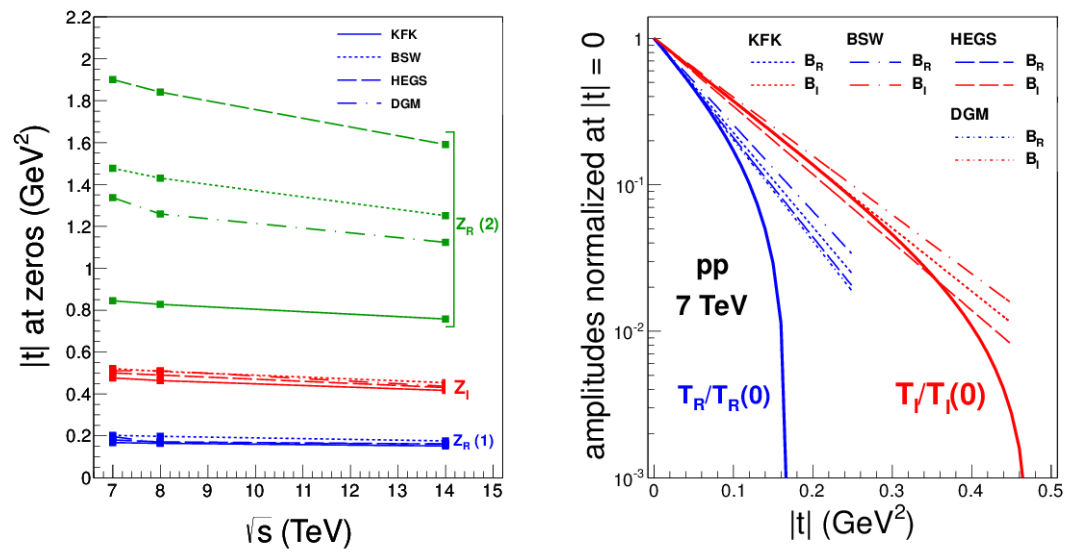
Figure 7.2: Positions of zeros of the amplitudes of KFK, HEGS, BSW and DGM models as a function of energy (left); real and imaginary amplitude of the models for small $|t|$ for $\sqrt{s} = 7$ TeV, with the slopes at $t = 0$, stressing that $B_R > B_I$ in all cases.

Chapter 8

Diffractive processes at LHC

Up to now we have concentrate on the elastic scattering amplitudes studding the topic as a non-perturbative process. Nevertheless there are diffractive processes which can be studied by perturbative methods. In this chapter we study the Pomeron structure in diffractive hadron-hadron collisions.

8.1 Theoretical formulation

Diffractive events in hadronic collisions were first observed at HERA [110, 111] and at the Tevatron [112, 113] more than 20 years ago, and since then, a large effort has been devoted to understand QCD dynamics involved in these processes. The description of diffractive processes in QCD had been challenging for decades, but the presence of a large momentum transfer in these events brought hope that one could be able to understand them with weak-coupling methods.

During many years the Regge phenomenology pointed to the existence of a colorless object called Pomeron exchanged in the t channel, which is responsible for the diffractive events in hadronic collisions. However the understanding of hard diffraction in QCD and the description of the Pomeron as a structure composed of quarks and gluons remains a challenge.

In the case of deep inelastic scattering (DIS) $\gamma p \rightarrow X$, where leptons collide

with protons at high energies through the exchange of a high-virtuality photon, the situation has reached a satisfactory level. Due to several years of experimental efforts at HERA, the diffractive part of the deep inelastic cross-section, which corresponds to about 10% of the events, has been measured with good accuracy [114–116]. On the theoretical side, the collinear factorization of the DIS cross section also holds for it's diffractive component [9], which allows to separate the short-distance partonic cross section computable in perturbation theory, from non-perturbative dynamics encoded in diffractive parton distribution functions (pdfs).

By contrast, the description of hard diffraction in hadron-hadron collisions still poses great theoretical problems. Indeed, Tevatron data provided evidence that even at very large momentum scales, collinear factorization does not apply in such cases [117]. In order to estimate hard diffractive cross sections when factorization does not hold, (a modern version of) the resolved Pomeron model RPM [24] is being widely used. It makes use of the diffractive parton distribution extracted from HERA, which give the distribution of quarks and gluons inside the Pomeron depending on the x (Bjorken variable) and Q^2 (transverse momentum scale) kinematical variables, while modelling the additional soft interactions that violate factorization. To better test the validity of this model, and to better understand the Pomeron structure, it is essential to find sensitive observables to be measured in the current colliders experiments.

One way to constrain quarks and gluons inside the Pomeron is to measure prompt photons in diffractive p+p collisions, as was suggested in [118]. However, this study relied on leading-order matrix-elements, since the Forward Physics Monte Carlo generator [119] was used. Subsequent works also relied on LO matrix elements [120]. In this thesis, we want to investigate the effects of higher-order corrections, and their impact for a center-of-mass energy of 13 TeV at the LHC, and we shall use instead the JetPhox Monte Carlo [121] to compute the matrix elements at leading order (LO) and at next-to-leading order (NLO).
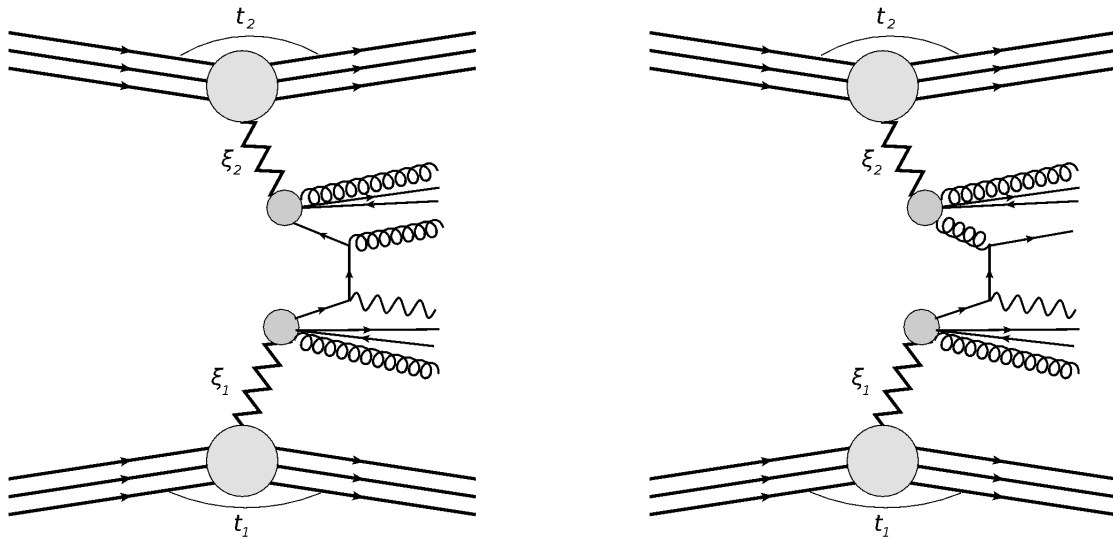
Figure 8.1: Leading-order diagrams for prompt photon production in double-Pomeron-exchange events in p+p collisions. Left: the annihilation partonic sub-processes are only sensitive to the quark content of the Pomeron. Right: the Compton partonic sub-processes are sensitive to the gluon content of the Pomeron as well.

On the theoretical side, prompt photons refers to high-p_t photons created in a hard process, either directly (direct photons) or though the fragmentation of a hard parton (fragmentation photons) [122]. On the experimental side, inclusive and isolated photons denote prompt photons measured without or with an isolation cut, respectively. These are two observables that shall estimate for double-Pomeron-exchange (DPE) events - meaning diffractive p+p collisions from which both protons escape intact - taking into account the kinematical constraints of the forward proton detectors of the CMS-TOTEM collaborations, or those to be installed by the ATLAS collaboration in the future.

8.1.1 Resolved Pomeron model

The resolved Pomeron model is a long-distance/short-distance collinear factorization framework commonly used to calculate hard single-diffraction and DPE processes. In this work, we focus on DPE prompt photon production at the LHC. In the case of direct photons, the leading-order diagrams for this process are pictured

in Fig. 8.1, and the cross section in the resolved Pomeron model reads:

$$d\sigma^{pp\to p\gamma Xp} = \mathcal{S}_{DPE} \sum_{i,j} \int f_{i/p}^D(\xi_1,t_1,\beta_1,\mu^2) f_{j/p}^D(\xi_2,t_2,\beta_2,\mu^2) \otimes d\hat{\sigma}^{ij\to\gamma X} \quad (8.1)$$

where $d\hat{\sigma}$ is the short-distance partonic cross-section, which can be computed order by order in perturbation theory (provided the transverse momentum of the photon is sufficiently large), and each factor $f_{i/p}^D$ denotes the diffractive parton distribution in a proton. These are non-perturbative objects, however their evolution with the factorization scale μ is obtained perturbatively using the Dokshitzer-Gribov-Lipatov-Altarelli-Parisi [123] evolution equations.

In (8.1), the variables $\xi_{1,2}$ and $t_{1,2}$ denote, for each intact proton, their fractional energy loss and the momentum squared transferred into the collision, respectively. The convolution is done over the variables $\beta_{1,2}$, $x_1 = \xi_1\beta_1$ and $x_2 = \xi_2\beta_2$ being the longitudinal momentum fractions of the partons i and j respectively, with respect to the incoming protons. However, hard diffractive cross sections in hadronic collisions do not obey such collinear factorization. This is due to possible secondary soft interactions between the colliding hadrons which can fill the rapidity gap(s). Formula (8.1) is reminiscent of such a factorization, but it is corrected with the so-called gap survival probability $\mathcal{S}_{DPE}$ which is supposed to account for the effects of the soft interactions. Since those happen on much longer time scales compared to the hard process, they are modelled by an overall factor, function of the collision energy only. This is part of the assumptions that need to be further tested at the LHC.

In our computations, we shall use diffractive parton distributions extracted from HERA data [124] on diffractive DIS (a process for which collinear factorization does hold). These are decomposed further into Pomeron and Reggeon fluxes $f_{\mathbb{P},\mathbb{R}/p}$ and parton distributions $f_{i/\mathbb{P},\mathbb{R}}$:

$$f_{i/p}^D(\xi,t,\beta,\mu^2) = f_{\mathbb{P}/p}(\xi,t) f_{i/\mathbb{P}}(\beta,\mu^2) + f_{\mathbb{R}/p}(\xi,t) f_{i/\mathbb{R}}(\beta,\mu^2) \ . \quad (8.2)$$

The secondary Reggeon contribution is important only at large values of ξ, at the edge of the forward proton detector acceptance, and therefore we do not take it into account in the following. Measurements at the LHC will allow to test the validity of this further factorization of the diffractive parton distributions into a Pomeron flux and Pomeron parton distributions, as well as the universality of those Pomeron fluxes and parton distributions.

8.1.2   Effective diffractive parton distribution functions (pdfs) with experimental constraints

In the following, we assume the intact protons in DPE events to be tagged in the forward proton detectors of the CMS-TOTEM collaborations, or those to be installed by the ATLAS collaboration in the future [125], called ATLAS Forward Proton (AFP) detectors. The idea is to measure scattered protons at very small angles at the interaction point and to use the LHC magnets as a spectrometer to detect and measure them. We use the following acceptances [126]:

- $0.015 < \xi < 0.15$ for ATLAS-AFP

- $0.0001 < \xi < 0.17$ for TOTEM-CMS .

Let us now explain how the diffractive pdfs (8.2) are constrained by those detector acceptances. We denote the diffractive quark and gluon distributions integrated over t and ξ by $q^D(x, \mu^2)$ and $g^D(x, \mu^2)$ respectively. These effective pdfs are obtained from the Pomeron pdfs $q_{\mathbb{P}}(\beta, \mu^2)$ and $g_{\mathbb{P}}(\beta, \mu^2)$, and from the Pomeron flux $f_{\mathbb{P}/p}(\xi, t)$. Let us first integrate the latter over the t variable:

$$f_{\mathbb{P}}(\xi) = \int_{t_{\min}}^{t_{\max}} dt \; f_{\mathbb{P}/p}(\xi, t) \quad \text{with} \quad f_{\mathbb{P}/p}(\xi, t) = A_{\mathbb{P}} \frac{e^{B_{\mathbb{P}} t}}{\xi^{2\alpha_{\mathbb{P}(t)} - 1}} \; . \tag{8.3}$$

The parameters of Eq.(8.3) are the slope of the Pomeron flux $B_{\mathbb{P}} = 5.5^{-2.0}_{+0.7}$ GeV^{-2}, and Pomeron Regge trajectory $\alpha_{\mathbb{P}}(t) = \alpha_{\mathbb{P}}(0) + \alpha'_{\mathbb{P}} \, t$ with $\alpha_{\mathbb{P}}(0) = 1.111 \pm 0.007$ and $\alpha'_{\mathbb{P}} = 0.06^{+0.19}_{-0.06}$ GeV^{-2}. The boundaries of the t integration are $t_{\max} = -m_p^2 \xi^2/(1-\xi)$ (m_p denotes the proton mass) and $t_{\min} = -1$ GeV^2. The normalization factor $A_{\mathbb{P}}$ chosen such that $\xi \times \int_{t_{\min}}^{t_{\max}} dt \; f_{\mathbb{P}/p}(\xi, t) = 1$ at $\xi = 0.003$. The above parameters were given in Ref. [124].

Next, to obtain the constrained diffractive pdfs, we convolute the Pomeron flux with the Pomeron pdfs while imposing a reduction in the phase space of ξ, according
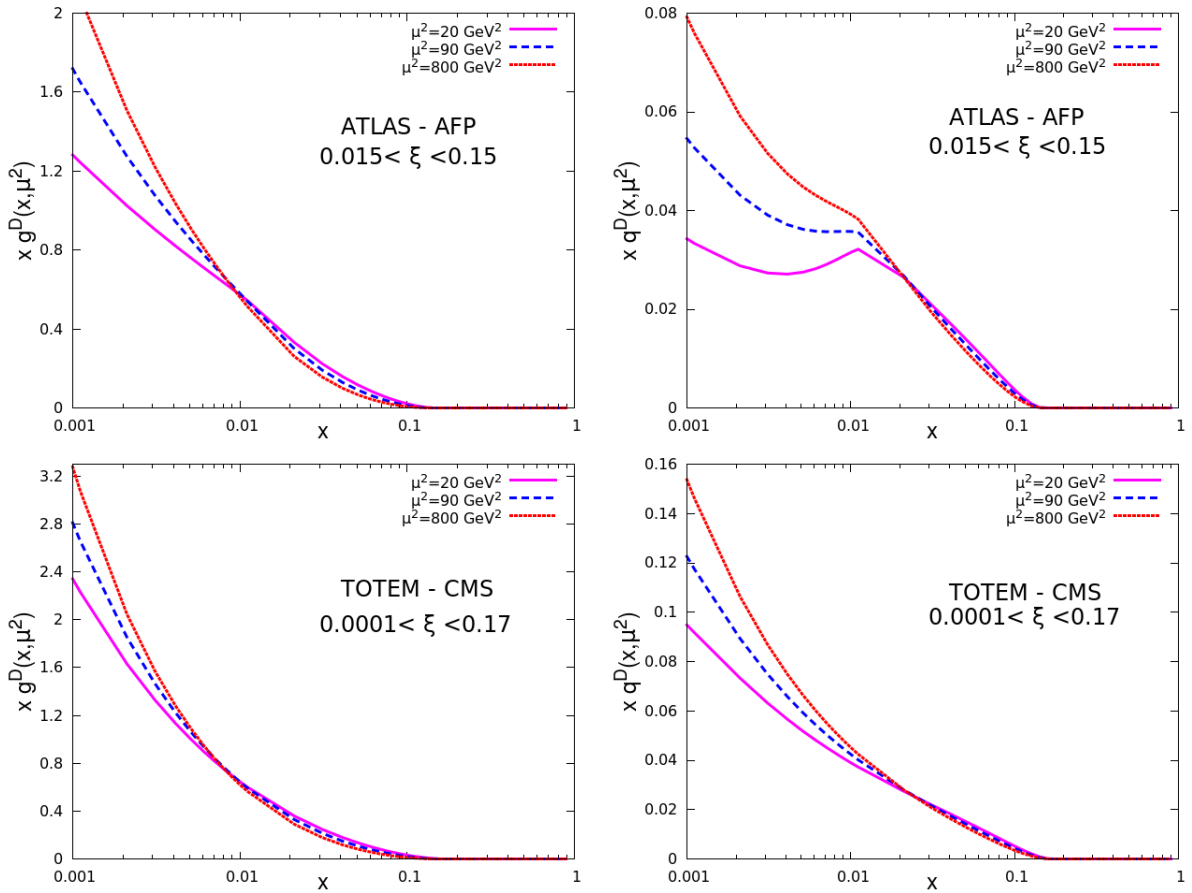
Figure 8.2: These plots represent diffractive parton distribution of the proton for three values of μ^2, with the constraint that the intact proton fall into a forward detector. As a result the distributions vanish for $z > \xi_{max}$, and feature a kink when z crosses ξ_{min}. Left: diffractive gluon distribution $g^D \equiv f_{g/p}^D$ with ATLAS-AFP (top) and TOTEM-CMS (bottom) constraints. Right: the sum of the valence quarks distribution $q^D \equiv \sum_{val} f_{q/p}^D$ with ATLAS-AFP (top) and CMS-TOTEM (bottom) constraints.

to the experimental acceptance of the forward detectors:

$$f_{i/p}^D(x, \mu^2) = \int_{\max(x, \ \xi_{\min})}^{\max(x, \ \xi_{\max})} \frac{d\xi}{\xi} \ f_{\mathbb{P}}(\xi) \ f_{i/\mathbb{P}}(x/\xi, \mu^2) \ . \tag{8.4}$$

For the Pomeron pdfs, we make use of the HERA fit B in [124]. In Fig. 8.2, we show the resulting effective diffractive pdfs for both the ATLAS-AFP and TOTEM-CMS constraints. These distributions are built in a way to be easily incorporated into the LHAPDF library [127] in the grid format.

8.1.3 Computing Double-Pomeron-Exchange (DPE) prompt photon production using JetPhox

JetPhox is a Monte Carlo generator built to compute hadronic cross sections for the process $pp \to \gamma X$ using the collinear factorization framework. Cross sections are calculated as a convolution of short-range matrix elements, computed at LO and NLO, and long-range (non-perturbative) parton distribution and fragmentation functions. Therefore, within the resolved Pomeron model (8.1), this program can also be used to compute the cross-sections $pp \to pp\gamma X$ in DPE events. In order to do this, we must substitute the regular pdfs by our effective diffractive pdfs:

$$f_{i/p}(x,\mu^2) \longrightarrow \int d\xi dt d\beta \; \delta(x - \beta\xi) \; f_{i/p}^D(\xi,t,\beta,\mu^2) \equiv f_{i/p}^D(x,\mu^2) \;, \qquad (8.5)$$

and multiply the resulting cross sections by the gap survival probability S_{DPE}.

JetPhox produces both inclusive and isolated photons with momentum p_t and rapidity y. In case of the inclusive cross section, it sums the direct and the fragmentation contribution in the following way:

$$\frac{d\sigma}{dp_t^2 dy} = \frac{d\hat{\sigma}^\gamma}{dp_t^2 dy} + \sum_a \int dz \; \frac{d\hat{\sigma}^a}{dp_{ta}^2 dy_a}(p_t/z, y) D_a^\gamma(z,\mu^2), \qquad (8.6)$$

where $d\hat{\sigma}^a$ is the hard cross section for producing a parton a=(q,q̄,g) which will then radiate a high-p_t photon during its fragmentation into a hadron. D_a^γ is the fragmentation function, the z variable is $z \equiv p_\gamma/p_a$, and we have chosen the fragmentation scale to be μ. In case of isolated photons, an additional criterion is imposed on the hadronic activity surrounding the high-p_t photon, as is discussed later.

In the following, we use JetPhox to compute the direct and the fragmentation contributions in (8.6), replacing, as explained previously, the regular pdfs by the diffractive pdfs extracted above. Technically, this program calls the parton distributions from the LHAPDF library [127]; we replaced one of those pdfs in grid format
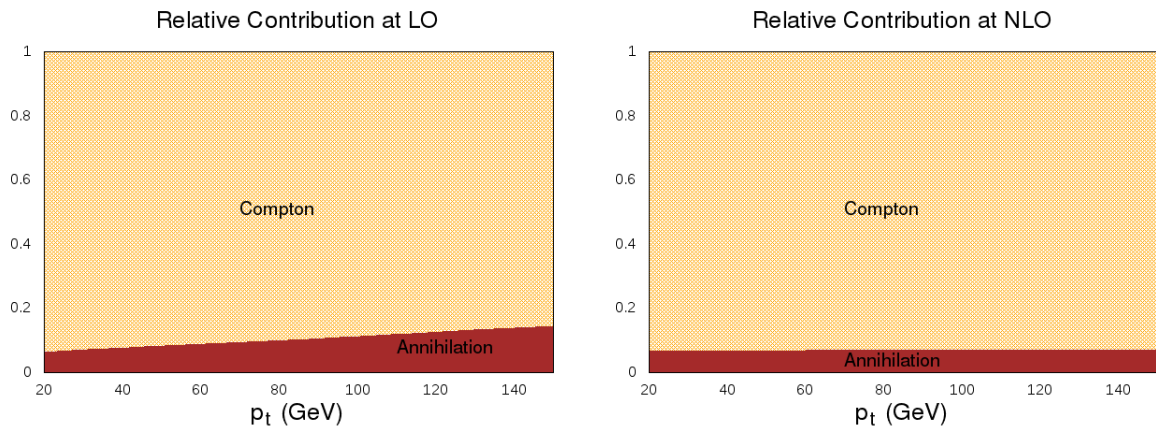
Figure 8.3: These figures show, for DPE direct photon production, the relative contributions of the Compton and annihilation processes at a function of photon p_t. Left: at LO, the Compton process represents about 90% of the differential cross section; the contribution of the annihilation process is slightly increasing with increasing p_t. Right: at NLO, the Compton process dominates around 95% of the differential cross section for all the p_t range analysed.

by our diffractive pdf constrained with the kinematical cuts.

8.2   Numerical results

In this section, we detail the future measurements to be performed at the LHC, in order to test the resolved Pomeron model and to constrain the quark and gluon content of the Pomeron, using photon production in DPE processes. We use the Monte Carlo program JetPhox (version 1.3.1) to simulate the results, with 2×10^8 events per channel.

8.2.1   DPE inclusive photons

In the inclusive mode, there are significant contributions from both direct and fragmentation photons; let us first focus on the direct photons. At LO ($\alpha_{em}\alpha_s$), both annihilation processes $q\bar{q} \to g\gamma$, and Compton processes $q(\bar{q})g \to q(\bar{q})\gamma$, contribute. Going to NLO ($\alpha_{em}\alpha_s^2$) opens an additionnal partonic sub-process, gg→gγ, but this channel contributes only to 1% of the events. Analysing the relative contributions
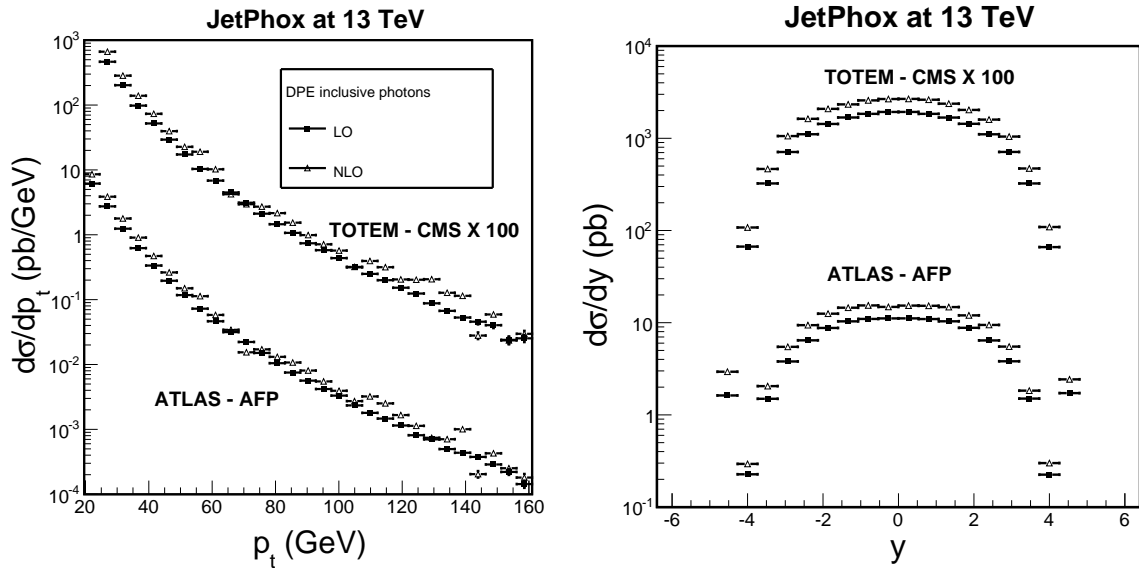
Figure 8.4: These figures show the p_t spectrum (left) and the rapidity distribution (right) of DPE inclusive photons ($pp \rightarrow pp\gamma X$) computed by summing the direct and fragmentation contributions for a center of mass energy of 13 TeV, for both ATLAS-AFP and TOTEM-CMS detector acceptances. The squares and the triangles represents respectively the LO and NLO calculations, the latter giving cross section about 20% greater than the former.

between these two channels in DPE events represents a direct way to constrain the quark and gluon structure of the Pomeron. This is done in Fig. 8.3, as a function of the photon transverse momentum and using ATLAS-AFP acceptance (very similar results are obtained in the TOTEM-CMS case). We observe a large dominance of the Compton processes, which could be expected considering the relative magnitude of the diffractive gluon and quark distribution shown in Fig. 8.2.

This means that extracting Pomeron quark distributions from DPE inclusive photon measurements will first require that the Pomeron gluon content is well constrained (for instance using DPE dijet measurements [118]). This is even more so, since fragmentation photons (which contribute to almost half of the inclusive cross section as we will see below) also come mostly from gluon-initiated process. We display in Fig. 8.4 (left) the differential cross section for the production of DPE inclusive photons as a function of the photon p_t, summing all the channels and com-

paring the results at LO and NLO. We show predictions for both ATLAS-AFP and TOTEM-CMS detectors at 13 TeV. In Fig. 8.4 (right), we show the photon rapidity distribution (for $p_t > 20$ GeV), and we note that the difference in magnitude between the LO and NLO calculation is about 20%. Obviously, NLO corrections are not negligible, they must be taken into account in order to extract correctly the Pomeron structure from future data. Note that due to the vanishing of the effective diffractive pdfs (8.4) for $x > \xi_{max}$, there are no photons produced at very forward or very backward rapidities.

Finally, to compare these cross sections with the future data from the experiments, we note that the gap survival probability factor may have to be readjusted. We have assumed $S_{DPE} \simeq 0.1$ [128], but the actual value is rather uncertain and must first be measured.

8.2.2 DPE isolated photons

Using the inclusive photon measurement discussed above in order to constrain the quark content of the Pomeron is not optimal, because this observable is contaminated by fragmentation photons, which mostly come from gluon-initiated process. In order to suppress the contribution from fragmentation processes, one can use an isolation criteria that will disregard the photons that are surrounded by too much hadronic activity. Indeed, generically a direct photon will be isolated from a large hadronic activity while a fragmentation photon won't. The isolation criteria we use is to require that the hadrons measured within a cone of radius $R = 0.4$ have a maximum of 4 GeV of transverse energy. This is one of the options available in JetPhox [121], we checked that our conclusions are independent of this particular choice for the isolation criteria.

Let us now compare the inclusive and isolated photon production. In Fig. 8.5 we show in both cases, the relative contribution of the direct and the fragmentation processes at NLO. The relative contribution of fragmentation processes is decreasing
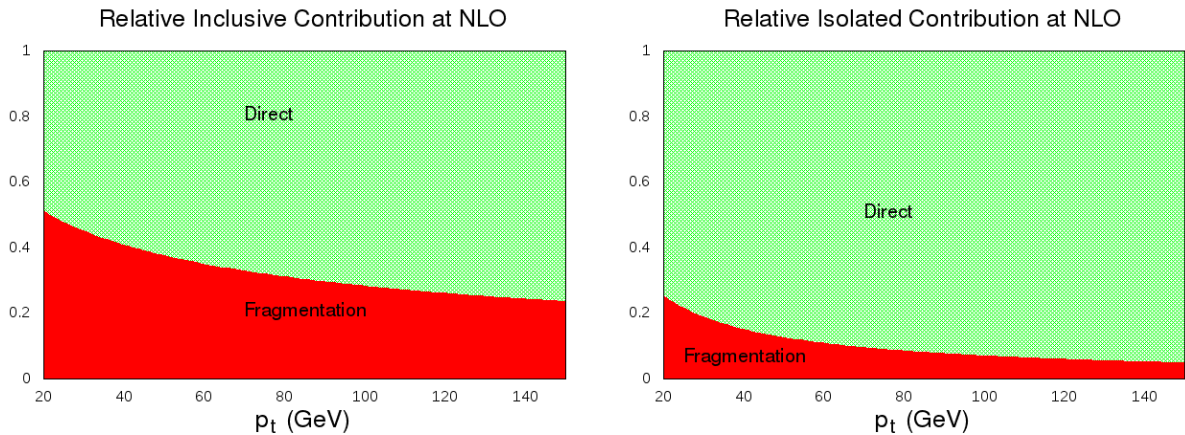

Figure 8.5: These figures show, for DPE prompt photon production at NLO, the relative contributions of the direct and fragmentation processes at a function of photon p_t. Left: in the inclusive case, the direct and fragmentation contributions are equal at $p_t \simeq 20$ GeV, and the relative contribution of direct processes increases with increasing p_t. Right: in the isolated case, the direct processes dominate; at $p_t \simeq 20$ GeV they represent about 75 % of the cross section, and that percentage increases with increasing p_t.

with increasing p_t, but it remains always large in the inclusive case: between 20 and 150 GeV, it goes from 50% to 25%. In the isolated case however, it is clear that the fragmentation contribution is strongly suppressed by the isolation criteria, and as the transverse momentum of the photon increases, this contribution eventually becomes negligible. In Fig. 8.6, we display our predictions for the p_t spectrum (left) and the rapidity distribution (right) of DPE isolated photons, for both ATLAS-AFP and TOTEM-CMS detectors at 13 TeV. Comparing the LO and NLO results, we note that the NLO cross sections are about 50% greater than the LO ones, which is a much bigger difference than in the inclusive case. In order to extract correctly the Pomeron structure from future data, NLO corrections are not even more crucial when the isolation criteria is applied.
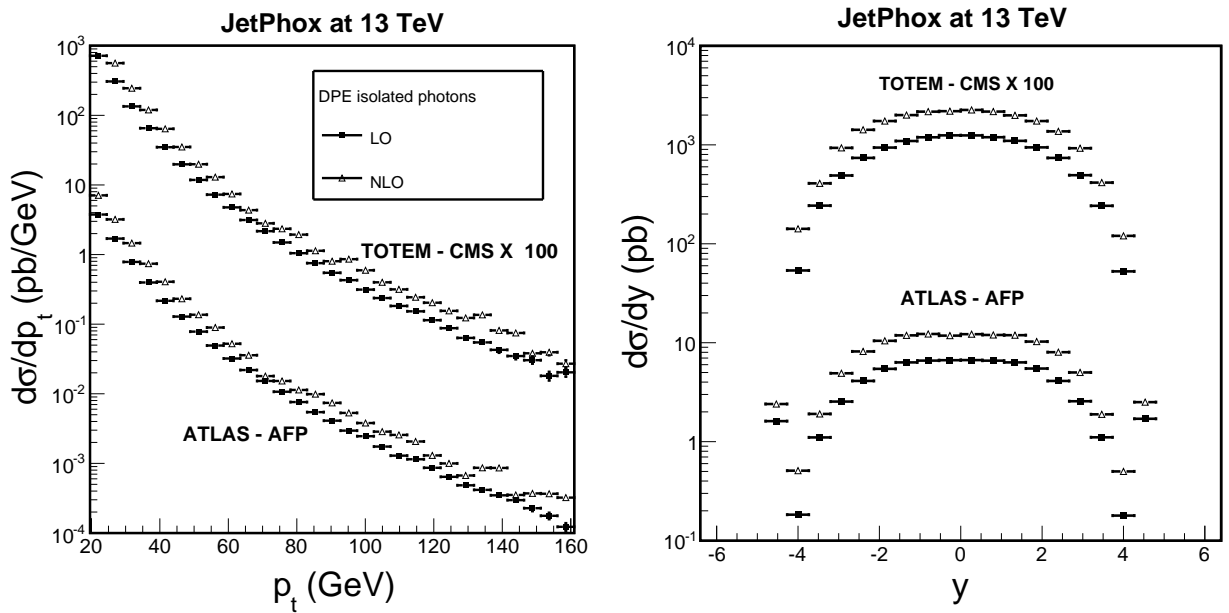
Figure 8.6: These figures show the p_t spectrum (left) and the rapidity distribution (right) of DPE isolated photons for a center of mass energy of 13 TeV, for both ATLAS-AFP and TOTEM-CMS detector acceptances. The differential cross sections at LO (squares) or NLO (triangles) are obtained by summing the direct and fragmentation contributions while requiring that the hadrons measured within a cone of radius 0.4 around the photon have transverse energy no greater than 4 GeV. The NLO cross sections are about 50% greater than the LO ones when such isolation criteria is applied.

Chapter 9

Comments and conclusions

Elastic scattering of hadrons at high energies are basic physical processes in the investigation of the dynamics of strong interactions. In most of this thesis we study soft processes, in which perturbative treatments are not applicable. In this regime the physical vacuum of QCD is seen to play an important role. The strong interactions between hadrons are mainly dominated by the vacuum correlators which are non-perturbative objects. As shown along this thesis, in spite of many attempts to explain the peripheral collisions, there is no complete and satisfactory solution to the soft QCD problem, and the physical vacuum of QCD still remains a challenge. Our purpose is to propose a bridge between the experiments and the theory, exploring and analysing the available pp and p$\bar{\text{p}}$ data with amplitudes first proposed in Ref. [48], originated in the Stochastic Vacuum Model. The goal is to determine as precisely as possible the complex amplitudes behind the data and provide to the high energy physics community a *tomography* of pp and p$\bar{\text{p}}$ elastic scattering. In our analysis, analytic and explicit representation of the amplitudes, in both t and b spaces as function of s are proposed. The resulting amplitudes are constructed satisfying the general requirements of the S-matrix, namely, dispersion relations and the unitarity conditions.

The theoretical basis of the model shows that the vacuum expectation values of

Wilson-loop operators (correlation functions) play an important role. As described in Chapter 2, the hadronic scattering amplitudes are expressed as the convolution of the quark/antiquark transverse distribution functions inside the hadrons and the eikonal amplitude that represents loop-loop scattering. In Ref. [48], an analytic ansatz of the final form of the amplitude is proposed interpolating the asymptotic behavior of the vacuum correlator and the known phenomenological exponential behavior in the forward region. While SVM describes the interactions between loops through the physical vacuum of QCD, the distribution of quarks inside the incident hadrons should be determined considering the structure of hadrons. As known from the behavior of the parton distribution function, the density of partons (color sources) inside the hadron is not a fixed quantity, depending on the energy scale involved in the process. In this work, we assume that the form of ansatz given in Ref. [48] is preserved for any energy, while the parameters contained there should be considered as energy dependent in order to account for virtual quark-antiquarks fluctuations within the hadron. This assumption should be verified in comparison with the data.

In Chapter 3 we perform a careful analysis of the experimental data which determines the behavior of the forward scattering amplitudes in a framework considering the amplitudes as simple exponential forms. The forward scattering amplitudes are essentially determined by the value at the origin ($t = 0$) and its derivative in t, and hence by the four real parameters (σ, ρ, B_I and B_R). However, these parameters are not completely independent due to the constraints given by dispersion relations, whose application depends on the knowledge of the energy dependence of the total cross section and of the imaginary slope. Some parameters are directly related to the experimental data measured in the forward region. We propose to the experimental collaborations a re-analysis of the forward parameters respecting the basic quantum mechanical principles such as the necessity of the real amplitude behaving differently from the imaginary part namely ($B_R \neq B_I$). The dispersion relations for

slopes predict that the real slope is larger than the imaginary one. Many experimental analyses make use of the parameter ρ coming from approximated dispersion relations forms that uses as an input a parametrized form for pp total cross section. We propose the use of the exact forms of derivative dispersion relations which have an important influence for low energies, where the differences between the pp and p$\bar{\text{p}}$ quantities are not negligible. In our studies we analyse the correlation between forward parameters, searching the minimum value of χ^2 between ρ and the defined quantity $\beta \equiv B_R/B_I$. This correlation method shows somehow the quality of the forward data of differential cross sections. We also introduce a free normalization parameter to adjust the dN/dt data to $d\sigma/dt$ using the interference of the realistic real with the Coulomb amplitude as the regulator. This method was extended to check in each dataset whether the normalization of $d\sigma/dt$ is correct or wrong relative to the Coulomb amplitude.

In Chapter 4, we perform the analysis of KFK amplitudes for the full t domain. As mentioned before, our amplitude has a unique analytical form in t-space for all energies, with the parameters representing the distribution of scattering sources carring the energy dependence. The amplitudes are described in SVM formalism as a geometric structure at a given energy. In the b-space representation the amplitudes are defined as a superposition of a Gaussian (similar to Pomeron exchange) and the shape function obtained from SVM. The normalization constants of these two terms are directly related to the total cross section (See Eq.(4.6)) through the optical theorem. In the case of pure Gaussian, this term corresponds to the factorized eikonal models with Gaussian profile function. In this case, the asymptotic energy dependence of the cross section would lead to $\sim \ln \sqrt{s}$, so that we expect that the normalization factor α_I should be linear in $\ln \sqrt{s}$. On the other hand, in the slope term $\Psi\left(\gamma\left(s\right), t\right)$, this is not the case. However, it is interesting to note that the determination of the parameters performed independently for each energy leads to very smooth and regular behavior of the parameters α_I and λ_I as function of

energy. Note that a simple factorized eikonal model with power law of the parton distribution in $\sqrt{s}$ leads to the general idea that when the matter distribution has a Gaussian tail the total cross section goes with $\ln \sqrt{s}$ and for the part with long range exponential tail, it goes with $\ln^2 \sqrt{s}$ [129].

The fact that the fittings of complete data at all energies for each energy lead to the above behavior of α_I and λ_I indicates that the variation with respect to $\sqrt{s}$ of the amplitudes as function of t help to disentangle the contributions from the Gaussian and the Yukawa terms. In fact, it is observed that the position and shape of the dip-bump structure in the differential cross section is very sensitive to the entanglement of the real and imaginary parts of the amplitudes. It seems that this sensitivity is responsible for the separation of the energy dependence of the Gaussian and the shape functions. We analyse the amplitudes for large t range where we believe that the pertubative three gluon exchange process will dominate. This term may have influence on the depths and slopes of the dips for low energies.

Along the present work we have learned many general properties of the complex scattering amplitudes, as the number of zeros, their positions, details in the shrinkage of the forward peak and the evolution of these quantities with the energy. We understand that the real amplitude plays a crucial role in the determination of the observables in the differential cross section in the full t range.

Although our model is not built in a form based explicitly in the Pomeron exchange mechanism, we can find relations with our amplitudes. We show that when we write the energy dependence of the total cross section in a Pomeron-like form, we obtain the intercept 0.096, which is exactly as given in Ref. [22]. However in t channel the Pomeron model is characterized by a trajectory being exchanged and it is interesting to write the t-dependence in a trajectory-like form. This can be made with an appropriate expansion of the terms of the imaginary amplitude for small t. Furthermore, when we write our amplitudes in the forward regime we may identify that the exponential part of KFK amplitude contains the Pomeron information

combined with terms due to vacuum structure.

In Chapter 5 we study geometric properties of the KFK amplitudes. It is shown that the amplitudes satisfy the unitarity constraint, and exhibit a remarkable geometric scaling behavior [97] in the asymptotic region, in the sense that

$$\frac{d\sigma}{db}\left(b, \sqrt{s}\right) \rightarrow f\left(x\right), \quad \sqrt{\frac{s}{s_0}} > 1,$$

where f is a function of the single scaling variable,

$$x = \frac{b}{\sqrt{\sigma\left(\sqrt{s}\right)}},$$

and $\sqrt{s_0}$ is an energy scale where the scaling law starts to be valid. This asymptotic region occurs at extremely high energies, such as $\sqrt{s_0} \sim 10^5$ TeV.

Another interesting finding is that

$$\frac{d^2\sigma}{db^2}\left(b, \sqrt{s}\right), \frac{d\sigma_{\text{el}}}{db^2}\left(b, \sqrt{s}\right) \tag{9.1}$$

in b-space have shapes very different from a black disk, presenting an appreciable semi-transparent halo around the core. This is so also for the asymptotic form $f\left(x\right)$, so that the black disk picture never occurs in our model, not even aymptoticaly as a consequence, the ratio, $\sigma_{\text{el}}/\sigma$ does not converge to 1/2 as is the case of the black disk, even in the asymptotic energy region. Since it is know that if a simple factorized eikonal ansatz is used, the black disk behavior in asymptotic energy region seems to be unavoidable, the non-black-disk nature of our amplitudes is due to its non-factorizable form. From the phenomenological side the measurement of the interaction range is contained in the imaginary forward slope which is related with second moment in impact parameter. We show that this slope should be quadratic in $\log \sqrt{s}$.

The above point may become particularly important in discussion of the scatter-

ing amplitude for more complex systems, such as in p-A, or A-A reactions. As we see, the scattering amplitudes depend crucially on how the colliding system "sees" the distribution of scattering centers as the modification of the physical vacuum in the corresponding scale associated to the incident energy. In Chapter 6, we apply our amplitudes to p-air collisions in order to compare with the data from cosmic ray experiments. We applied the Glauber approach [98] to obtain the scattering amplitude for p-air collisions as the superposition of scattering amplitudes from p-p (nucleon-nucleon) collisions. Comparison with experiments is made. The calculated cross sections are found to be fairly consistent with the observed data up to the energy $\sqrt{s} \lesssim 100$ TeV (in correspondinf pp system), with remark to the recent Telescope Array experiment at $\sqrt{s} = 95$ TeV [130]. However, as pointed above, the correct cross sections should be calculated using the distribution of partons which participate in the collision, and this is not a simple superposition of independent nucleons inside a nucleus, since at very high energy, the partons of different nucleons start to overlap. In such a situation, a simple Glauber approximation based on the nucleon multiple scattering may fail. Thus, we need to know the wavefunction of partons inside a nucleus at high energy. Some techniques to calculate the parton distribution for the initial state of the relativistic heavy ion collisions such as IP-Sat/Glasma approaches [131] might be helpful. Especially this may change the energy dependence of the total or production cross section for p-air collisions at high energies.

To our knowledge, our model is particularly interesting and useful for givin an explicit forms of imaginary and real amplitudes that are closed and analitic. In Chapter 7, we present a short comparative study of our amplitudes with some available models of the literature. Although the models present quantitatively different behavior in the real and imaginary amplitudes, they have qualitatively remarkable similar behavior. The imaginary amplitudes have the first zero very close in all the four cases analysed, as determined by the position of the dip. The differences of the

positions of the second real zero teaches us that more precise measurements of the differential cross section after the dip are necessary in order to determine the real amplitude. The slopes of the real amplitude confirm the difference with respect to the imaginary slope, showing the necessity of further analysis of differential cross section data, taking into account this property.

Due to the importance of the Pomeron phenomenology in soft high energy physics in Chapter 5, we made connection of KFK amplitudes with the Pomeron-like description showing the correspondence between the two visions. The Pomeron model is also applicable to describe the inelastic diffractive processes. So, finding some relation between our amplitude and the Pomeron model may open a space to include the inelastic channels within the SVM approach.

Among many Pomeron models, the so-called Resolved Pomeron Model described in Chapter 8, investigates the possible partonic structure of this hypothetical particle, Pomeron. In our approach, the density of color scattering centers at a given energy scale plays as of the important ingredient. Thus, this may give an interesting vlue to extend our approach to include inelastic channels in the future.

In the framework of the resolved Pomeron model presented in Section 8.1, we have analyzed prompt photon production in double Pomeron exchange (DPE) processes in p+p collisions. We perform our calculations of inclusive and isolated photons using the JetPhox program. This is done by substituting the regular pdfs by the diffractive pdfs (see Eq. (8.4)) which also take into account the acceptance of the forward proton detectors. Then, in order to obtain the DPE cross section, we multiply the results by the gap survival probablity S_{DPE}, which we assume to be 0.1 for a center of mass energy 13 TeV.

The use of JetPhox allows us to compute the DPE prompt photon production cross sections with, for the first time, next-to-leading order hard matrix elements. Our main result is that the NLO cross sections are larger than the LO ones, by about 20% in the inclusive case and 50% in the isolated case. NLO corrections

are therefore crucial in such processes in LHC at 13 TeV in LHC. In addition, we observe that the isolation criteria is necessary in order to suppress the contribution of fragmentation photons, radiated by high-p_t partons during their fragmentation, and to access in a clean way the direct processes of photon production.

We also show that in DPE direct photon production, the Compton partonic sub-processes (Fig 8.1-right) clearly dominate over the annihilation ones (Fig 8.1-left). This is largely explained by the relative magnitude of the diffractive gluon and quark distribution shown in Fig. 8.2. As a consequence, extracting Pomeron quark distributions from DPE prompt photon measurements will first require that the Pomeron gluon content is already well constrained, which can be done using for instance DPE dijet production [118].

Finally, we have analyzed different possible scenarios to be tested by LHC experiments Atlas-AFP and Totem-CMS, and we expect that future data on DPE prompt photon production will provide a quantitative way to test the validity of resolved Pomeron model, the factorization of diffractive pdfs into a Pomeron and a Pomeron pdf, as well as to extract the gap survival probability and understand its behavior with increasing energy. We also hope that measurements at 13 TeV will allow to constraint the quark and gluon structure of the Pomeron.

As steps for the future, we plan to investigate the possibility of establish the relation between our amplitudes and the QCD evolution equation with the gluon saturation phenomena. As mentioned before the scaling behavior appearing for high energies motivate us to think of elastic scattering as a diffusive process in impact parameter which can be governed by an evolution equation for high energies. We want to understand the general mechanism responsible to give the energy dependence of hadron-hadron scattering. Efforts in this direction was done by Giordano and Meggiolaro [132] in an approach similar to SVM, where they made a connection between the angle formed along the hadrons trajectories in the light cone coordinates and the center of mass energy.

Another challenge in SVM approach is to include the inelastic channels of diffraction. Important experimental information about the structure of diffraction obtained in HERA is in exclusive vector meson production and deep virtual Compton scattering (DVCS), in which the electron colliding with proton in the initial state produces vector meson/gamma in the final state, keeping the proton structure intact. The electron recoil emits a virtual photon. An usual approach, the dipole model [133]. In this framework the photon emitted by the electron fluctuates into a color singlet quark/antiquark pair, interacting with the proton strongly producing a vector meson or photon in the final state. From QCD viewpoint the dipole interacts with the proton via exchange of a two gluon singlet. The dipole framework is basis of many theoretical models [134–137], and depends on nonperturbative ingredients as the vector meson wave functions and distribution functions.

In LHC experiments, the analogous gamma production in proton-proton collisions have been measured. As proton is much heavier than the electron its recoil is much smaller and the photon exchanged in this process is almost real ($Q^2 \approx 0$). The interaction of the photon with the proton is similar to HERA process. Essentially both HERA and LHC process should share the same problems in the strong interaction sector.

We wish to investigate other approaches such as developments of the Stochastic Vacuum Model [17] in which the interaction occurs between Wilson quark/antiquark loops. Details of the loop-loop calculation can be found in the literature [138–141]. This model was tested for all the vector mesons measured at HERA (ρ, ω, ϕ, J/ψ and Υ) [142] and has the advantage of having no free parameters. In this sense we wish to investigate the new processes available at the LHC in parallel with the present HERA data comparing different approaches and different kinematical conditions of the processes.

Appendix A

Relativistic kinematics

In this section we present the relativistic kinematics variables and the relation between them.

The movement of objects travelling at high energies is described by the relativistic 4-momentum
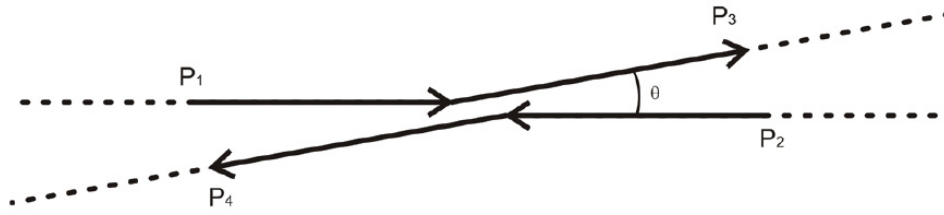
$$P^\mu = (P^0, \vec{p}) = (E/c, \vec{p}), \tag{A.1}$$

with E being the relativistic energy

$$E^2 = |\vec{p}|^2 \ c^2 + m^2 \ c^4 \ , \tag{A.2}$$

$\vec{p}$ is the particle 3-momentum and m is the invariant mass. From now on, we use the unity system where $c = 1$. The scalar product $P^\mu P_\mu$ is a Lorentz invariant quantity,

$$P^\mu P_\mu = E^2 - |\vec{p}|^2 = m^2 \ . \tag{A.3}$$

In order to describe the process in terms of relativistic invariant quantities we define the Mandelstam variables

$$s = (P_1 + P_2)^2 = (P_3 + P_4)^2 \ , \tag{A.4}$$

$$t = (P_1 - P_3)^2 = (P_4 - P_2)^2 \ , \tag{A.5}$$

$$u = (P_1 - P_4)^2 = (P_3 - P_2)^2 \ , \tag{A.6}$$

where P_1 and P_2 are the incident particle 4-momentum and P_3 , P_4 are refer to the scattered particles. This set of variables contains the kinematics information of the particles involved in the collision process. The Mandelstam variables follow the identity

$$s + t + u = \sum_{i=1}^{4} m_i^2 \ , \tag{A.7}$$

which constraints the three variables.

The description of physical processes must be invariant under change of reference frame.

A.0.3   Center of mass frame

We indicate with stars (*) the variables in the CM system. The 3-momentum conservation is

$$\vec{p_1}^* + \vec{p_2}^* = \vec{p_3}^* + \vec{p_4}^* = 0 \ . \tag{A.8}$$

We write $\vec{p_1}^* = -\vec{p_2}^* = \vec{p_i}^*$ and $\vec{p_3}^* = -\vec{p_4}^* = \vec{p_f}^*$, where $|\vec{p_i}^*| = p_i^*$ and $|\vec{p_f}^*| = p_f^*$. The s variable is

$$s = (E_1^* + E_2^*)^2 = (E_3^* + E_4^*)^2 \ . \tag{A.9}$$

The energies of the particles can be written as

$$E_1^* = \frac{1}{2\sqrt{s}}(s + m_1^2 - m_2^2) \ , \tag{A.10}$$

$$E_2^* = \frac{1}{2\sqrt{s}}(s + m_2^2 - m_1^2) \ , \tag{A.11}$$

$$E_3^* = \frac{1}{2\sqrt{s}}(s + m_3^2 - m_4^2) \ , \tag{A.12}$$

$$E_4^* = \frac{1}{2\sqrt{s}}(s + m_4^2 - m_3^2) \ . \tag{A.13}$$

Replacing Eq.(A.10) in Eq.(A.2) it follows

$$p_i^{*2} = \frac{1}{4s}(s - (m_1 + m_2)^2)(s - (m_1 - m_2)^2) \ , \tag{A.14}$$

$$p_f^{*2} = \frac{1}{4s}(s - (m_3 + m_4)^2)(s - (m_3 - m_4)^2) \ . \tag{A.15}$$

In our case of pp and $p\bar{p}$ elastic scattering $m_1 = m_2 = m_3 = m_4 = m$ and consequently $p_i^{*2} = p_f^{*2} = p^{*2}$ and $E_1^* = E_2^* = E_3^* = E_4^* = E^*$. The expressions for the energy and 3-mometum become respectively

$$E^* = \frac{\sqrt{s}}{2} \tag{A.16}$$

and

$$p^{*2} = \frac{1}{4}(s - 4m^2) \ . \tag{A.17}$$

Using the expressions above, the Mandelstam variables are written in terms of the magnitudes of particle's 3-momentum, particle's masses and scattering angle θ_{cm}

between particles in initial and final states in CM frame,

$$s = 4(p^{*2} + m^2) \tag{A.18}$$

$$t = -2p^{*2}(1 - \cos\theta_{\text{cm}}) \tag{A.19}$$

$$u = -2p^{*2}(1 + \cos\theta_{\text{cm}}) . \tag{A.20}$$

A.0.4   Laboratory rest frame

Frequently analysis of experiments give physical quantities in terms of laboratory rest frame. The general expression for total invariant energy is given by :

$$s = (P_1 + P_2)^2 = 2m^2 + 2E_1 E_2(1 - \beta_1\beta_2\cos(\theta)) , \tag{A.21}$$

where θ is the angle between two particles and $\vec{\beta} = \vec{p}/E$ is the particle velocity. In the rest frame of particle 2 the above expression simplifies

$$s = 2m^2 + 2mE_{1\text{lab}} . \tag{A.22}$$

In the limit of high energies the particle's masses becomes negligible and one can approximate

$$s \simeq 2mE_{1\text{lab}} . \tag{A.23}$$

This expression will be useful to treat the PDG parametrization and connect with dispersion relations formula and we will refer to $E_{1\text{lab}}$ simply as E.

Appendix B

Integral dispersion relations and exact local DDR forms

From the unitarity conditions (2.13), the sum over final states contributes with the imaginary part for the cases where the incident energy is greater than the invariant mass of the n-particle observed in the final states. On the other hand, the imaginary part shows discontinuities of the scattering amplitude over the real axis. These discontinuities are associated with the cuts attached to the branching points chosen conveniently along the real axis. The analytical continuation of the amplitude in the complex energy plane should contour the poles and the cuts. From Cauchy's integral theorem we write,

$$F(s, t, u) = \frac{1}{2\pi i} \oint \frac{F(s', t, u)}{s' - s} \, ds'. \tag{B.1}$$

The hypothesis of analyticity of the scattering amplitude implies that the integrand of Cauchy's integral must vanish as the modulus of s goes to infinity $|s| \to \infty$. The integration result depends on the remaining poles inside the circuit. In the case of elastic scattering of pp and p$\bar{\text{p}}$ there are no poles and the branching point starts at $s = 2m^2$, where m is the proton/antiproton's mass, and is extended in the real axis. The Cauchy integrals can be written as

$$F(s,t,u) = \frac{1}{2\pi i}\left[\int_{2m^2}^{\infty} \frac{F(s'+i\epsilon,t,u) - F(s'-i\epsilon,t,u)}{s'-s} ds' \right.$$
$$\left. + \int_{2m^2}^{\infty} \frac{F(-s'+i\epsilon,t,u) - F(-s'-i\epsilon,t,u)}{s'+s} ds' \right]. \qquad (B.2)$$

From Eq. (2.12) we can write the integral above in terms of the forward imaginary amplitude .

$$\mathrm{Re}F(s,u) = \frac{1}{\pi}\left[\int_{2m^2}^{\infty} \frac{\mathrm{Im}F(s',u)}{s'-s} ds' + \int_{2m^2}^{\infty} \frac{\mathrm{Im}F(-s',u)}{s'+s} ds' \right] \qquad (B.3)$$

whose left side is the real amplitude. The amplitudes can be defined by its parity through the signal exchange in Mandelstam variables. If the amplitude is even, (e.g) $\mathrm{Im}F(s',u) = \mathrm{Im}F(-s',u) = \mathrm{Im}F^{+}(s',u)$,

$$\mathrm{Re}F_{+}(s,u) = \frac{2}{\pi}P \int_{2m^2}^{\infty} \frac{s'\,\mathrm{Im}F_{+}(s',u)}{s'^2 - s^2} ds' . \qquad (B.4)$$

If the imaginary amplitude is odd in s, $\mathrm{Im}F(s',u) = -\mathrm{Im}F(-s',u) = \mathrm{Im}F_{-}(s',u)$,

$$\mathrm{Re}F_{-}(s,u) = \frac{2s}{\pi}P \int_{2m^2}^{\infty} \frac{\mathrm{Im}F_{-}(s',u)}{s'^2 - s^2} ds' , \qquad (B.5)$$

where P the principal value of integral.

Crossing symmetry is another important feature of the scattering amplitudes. If the amplitudes can be analytic continued over the 3 physical channels s, t and u, then the same scattering amplitude can explain different physical processes.

Let $F_{\mathrm{pp}\to\mathrm{pp}}(s,t,u)$ be pp scattering amplitude. By crossing symmetry, replacing s by u we obtain

$$F_{\mathrm{pp}\to\mathrm{pp}}(s,t,u) = F_{\mathrm{p\bar{p}}\to\mathrm{p\bar{p}}}(u,t,s) . \qquad (B.6)$$

The result above means that the same pp scattering amplitude gives the information

Figure B.1: Amplitudes pp and p$\bar{\text{p}}$ in complex energy plane
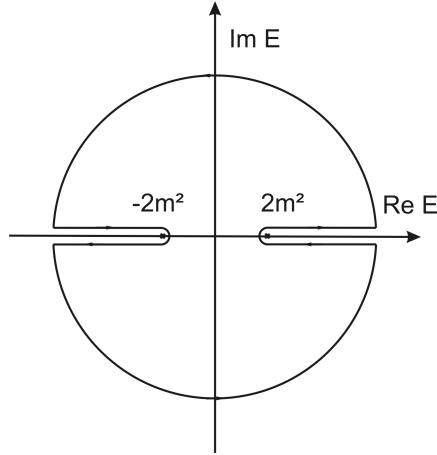
of p$\bar{\text{p}}$ by analytical continuation in the Mandelstam plane. We can define even and odd amplitudes by exchanging of two variables. We here fix t.

$$F_+(s,u) \equiv [F_{\text{pp}\to\text{pp}}(s,u) + F_{\text{p}\bar{\text{p}}\to\text{p}\bar{\text{p}}}(u,s)]/2 \tag{B.7}$$

and

$$F_-(s,u) \equiv [F_{\text{pp}\to\text{pp}}(s,u) - F_{\text{p}\bar{\text{p}}\to\text{p}\bar{\text{p}}}(u,s)]/2 , \tag{B.8}$$

For a fixed t, from even and odd terms we can write pp and p$\bar{\text{p}}$ amplitudes

$$F_{\text{pp}\to\text{pp}}(s,u) = F_+(s,u) + F_-(s,u) \tag{B.9}$$

and

$$F_{\text{p}\bar{\text{p}}\to\text{p}\bar{\text{p}}}(s,u) = F_+(s,u) - F_-(s,u) . \tag{B.10}$$

If the behavior of the integral is divergent, we need to regularize the complex amplitude by choosing a defined point s_0 and subtract it, $F(s,t) - F(s_0,t)$. Applying

the subtracted function to even DR Eq.(B.1)

$$F(s,u) - F(s_0, u) = \frac{1}{2\pi i} \oint F(s', u) \left[\frac{1}{s' - s} - \frac{1}{s' - s_0} \right] ds' \ . \qquad \text{(B.11)}$$

As consequence the even amplitude is

$$\mathrm{Re}F_+(s,u) - \mathrm{Re}F_+(s_0,u) = \frac{2}{\pi} s^2 P \int_{2m^2}^{\infty} \frac{\mathrm{Im}F_+(s')}{s'(s'^2 - s^2)} \, ds' \ , \qquad \text{(B.12)}$$

and the odd amplitude

$$\mathrm{Re}F_-(s,u) = \frac{2}{\pi} s P \int_{2m^2}^{\infty} \frac{\mathrm{Im}F_-(s')}{s'^2 - s^2} \, ds' \ , \qquad \text{(B.13)}$$

where $K = \mathrm{Re}\, F_+(s_0, u)$ is the subtraction constant. Notice that the odd amplitude does not depend on a subtraction constant.

Now we present the derivative dispersion relation exact forms and useful inputs for the phenomenology. The mathematical properties of dispersion relations can help to constrain the real and imaginary amplitudes in the forward regime. For forms of the amplitudes occurring in the phenomenology of high energy scattering, these expressions can be substituted exactly by Derivative Dispersion Relations (DDR) , with well proved convergent expressions [35–37].

Accord to the most recent studies [143],the general form for the integrals is given in Eq.(2.24)

$$I(n, \lambda, x) = \mathbf{P} \int_1^{+\infty} \frac{x'^\lambda \log^n(x)}{[x'^2 - x^2]} \, dx' \qquad \text{(B.14)}$$

$$= -\frac{\pi}{2x^2} \frac{\partial^n}{\partial \lambda^n} [x^{1+\lambda} \cot\left(\frac{\pi}{2}(1+\lambda)\right)] + \frac{(-1)^n}{x^2} 2^{-(n+1)} n! \ \Phi(\frac{1}{x^2}, n+1, \frac{1+\lambda}{2}) \ .$$

These forms are valid (exact) for real x , with $x > 1$, n zero or positive integer, $\Re(\lambda) \leq 1$. Cases of $\lambda = -(2N+1)$ require a limit procedure [36] because the

trigonometric part and the Φ functions have singularities, that cancel. It was treated in [36, 37].

The functions Φ in these expressions are presented in Digital Library of Mathematical Functions (http://dlmf.nist.gov) Sec. 25.14. , with the name of Lerch's Transcendent.

We thus have (with $x > 1$)

$$
\begin{aligned}
I(0, \lambda, x) \quad &= \mathbf{P} \int_1^{+\infty} \frac{[x'^\lambda]}{[x'^2 - x^2]} \, dx' \\
&= \frac{\pi}{2} \, x^{\lambda-1} \tan\left(\frac{\pi\lambda}{2}\right) + \frac{1}{2x^2} \, \Phi(\frac{1}{x^2}, 1, \frac{1+\lambda}{2}) \ ,
\end{aligned}
\tag{B.15}
$$

$$
\begin{aligned}
I(1, \lambda, x) \quad &= \mathbf{P} \int_1^{+\infty} \frac{[x'^\lambda \log(x)]}{[x'^2 - x^2]} \, dx' \\
&= \frac{\pi}{2} \, x^{\lambda-1} \left[\log(x) \tan\left(\frac{\pi\lambda}{2}\right) + \frac{\pi}{2} \sec^2\left(\frac{\pi\lambda}{2}\right) \right] - \frac{1}{4x^2} \, \Phi(\frac{1}{x^2}, 2, \frac{1+\lambda}{2}) \ ,
\end{aligned}
\tag{B.16}
$$

$$
\begin{aligned}
I(2, \lambda, x) \quad &= \mathbf{P} \int_1^{+\infty} \frac{[x'^\lambda \log^2(x)]}{[x'^2 - x^2]} \, dx' \\
&= \frac{\pi}{2} \, x^{\lambda-1} \left[\log^2(x) \tan\left(\frac{\pi\lambda}{2}\right) + \pi \sec^2\left(\frac{\pi\lambda}{2}\right)[\log(x) + \frac{\pi}{2}\tan\left(\frac{\pi\lambda}{2}\right)] \right] \\
&\quad + \frac{1}{4x^2} \, \Phi(\frac{1}{x^2}, 3, \frac{1+\lambda}{2}) \ .
\end{aligned}
\tag{B.17}
$$

$$
\begin{aligned}
I(3, \lambda, x) \quad &= \mathbf{P} \int_1^{+\infty} \frac{[x'^\lambda \log^3(x)]}{[x'^2 - x^2]} \, dx' \\
&= \frac{\pi}{2} \, x^{\lambda-1} \left[\log^3(x) \tan\left(\frac{\pi\lambda}{2}\right) + \frac{\pi}{2} \sec^2\left(\frac{\pi\lambda}{2}\right) \left(3\log^2(x) + 3\pi \log(x) \tan\left(\frac{\pi\lambda}{2}\right) \right. \right. \\
&\quad \left. \left. + \frac{\pi^2}{2}[1 + 3\tan^2\left(\frac{\pi\lambda}{2}\right)] \right) \right] - \frac{3}{8x^2} \, \Phi(\frac{1}{x^2}, 4, \frac{1+\lambda}{2}) \ ,
\end{aligned}
\tag{B.18}
$$

$$I(4, \lambda, x) = \mathbf{P} \int_{1}^{+\infty} \frac{[x'^{\lambda} \log^4(x)]}{[x'^2 - x^2]} \, dx' \tag{B.19}$$

$$= \frac{\pi}{2} \, x^{\lambda-1} \left[\log^4(x) \tan\left(\frac{\pi\lambda}{2}\right) + \pi \sec^2\left(\frac{\pi\lambda}{2}\right) \left(2\log^3(x) + (3\pi) \log^2(x) \tan\left(\frac{\pi\lambda}{2}\right) \right. \right.$$

$$\left. \left. + (\pi^2) \log(x) [1 + 3\tan^2\left(\frac{\pi\lambda}{2}\right)] + \frac{\pi^3}{2} \tan\left(\frac{\pi\lambda}{2}\right) [2 + 3\tan^2\left(\frac{\pi\lambda}{2}\right)] \right) \right] + \frac{3}{4x^2} \, \Phi(\frac{1}{x^2}, 5, \frac{1+\lambda}{2}) \;.$$

The functions Φ in these expressions are the Hurwitz-Lerch transcendents, $\Phi\left(1/x^2, N, (1+\lambda)/2\right)$, that for large x have the series expansions

$$\frac{1}{2^N} \frac{1}{x} \, \Phi(\frac{1}{x^2}, N, \frac{1+\lambda}{2}) = \frac{x^{-1}}{(1+\lambda)^N} + \frac{x^{-3}}{(3+\lambda)^N} + \frac{x^{-5}}{(5+\lambda)^N} + \dots \tag{B.20}$$

HurwitzLerchPhi is the name to call this function in Mathematica. It is presented in Digital Library of Mathematical Functions (http://dlmf.nist.gov) Sec. 25.14. , with the name of Lerch's Transcendent. Its derivative has the property used above

$$\frac{\partial}{\partial\lambda}\Phi(z, N, \frac{1+\lambda}{2}) = -\frac{N}{2} \, \Phi(z, N+1, \frac{1+\lambda}{2}) \;. \tag{B.21}$$

General Properties of Derivatives, Recurrences and Series of the $\Phi(z, N, q)$ function

The Φ functions are defined by the identities

$$\Phi(z, s, a+1) = \frac{1}{z} \left(\Phi(z, s, a) - \frac{1}{a^s} \right), \tag{B.22}$$

$$\Phi(z, s-1, a) = \left(a + z\frac{\partial}{\partial z} \right) \Phi(z, s, a), \tag{B.23}$$

$$\Phi(z, s+1, a) = -\frac{1}{s} \frac{\partial}{\partial a}\Phi(z, s, a), \tag{B.24}$$

stemming from the series representation of the Lerch's transcendent [**?**, Eq. 25.14.1]

$$\Phi(z, s, a) = \sum_{m=0}^{\infty} \frac{z^m}{(a + m)^s} \, , \tag{B.25}$$
$$a \neq 0, -1, -2, \ldots, \quad |z| < 1; \qquad \Re s > 1, \quad |z| = 1 \, .$$

We rewrite the equations in forms more similar to those used in this text

$$\frac{\partial \Phi(z, \nu, q)}{\partial q} = -\nu \; \Phi(z, \nu + 1, q) \, , \tag{B.26}$$

$$\left(q + \frac{\partial}{\partial \log(z)} \right) \Phi(z, \nu, q) = \Phi(z, \nu - 1, q) \tag{B.27}$$

$$\Phi(z, \nu, q + 1) = \frac{1}{z} [\Phi(z, \nu, q) - \frac{1}{q^\nu}] \tag{B.28}$$

For $z < 1$,

$$\Phi(z, \nu, q) = \frac{1}{q^\nu} + \frac{z}{(1 + q)^\nu} + \frac{z^2}{(2 + q)^\nu} + \frac{z^3}{(3 + q)^N} + \frac{z^4}{(4 + q)^\nu} + \ldots \tag{B.29}$$

The sums converge rapidly for energies above 10 GeV, and are easily included in practical computations, requiring only one or a few terms of the series. The singularities of the Φ functions and of the trigonometric logarithmic part of Eq.(B.15) occurring for λ negative odd integer exactly cancel each other, and the limit procedures have been studied in [37]

Appendix C

Calculation of the Coulomb phase

with $B_R \neq B_I$

Here we give details of the evaluation of the phase of West and Yennie given by Eq. (3.54) in the case where we let $B_R \neq B_I$.

After Eq. (3.55) we define

$$
\begin{aligned}
G_R &= \frac{c}{c+i} = \frac{c(c-i)}{c^2+1} \\
G_I &= \frac{1}{c+i} = \frac{(c-i)}{c^2+1} \ ,
\end{aligned}
\tag{C.1}
$$

and the integral in Eq.(3.54) is written

$$
\begin{aligned}
&\int_{-4p^2}^{0} \frac{dt'}{|t'-t|} \left[1 - \frac{F^N(s,t')}{F^N(s,t)} \right] \\
&= G_R \int_{-4p^2}^{0} \frac{dt'}{|t'-t|} \left[1 - e^{B_R(t'-t)/2} \right] + iG_I \int_{-4p^2}^{0} \frac{dt'}{|t'-t|} \left[1 - e^{B_I(t'-t)/2} \right]
\end{aligned}
\tag{C.2}
$$

and then

$$
\begin{aligned}
\Phi(s,t) \;=\;& (-/+)\left[\ln(-\frac{t}{s}) + G_R \int_{-4p^2}^{0} \frac{dt'}{|t'-t|}\left[1 - e^{B_R(t'-t)/2}\right] \right. \\
& \left. +\; iG_I \int_{-4p^2}^{0} \frac{dt'}{|t'-t|}\left[1 - e^{B_I(t'-t)/2}\right] \right] .
\end{aligned}
\tag{C.3}
$$

We note that both integrals are of the form

$$
I(B) = \int_{-4p^2}^{0} \frac{dt'}{|t'-t|}\left[1 - e^{B(t'-t)/2}\right]
\tag{C.4}
$$

which has been studied by V. Kundrát and M. Lokajicek [59]. With $x = t' - t$ and $y = Bx/2$, we have

$$
\begin{aligned}
I(B) \;=\;& \int_{-4p^2}^{0} \frac{dx}{|x|}\left[1 - e^{Bx/2}\right] = \int_{-B(4p^2+t)/2}^{-Bt/2} \frac{dy}{|y|}\left[1 - e^{y}\right] \\
=\;& \int_{-B(4p^2+t)/2}^{0} \frac{dy}{|y|}\left[1 - e^{y}\right] + \int_{0}^{-Bt/2} \frac{dy}{|y|}\left[1 - e^{y}\right] \\
=\;& \int_{0}^{B(4p^2+t)/2} \frac{dy}{|y|}\left[1 - e^{-y}\right] - \int_{0}^{-Bt/2} \frac{dy}{|y|}\left[e^{y} - 1\right]
\end{aligned}
\tag{C.5}
$$

These expressions can be written in terms of exponential integrals, as can be seen in the Handbook of Mathematical Functions of M. Abramowitz and L.A. Stegun [61] as

$$
\int_{0}^{B(4p^2+t)/2} \frac{dy}{|y|}\left[1 - e^{-y}\right] = E_1\left[\frac{B}{2}\left(4p^2 + t\right)\right] + \ln\left[\frac{B}{2}\left(4p^2 + t\right)\right] + \gamma
\tag{C.6}
$$

and

$$
\int_{0}^{-Bt/2} \frac{dy}{|y|}\left[e^{y} - 1\right] = E_i\left(-\frac{B}{2}t\right) + \ln\left(-\frac{B}{2}t\right) - \gamma
\tag{C.7}
$$

where $\gamma = 0.5772$ is the Euler constant.

Thus the integrals that appear in Eq. (C.2) have the functional form

$$I(B) = E_1\left[\frac{B}{2}\left(4p^2 + t\right)\right] - E_i\left[-\frac{Bt}{2}\right] + \ln\left[\frac{B}{2}\left(4p^2 + t\right)\right] + \ln\left[-\frac{Bt}{2}\right] + 2\gamma , \quad (C.8)$$

and the phase can be written

$$\Phi(s,t) = (-/+)\left[\ln\left(-\frac{t}{s}\right) + G_R\ I(B_R) + iG_I\ I(B_I)\right] \quad (C.9)$$

or

$$\Phi(s,t) = (-/+)\left[\ln\left(-\frac{t}{s}\right) + \frac{1}{c^2+1}\left[c^2 I(B_R) + I(B_I)\right] + i\frac{c}{c^2+1}\left[I(B_I) - I(B_R)\right]\right] .$$
$$(C.10)$$

Bibliography

[1] H. Fritzsch and M. Gell-Mann, eConf C720906V2 (1972) 135.

[2] H. Fritzsch, M. Gell-Mann and H. Leutwyler, *Phys. Lett.* **B47** (1973) 365.

[3] H. Fritzsch, CERN Cour. 52N8 (2012) 21.

[4] Y. V. Kovchegov and E. Levin, *Quantum Chromodynamics at High Energies* , Cambridge Univ. Press (2012).

[5] W. Greiner, S. Schramm and E. Stein, *Quantum Chromodynamics* , ISBN 3-540-57103-5, Springer (2002).

[6] D. J. Gross and F. Wilczek, *Phys. Rev. Lett.* 30 (1973) 1343.

[7] H. D. Politzer, *Phys. Rev. Lett.* 30 (1973) 1346.

[8] K.G. Wilson, *Phys. Rev.* **D10**, 2445 (1974).

[9] J. C. Collins, *Phys. Rev.* **D57**, 3051 (1998) [Erratum-ibid. **D61**, 019902 (2000)].

[10] I. Ia. Pomeranchuk, *Soviet Phys. JETP*, **34**, 499 (1958).

[11] H. Miyazawa, *Soryushiron Kenkyu* **17**, 206 (1958).

[12] M Froissart, *Phys. Rev.* **123** (1961) 1053.

[13] A. Martin, *Nuov. Cimen.* **42**, 930 (1966).

[14] L. Lukaszuk and A. Martin, *Nuovo Cimento A* **52**, 122 (1967).

[15] A. Martin and S. M. Roy, *Phys. Rev.* **D89** , 045015 (2014); *Phys. Rev.* **D91** , 076006 (2015).

[16] H.G. Dosch, E. Ferreira and A. Kramer, *Phys. Lett.* **B289**, 153 (1992); *Phys. Lett.* **B318**, 197 (1993); *Phys. Rev.* **D50**, (1994).

[17] H. G. Dosch, *Phys. Lett.* **B190**, 177 (1987).

[18] E. Ferreira, F. Pereira, *Phys. Rev.* **D59**, 014008 (1998).

[19] E. Ferreira, F. Pereira, *Phys. Rev.* **D61**, 077507 (2000).

[20] A. Kendi Kohara, E. Ferreira and T. Kodama, *Eur. Phys. J.* , **C73**, 2326 (2013).

[21] A. Kendi Kohara, E. Ferreira and T. Kodama, *Eur. Phys. J.* , **C74**, 3175 (2014).

[22] S. Donnachie, H. G. Dosch, P. Landshoff and O. Nachtmann, *Pomeron Physics and QCD* , Cambridge Univ. Press 2002.

[23] V. Barone E. Predazzi, *High-Energy Particle Diffraction* , ISBN 978-3-642-07567-4 , Springer 2002.

[24] G. Ingelman and P. E. Schlein, *Phys. Lett.* **B152** (1985) 256.

[25] D.A. Fagundes, M.J. Menon, P.V.R.G. Silva *J. Phys.* **G40**, 065005 (2013).

[26] A. K. Kohara, E. Ferreira and T. Kodama, *J. Phys.* **G41**, 115003 (2014).

[27] P. Abreu et al , Auger Coll., *Phys. Rev. Lett.* **109**, 062002 (2012).

[28] K. Belov et al. , HiRes Coll., Fly's Eye Exp., *Nucl. Phys. (Proc. Suppl)* **B151** (2006) 197-204.

[29] R. M. Baltrusaitis, et al., Fly's Eye Experiment , *Phys. Rev. Lett.* **52** (1984) 1380-1383.

[30] M. Honda , Akeno Coll., *Phys. Rev. Lett.* **70** (1993) 525-528.

[31] S. P. Knurenko et al. , Yakutsk Array Coll. , (1999) , Proc. of 26th ICRC (ICRC 99) (Salt Lake City, USA) Vol 1, p. 372.

[32] G. Aielli et al., ARGO-YBJ experiment, *Phys. ReV.* **D80**, 092004 (2009).

[33] H. H. Mielke et al., *Jour. Phys.* **G20** (1994) 637.

[34] M. Aglietta et al., *Phys. Rev.* **D79**, 032004 (2009).

[35] R.F. Ávila and M.J. Menon, *Nucl. Phys. A* **744** (2004) 249; *Braz. J. Phys.* **37**, 358 (2007).

[36] E. Ferreira and J. Sesma, *J. Math. Phys.* **49**, 033504 (2008).

[37] E. Ferreira and J. Sesma *J. Math. Phys.* 54, 033507 (2013).

[38] E. Ferreira, *Int. J. Mod. Phys.* **E16**, 2893 (2007).

[39] M.A. Shifman, A.I. Vainshtein, V.I. Zakharov, *Nucl Phys.* **B147**, 385 (1979).

[40] O. Nachtmann , *Ann. of Phys.* (N.Y.) **209**, 436 (1991).

[41] H.G. Dosch, A.Kramer *Phys. Lett.* **B252**, 669 (1990).

[42] H.G. Dosch and Yu.A. Simonov, *Phys. Lett.* **B205** (1988) 399; Yu.A. Simonov,*Nucl. Phys.* **B307** (1988) 512.

[43] A. Kramer and H.G. Dosch, *Phys. Lett.* **B272** (1991) 114.

[44] E. Ferreira, H.G. Dosch, A.Kramer *Phys. Lett.* **B289**, 153 (1992).

[45] N.E Bralic, *Phys. Rev.* **D22**, 3090 (1980).

[46] M. D'Eglia, A. Di Giacomo and E. Meggiolaro, *Phys. Lett.* **B408** (1997) 315.

[47] F. Pereira and E. Ferreira, *Phys. Rev.* **D55**, 130 (1997).

[48] F. Pereira and E. Ferreira, *Phys. Rev.* **D59**, 014008 (1998); *Phys. Rev.* **D61**, 077507 (2000).

[49] K.A. Olive et al. (Particle Data Group), *Chin. Phys.* **C38**, 090001 (2014).

[50] A.K. Kohara, E. Ferreira, T. Kodama 2012. 3 pp. Published in AIP Conf.Proc. 1520 (2013) 321-323.

[51] A. Kendi Kohara, E. Ferreira and T. Kodama , *Phys.Rev.* **D87**, 054024 (2013).

[52] H. G. Dosch, P. Gauron and B. Nicolescu, *Phys. Rev.* **D67** 077501 (2003).

[53] M. Giordano and E. Meggiolaro *JHEP* **1403** , (2014) 002 ; *Phys. Lett.* **B744** (2015) 263.

[54] A. Martin, *Phys. Lett.* **B404**, 137 (1997).

[55] H.A. Bethe, *Phys. Lett.* **B404**, 137 (1997).

[56] G. B. West and D. Yennie , *Ann. of Phys.* **3**, 190 (1958).

[57] O. V. Selyugin , *Mod. Phys. Lett.* **A11**, 2317 (1996); *Mod. Phys. Lett.* **A12**, 1379 (1997); *Phys. Rev.* **D60**, 074028 (1999).

[58] V.A. Petrov, E. Predazzi and A. Prokudin, *Eur. Phys. J.* **C28**, 525 (2003).

[59] V.Kundrát and M.Lokajicek, *Phys. Lett.* **B611**, 102 (2005); V.Kundrát, M.Lokajicek and I. Vrococ, *Phys. Lett.* **B656**, 182 (2007).

[60] K. Kang and B. Nicolescu, Phys. Rev. **D11**,2461 (1975); P. Gauron, B. Nicolescu and O.V. Selyugin, *Phys. Lett.* **B629**, 83 (2005).

[61] M. Abramowitz and I. Stegun, *Handbook of Mathematical Functions* , Dover, New York, 1972.

[62] A. K. Kohara *Master Thesis* , UFRJ, Rio de Janeiro, 2012.

[63] A. A. Kuznetsov et al. , *Sov. J. Nucl. Phys.* **33**, 74 (1981), and *Yad. Fiz.* **33**, 142 (1981).

[64] L.A. Fajardo et al, *Phys. Rev.* **D24**, 46 (1981).

[65] J.P. Burq et al, *Phys. Lett.* **B190**, 124 (1982); *Nucl. Phys.* **B217**, 285, (1989).

[66] R.E. Breedon et al, *Phys. Lett.* **B216**, 459 (1989); R.E. Breedon, PhD Thesis, Rockefeller Univ. (1988).

[67] A. Schiz et al. , exp. FNAL-069A , *Phys. Rev.* **D24**, 26 (1981). *Nucl. Phys.* **B262**, 689 (1985).

[68] W. Faissler et al. , *Phys. Rev.* **D23**, 33 (1981).

[69] U. Amaldi and K. R. Schubert , *Nucl. Phys.* **B166**, 301 (1980).

[70] N. A. Amos et al., *Nucl. Phys.* **B262**, 689 (1985).

[71] C. Augier et al. , CERN UA4/2 Coll. , *Phys. Lett.* **B316**, 448 (1993).

[72] G. Arnison et al. , CERN UA1 Coll. , *Phys. Lett.* **B128**, 336 (1983).

[73] D. Bernard et al., CERN UA4 Coll., *Phys. Lett.* **B198**, 583 (1987).

[74] F. Abe , Fermilab CDF Coll., *Phys. Rev.* **D50**, 5518 (1993).

[75] M. Bozzo et al., CERN UA4 Coll., *Phys. Lett.* **B147**, 385 (1984).

[76] M. Bozzo et al., CERN UA4 Coll., *Phys. Lett.* **B155**, 197 (1985).

[77] N. Amos et al, Fermilab E-710 Coll, *Phys. Lett.* **B262**, 127, (1990).

[78] F. Abe et al. , Fermilab CDF Coll., *Phys. Rev.* **D50**, 5518 (1994).

[79] CERN-PH-EP-2012-239 and Durham Data Basis ; K. Eggert , talk at 2012 LHC Days, Split, Croatia, 1-6 October 2012.

[80] G. Antchev et al.(TOTEM Collaboration), *Europhys. Lett.* **101**, 21002 (2013).

[81] G. Antchev et al.(TOTEM Collaboration), *Nucl. Phys.* **B899** (2015) 527–546.

[82] A. Donnachie, P. Landshoff, *Zeit. Phys.* **C2**, 55 (1979); *Phys. Lett.* **B387**, 637 (1996).

[83] E. Nagy *et al. Nucl.Phys.* **B150** (1979) 221 ; N. Amos *et al. Nucl. Phys.* **B262** (1985) 689.

[84] V. M. Abazov et al, D0 Coll., *Phys. Rev.* **D86** , 012009 (2012).

[85] N. Amos et al. *Phys. Rev. Lett.* **68**, 2433 (1992); C. Avila et al., *Phys. Lett.* **B537**, 41 (2002).

[86] F. Abe et al. *Phys. Rev.* **D50**, 5550 (1994).

[87] G. Antchev et al., Totem Coll., *Eur. Phys. Lett.* **101** (2013) 21003.

[88] G. Antchev et al., Totem Coll., *Eur. Phys. Lett.* **101** (2013) 21004.

[89] B. Abelev et al., ALICE Coll., *Eur. Phys. J.* **C73** (2013) 2456.

[90] G. Aad et al., *Nature Commun.* 2:463 (2011).

[91] S. Chatrchyan et al., CMS Coll., *Phys. Lett.* **B722** (2013) 5.

[92] S. Klimenko, J. Konigsberg and T. M. Liss, FERMILAB-FN-0741 (2013).

[93] A. Kendi Kohara, E. Ferreira and T. Kodama, [arxiV:hep-ph/1406.5773].

[94] G. Antchev et al., Totem Coll., *Phys. Rev. Lett.* **111** (2013) 012001.

[95] M. Deile, Totem Coll., Talk at DIS 2014 (Warsaw, April 2014); J. Kaspar, Totem Coll., talk at XXX-th International Workshop on High Energy Physics, Protvino, June 2014.

[96] V. Kundrát and M. Lokajícek, *Phys. Lett.* **B611** (2005) 102 ; R. Cahn, *Z. Phys.* **C15** (1982) 253.

[97] J. Dias de Deus, *Nucl. Phys.* , **B59** (1973) 231; A.J. Buras, J. Dias de Deus, *Nucl.Phys.* , **B71** (1974) 481; J. Dias de Deus, P. Kroll, *J. Phys.* , **G9** (1983) L81; J. Dias de Deus, *Acta Phys. Polon.* , **B6** (1975) 613.

[98] R.J. Glauber, *Phys. Rev.* **100** (1955) 242-248 ; R.J. Glauber and G. Matthiae, *Nucl. Phys.* **B21** (1970) 135-157.

[99] M. L. Good and W. D. Walker, *Phys. Rev.* **120** (1960) 1857-1860.

[100] R. Engel and R. Ulrich , Internal Pierre Auger Note GAP-2012, March 2012.

[101] R. C. Barret and D. F. Jackson, *Nuclear Size and Structure*, Clarendon Oxford 1977.

[102] C. Bourrely, J. Soffer, T. T. Wu, *Phys. Rev.* **D19**, 3249 (1979); C. Bourrely, J. Soffer, T. T. Wu, *Nucl. Phys.* **B247**, 15 (1984); C. Bourrely, J. Soffer, T. T. Wu, *Eur. Phys. J.* **C28**, 97 (2003).

[103] C. Bourrely, J. M. Myers, J. Soffer, T. T. Wu, *Phys. Rev.* **D85**, 096009 (2012).

[104] C. Bourrely, *Eur. Phys. J.* **C74**, 2736 (2014).

[105] O. V. Selyugin, *Eur. Phys. J.* **C72**, 2073 (2012).

[106] O. V. Selyugin, *Phys. Rev.* **D91**, 113003 (2015) (private communication is gratefully acknowlodged).

[107] O. V. Selyugin, EDSBLOIS-2013-08, [arXiv:hep-ex/1310.0928].

[108] E. G. S. Luna, A. F. Martini, M. J. Menon, A. Mihara, and A. A. Natale *Phys. Rev.* **D72**, 034019 (2005); D.A.Fagundes, E.G.S. Luna, M.J. Menon and A.A. Natale , *Nucl. Phys.* **A886**, 48 (2012).

[109] J. M. Cornwall, *Phys. Rev.* **D26**, 1453 (1982).

[110] M. Derrick *et al.* [ZEUS Collaboration], *Phys. Lett.* **B315** (1993) 481.

[111] T. Ahmed *et al.* [H1 Collaboration], *Nucl. Phys.* **B429** (1994) 477.

[112] S. Abachi *et al.* [D0 Collaboration], *Phys. Rev. Lett.* **72** (1994) 2332.

[113] F. Abe *et al.* [CDF Collaboration], *Phys. Rev. Lett.* **74** (1995) 855.

[114] S. Chekanov *et al.* [ZEUS Collaboration], *Nucl. Phys.* **B816**, 1 (2009).

[115] F. D. Aaron *et al.* [H1 Collaboration], *Eur. Phys. J.* **C72**, 2074 (2012).

[116] F. D. Aaron *et al.* [H1 and ZEUS Collaborations], *Eur. Phys. J.* **C72** (2012) 2175.

[117] T. Affolder *et al.* [CDF Collaboration], *Phys. Rev. Lett.* **84** (2000) 5043.

[118] C. Marquet, C. Royon, M. Saimpert and D. Werder, *Phys. Rev.* **D88** (2013) 7, 074029.

[119] M. Boonekamp, A. Dechambre, V. Juranek, O. Kepka, M. Rangel, C. Royon and R. Staszewski, [arXiv:hep-ph/1102.2531].

[120] C. Brenner Mariotto and V. P. Goncalves, *Phys. Rev.* **D88** (2013) 7, 074023.

[121] S. Catani, M. Fontannaz, J. P. Guillet and E. Pilon, JHEP **0205** (2002) 028; P. Aurenche, M. Fontannaz, J. P. Guillet, E. Pilon and M. Werlen, *Phys. Rev.* **D73** (2006) 094007.

[122] J. F. Owens, *Rev. Mod. Phys.* **59** (1987) 465.

[123] G. Altarelli and G. Parisi, *Nucl. Phys.* **B126**, 298 (1977); V. N. Gribov and L. N. Lipatov, *Sov. J. Nucl. Phys.* **15**, 438 (1972); *Sov. J. Nucl. Phys.* **15**, 675 (1972); Y. L. Dokshitzer, *Sov. Phys. JETP* **46**, 641 (1977).

[124] A. Aktas *et al.* [H1 Collaboration], *Eur. Phys. J.* **C48**, 715 (2006).

[125] ATLAS Collaboration, Letter of Intent for the Phase-I Upgrade of the ATLAS Experiment, CERN-LHCC-2011-012.

[126] M. Trzebiński, *Proc. SPIE Int. Soc. Opt. Eng.* **9290** (2014) 929026.

[127] M. R. Whalley, D. Bourilkov and R. C. Group, [arXiv:hep-ph/0508110].

[128] V. A. Khoze, A. D. Martin and M.G. Ryskin *Eur. Phys. J.* **C18** (2000) 167-179.

[129] L. Portugal and T. Kodama, *Nuc. Phys.* **A837** (1), 1-14 (2010).

[130] Abassi et al *Phys. Rev.* **D92** (2015), 032007

[131] J. Bartels, K. J. Golec-Biernat and H. Kowalski, *Phys. Rev.* **D66** (2002) 014001; H. Kowalski and D. Teaney, *Phys. Rev.* **D68** (2003) 114005; B. Schenke, P. Tribedy and R. Venugopalan, *Phys. Rev. Lett.* **108** (2012) 252301.

[132] M. Giordano and E.Meggiolaro, *Jour. High Energy Phys.* **03** (2014) 002.

[133] A. H. Mueller, *Nucl. Phys.* **B415**, 373 (1994).

[134] H. Navelet, Robert B. Peschanski (Saclay), C. Royon (DAPNIA, Saclay). Aug 1995. 10 pp. Published in *Phys.Lett.* **B366** (1996) 329-336.

[135] H. Navelet, Robert B. Peschanski (Saclay), C. Royon (DAPNIA, Saclay), S. Wallon (Saclay). May 1996. 14 pp. Published in *Phys.Lett.* **B385** (1996) 357-364.

[136] A. Bialas (Jagiellonian U.), Robert B. Peschanski (Saclay), C. Royon (DAPNIA, Saclay). Dec 1997. 19 pp. Published in *Phys.Rev.* **D57** (1998) 6899-6905.

[137] C. Marquet (RIKEN BNL), Robert B. Peschanski (Saclay, SPhT), G. Soyez (Paris, LPTHE). Feb 2007. 10 pp. Published in *Phys.Rev.* **D76** (2007) 034011.

[138] H.G. Dosch, E. Ferreira, *Eur. Phys. J.* **C29**, 45 (2003).

[139] H.G. Dosch, E. Ferreira, *Phys. Lett.* **B576**, 83 (2003).

[140] H.G. Dosch, E. Ferreira, A. Kramer, *Phys. Rev.* **D50**, (1992) (1994) [arXiv:hep-ph/9405237].

[141] H.G. Dosch, T. Gousset, G. Kulzinger, H.J. Pirner, *Phys. Rev.* **D55**, 2602 (1997).

[142] H.G. Dosch, E. Ferreira, *Eur. Phys. J.* **C51**, 831 (2007).

[143] E. M. Ferreira, A. K. Kohara and J. Sesma [arXiv:math/1601.02094] (2016).